REPORT DOCUMENTATION PAGE

1. REPORT NUMBER	2. GOVT ACCESSION NO.	3. RECIPIENT'S CATALOG NUMBER
RADC-TR-77-362		

4. TITLE (and Subtitle)	5. TYPE OF REPORT & PERIOD COVERED
See Title page	Final Report - 6 April 1975 - 30 September 1976
	6. PERFORMING ORG. REPORT NUMBER

7. AUTHOR(s)	8. CONTRACT OR GRANT NUMBER(s)
Shashanka S. Mitra	F19628-75-C-0163 URI 9804-4263

9. PERFORMING ORGANIZATION NAME AND ADDRESS	10. PROGRAM ELEMENT, PROJECT, TASK AREA & WORK UNIT NUMBERS
University of Rhode Island Electrical Engineering Department Kingston, Rhode Island 02881	

11. CONTROLLING OFFICE NAME AND ADDRESS	12. REPORT DATE
Deputy for Electronic Technology RADC/ETSS Hanscom AFB, Massachusetts 01731	February, 1977
	13. NUMBER OF PAGES
	iv plus 273

14. MONITORING AGENCY NAME & ADDRESS(if different from Controlling Office)	15. SECURITY CLASS. (of this report)
ONR 495 Summer Street Boston, Massachusetts	Unclassified
	15a. DECLASSIFICATION/DOWNGRADING SCHEDULE

16. DISTRIBUTION STATEMENT (of this Report)

Approved for public release, distribution unlimited.

17. DISTRIBUTION STATEMENT (of the abstract entered in Block 20, if different from Report)

DDC RECEIVED
OCT 19 1979
A

18. SUPPLEMENTARY NOTES

19. KEY WORDS (Continue on reverse side if necessary and identify by block number)

CO_2 laser, HF laser, DF laser, CO laser, 10.6 μm radiation, 2 to 6 μm radiation, infrared transmitting materials, multiphonon absorption, amorphous materials, mixed crystals, electronic band structure, opto-elastic coefficients, alkaline earth fluorides, diamond, Ge, Si, III-V semiconductors.

20. ABSTRACT (Continue on reverse side if necessary and identify by block number)

Several optical properties of materials suitable as components useable with CO_2 (10.6 μm) and other chemical lasers (2 to 6 μm) are considered. Frequency and temperature dependence of absorption coefficient in the transparent regime of alkaline earth fluorides and mixed fluorides have been measured and understood on the basis of current theories and their desirability as window materials in the 2 to 6 μm region has been assessed. Lattice dynamics of mixed crystals and structurally disordered solids

DISCLAIMER NOTICE

THIS DOCUMENT IS BEST QUALITY
PRACTICABLE. THE COPY FURNISHED
TO DDC CONTAINED A SIGNIFICANT
NUMBER OF PAGES WHICH DO NOT
REPRODUCE LEGIBLY.

20

have been considered in the context of their phonon optical properties. The optical properties and electronic structure of amorphous semiconductors have been investigated emphasizing the changes relative to the ordered state resulting from the structural disorder. Also considered here are the properties, e.g., elasto-optic coefficients, responsible for beam distortion at high photon flux in an optical component.

Accession For	
NTIS GRA&I	✓
DDC TAB	☐
Unannounced	☐
Justification	
By	
Distribution/	
Availability Codes	
Dist.	Avail and/or special
A	

REPLY TO
ATTN OF: TSR/2235   25 Sep 79

SUBJECT: Correction to RADC TR-77-362

TO: DDC/TCA, Mr Cundiff

Request a correction be made to the DD Form 1473 of subject
document to reflect the following title: Optical Materials for
2 to 6μm and 10.6μm High Power Lasers. This is the same title
that is reflected on the cover of the document.

KENNETH M. ZIMMERMAN
Chief, Tech Reports Section
Tech Data & Info Branch

6

OPTICAL MATERIALS FOR 2 to 6 *micrometers*
AND 10.6 ☐ HIGH POWER LASERS.
micrometers

10

Shashanka S. Mitra
Electrical Engineering Department
University of Rhode Island
Kingston, Rhode Island 02881

18 RADC   19 TR-77-362

14

URI-9804/4263

12 284

9

FINAL REPORT.

Period covered: 6 April 1975 to 30 September 1976,

11 February 1977

15   F19628-75-C-0163

SOLID STATE SCIENCE DIVISION
DEPUTY FOR ELECTRONIC TECHNOLOGY
RADC/ETSS
HANSCOM AFB, MASSACHUSETTS 01731

305 570

FOREWORD

This final report describes the research performed under Contract No. F19628-75-C-0163 from 6 April 1975 to 30 September 1976. The primary research objective of this project was experimental and theoretical investigations of materials suitable as windows and optical components for the high power CO_2 laser operating in the 10.6 μm region and chemical lasers in the 2 to 6 μm region. Particular emphasis was given to characterizing such materials and to determine the factors limiting their performance. Research included the following areas: (i) Frequency and temperature dependence of absorption coefficient in the transparent regime of solids; (ii) lattice dynamics and phonon optical properties of structurally disordered solids; (iii) optical and electronic properties of crystalline and amorphous semiconductors and (iv) theory of Brillouin effect, calculation of elasto-optic constants. During the tenure of the contract, eleven papers were written under the sponsorship of the contract. A majority of these papers have been published in relevant journals. The reprints and preprints of these papers constitute the final report. Also included are reprints of papers covering work initiated at the Solid State Sciences Division, Deputy for Electronic Technology, RADC and other laboratories to which the principal investigator has contributed. The principal investigator was assisted by several graduate research assistants in carrying out this research. Helpful discussions with and close collaboration of Dr. B. Bendow, Mr. H. G. Lipson

and Dr. Y. F. Tsay of the Air Force are gratefully acknow-
ledged. The names of various individuals appear in the ap-
propriate sections of this report to which they have made
contributions.

S. S. Mitra
Professor of Electrical Engineering

ii

CONTENTS

I. INTRODUCTION

1.1 General

In the past few years, considerable progress has been made in the investigation of materials and components for high power CO_2 lasers emitting at 10.6 μm. Materials suitable for transmitting infrared radiation at 10.6 μm have been identified, and the absorption processes that limit the transparency of such solids have been, to a certain extent, explored. There are two chief sources of absorption in a pure solid, viz., lattice vibrations and electronic transitions. For most materials a sufficiently wide spectral window exists between these two limits where the material is transparent. However, this transparent regime displays residual absorption due to (i) multiphonon processes, (ii) defects and impurities, (iii) phonon-assisted electronic transitions in the long-wavelength tail of the fundamental absorption edge, and/or (iv) multiphoton electronic transitions in the case of high photon flux. The limiting absorption in transparent solids in the 10.6 μm region is entirely due to mechanisms (i) and (ii). A number of theoretical treatments have been presented[1] to account for absorption due to higher order phonon processes and its temperature dependence. The agreement, wherever experimental data exist, has been reasonably good. Although some experimental data exist on the effects of impurities and defects on the absorption of a solid in the transparent regime, only limited progress has been made[2] towards a proper delineation of causes and sources of this

1

additional absorption process in the 10.6 μm region. In shorter wavelength regions the situation gets further complicated due to contributions from the other two mechanisms mentioned above.

Recently, much interest has been evidenced in the development and use of chemical lasers, operating in the two to six micron region. However, research on the materials problem for these lasers so far has not attracted a comparable amount of concentrated effort as in the case of the CO_2 laser. In the present project, we have considered a number of basic problems concerning the window materials for chemical lasers operating in the 2 to 6 μm region, and their possible resolution. Of particular interest among chemical lasers are HF, DF and CO lasers operating in the range of 2.6 to 3.5 μm, 3.6 to 5 μm, and 4.9 to 5.7 μm, respectively.

The residual absorption plays an important role in the selection of a material for use as an optical component in high power laser applications. A number of other optical properties also play a significant role in such a selection. The optical property also of interest in this connection is the refractive index, n and its temperature, stress and pressure dependence. The pressure dependence of n for example, contributes to pressure-induced distortion[3] of a laser beam. The stress dependence of n is associated with a variety of unacceptable distortion effects on the transmission of laser beams and the associated degeneration of the transmitted beam through interference and multiple refraction. The temperature derivative of n and its sign, on the other hand,

2

determine[5] the extent and nature (concave or convex) of thermal lensing, which becomes an important consideration in high electric fields. Both internal and external stresses are capable of distorting the beam and thus limiting the optical performance of laser windows. These effects have already been considered[6] to some extent for materials pertaining to 10.6 μm radiation. Further consideration is given to materials particularly suitable as optical compenents in the 2 to 6 μm region.

1.2 Multiphonon Absorption

Experimentally observed exponential dependence of absorption coefficients, α on frequency

$$\alpha = A \exp\left(-\frac{\omega}{\omega_o}\right) \tag{1}$$

in the transparent regime in the high frequency side of the fundamental lattice optical mode frequencies is attributed to multiphonon interactions. The minimum residual absorption by a solid in this regime is due to multiphonon processes, and any additional absorption is thus to be attributed to other effects, particularly defects, surface conditions and impurities.

We have already proposed[7] a treatment for the frequency dependence of absorption coefficient due to higher order multiphonon processes in alkali halides. Joint phonon density of states for higher order processes were obtained using a breathing shell model of lattice dynamics and relaxation of the wave-vector selection rule restrictions. The absorption

3

from three and higher order multiphonon processes was shown
to be given by

$$\alpha = \sum_{j>2} \frac{A_j \rho_j(\omega) \hbar \omega^2}{2c \varepsilon'^{1/2}} \qquad (2)$$

where A_j denotes the oscillator strength for the jth order
process, $\rho_j(\omega)$ the j-phonon joint density of states given by
the jth convolution of the one-phonon density of states, and
ε' the essentially frequency independent real part of dielec-
tric constant for this region. In the case of alkali halides,
the calculated values were found to be in good agreement with
experimental ones.

If the incident light intensity is relatively high, even
a very transparent window may absorb a significant amount
of energy resulting in an increase in temperature. It is
needless to say that the absorption coefficient is strongly
temperature dependent. In determing α for $T > 0^\circ K$, one must
account for both explicit and implicit temperature dependence.
α is a fundtion of T through the temperature dependence of
A_j and $\rho_j(\omega)$. It was shown that the temperature dependence
of A_j comes mainly through phonon-occupation number, and in
the limit of not too low a temperature, it is given by

$$A_j \propto T^{j-1} \qquad (3)$$

The temperature dependence of ρ_j poses a difficult problem.
It is well known that all phonon frequencies shift with tem-
perature, in general to lower values. Thus at a higher tem-
perature and for a fixed photon frequency, higher order
phonon processes start contributing. One may account for

4

this effect in several ways. One may assume that all phonons shift equally with T, and take a representative phonon [ω_o of eq. (1)], e.g., the long-wavelength transverse and/or longitudinal optic phonon frequencies, ω_{TO} or ω_{LO}. The temperature dependence of ω_{TO} and ω_{LO} are known in some cases, and are obtainable for others from the measurement of temperature dependent reststrahlen and Raman spectra, depending on the structure and nature of bonding of the crystal under consideration. It has generally been assumed that high frequency (optical) phonons contribute more to this absorption process than low frequency phonons. Then one may possibly use the "Brout sum average" phonon frequency given (for a diatomic cubic crystal) by

$$\bar{\omega}_B = \left(\frac{\omega_{LO}^2 + 2\omega_{TO}^2}{3} \right)^{1/2} \tag{4}$$

The temperature dependence of $\bar{\omega}_B$ is readily obtainable from the temperature dependence of bulk modulus and thermal expansion coefficient, since[8]

$$\bar{\omega}_B = \text{const} \left(\frac{aB}{\mu} \right)^{1/2} \tag{5}$$

where the constant depends on the crystal structure, B is the bulk modulus, a the lattice constant and μ the reduced mass. A third possibility is to actually obtain the one-phonon density of states as functions of temperature for an anharmonic lattice. Some of these possibilities have been explored, and the calculation has been extended to candidate materials for the two to six micron region.

1.3 Effects of Impurities, Defects and Disorder

It was remarked earlier that with the absorption decreasing rapidly by orders of magnitude away from the fundamental lattice region, it is evident that the limiting absorption mechanism for many cases of interest will be that due to impurities. In alkali halides the principal impurities contributing to infrared absorption are the molecular variety such as OH^-, $CO_3^=$, ClO_3^-, $SO_4^=$, NO_3^-, and similar ions, depending on the particular material and growth condition. At the CO_2 laser frequency, 943 cm^{-1} the intrinsic absorption coefficient due to multiphonon processes is for example $\sim 5 \times 10^{-7}$ cm^{-1} for KBr and $\sim 8 \times 10^{-5}$ cm^{-1} for KCl, respectively. These are extrapolated values from higher absorption region. On the other hand, purest samples of these two alkali halides display absorption coefficient $>10^{-4}$ cm^{-1} at 943 cm^{-1}, showing the importance of the contribution from impurities. A typical impurity like the carbonate ion has absorption bands in the vicinity of 670 cm^{-1}, 710 cm^{-1}, 880 cm^{-1}, 1060 cm^{-1}, and 1450 cm^{-1}; likewise the chlorate ion has absorption bands around 490 cm^{-1}, 610 cm^{-1}, 910 cm^{-1}, and 960 cm^{-1}. Thus it is obvious that any of these ions inadvertently introduced in a window material or produced during the growth process may individually or in concurrence with other impurities may produce undesirable structures and significant increases in the absorption level in the region of interest. Further complicating factors may arise from overtones and combinations of these molecular vibrational

6

modes and their interaction with host lattice phonons. Some progress has been made in the study of selected impurity ions in alkali halides and other matrices[2,9]. Theoretical treatments of sufficiently general nature also exist[10] to handle the interaction of a specific impurity (or impurities) with a specific host lattice.

In the shorter wavelength, e.g., 2 to 6 μm region, electronic transitions of impurities may also contribute to unwanted absorption. This is particularly true for certain fluorides and oxides like CaF_2, MgO or Al_2O_3, in which certain rare earth and/or transition metal ions customarily found as di- or tri-valent substitutional impurities. A transition metal ion Mn^{+2}, for example, has unfilled 3d shell electrons; likewise a rare earth ion like Sm^{+2} has unfilled 4f electrons. Transitions of these unfilled electrons to higher energy levels give rise to a rich spectrum in the visible, near and mid infrared regions[11]. Such spectra are both characteristic of the ion and the host lattice. Modifications in the free ion spectrum are caused by the crystal field of the host lattice and the vibronic interactions with phonons. The problem of residual absorption in the 2 to 6 μm region window materials thus encompasses consideration of this effect also, although much information regarding it already exists in the literature.

So far, above discussions pertained to substitutional impurities. The optical property of a transparent material may also be affected by other forms of defect or disorder,

7

e.g., structural and compositional. Structural disorder causes formation of amorphous or glassy phase, whereas compositional disorder may be considered in the context of mixed crystal systems. Although such disorders will contribute to undesirable absorption in transparent materials chiefly through the breakdown of wave-vector selection rules, and through occasional resonant absorptions (e.g., local and gap modes), such disorders may also be profitably utilized in the context of laser window applications.

In recent years, considerable amount of interest has been evidenced in the use of amorphous or glassy substances as optical materials. As window materials for transmission of high energy radiant flux, glassy materials offer certain advantages as well as disadvantages. Consideration has also been given to the use of reflecting or anti-reflecting protective amorphous coatings on standard window materials. However, a search of the literature reveals that apart from some scattered experimental data, very little is available in the way of a comprehensive understanding of basic optical properties of amorphous materials. In particular, for the 10.6 μm region, a number of candidate window materials may now be prepared in amorphous form as well. The tetrahedrally bonded semiconductors like Si, Ge, the III-V and some II-VI compounds fall in this category. In addition to these, several other binary and ternary chalcogenide glasses have also been considered for possible use as high power gas laser window materials. Before a reliable appraisal of the suit-

8

ability of amorphous materials as windows or as window coatings be made, it is essential to have an understanding of relevant optical properties, expecially the modifications they undergo in the transition from the crystalline to the amorphous state. Some advances in this direction are reported here.

If the impurity content of a solid is increased to such an extent that interaction between impurity atoms begins to play an effective role, the system should then be termed a compositionally disordered solid rather than an impure crystal. If the impurity content of a disordered lattice is not isotopic in nature but of a different chemical element, one then has the so-called mixed crystal. A mixed crystal is a single crystal or polycrystalline aggregate which is formed by two elements or compounds with a range of concentration ratios. One may vary this concentration to obtain a mixed crystal system, sometimes over the whole range of compositions and the system is said to show complete solid solubility. Most alkali halides, II-VI and III-V coumpounds form mixed crystal systems. The study of vibrational properties of mixed crystals reveal two classes of mixed crystals: (i) the one-mode type in which only one set of long wavelength optic phonons occur which shifts continuously and, in most cases linearly with concentration from the frequencies of the lighter component downward to the mode frequencies of the heavier component. Examples are Na_xK_{1-x}, KCl_xBr_{1-x}, $Ni_xCo_{1-x}O$, $(Ca,Ba)_xSr_{1-x}F_2$, etc; (ii) the two-

9

mode type in which two sets of long wavelength optic phonons occur, one set of LO and TO characteristic of the lighter component, and one set characteristic of the heavier component, the strength of each mode being approximately proportional to the mole fraction of each component. Examples are Ge_xSi_{1-x}, GaP_xAs_{1-x}, ZnS_xSe_{1-x}, etc. The criteria that distinguish the so-called one- and two-mode behaviors, and their long wavelength vibrational spectra have recently been thoroughly reviewed[12] and will not be dealt upon any further. A complete lattice dynamical model has recently been developed by the principal investigator and his co-workers[13] for mixed crystal systems. It must be obvious from the foregoing discussion that both kinds of mixed crystals can be advantaneously used in the context of laser window problem. By varying the mixing ratio, one may shift the lattice resonance frequencies over a relatively wide frequency range, and thus being able to tailor the transparency and/or reflectance in a narrow frequency range. Mixed crystal systems thus offer certain advantages both as a bulk transmitting material or as reflecting or anti-reflecting coatings. The other advantage of the mixed crystal systems is that a mixed crystal is usually harder than either of the pure components[14]

Disorders like voids, dislocations, surface state which are usually inadvertently introduced during the fabrication process also affect the optical properties, usually in an undesirable manner. A systematic investigation of the effect

10

of these growth or fabrication-induced disorders on the optical properties, viz., reststrahlen spectrum, multiphonon absorption, the refractive index and its temperature coefficient will be interesting. It is envisioned that properly planned step-annealing procedures may reduce some of these unwanted effects.

1.4 Thermal Lensing and Beam Distortion

When a laser beam of non-uniform intensity passes through a semitransparent window the beam will suffer distortion as the window temperature increases. It has been established[15] that a considerable amount of thermal lensing will occur in an infrared window even if it withstands other failure mechanisms[16]. We shall not go into the details of the thermal lensing problem here, as it has been treated in great detail elsewhere[17,18]. However, it is well understood that the thermal lensing effect is caused by the temperature dependence of the refractive index at the wavelength in question. What is of importance is the time a diffraction-limited focus can be held in the far-field. The longer this time for a material, the better it is as a laser window if all other criteria are already met. It has been shown[18] that this diffraction-limited time is strongly dependent on the sign and the magnitude of dn/dT. In general, it can be said that a large negative value of dn/dT is desirable. Other beam distortions may be expressed in terms of elasto-optic coefficients $p_{ijk\ell}$ defined as

11

$$\Delta(1/n^2)_{ij} = P_{ijk\ell} \tau_{k\ell} , \qquad (6)$$

where τ is the strain tensor. In a number of recent papers, we have developed[19] a two-oscillator model for the understanding of the temperature, pressure and stress derivatives of refractive index. In this report we give a method for the calculation of elasto-optic coefficients of a number of tetrahedrally bonded semiconductors.

REFERENCES

1.   M. Sparks and L. J. Sham, Sol. St. Comm. 11, 1451 (1973);
      D. L. Mills and A. A. Maradudin, Phys. Rev. B8, 1617
      (1973); B. Bendow, S. C. Ying and S. P. Yukon, Phys. Rev.
      B8, 1679 (1973); M. Sparks and L. J. Sham, Phys. Rev.
      B8, 3037 (1973); H. B. Rosenstock, J. Appl. Phys. 44,
      4473 (1973); T. C. McGill, R. W. Hellwarth, M. Mangir
      and H. V. Winston, J. Phys. Chem. Sol. 34, 405 (1973);
      K. V. Namjoshi and S. S. Mitra, Phys. Rev. B9, 815
      (1974); and H. B. Rosenstock, Phys. Rev. B9, 1973 (1974).

2.   C. J. Duthler, J. Appl. Phys. 45, 2668 (1974); H. G.
      Lipson, J. J. Larkin, B. Bendow and S. S. Mitra, J.
      Elec. Mater., J. Elec. Mat., 4, 1 (1975).

3.   See, for example, M. Sparks and M. Cottis, J. Appl.
      Phys. 44, 787 (1973).

4.   M. Born and E. Wolf, "Principles of Optics" (MacMillan,
      New York, 1964); J. F. Nye, "Physical Properties of
      Crystals" (Oxford U.P., London, 1964).

5.   Y. F. Tsay, B. Bendow and S. S. Mitra, Phys. Rev. B8,
      2688 (1973).

6. S. S. Mitra, Quarterly Technical Reports, AFCRL, Contract No. F19628-72-C-0286.

7. K. V. Namjoshi and S. S. Mitra, Phys. Rev. B9, 815 (1974); Solid State Commun. 15, 317 (1974).

8. See, for example, S. S. Mitra in "Optical Properties of Solids", ed. S. Nudelman and S. S. Mitra (Plenum, New York, 1969), p. 421.

9. B. Fritz, F. Luty and J. Anger, Z. Phys. 174, 240 (1963); R. Bonn, R. Metselaar and J. van der Elsken, J. Chem. Phys. 46, 1988 (1967); J. C. Decius, E. H. Coker and G. L. Brenna, Spectrochim, Acta 19, 1281 (1963); D. N. Mirlin and I. I. Reshina, Sov. Phys.-Solid State 10, 895 (1968).

10. L. Genzel in "Optical Properties of Solids", ed. S. Nudelman and S. S. Mitra (Plenum, New York, 1968); M. V. Klein in "Physics of Color Centers", ed. W. B. Fowler (Academic Press, 1968); S. S. Mitra and R. S. Singh, Solid State Commun. 12, 867 (1973).

11. See, for example "Optical Properties of Ions in Crystals", ed. H. M. Crosswhite and H. W. Moos (Interscience, New York, 1967).

12. I. F. Chang and S. S. Mitra, Adv. Phys. 20, 359 (1971); R. J. Elliot, J. A. Krumhansl and P. L. Leath, Revs. Mod. Phys. 46, 465 (1974).

13. S. Varshney, J. F. Vetelino and S. S. Mitra, Phys. Rev. B 12, 5912 (1975).

14. J. N. Plendl, S. S. Mitra and P. J. Gielisse, Appl. Optics 10, 1129 (1971).

15. M. Sparks, "Optical Distortion by Heated Windows in High-Power Laser Systems", The Rand Corp., R-545-PR (April, 1971), unpublished.

16. F. Horrigan, C. Klein, R. Rudko and D. Wilson, Microwaves $\underline{8}$, 68 (1969).

17. J. D. Foster and L. M. Osternik, J. Appl. Phys. $\underline{41}$, 3656 (1970).

18. B. Bendow and P. D. Gianino, J. Elec. Mater. $\underline{2}$, 87 (1973); Appl. Phys. $\underline{2}$, 1, 71 (1973).

19. Y. F. Tsay, B. Bendow and S. S. Mitra, Phys. Rev. B$\underline{8}$, 2688 (1973); Y. F. Tsay, S. S. Mitra and B. Bendow, Phys. Rev. B$\underline{10}$, 1476 (1974); B. Bendow, P. D. Gianino, Y. F. Tsay and S. S. Mitra, Appl. Optics $\underline{13}$, 2382 (1974).

II

INFRARED ABSORPTION DUE TO

MULTIPHONON PROCESSES

2.1   Multiphonon infrared absorption in the transparent regime of alkaline-earth fluorides

Herbert G. Lipson and Bernard Bendow

Solid State Sciences Laboratory, Air Force Cambridge Research Laboratories, Hanscom Air Force Base, Massachusetts 01731†

Nestor E. Massa*† and Shashanka S. Mitra*

Department of Electrical Engineering, University of Rhode Island, Kingston, Rhode Island 02881

(Received 28 October 1975)

We present an experimental investigation of the frequency and temperature dependence of the multiphonon infrared absorption coefficient in the alkaline-earth fluorides CaF_2, SrF_2, and BaF_2. Over the range investigated, a nearly structureless, exponential-like behavior is found for the frequency dependence of the absorption, and a Bose-Einstein-like multiphonon behavior for the temperature dependence. The data are analyzed employing a simplified model of multiphonon absorption; the overall agreement with experiment is quite good, although various discrepancies are present. We conclude that alkaline-earth fluorides do indeed display intrinsic multiphonon absorption over an extended frequency and temperature range, and we determine the parameters governing this behavior.

I. INTRODUCTION

The alkaline-earth fluorides are promising candidate materials for infrared applications requiring optical components of high transparency.[1] The limiting absorption in the transparent-frequency (ω) regime above the reststrahl in ionic solids stems from intrinsic multiphonon processes. Thus, detailed knowledge of the multiphonon infrared absorption coefficient $\alpha(\omega, T)$, where T is temperature, is of paramount importance. The latter has been investigated extensively in a wide variety of materials,[2-5] including the alkaline-earth fluorides,[6,7] and theoretical analyses have been pursued as well.[8-14] The present work provides the first detailed experimental investigations of $\alpha(\omega, T)$ for CaF_2, SrF_2, and BaF_2 over extended frequency and temperature ranges. The results are analyzed in terms of a simplified model of multiphonon absorption. A preliminary account of aspects of this work was presented previously.[15]

Recent investigations of $\alpha(\omega, T)$[3,4] have demonstrated that in ionic solids α decreases nearly exponentially with increasing frequency over the range typically accessible to measurement (one to four phonons). Moreover, at room temperature and above very little structure is manifested by $\alpha(\omega)$ within or beyond the three-phonon regime. The observed T dependence in the many-phonon regime[16] is substantially less than that predicted for intrinsic multiphonon processes, a result which has been interpreted in terms of the T dependence of the phonon spectrum.[17-21] We will here find analogous behavior for the ω and T dependence of α in the transparent regime of alkaline-earth fluorides. However, the T dependence of the phonon spectrum will play a lesser role, because the frequencies ω, ω_{TO} considered here are much smaller than those in the halide experi-

ments; moreover, thermal-expansion effects are smaller for fluorites than for alkali halides.

II. EXPERIMENTAL PROCEDURE AND RESULTS

Single-crystal fluorite samples, 1.90 cm in diameter, with the following polished thicknesses (CaF_2, 0.645 and 1.285 cm; SrF_2, 0.334 and 1.640 cm; and BaF_2, 0.291 and 1.416 cm) cut from long (5–10-cm) rods of high-purity Optovac material were used for the investigations at elevated temperatures. The room-temperature transmissions of these samples, as well as those of the original rods with polished ends, were determined with a Beckman IR-7 spectrometer. The long-sample measurements were used to extend room-temperature data to the range of lower absorption coefficients (higher frequencies) and to detect the possible presence of weak impurity bands. The room-temperature spectrophotometric measurements did not reveal any impurity bands in the frequency region investigated.

To obtain the transmissions at elevated temperatures the exit beam from a Perkin-Elmer Model 98 spectrometer equipped with a NaCl prism was focused on a sample positioned at the center of a wire-wound tube furnace and the transmitted beam was collected and imaged on a thermocouple detector. A thermocouple was employed since it was found to be less affected by fluctuations in background thermal radiation than more sensitive photoconductive detectors. Sample temperatures were measured with a Cu-constantan thermocouple placed at the edge of the sample and were monitored by a Doric digital thermocouple meter. At temperatures above 670 °K an extended Cu-constantan calibration was used.[22] The furnace was allowed to stabilize at each temperature before measurement. The temperature variation

during measurement was less than ± 5 °C at the highest temperature (800 °K). The initial temperature gradient between the edge and the center of the sample was found to be approximately 15 °K at the highest temperature but became almost negligible after a stabilization period of about 1 h. The entire furnace was baffled with firebrick to keep direct thermal radiation from reaching the detection thermocouple.

Optical transmission measurements were made by an in-out technique with the I_0 level measured throughout the spectral range at each temperature in order to minimize the effects of small intensity changes arising from the shift of sample and furnace emission peaks with temperature. The measurements were carried out at frequencies between 700 and 1600 cm^{-1} over a temperature range of 295–800 °K. Absorption values were determined from the transmission measurements utilizing a computer program which relates absorption, transmission, reflectivity, and sample thickness, taking multiple internal reflections into account.[23] The reflectivity used for these computations was determined in each case from the maximum transmission in a frequency range where absorption is negligible. Refractive-index variations with frequency and temperature in the ranges of interest were estimated to be small and were not taken into account. With the long optical path involved some error in determining the maximum transmission can be introduced by even small variations in position of the sample in the furnace. A comparison of room-temperature data obtained for samples measured both in the furnace and with the Beckman IR-7 spectrophotometer indicated differences of up to 5% in absorption values in some frequency regions.

To provide an additional check of absorption variation with temperature at a single frequency, transmissions of the 0.334-cm SrF_2 and 0.291-cm

BaF_2 samples were also determined at the 10.6-μm CO_2 laser frequency by directing the beam through the sample in the furnace as it was heated from room temperature to 800 °K. Incident and transmitted laser power were measured by a Coherent Radiation 201 power meter, and temperature at the edge of the sample was recorded continuously during the heating cycle. Calorimetric measurements made at the laser frequency (943 cm^{-1}) with 2–3-W power levels indicated a rapid rise in temperature due to laser heating, particularly with the larger absorption coefficients found for SrF_2 and BaF_2 at the higher temperatures. This implies that, with the present laser beam to sample diameter ratio of 1:3 and the power levels employed, the center of the sample may be locally heated to a higher temperature than that indicated by a thermocouple placed at the edge. This effect, which will be more pronounced if insufficient time is allowed for the sample temperature to stabilize, may introduce an uncertainty in the measured temperature and lead to a possible discrepancy between laser and spectrometer absorption values. Thus the laser measurements are believed useful as qualitative rather than quantitative checks on the spectrometer data.

The results of spectrometer measurements of $\alpha(\omega, T)$ for CaF_2, SrF_2, and BaF_2 samples are indicated in Fig. 1. These results display the typical exponential-like decrease in α vs ω, which we analyze in some detail in Sec. III. In general, these curves appear very similar to those presented previously for alkali halides by Barker.[24]

Laser transmission data for BaF_2 and SrF_2 are indicated in Fig. 2 along with our spectrometer data, and the laser data of Chen *et al.*[7] for comparison. Although some deviations are observed at the higher temperatures, possibly for the reason indicated previously, the various data are nevertheless seen to agree quite well overall.
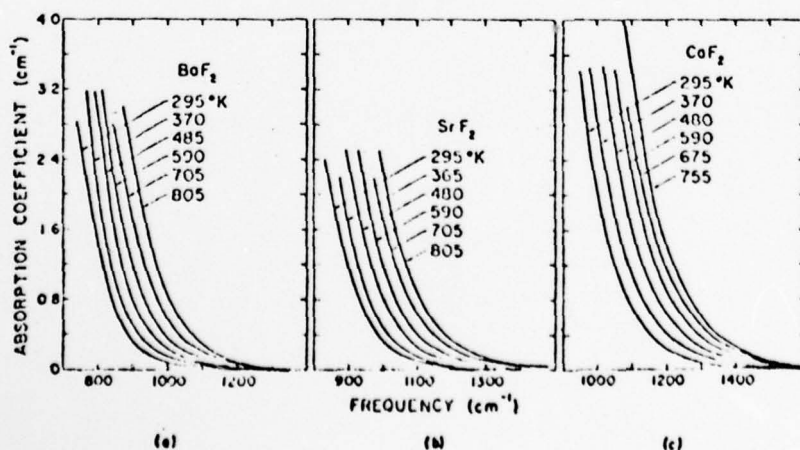

FIG. 1. Measured absorption coefficient versus frequency for alkaline-earth fluorides at various temperatures: (a) BaF_2, (b) SrF_2, and (c) CaF_2.
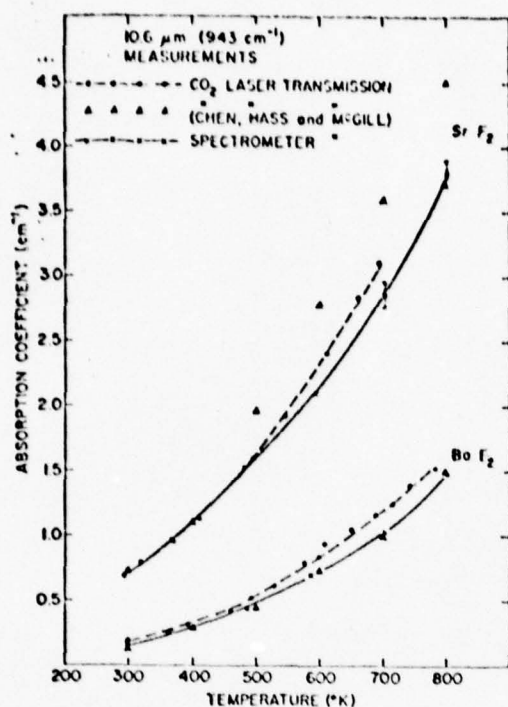
FIG. 2. Comparison of absorption versus temperature of BaF_2 and SrF_2 as determined by CO_2-laser measurements and by spectrometer transmission measurements at 10.6 μm.

III. DISCUSSION

As mentioned in Sec. I, ionic solids are characterized by a relatively structureless exponential-like α vs ω. In Fig. 3 we plot the room-temperature absorption of the three crystals on a logarithmic scale versus frequency, along with data of Deutsch.[3] Our data agree reasonably well with the latter, and both are seen to fall nearly on straight lines. In Fig. 4 we plot the absorption on a logarithmic scale vs ω for BaF_2 at various temperatures, from which it can be seen that the exponential-like behavior of $\alpha(\omega)$ is preserved at elevated T.

To interpret the room-temperature data, we can utilize the results of calculations for fluorites performed earlier by Namjoshi et al.,[6] in which the absorption is related to a sum over n-phonon densities of state, weighted by coefficients determined from the interionic potential. The details are described in the latter reference; we here merely display the results as the solid lines in Fig. 3. The agreement between theory and experiment is observed to be quite good.

Although one could, in principle, utilize the approach of Namjoshi and Mitra[13] as well as those

of others which properly incorporate detailed crystalline properties [8,9,12] to interpret the high-temperature spectra, such treatments tend to become cumbersome and unwieldy. In general, we require the temperature dependence of all optical phonons, and we must incorporate these into the calculated n-phonon densities of state. We have therefore chosen to analyze the present results in terms of a more approximate but substantially simpler approach which is based on the properties of an average oscillator for the phonons.[9] We note that this approach has previously provided good agreement with experiment for the alkali halides.[25]

Following Bendow,[9] we express the absorption in terms of a suitable effective phonon frequency $\omega_0(T)$ with an appropriate average T dependence, the choice of which will be discussed in more detail below. One has

$$\alpha(\omega, T) = \alpha_0 \left[\frac{n(\omega_0(T)) + 1}{n(\omega) + 1} \right]^{\omega/\omega_0(T)} \exp[-A\omega/\omega_0(T)]$$
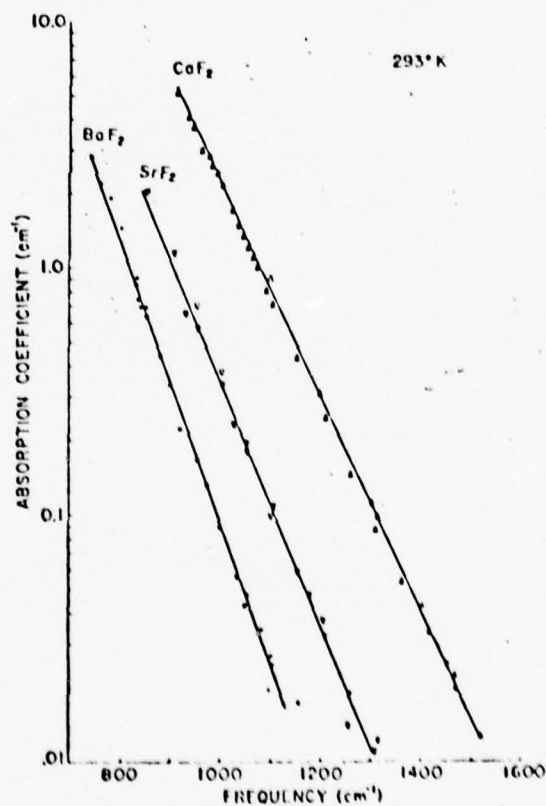

FIG. 3. Room-temperature absorption coefficient versus frequency for alkaline-earth fluorides. Solid symbols, present data; open symbols, data of Deutsch (Ref. 3); solid lines, theoretical calculations from Ref. 6.
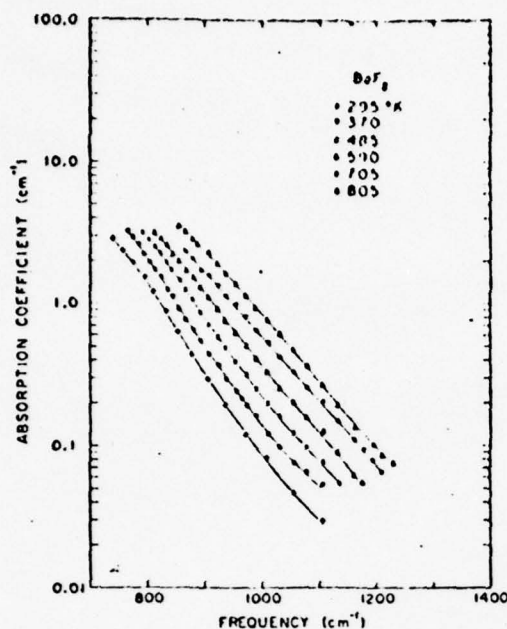
FIG. 4. Measured absorption coefficient versus frequency plotted on a semilog scale to demonstrate the persistence of the exponential-like character of the absorption at elevated temperatures.

$$= \alpha_0 \frac{\exp\left[\{-A + \ln[n(\omega_0(T)) + 1]\}\, \omega/\omega_0(T)\right]}{n(\omega) + 1}$$
$$n(\omega) = [\exp(\hbar\omega/kT) - 1]^{-1} , \tag{1}$$

where α_0 and A depend weakly on ω_0 and/or T. From the above formula, it is clear that α is enhanced at high T according to the usual T^{j-1} law for a $j(=\omega/\omega_0)$-phonon process, provided that ω_0 is independent of temperature. In general, $\omega_0(T)$ decreases with increasing T, which tends to suppress the T dependence of α arising from the Bose-Einstein factors $[n(\omega_0) + 1]^{\omega/\omega_0}$.

To apply Eq. (1) we must specify the effective oscillator frequency $\omega_0(T)$. Because the contributions of acoustic phonons are suppressed due to energy conservation, the average frequency $\bar{\omega}$ defined by the first moment of the density of states should not be an appropriate choice. On the other hand, an average optical phonon frequency, such as the Brout frequency[26] ω_B, should be more appropriate. For the present case,

$$\omega_B = [\tfrac{1}{6}(2\omega_{TO}^2 + \omega_{LO}^2 + 3\omega_R^2)]^{1/2} , \tag{2}$$

where ω_R is the Raman frequency. It turns out that ω_B is close to the Debye frequency ω_D for most polyatomic crystals and that both are related to the bulk modulus; values for the characteristic frequencies for the fluorites are listed in Table I. Regarding the T dependence of ω_0, we note that

for ionic solids the principal T dependence arises from thermal-expansion effects, so that one obtains[26]

$$\omega_i(T) \approx \omega_i(0) \exp\left(-3\gamma_i \int_0^T \alpha_T\, dT\right), \tag{3}$$

where α_T is the coefficient of linear expansion and γ_i the mode Grüneisen parameter. A more exact theory would account for the effects of anharmonicity on the T dependence, but fortunately cancellations between the contributions of cubic and quartic anharmonicities tend to suppress anharmonic effects in most cases. Extending Eq. (3) to the average oscillator yields

$$\omega_0(T) = \omega_0(0) \exp\left(-3\gamma_0 \int_0^T \alpha_T\, dT\right), \tag{4}$$

where γ_0 is now a suitably averaged (macroscopic) Grüneisen parameter. The obvious choice of γ corresponding to $\bar{\omega}$ is the thermal average[27]

$$\tilde{\gamma} = \sum_i C_i \gamma_i \Big/ \sum_i C_i . \tag{5}$$

where the C_i's are Einstein heat capacities and the sum is over all modes of the crystal. If one utilizes ω_D for ω_0, then[28]

$$\gamma_D = -\frac{d \ln\omega_D}{d \ln V} = -\frac{3\alpha_T V B}{C_v}, \tag{6}$$

where B is the isothermal bulk modulus and C_v the specific heat at constant volume. $\bar{\gamma}$ and γ_D are usually very close in value, as demonstrated for CaF_2 by Ganesan[29] and for SrF_2 and BaF_2 by Vetelino.[30] The γ corresponding to ω_B follows

TABLE I. Characteristic phonon frequencies (cm^{-1}) and Grüneisen constants for alkaline-earth fluorides.

	CaF_2	SrF_2	BaF_2
ω_{TO} [a]	261	223	188
ω_{LO} [a]	482	395	344
ω_R [b]	322	283	243
ω_B	337	288	247
ω_D	329[c]	288–299[d]	215–240[d]
ω_0	315	280	255
$\bar{\omega}$	259[e]	...	237[f]
γ_B	1.85	1.86	1.85

[a] R. P. Lowndes, J. Phys. C 4, 3083 (1971).
[b] R. S. Krishnan and P. S. Narayanan, Indian J. Pure Appl. Phys. 1, 196 (1973).
[c] American Institute of Physics Handbook (McGraw-Hill, New York, 1957).
[d] J. F. Vetelino, Ph.D. thesis (University of Rhode Island, 1969) (unpublished).
[e] Calculated from phonon density of states given by M. M. Elcombe and A. W. Pryor [J. Phys. C 3, 492 (1970)].
[f] Calculated from J. P. Harrel and V. J. Minkiewicz, Solid State Commun. 8, 463 (1970).
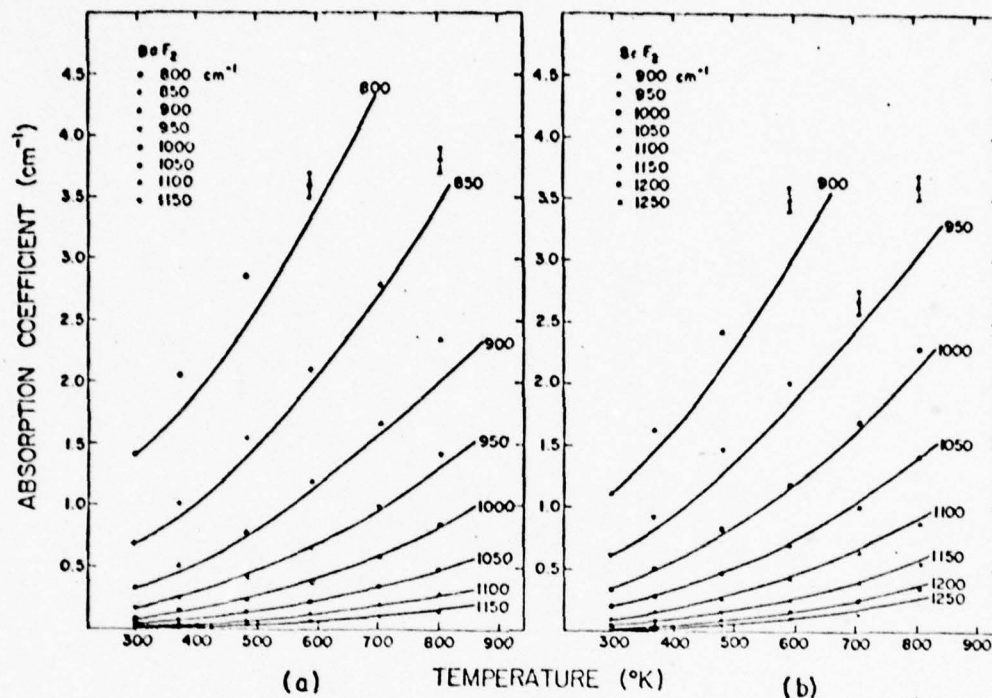
FIG. 5. Absorption coefficient versus temperature for (a) BaF$_2$, (b) SrF$_2$, and (c) CaF$_2$, at various representative frequencies. The solid lines are calculations obtained from Eq. (1) utilizing ω_0 values given in Table I, while the individual points are experimental data. Values designated with error bars are obtained by extrapolating the logarithm of the measured absorption versus frequency curve at that temperature.

directly as

$$\gamma_B = \frac{1}{6}\left(\gamma_{LO}\frac{\omega^2_{LO}}{\omega^2_B} + 2\gamma_{TO}\frac{\omega^2_{TO}}{\omega^2_B} + 3\gamma_R\frac{\omega^2_R}{\omega^2_B}\right); \quad (7)$$

The value of γ_B, which is listed in Table I, is close to that of the other γ's as well.

We have performed numerical computations utilizing the values of Table I in Eq. (1) to analyze the experimental data. Since the constants α_0 and A were determined from the room-temperature spectra (see Fig. 3), in principle no adjustable parameters appear in the computations. We find that the use of $\bar{\omega}$ for ω_0 leads to too strong a T dependence for α, while use of ω_R, ω_B, or ω_B gives an improved but not perfect fit. These results imply that acoustic phonons have a relatively minor influence on the multiphonon absorption, and that α is best characterized by an average optical phonon. The latter conclusions are consistent with the results of other related analyses as well.[4,5] Regarding γ, it was found that for the range of frequencies of interest here $\alpha(T)$
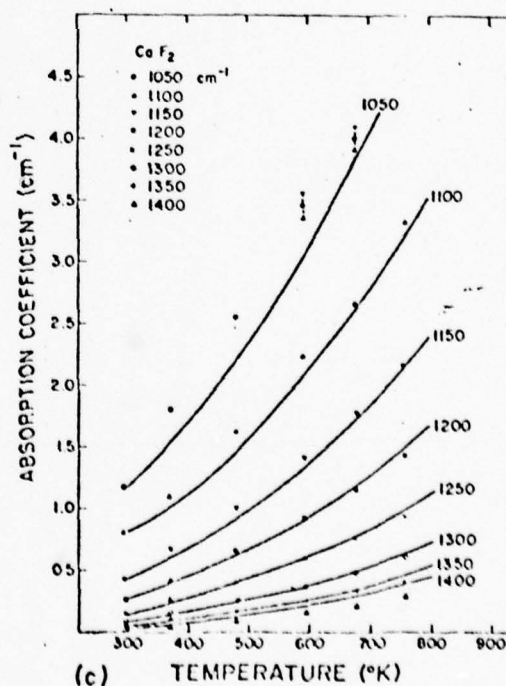
was relatively insensitive to the particular γ chosen.

To test the wider applicability of Eq. (1) to the present case, calculations of $\alpha(T)$ were performed for the three fluorides using values of

$\omega_0 \sim \omega'_B$. It was not possible to obtain good agreement over the full range of frequencies in all cases when a single fixed ω_0 was utilized; rather, to obtain the best fit it would have been necessary to increase ω_0 with increasing frequency. This suggests that at lower frequencies more acoustic (or, in general, lower-energy phonons) take part in the absorption. However, such a variation of ω_0 with frequency is not contained in Eq. (1) and does not provide a consistent basis for interpretation of the data utilizing this equation. We therefore chose to search for the single ω_0 which gave the best fit to the entire set of data for each solid. γ_B of Eq. (7) was utilized for γ, with γ_{TO} taken from Ref. 31, γ_R from Ref. 32, and with γ_{LO} estimated utilizing the method of Ref. 33. The values obtained for ω_0 are indicated in Table I and are seen to lie quite close ($\gtrsim 5\%$) to ω_B. The calculated α's for these values are displayed in Fig. 5. The agreement with experiment is excellent for BaF_2 and quite good for SrF_2. The fit is qualitatively, but not quantitatively, adequate for CaF_2 over the full range of frequencies. While the origin of the discrepancies is not clear,

it must be realized that the higher-frequency (low α) data where the largest disparities occur are, in fact, the most susceptible to experimental error. Moreover, Eq. (1) which we have utilized here does not take detailed account of selection rules and/or density of state effects[12,13,29] and may well be inadequate for a quantitative analysis over a wide range of frequencies and temperature. Nevertheless, we believe it is fair to conclude on the basis of the present results that the alkaline-earth fluorides do, in fact, display intrinsic multi-phonon absorption over an extended frequency and temperature range. In particular, we find that the absorption is relatively structureless and displays a nearly exponential frequency dependence over most of the range investigated. The temperature dependence is close to the Bose-Einstein form $\{\sim [n(\omega_0) + 1]^{\omega/\omega_0}\}$ with $\omega_0 \sim \omega_B$.

ACKNOWLEDGMENT

‡As of Jan 1, 1976 Solid State Sciences Division, Deputy for Electronic Technology, Rome Air Development Center (AFSC), Hanscom AFB, Mass 01731.

*Research supported by Air Force Cambridge Research Laboratories (AFSC) under Contract No. F19628-72-C-0286.

†On leave of absence from Department of Physics, Vanderbilt University, Nashville, Tenn.

¹See, for example, S. S. Mitra and B. Bendow, in *Optical Properties of Highly Transparent Solids*, edited by S. S. Mitra and B. Bendow (Plenum, New York, 1975), Preface.

²G. Rupprecht, Phys. Rev. Lett. 12, 580 (1964).

³T. F. Deutsch, J. Phys. Chem. Solids 34, 2091 (1973).

⁴T. F. McNelly and D. W. Pohl, Phys. Rev. Lett. 32, 1305 (1974); D. W. Pohl, in Ref. 1.

⁵L. H. Skolnik, H. G. Lipson, B. Bendow, and J. Schott, Appl. Phys. Lett. 25, 442 (1974).

⁶K. V. Namjoshi, S. S. Mitra, B. Bendow, J. A. Harrington, and D. L. Stierwalt, Appl. Phys. Lett. 26, 41 (1975).

⁷M. Chen, M. Hass, and T. C. McGill, in Ref. 1.

⁸M. Sparks and L. J. Sham, Phys. Rev. B 8, 3037 (1973).

⁹B. Bendow, Phys. Rev. B 8, 5821 (1973).

¹⁰D. L. Mills and A. A. Maradudin, Phys. Rev. B 8, 1617 (1973).

¹¹T. C. McGill, R. W. Hellwarth, M. Mangir, and H. V. Winston, J. Phys. Chem. Solids 34, 2105 (1973).

¹²H. B. Rosenstock, Phys. Rev. B 9, 1973 (1974); L. L. Boyer, J. A. Harrington, M. Hass, and H. B. Rosenstock, Phys. Rev. B 11, 1665 (1975).

¹³K. V. Namjoshi and S. S. Mitra, Phys. Rev. B 9, 815 (1974).

¹⁴A. Nedoluha, in Ref. 1.

¹⁵H. G. Lipson, B. Bendow, and S. S. Mitra, in Ref. 1.

¹⁶J. A. Harrington and M. Hass, Phys. Rev. Lett. 31, 710 (1973).

¹⁷B. Bendow, Appl. Phys. Lett. 23, 133 (1973).

¹⁸M. Sparks and L. J. Sham, Phys. Rev. Lett. 31, 714 (1973).

¹⁹A. A. Maradudin and D. L. Mills, Phys. Rev. Lett. 31, 718 (1973).

²⁰T. C. McGill and H. V. Winston, Solid State Commun. 13, 1457 (1973).

²¹K. V. Namjoshi and S. S. Mitra, Solid State Commun. 15, 317 (1974).

²²National Bureau of Standards Report No. RP-1080 (1938) (unpublished).

²³A. Kahan and H. G. Lipson, AFCRL Research Report No. 63-325, 1973 (unpublished) (available from the authors or from the Defense Documentation Center).

²⁴A. J. Barker, J. Phys. C 5, 2276 (1972).

²⁵A. J. Barker, G. R. Wilkinson, N. E. Massa, and S. S. Mitra, in Ref. 1.

²⁶See, for example, S. S. Mitra, in *Optical Properties of Solids*, edited by S. Nudelman and S. S. Mitra (Plenum, New York, 1969).

²⁷See, for example, B. Yates, *Thermal Expansion* (Plenum, New York, 1972), p. 77.

²⁸See, for example, M. Born and K. Huang, *Dynamical Theory of Crystal Lattices* (Oxford U. P., London, 1954), Chap. II.

²⁹G. Ganesan and R. Srinivasan, Can. J. Phys. 40, 74 (1962).

³⁰J. F. Vetelino, Ph. D. thesis (University of Rhode Island, 1969) (unpublished).

³¹R. P. Lowndes, J. Phys. C 4, 3083 (1971).

³²S. S. Mitra and O. Brafman (unpublished data).

³³J. R. Ferraro, S. S. Mitra, and A. Quattrochi, J. Appl. Phys. 42, 3679 (1971).

2.2 FREQUENCY AND TEMPERATURE DEPENDENCE STUDIES OF RESIDUAL INFRARED ABSORPTION IN THE HIGHLY TRANSPARENT FREQUENCY REGIME OF TETRAHEDRAL SEMICONDUCTORS

BERNARD BENDOW, LYN H. SKOLNIK AND HERBERT G. LIPSON
Solid State Sciences Division
Deputy for Electronic Technology, RADC (AFSC)
Hanscom AFB, MA 01731

STANFORD P. YUKON[*+] AND SHASHANKA S. MITRA[*]
Dept of Electrical Engineering
University of Rhode Island, Kingston, RI 02881

We report studies of residual infrared absorption in the highly transparent regime of diamond and zincblende type semiconductors, with emphasis on Si and ZnSe.

INTRODUCTION

There has been considerable interest in recent years in the multiphonon infrared absorption[1] which limits the transparency of infrared materials. Although extensive measurements and theoretical calculations have been reported for ionic crystals,[2] only limited work has appeared for semiconducting crystals.[3] The purpose of the present work is to extend existing measurements to higher frequencies and over a greater range of temperatures for state-of-the-art semiconducting crystals, and to provide a theoretical basis for interpretation of the results, especially with respect to structure in higher order spectra, and the influence of nonlinear moments on the spectra. A combination of three techniques described in detail previously[4] were employed in the measurements, namely, standard transmission spectroscopy, emittance spectroscopy, and calorimetry. In the present report, we restrict attention principally to Si and ZnSe, and provide as well a brief sketch of the theoretical approach utilized to interpret the data.

Typical results of the experiments are illustrated in Figs. 1-2. Fig. 1 indicates the frequency dependence for the absorption coefficient α in Si for the three and four phonon regimes at selected temperatures, while Fig. 2 displays the temperature dependences for selected frequencies. Frequency spectra for CVD polycrystalline ZnSe at selected temperatures are displayed in Fig. 3. More complete spectra for these materials as well as other semiconductors will be given elsewhere.

The present results are indicative of various general trends manifested in the multiphonon spectra of semiconductors.[5] For the more highly covalent semiconductors substantial structure persists into higher order spectra, and at elevated temperatures as well, as evidenced by Fig. 1. As the bonding becomes more ionic (going from IV's to III-V's to II-VI's, e.g.) the structure is less persistent and washes out noticeably at higher temperatures. The latter effect is reasonably attributed to the increased anharmonicity which characterizes the more ionic materials. We note that in many
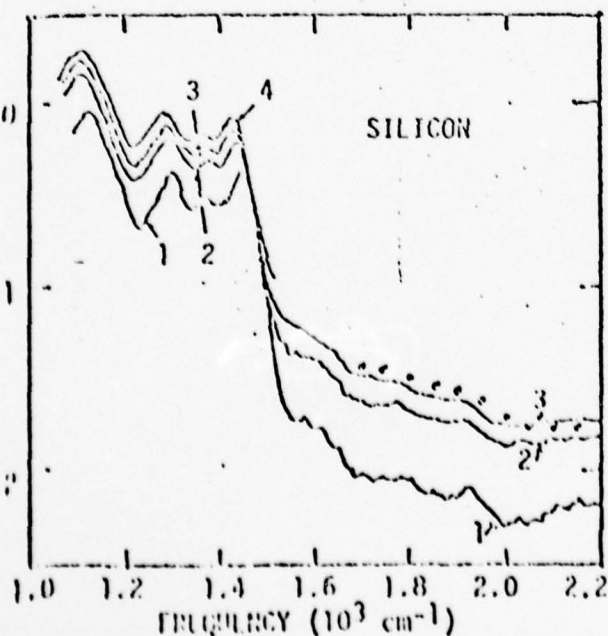

Fig. 1. Log_{10} absorption coefficient vs frequency for high resistivity Si in the three and four phonon regime. Curves 1,2,3,4 are for temperatures 295, 410, 440 and 500°K, respectively. The solid lines indicate data obtained by transmission, and the dots indicate emittance data at ~450°K. Emittance at other temperatures is in overall agreement with the data shown.
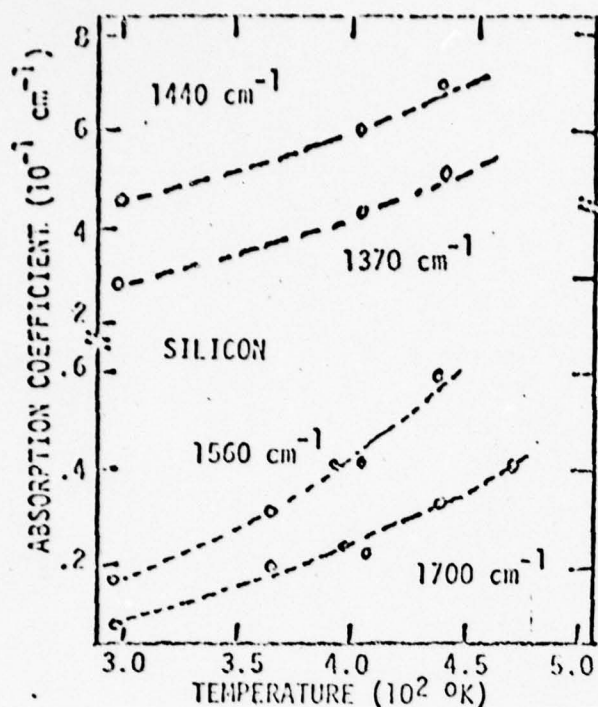
of Si vs temperature at selected wavelengths. Dots indicate experimental points taken by various methods.

Ionic materials such as alkali-halides and alkaline-earth fluorides structure is often nearly absent beyond the two phonon regime at room temperature.[5]

Temperature dependence plots such as given in Fig. 2 are useful as quick indications of the multiphonon character of the absorption. An approximate dependence of the form $[n(\omega_o) + 1]^j/[n(\omega) + 1]$, where n is the Bose-Einstein function, is anticipated for intrinsic absorption in the jth phonon regime, although implicit T-dependence may influence the spectra of the more ionic materials.[6] One finds that the data in the three phonon regime satisfies this approximate dependence quite well, while that for the four-phonon regime displays a somewhat greater T-dependence than predicted. Nevertheless, the agreement is sufficient to suggest that intrinsic multiphonon behavior is being observed, although possibly in combination with other extrinsic contributions.

THEORETICAL CONSIDERATIONS

Our multiphonon calculations are based on a variant of the non-interacting cell approach described in Ref. 7, in which full phonon spectral properties are retained but multi-cell dynamic interactions are neglected. The final expressions involve a sum over n phonon densities of states, and coefficients involving higher order derivatives of bond interaction potentials and electric moments. Among
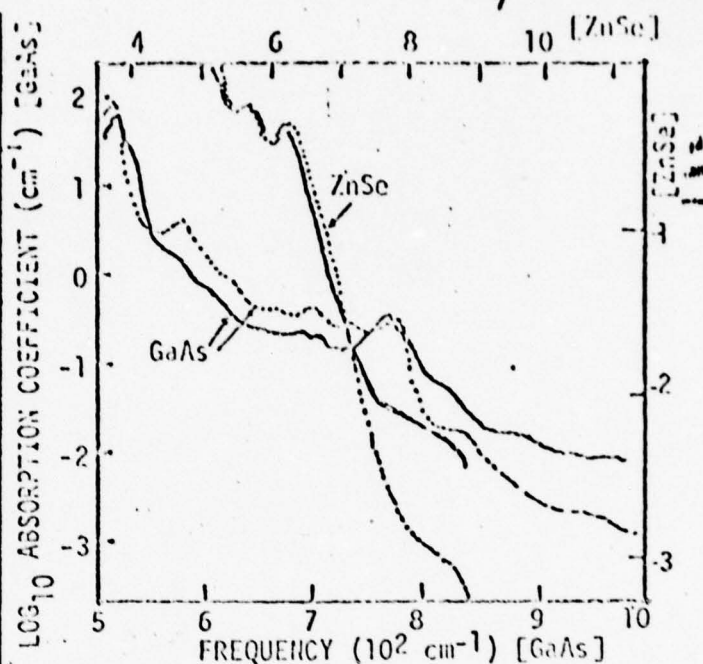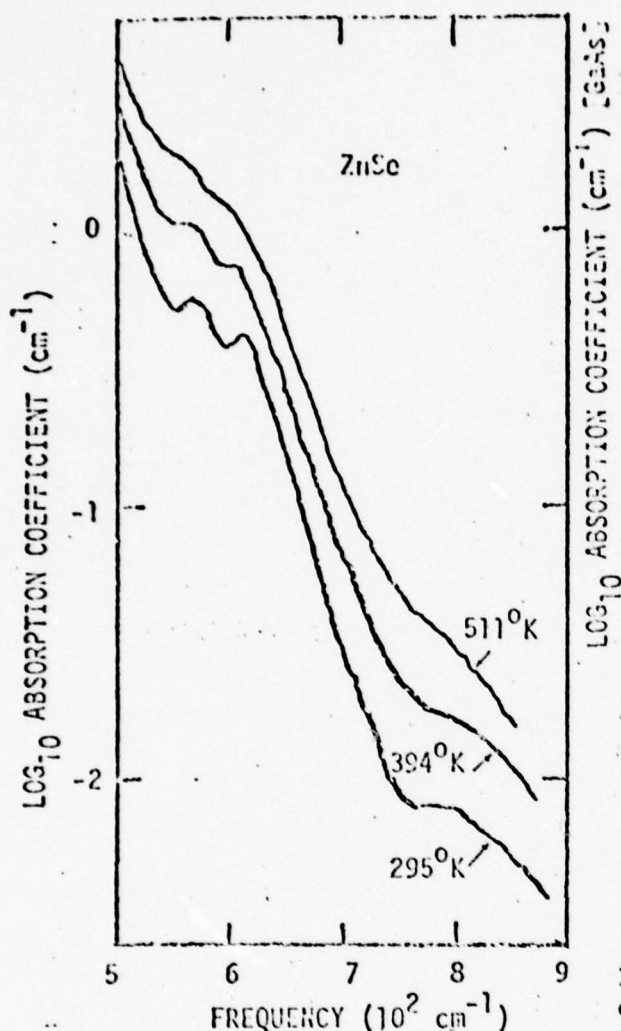
Fig 4. Room temperature spectra for GaAs and ZnSe (solid lines) compared with theoretical calculations within a linear moment model (dashed lines) Experimental values for GaAs above 800 cm^{-1} are obtained by emittance spectroscopy.

Fig. 3. Log_{10} absorption coefficient vs frequency for CVD ZnSe, measured by transmission.

other approximations, all k-selection rules are suppressed.

Initial computations for ZnSe and GaAs, retaining just linear moments are indicated in Fig. 4. One finds most structural features in higher order spectra reasonably well accounted for within this model, although the calculated rate of decrease is too great, suggesting that either input potential parameters are too low, or nonlinear moments enhance the absorption.

REFERENCES

1. See, e.g., "Optical Properties of Highly Transparent Solids", edited by S.S. Mitra and B. Bendow (Plenum, NY, 1975).
2. See, e.g., T.F. Deutsch, J. Phys. Chem. Sol. 34, 2091 (1973); L.L. Boyer, et al, Phys. Rev. B11, 1665 (1975); and Ref. 1.
3. See, e.g., T.F. Deutsch, op cit.
4. L.H. Skolnik, in Ref. 1.
5. A. Bendow, in "Solid State Physics", to be published.
6. B. Bendow, Appl. Phys. Lett. 23, 133 (1973).
7. B. Bendow et al, Phys. Rev. B10, 2386 (1974).
8. C.J. Duthler, Phys. Rev. B, to be published.

2.3 OPTICAL PHENOMENA IN INFRARED MATERIALS

A digest of technical papers presented at the topical meeting on
Optical Phenomena in Infrared Materials
December 1-3, 1976, Annapolis, Maryland

MIXED FLUORIDES FOR MID-IR LASER WINDOWS

J. J. Martin*
Dept. of Physics, Oklahoma State Univ.
Stillwater, OK 74074

Herbert G. Lipson, Bernard Bendow and Audun Hordvik
Deputy for Electronic Tech., Rome Air Development Center
Hanscom AFB, MA 01731

Shashanka S. Mitra**
Dept. of Electrical Engineering, Univ. of Rhode Island
Kingston, RI 02881

We report investigations of crystal growth and infrared optical evaluation of mixed fluorides, including $KMgF_3$, $RbMgF_3$ and $KZnF_3$. Single crystals of the latter, which have the Perovskite structure, were grown by the Bridgeman method, utilizing the system described by Butler (Ph.D. Thesis, O.S.U., 1972, unpublished). We have also pulled crystals of $KMgF_3$ and $RbMgF_3$, using a modification of a puller for KCl, which has a graphite radiation shield and a special thermocouple added to allow operation at higher temperature. Various details of the crystal growth process will be discussed.

The infrared absorption of the grown crystals of $KMgF_3$, $RbMgF_3$ and $KZnF_3$ was measured by Fourier spectroscopy and photoacoustic calorimetry, at room temperature, in the frequency range 800-1800 cm^{-1}. In the range of higher absorptions ($\gtrsim 10^{-2}$ cm^{-1}) we obtain a characteristicly smooth, exponential-like variation of absorption with increasing frequency, although $KZnF_3$ does show enhancement suggestive of extrinsic effects, towards higher frequencies. The exponential decrease and absence of marked structure are features familiar from alkali-halide and alkaline earth fluoride spectra measured previously, and are believed to be a result of the dominance of anharmonic broadening and the lack of structure in the lattice density of

states. The magnitude and rate of decline for $KMgF_3$ and $RbMgF_3$ are nearly the same, implying that the Mg-F bond is the principal influence on the multiphonon spectrum. This is also supported by the similarity of these spectra to that of MgF_2, although the rate of decrease in the mixed fluorides is slightly slower than for MgF_2, and the overall magnitude is from 50% to 20% smaller in the range investigated.

III

STRUCTURALLY DISORDERED SOLIDS:

PHONON OPTICAL PROPERTIES

3.1

DYNAMICS OF STRUCTURALLY DISORDERED SOLIDS

J. F. Vetelino
Department of Electrical Engineering
University of Maine, Orono, Maine 04473

and

S. S. Mitra[*]
Department of Electrical Engineering
University of Rhode Island, Kingston, R.I. 02881

I. INTRODUCTION

In this chapter the dynamics of disordered lattices is discussed. The extent of disorder is assumed small such that the properties of the disordered system can, in principle, be obtainable as an appropriate extention of the corresponding properties of the ideal ordered system. Such an approach, albeit limiting, affords a convenient starting point for disordered systems, since the information regarding the corresponding ordered systems is assumed known.

The presence of even a small concentration of defects may significantly affect properties of a solid through the destruction of the translational symmetry of the unperturbed perfect lattice. Such changes are often sufficient to allow interaction with light in cases where it would not otherwise occur. The defects may be of a chemical nature such as an impurity atom, or they may be of a mechanical nature such as vacancies at particular lattice sites, and extended defects such as dislocations. If the impurity content of a solid is increased to such an extent that interactions between impurity atoms become significant the system is then termed a disordered solid rather than an impure crystal. Disordered lattices are of two main types: the disordered alloy (isotopic mixture

30

or mixed crystals) and the glass-like substance in which
the disorder is spatial rather than configurational.

It is the purpose of these lectures to discuss the
atomic vibrations of the following three types of dis-
ordered solids: (i) Crystals with substitutional im-
purities, (ii) mixed crystals or alloy systems, and (iii)
amorphous materials. In particular, the lattice dynami-
cal theory will be presented and the theoretical results
will be compared with experimental data whenever avail-
able.

II. CRYSTALS WITH SUBSTITUTIONAL IMPURITIES

It is well known that the introduction of impurity
atoms modifies the potential energy function in a lat-
tice. Hence, the phonon spectrum of the crystal is mo-
dified and consequently any physical property of the
crystal in which the lattice vibrations play a central
role. In the case of a substitutional impurity whose
mass is different from that of the atom it replaces, the
modification of the phonon spectrum is usually manifested
in the appearance of localized frequencies. These fre-
quencies may appear within the allowable frequency range
of the perfect crystal in which case they are known as
resonant modes or outside the frequency spectrum in which
case they are known as gap or local modes.

The first theoretical discovery of localized vibra-
tional modes in crystals was made by Lifshitz[1] in 1943.
This work was followed by the work of Montroll and Potts[2]
and Mazur[3]. However, this early work was restricted to
one and two dimensional lattices and therefore was only
of qualitative value.

The first experimental discovery of the existence
of localized vibrational modes was made by Schaefer[4] in
1960. He observed a strong peak in the infrared lattice
vibrational absorption spectra of alkali halide crystals
containing U-centers which are H^- ions substituted for
the halogen ions. It was after this experimental dis-
covery that much of the theoretical work on the lattice
dynamical behavior of point defects in three dimensional
cystals was undertaken. This initial experimental dis-
covery was also followed by the appearance of a large in-
flux of experimental data[5] in the literature.

In addition to infrared techniques to study local-
ized modes, various other experimental techniques were

31

developed and utilized. Among the most prominent of
these techniques are: Specific heat measurements, tun-
neling between superconductors, the Mössbauer effect,
neutron scattering and Raman spectroscopy. However, the
method which has yielded the most detailed and accurate
information about the frequency and amplitude of the im-
purity modes is the infrared technique, and to some ex-
tent Raman scattering.

The theoretical understanding of the impurity mode
absorption is based on the lattice dynamical behavior of
crystals with defects. In 1962, Dawber and Elliott[6] pre-
sented the formalism of a Green's function method, intro-
duced by Lifshitz[7], to calculate the frequency and ampli-
tude of vibration of a substitutional impurity in a cubic
crystal. This method requires a complete knowledge of
the frequency and amplitude of vibration of all the phonon
states in the perfect crystal. This technique was then
applied by Dawber and Elliott[8] to calculate the impurity
mode frequency in silicon. In 1965, a molecular model
was proposed by Jaswal[9] to describe the dynamical be-
havior of the impurity atom. This model was localized
in that it considered the motion of the impurity ion and
its nearest neighbors while the remainder of the lattice
was assumed to be at rest. The results obtained from
this technique were not as good as the results obtained
from the Green's function technique. Since 1965, the
Green's function technique or modifications thereof, have
been used to calculate the frequency and amplitude of the
phonon states of substitutional impurities in various al-
kali halide[10-13] and zinc-blende crystals[14-16].

A. Linear Diatomic Chain with a Substitutional
   Impurity

The perfect linear diatomic chain modified by the
replacement of one of the constituent atoms by an im-
purity particle is shown in Figure 1. The index " 0 "
designates the impurity particle of mass m_I. It is as-
sumed in this analysis that only nearest neighbor forces
are operative. The perfect lattice near neighbor force
constant is defined as "f" while the nearest neighbor
force constant due to the impurity is denoted by f_I.
Writing the appropriate equations of motion for this lat-
tice and assuming a standard traveling wave solution,
the following system of equations result for the center
of the Brillouin zone ($\underline{k} = 0$),

32
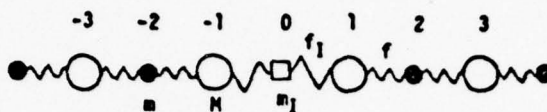
Fig. 1 Linear diatomic lattice containing a substitutional impurity particle with mass defect and force constant defect.

$$
\begin{bmatrix}
(-f) & (2f-m\omega^2) & (-f) & & & & 0 \\
 & (-f) & (f_I+f-M\omega^2) & (-f_I) & & & \\
 & & (-f_I) & (2f_I-m_I\omega^2) & (-f_I) & & \\
 & & & (-f_I) & (f_I+f-M\omega^2) & (-f) & \\
0 & & & & (-f) & (2f-m\omega^2) & (-f)
\end{bmatrix}
\begin{bmatrix}
\sigma'_3 \\
\sigma'_2 \\
\sigma'_1 \\
\sigma'_0 \\
\sigma'_{-1} \\
\sigma'_{-2} \\
\sigma'_{-3}
\end{bmatrix}
= 0
$$

$$(1)$$

The σ'_i's are the appropriate eigen-amplitudes of the imperfect lattice.

It will be shown that the solution to the diatomic chain with an impurity can be expressed in terms of the solution to the perfect diatomic chain. The equations for the perfect diatomic chain can be obtained by setting $m_I = m$ and $f_I = f$ in equation (1). This yields the following matrix equation

$$[[\underline{F}] - \omega^2[I]][\sigma] = 0 \qquad\qquad (2)$$

$[F]$ is the coupling coefficient matrix of the perfect lattice $[\sigma]$, the associated column matrix representing the eigen-amplitudes and $[I]$ the identity matrix. The eigenvalues, ω^2, are determined by the solution to the secular equation,

$$|[F]-\omega^2[I]| = 0, \qquad\qquad (3)$$

33

In matrix notation the equations of motion for the linear diatomic chain with a substitutional impurity can be written as,

$$[F][\sigma']-\omega'^2[I][\sigma'] = [S][\sigma'] \tag{4}$$

$[\sigma']$ and ω'^2 are the eigen-vectors and eigen-values respectively of the imperfect diatomic chain, and $[S]$ is a perturbation matrix of low rank incorporating the change of mass and force constants due to the impurity. The rank of the perturbation matrix, $[S]$, is determined by the spatial extension of the defect. For example, if one considers the second neighbor interactions from the impurity particle also, the rank of the perturbation matrix would naturally increase. An examination of eqs. (1) and (2) reveals that the following expression may be written for the perturbation matrix,

$$[S] = \begin{bmatrix} \ddots & & & 0 & & \\ & (\Delta f) & (-\Delta f) & & 0 & \\ 0 & (-\Delta f) & (2\Delta f-\Delta m\omega^2) & (-\Delta f) & 0 & \\ & 0 & (-\Delta f) & (\Delta f) & & \\ & & 0 & & & \ddots \end{bmatrix} \tag{5}$$

where $\Delta f=f-f_I$ and $\Delta m=m-m_I$. Δf and Δm denote the force constant defect and the mass defect parameters respectively. In the isotropic case, where $\Delta f = 0$, or what is commonly called the mass defect approximation, the perturbation matrix $[S]$ has only the element $(-\Delta m\omega^2)$ at the center.

Due to the limited spatial extension of the perturbation matrix $[S]$, a Green's function method[7] can be used to calculate the frequency and the amplitude of vibration of the impurity particle. Since this technique will be used to calculate the impurity modes in the three dimensional crystal, it is convenient to use matrix notation. Furthermore, since the basic equations of motion in the three dimensional lattice are of the same form as the linear diatomic chain, the analysis will be formulated so as to apply to the three dimensional case as well.

The equation of motion for the linear diatomic chain

34

with a substitutional impurity may be written as follows,

$$[L][\sigma'] = [S][\sigma'], \tag{6}$$

where

$$[L] = [F] - \omega'^2[I].$$

A Green's function matrix $[G]$ is then defined in the following fashion,

$$[L][G] = [I]. \tag{7}$$

With the use of the defining equation for the Green's function matrix, eq. (6) may be written as

$$[\sigma'] = [G][S][\sigma'], \tag{8}$$

where

$$[G] = [L]^{-1}.$$

In terms of the matrix elements, eq. (8) can be written as,

$$\sigma'_x = \sum_{x'} g_{xx'} \sum_{x''} S_{x'x''} \sigma'_{x''} . \tag{9}$$

The eigen values ω'^2 can be obtained by solving the secular equation,

$$|[L]^{-1}[S] - [I]| = 0 \tag{10}$$

or

$$|[G][S] - [I]| = 0.$$

In order to solve eqs. (9) and (10) for the amplitude and frequency of vibration of the impurity particle, one needs an explicit representation of the elements $g_{xx'}$ of the Green's function matrix. Premultiplying eq. (6) by the eigen-vector $[\sigma] = [\sigma(\underline{k},j)]$ of the perfect lattice where j denotes the particular branch and $\underline{k}$, the corresponding wave vector, one obtains

35

$$<[\sigma],[F][\sigma']> - \omega'^2<[\sigma],[\sigma']> = <[\sigma],[S][\sigma']>. \tag{11}$$

$[F][\sigma']$ and $[S][\sigma']$ are column matrices and the product $<,>$ is defined such that for two column matrices $[A]$ and $[B]$,

$$<[A],[B]> = (a_1^* a_2^* \ldots) \begin{bmatrix} b_1 \\ b_2 \\ \cdot \\ \cdot \\ \cdot \\ \cdot \end{bmatrix} = \sum_i a_i^* b_i, \tag{12}$$

where a_i and b_i are the elements of $[A]$ and $[B]$ respectively and a_i^* is the complex conjugate of a_i.

In the case of the linear diatomic chain, the matrix $[F]$ is symmetric, therefore the first term in eq. (11) can be transformed as,

$$<[\sigma],[F][\sigma']> = <[F][\sigma],[\sigma']>. \tag{13}$$

From eqs. (3) and (13) one obtains

$$<[\sigma],[F][\sigma']> = <\omega^2[\sigma],[\sigma']>. \tag{14}$$

Substitution of equation (14) into equation (11) yields,

$$<[\sigma][\sigma']> = \frac{<[\sigma],[S][\sigma']>}{\omega^2-\omega'^2} . \tag{15}$$

Since the eigen vectors $[\sigma(\underline{k},j)]$ of the perfect lattice can be represented as a set of orthonormal vectors[17], an arbitrary vector $[\sigma']$ can be expressed uniquely as a linear combination of this orthonormal set, $[\sigma(\underline{k},j)]$, as

$$[\sigma'] = \sum_{\underline{k},j} \alpha(\underline{k},j)[\sigma(\underline{k},j)], \tag{16}$$

where $\alpha(k,j)$ are the expansion coefficients.

36

Premultiplying eq. (16) by the eigen-vectors $[\sigma(\underline{k},j)]$ of the perfect lattice and using the orthonormality condition of $[\sigma(\underline{k},j)]$, the constants $\alpha(\underline{k},j)$ can be expressed as,

$$\alpha(\underline{k},j) = \langle[\sigma],[\sigma']\rangle. \tag{17}$$

From eqs. (15) and (17) one obtains

$$\alpha(\underline{k},j) = \frac{\langle[\sigma],[S][\sigma']\rangle}{\omega^2 - \omega'^2}. \tag{18}$$

Therefore eq. (16) can be written as

$$[\sigma'] = \sum_{\underline{k},j} \frac{\langle[\sigma],[S][\sigma']\rangle}{\omega^2 - \omega'^2}[\sigma] \tag{19}$$

or in terms of the matrix elements,

$$\sigma_{x'} = \sum_{\underline{k},j}\sum_{x'} \frac{\sigma_{x'}^*([S][\sigma'])_{x'}}{\omega^2 - \omega'^2}\sigma_x \tag{20a}$$

$$= \sum_{x'}\left(\sum_{\underline{k},j} \frac{\sigma_{x'}^*\sigma_x}{\omega^2 - \omega'^2}\right)([S][\sigma'])_{x'} \tag{20b}$$

$$= \sum_{x'}\left(\sum_{\underline{k},j} \frac{\sigma_{x'}^*\sigma_x}{\omega^2 - \omega'^2}\sum_{x''}S_{x'x''}\sigma_{x'}\right. \tag{20c}$$

A comparison of eqs. (20c) and (9) results in the following representation of the Green's function matrix elements

$$G_{xx'} = \sum_{\underline{k},j} \frac{\sigma_{x'}^*(\underline{k},j)\sigma_x(\underline{k},j)}{\omega^2 - \omega'^2}. \tag{21}$$

Having obtained the Green's function matrix $[G]$, eqs. (9) and (10) can now be used to calculate the frequency and the amplitude of vibration of the impurity atom. The essential point of this technique is the limited extension of the perturbation matrix $[S]$. This

37

results in a solution of equations (9) and (10) in the perturbed region only. For a linear diatomic lattice of Fig. 1, the matrix $[S]$, viz., eq. (5) has the elements,

$$S_{0,0} = 2\Delta f - \Delta m \omega^2$$

$$S_{1,1} = S_{-1,-1} = \Delta f \tag{22}$$

$$S_{-1,0} = S_{1,0} = S_{0,-1} = S_{0,1} = -\Delta f$$

while the other elements are zero. Substituting the matrix elements of $[S]$ into eq. (9) one obtains

$$\sigma'_x = \sigma'_{-1} \Delta f(g_{x,-1} - g_{x,0}) + \sigma'_1 \Delta f(g_{x,1} - g_{x,0})$$

$$+ \sigma'_0 [(2\Delta f - \Delta m \omega^2) g_{x,0} - \Delta f(g_{x,1} + g_{x,-1})]. \tag{23}$$

By setting x equal to -1, 0, 1 three equations for σ'_{-1}, σ'_0 and σ'_1 evolve. Since the impurity is a center of inversion for the linear diatomic chain shown in Fig. 1,

$$\sigma_{-1} = \pm \sigma_1. \tag{24}$$

Also since the Green's function matrix elements g_{xx}, defined by equation (21) have the same symmetry property, two equations in σ'_0 and $\sigma'_{\pm 1}$ will result. After obtaining these, all other σ'_x's are obtained by recursion. The eigenfrequencies ω'^2 of the perturbed lattice which are the solution of the secular equation $|[G][S] - [I]| = 0$, are now determined by the determinant of the coefficients of two homogeneous equations for σ'_0 and $\sigma'_{\pm 1}$.

The frequency of vibration of the substitutional atom may occur either within or outside the vibrational spectrum of the perfect crystal. If the impurity atom is lighter in mass than the atom it replaces in the crystal, it is possible for certain exceptional vibrational modes called localized modes to appear. These modes are characterized by the fact that their frequencies lie above the maximum frequency of the unperturbed crystal. The displacement amplitudes of the atoms of a crystal with a localized mode decay very quickly with increasing distance from the impurity site.

If the frequency distribution function of the perfect crystal has a gap between the acoustic and optic branches, it is possible for an allowed localized vibrational mode to occur in this gap. This localized vibrational mode is usually referred to as a gap mode. Gap modes occur when the mass of the impurity atom may be lighter or heavier than one or both of the host lattice masses. Since a gap mode has a frequency which lies in the forbidden frequency band of the perfect crystal, the displacement of the atoms vibrating in the neighborhood of the impurity decay rapidly with increasing distance from the impurity site.

Due to the fact that the frequency of a local or a gap mode lies outside the allowed frequency range of the perfect crystal, there is no mixing between the impurity mode and the unperturbed modes of the crystal. Therefore the localized and gap mode may occur at any wave vector point in any direction and there is no dispersion for these modes.

A third kind of vibrational mode, introduced into the crystal by the presence of impurities, is the resonance mode. Unlike localized and gap modes, resonance modes are not true normal modes of a perturbed crystal. These modes are localized in frequency but not in space. Since the frequency of a resonance mode falls in the range of the allowed frequency band of the host crystal, it can decay into the continuum of unperturbed band modes. A crude physical explanation of the nature of these modes can be given as follows. In the low frequency acoustic branches all the atoms are moving in phase with each other independent of their masses. If the impurity atom is very heavy or if it is coupled very weakly to the surrounding host crystal, it will be vibrating in phase with its neighbors at very low frequencies. However, as the frequency of the lattice vibrations increases the impurity atom begins to lag behind its neighbors because of its heavy mass or weak binding to the crystal. This continues until a frequency is reached at which the impurity atom vibrates 180° out of phase with its neighbors. This frequency is defined as the frequency of a resonance mode. As might be expected, the mean square vibrational amplitude of the impurity atom as a function of frequency is sharply peaked at the resonance mode frequency, in comparison to the amplitudes of its neighbors. Resonant modes may occur in the acoustic or the optic band of the frequency distribution function of the perfect crystal. The impurity masses associated with resonant modes may

39

be heavier or lighter than the host crystal atom masses.
The force constants with which the impurity particle
couples to its nearest neighbors play an important role
in determining the frequency of the resonant mode.

Mazur and co-workers[3] have solved the problem of
impurity modes in a linear diatomic chain with an impur-
ity atom of mass m_I which replaces either the heavy mass,
M, or the light mass, m, of the chain as shown in Fig. 1.
Since in this analysis it is assumed that $m < M$, there is
a gap present in the frequency distribution function.
The solutions of this impurity problem are shown in Fig.
2 for m_I replacing M and m respectively. For the case
where $m_I < M$, a local mode above the top of the optic spec-
trum and a gap mode between the acoustic and optic bran-
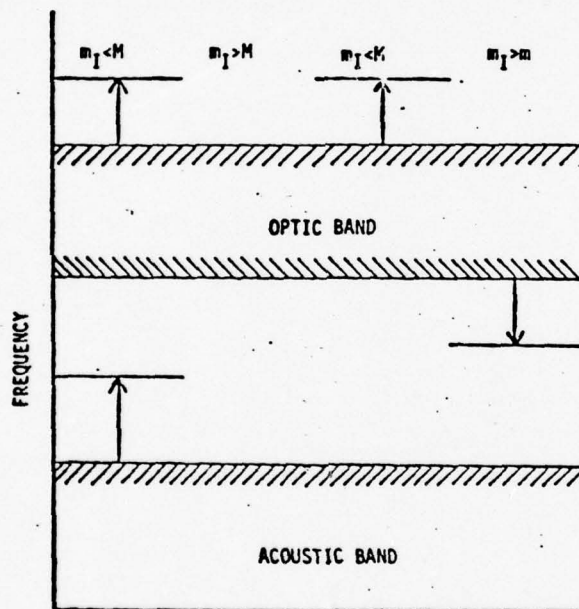ches is predicted. For the case where $m_I > M$ neither local

FIG. 2 Impurity modes in a linear diatomic chain $(m < M)$.
Four cases shown are:
(1) a light impurity atom replaces the heavy atom of the
    host lattice $(m_I < M)$,
(2) a heavy impurity atom replaces the heavy atom $(m_I > M)$
(3) a light impurity atom replaces the light atom $(m_I < m)$
and (4) a heavy impurity atom replaces the light atom
$(m_I > m)$.

552   J. F. VETELINO AND S. S. MITRA

nor gap mode is predicted. When the impurity atom re-
places the lighter host atom such that $m_I < m$, a local
mode above the optic spectrum is predicted. Finally,
when $m_I > m$, a gap mode between the optic and acoustic
branches is predicted.

It will be shown that three dimensional crystals
having a gap in the frequency distribution function con-
form with the predictions for the case 1, 3, and 4 for
Figure 2. For the second case where $m_I > M$, a gap mode is
predicted which constitutes a new condition hitherto un-
noticed.

The amplitude of an impurity ion and its neighbors
in a linear diatomic chain have been calculated by Renk[18]
for the local and gap modes. These are shown in Figure
3. For local modes, the negative ions move in one direc-
tion while the positive ions move in the opposite direc-
tion. The maximum amplitude is associated with the im-
purity ion and decays exponentially with increasing dis-
tance from the impurity ion. For the gap mode similar
ions vibrate $180°$ out of phase with each other. The
maximum amplitude is associated with the impurity ion
and decays exponentially with increasing distance from
the impurity ion. In contrast with the localized and
gap modes, the resonant mode is not spatially localized
but extends far into the lattice. The amplitude of the
impurity ion and its neighbors for a low frequency reson-
ant mode in a linear diatomic chain have been calculated
by Weber[19] and are shown in Fig. 3.

B. Three Dimensional Lattice with a Substitutional
   Impurity.

Before digressing into the explicit mathematical
formalism for this system, it is worthwhile to spend some-
time reviewing the lattice dynamics for perfect crystals
in three dimensions and the concept of normal coordinates.
The total potential energy of the atoms in a crystalline
solid will be denoted as Φ. Assuming that each atom un-
dergoes a small displacement, $\underline{u}\binom{l}{K} = [u_x\binom{l}{K}, u_y\binom{l}{K}, u_z\binom{l}{K}]$

from its equilibrium position, the potential energy func-
tion Φ can be expanded in a Taylor series about the equi-
librium position in terms of the powers of the displace-
ments:

DYNAMICS OF STRUCTURALLY DISORDERED SOLIDS

Local Mode

Gap Mode
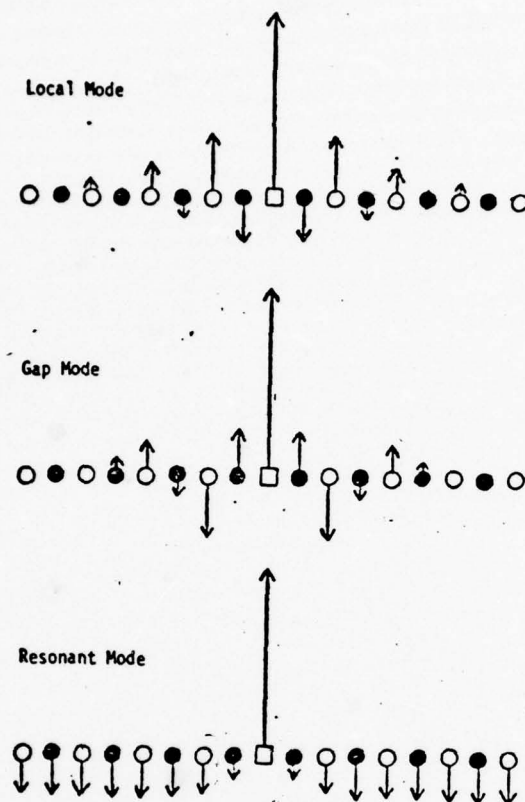
Resonant Mode

Fig. 3 Eigenvectors for local, gap and resonant modes in a linear diatomic chain.

$$\Phi = \Phi_0 + \sum_{\ell, K, \alpha} \Phi_\alpha \left({}^\ell_K \right) u_\alpha \left({}^\ell_K \right)$$

$$+ 1/2 \sum_{\ell, K, \alpha} \sum_{\ell', K', \beta} \Phi_\alpha \left({}^{\ell \ell'}_{KK'} \right) u_\alpha \left({}^\ell_K \right) u_\beta \left({}^{\ell'}_{K'} \right) + \ldots ,$$

(25)

where the subscripts α and β refer to the x, y and z component of the displacement and

J. F. VETELINO AND S. S. MITRA

$$\Phi_\alpha\binom{\ell}{K} = \frac{\partial\Phi}{\partial u_\alpha\binom{\ell}{K}}\bigg|_0 \qquad (26)$$

and

$$\Phi_{\alpha\beta}\binom{\ell\ell'}{KK'} = \frac{\partial^2\Phi}{\partial u_\alpha\binom{\ell}{K}\partial u_\beta\binom{\ell'}{K'}}\bigg|_0 \qquad (27)$$

The subscript "0" means that the derivatives are evaluated at the equilibrium configuration of the lattice. Physically, the coefficient, $\Phi_\alpha\binom{\ell}{K}$, defined in eq. (26)

can be explained as being the negative of the force acting in the α-direction on the atom at $\underline{r}\binom{\ell}{K}$ in the equilibrium configuration. However, in the equilibrium configuration the force on any particle must vanish, therefore,

$$\Phi_\alpha\binom{\ell}{K} = 0. \qquad (28)$$

Under the harmonic approximation the potential energy expansion contains terms only up to the second power in displacement. Mathematically the resulting equation of motion could not be solved exactly if higher ordered terms were retained. The harmonic approximation is quite reasonable because we are dealing with very small displacements of the particles. The equations of motion of the lattice can now be written under the harmonic approximation as,

$$m_K \ddot{u}_\alpha\binom{\ell}{K} = -\frac{\partial\Phi}{\partial u_\alpha\binom{\ell}{K}} = -\sum_{\ell',K',\beta}\Phi_{\alpha\beta}\binom{\ell\ell'}{KK'} u_\beta\binom{\ell'}{K'}. \qquad (29)$$

It is obvious from the form of eq. (29) that the coefficient, $\Phi_{\alpha\beta}\binom{\ell\ell'}{KK'}$, is a force constant. Physically it

describes the force exerted in the α-direction on the atom at $\underline{r}\binom{\ell}{K}$ when the atom at $\underline{r}\binom{\ell'}{K'}$ is displaced in the β-direction. It is also interesting to point out that from eq. (27) the coefficient $\Phi_{\alpha\beta}\binom{\ell\ell'}{KK'}$ satisfies the

following symmetry condition,

$$\Phi_{\alpha\beta}\binom{\ell\ell'}{KK'} = \Phi_{\beta\alpha}\binom{\ell'\ell}{K'K}. \tag{30}$$

The periodicity of the lattice requires that if the lattice as a whole is translated relative to itself by a lattice vector $\underline{r}\binom{\ell}{K}$, it coincides with itself. Due to this fact, the same triplet of integers (ℓ_1, ℓ_2, ℓ_3) can be added to the cell index ℓ in the coefficient $\Phi_\alpha\binom{\ell}{K}$

and to both of the cell indices in the coefficient $\Phi_{\alpha\beta}\binom{\ell\ell'}{KK'}$ without changing their value. Thus $\Phi_\alpha\binom{\ell}{K}$ must be independent of ℓ, while $\Phi_{\alpha\beta}\binom{\ell\ell'}{KK'}$ can only depend on the relative cell index $\ell-\ell'$ and not on ℓ and ℓ' separately. These results can be expressed as,

$$\Phi_\alpha\binom{\ell}{K} = \Phi_\alpha\binom{0}{K}$$

and

$$\Phi_{\alpha\beta}\binom{\ell\ell'}{KK'} = \Phi_{\alpha\beta}\binom{\ell-\ell'}{KK'}. \tag{31}$$

Due to the translational symmetry within the lattice, the equation of motion should be invariant for rigid translations of the lattice as a whole, namely,

$$\sum_{\ell'K'} \Phi_{\alpha\beta}\binom{\ell\ell'}{KK'} = \sum_{\ell K} \Phi_{\alpha\beta}\binom{\ell\ell'}{KK'} = 0, \tag{32}$$

and also invariant for a rigid rotation of the lattice[20].

The equations of motion form an infinite set of simultaneous linear differential equations. The solution of eq. (29) can be expressed in terms of a traveling wave given by,

$$u_\alpha\binom{\ell}{K} = \frac{1}{\sqrt{m_K}} \sigma_\alpha(K) \exp[-i\omega t + 2\pi \underline{k} \cdot \underline{r}(\ell)]. \tag{33}$$

ω is the angular frequency of the wave, $\dfrac{\sigma_\alpha(K)}{\sqrt{m_K}}$, the wave amplitude which is independent of ℓ and k, the wave vector. Substitution of eq. (33) into eq. (29) yields,

$$\omega^2 (m_K)^{1/2} \sigma_\alpha(K) = \sum_{\ell' k' \beta} \Phi_{\alpha\beta} \binom{\ell\ell'}{KK'} \frac{\sigma_\beta(K')}{(m_{K'})^{1/2}}$$

$$\exp[i2\pi\underline{k}\cdot r\binom{\ell'}{K'}) - r\binom{\ell}{K})]. \qquad (34)$$

Using the periodic symmetry condition of the lattice, given in eq. (31), eq. (34) may be shown to reduce to the following,

$$\omega^2 \sigma_\alpha(K) = \sum_{k'\beta} F_{\alpha\beta}\binom{k}{KK'})\sigma_\beta(K'), \qquad (35)$$

where

$$F_{\alpha\beta}\binom{k}{KK'}) = \frac{1}{(m_K m_{K'})^{1/2}} \sum_\ell \Phi_{\alpha\beta}\binom{\ell}{KK'})$$

$$\times \exp[-2\pi i\underline{k}\cdot r\binom{0\ell}{KK'})] \qquad (36)$$

and

$$r\binom{0\ell}{KK'}) = r\binom{\ell}{K'}) - r\binom{0}{K}). \qquad (37)$$

$F_{\alpha\beta}\binom{k}{KK'})$ is defined as the coupling coefficient.

Due to the fact that $\Phi_{\alpha\beta}\binom{\ell\ell'}{KK'})$ is a function of $\ell-\ell'$ only and does not depend on ℓ and ℓ' separately, the coefficients $F_{\alpha\beta}\binom{k}{KK'})$ are independent of ℓ. Therefore, the problem of solving the infinite set of equations of motion (29) is now reduced to the problem of solving a set of 3s linear homogeneous equations in 3s unknowns, $\sigma_\alpha(K)$, given in eq. (35), where s is the number of particles per unit cell.

The equations of motion can be written more concisely in matrix notation as,

$$[F][\sigma] - \omega^2[\sigma] = 0. \qquad (38)$$

$[\sigma]$ is a 1 x 3s matrix written as,

45

$$[\sigma] = \begin{bmatrix} \sigma_x(1) \\ \vdots \\ \sigma_x'(S) \\ \sigma_y(1) \\ \vdots \\ \sigma_y'(S) \\ \sigma_z(1) \\ \vdots \\ \sigma_z'(S) \end{bmatrix} \tag{39}$$

and $[F]$ is a $3s \times 3s$ matrix defined as

$$[F] = \begin{bmatrix} F_{xx}(^{k}_{11}) \cdots F_{xx}(^{k}_{1S})F_{xy}(^{k}_{11}) \cdots F_{xy}(^{k}_{1S})F_{xz}(^{k}_{11}) \cdots F_{xz}(^{k}_{1S}) \\ F_{xx}(^{k}_{S1}) \cdots F_{xx}(^{k}_{SS})F_{xy}(^{k}_{S1}) \cdots \\ F_{yx}(^{k}_{11}) \cdots F_{yx}(^{k}_{1S}) \\ F_{yx}(^{k}_{S1}) \\ F_{zx}(^{k}_{11}) \\ F_{zx}(^{k}_{S1}) \cdots \quad \cdots F_{zz}(^{k}_{S1}) \quad F_{zz}(^{k}_{SS}) \end{bmatrix} \tag{40}$$

The condition for these $3s$ homogeneous simultaneous equations to have a non-trival solution is

$$|[F] - \omega^2[I]| = 0. \tag{41}$$

Eq. (41) is an equation of degree $3s$ in ω^2. The $3s$ solutions for each value of wave vector $\underline{k}$ are denoted by $\omega_j(\underline{k})$ where $j = 1, 2, \ldots, 3s$. Examination of eq. (36) reveals that the matrix $[F]$ is hermitian, and hence the eigenvalues, $\omega_j^2(\underline{k})$, are real[17]. The physics of the problem also requires $\omega_j(\underline{k})$ to be positive.

For each of the $3s$ values of $\omega_j(\underline{k})$ corresponding to a given value of $\underline{k}$ there exists a vector $[e(K|^{k}_{j})]$. The vector $[e(K|^{k}_{j})]$ is not to be confused with $[\sigma(K)]$. The

46

former refers to the eigenvector associated with a par-
ticular eigenfrequency, $\omega_j(\underline{k})$, whereas $[\sigma(K)]$ refers to
the general set of eigenvalues, ω^2. The components of
the vector $[e(K|\frac{k}{j})]$ are the solutions to the set of equa-
tions (35), which can be written as

$$\omega_j(\underline{k}) = e_\alpha(K|\tfrac{k}{j}) = \sum_{k'\beta} F_{\alpha\beta}(\tfrac{k}{KK'}) \, e_\beta(K'|\tfrac{k}{j}). \qquad (42)$$

Eq. (42) defines $[e(K|\frac{k}{j})$ to within a constant factor and
this factor can be chosen in such a way that $[e(K|\frac{k}{j})]$
satisfies the orthonormality conditions,

$$\sum_{k,\alpha} e_\alpha^*(K|\tfrac{k}{j}) \, e_\alpha(K|\tfrac{k}{j}) = \sigma_{jj'} , \qquad (43)$$

and

$$\sum_j e_\beta^*(K'|\tfrac{k}{j}) \, e_\alpha(K|\tfrac{k}{j}) = \sigma_{\alpha\beta}\sigma_{KK'} , \qquad (44)$$

where $\sigma_{\alpha\beta}$ and $\sigma_{jj'}$ are Kronecker deltas.

The values which the wave vector $\underline{k}$, introduced in
eq. (33), one can assume are determined by the boundary
conditions imposed on the components of the displacement
vectors $\underline{u}(\tfrac{\ell}{K})$. The equations of motion are derived for an
infinitely extending lattice. This lattice can then be
normalized to a finite volume by partitioning the lat-
tice into cubes of dimension L^3 each. It is assumed that
the cube contains N lattice cells with L lattice cells
along each edge. These partitions form a macro-lattice
with the cube of N cells being the macro-cell with $L\underline{a}_1$,
$L\underline{a}_2$, $L\underline{a}_3$ as basis vectors. The periodic boundary condi-
tion postulates that the atomic displacement be periodic
with the periodicity of the macro-cells, that is,

$$\underline{u}(\tfrac{\ell+L}{K}) = \underline{u}(\tfrac{\ell}{K}). \qquad (45)$$

This cyclic boundary condition simplifies the lattice
dynamical behavior which does not depend explicitly on
the crystal's surface. When applied to the components
of the displacement vector given by eq. (33) the cyclic
boundary condition requires that

$$e^{2\pi i \underline{k} \cdot L\underline{a}_1} = e^{2\pi i \underline{k} \cdot L\underline{a}_2} = e^{2\pi i \underline{k} \cdot L\underline{a}_3} = 1. \qquad (46)$$

The reciprocal lattice vector can be represented as

$$\underline{g}(h) = h_1\underline{b_1} + h_2\underline{b_2} + h_3\underline{b_3} \,, \tag{47}$$

where h_1, h_2, h_3 are arbitrary integers which can be positive, negative or zero. The scalar product between a direct lattice vector and a reciprocal lattice vector is just an integer:

$$\underline{r}(\ell) \cdot \underline{g}(h) = \ell_1 h_1 + \ell_2 h_2 + \ell_3 h_3. \tag{48}$$

Therefore an expression for $\underline{k}$ which satisfies equation (46) is given by

$$\underline{k} = \frac{1}{L}\,\underline{g}(h) = \frac{h_1}{L}\,\underline{b_1} + \frac{h_2}{L}\,\underline{b_2} + \frac{h_3}{L}\,\underline{b_3} \,. \tag{49}$$

The values of the integers h_1, h_2, h_3 are now restricted by eqs. (45) and (48) such that if any reciprocal lattice vector $\underline{y}(h)$ is added to $\underline{k}$, the value of $u_\alpha(\begin{smallmatrix}\ell\\K\end{smallmatrix})$ remains the same. Hence, it is possible to obtain all distinct solutions if the value of $\underline{k}$ is restricted to lie in one unit cell of the reciprocal lattice:

$$\underline{k} = \frac{h_1}{L}\,\underline{b_1} + \frac{h_2}{L}\,\underline{b_3} + \frac{h_3}{L}\,\underline{b_3} \,,$$

where (50)

$$h_1, h_2, h_3 = 1, 2, \ldots.$$

Thus there are $L^3 = N$ allowed values of wave vector $\underline{k}$. For most calculations it is important that these values are uniformly distributed. From eq. (50) the volume in reciprocal space which contains all the allowed values of the wave vector $\underline{k}$ can be seen to be that generated by a reciprocal lattice vector $\underline{b}$. An equivalent volume in reciprocal space which displays a higher degree of symmetry than the reciprocal lattice can be obtained by drawing vectors from the origin of the reciprocal lattice to all lattice points and then constructing planes which are the perpendicular bisectors of these vectors. The smallest volume in the reciprocal space which is enclosed by these planes can be shown to be completely equivalent to the unit cell in that every allowed value of $\underline{k}$ in the unit cell differs from a corresponding point in the symmetric polyhedron only by a translation vector of the

reciprocal lattice, and hence the two are equivalent. The symmetric polyhedron constructed in this fashion and containing all allowed values of $\underline{k}$ is known as the first Brillouin zone of the reciprocal lattice.

Due to the symmetry of the first Brillouin zone, one need only consider $\underline{k}$ values in a small region (the irreducible element) of this zone to evaluate any vibrational property of the lattice. For cubic crystals, the volume of the irreducible element is $1/48^{th}$ of the volume of the Brillouin zone. Thereafter, the totality of frequencies, $\omega_j(\underline{k})$ can be obtained by solving equation (35) for values of $\underline{k}$ in $1/48^{th}$ of the irreducible volume of the total Brillouin zone.

Since the displacements $\underline{u}\binom{\ell}{k}$ are small and the potential energy expansion (25) contains quadratic terms in displacement, the general motion of the lattice can be given by the principle of superposition. Each of the waves given by equation (33) travels through the lattice independent of the others. The whole configuration of the lattice may then be expressed in terms of the displacements due to this set of independent waves, just as well as in terms of the coordinates of the individual lattice points. Therefore, the waves can be considered as themselves constituting an independent set of coordinates known as normal coordinates. Each normal coordinate describes an independent mode of vibration of the crystal with only one frequency and phase and is referred to as a normal mode. In general there are $3Ns$ normal modes of vibration. In terms of these normal coordinates, $\underline{Q}\binom{k}{j}$, the general motion of the lattice can be defined in the following fashion,

$$u_\alpha(\ell) = \frac{1}{(Nm)^{1/2}} \sum_{\underline{k},j} e_\alpha\binom{k}{j}\underline{Q}\binom{k}{j}\exp[i2\pi\underline{k}\cdot\underline{r}(\ell)] , \quad (51)$$

where the subscript k of equation (33) has been suppressed and the time dependence is understood in the $\underline{Q}\binom{k}{j}$ term. m and $e_\alpha\binom{k}{j}$ in equation (51) are the mass and the eigenamplitude corresponding to the frequency $\omega_j(\underline{k})$, of both the positive and the negative ions, respectively. By defining the function, $\chi_\alpha(\ell|\frac{k}{j})$ as

$$\chi_\alpha\left(\ell\Big|\frac{k}{j}\right) = (Nm)^{1/2}e_\alpha\binom{k}{j}\exp[i2\pi\underline{k}\cdot\underline{r}(\ell)] \qquad (52)$$

49

equation (51) can be written in the following fashion,

$$u_\alpha(\ell) = \sum_{\underline{k},j} \chi_\alpha(\ell|{}_j^{\underline{k}})\underline{Q}({}_j^{\underline{k}}) \tag{53}$$

Substitution of the displacements $u_\alpha(\ell)$, defined in equation (51), into equation (29) yields,

$$\sum_{\beta\ell'} \Phi_{\alpha\beta}(\ell\ell')\chi_\beta(\ell'|{}_j^{\underline{k}}) = m\omega_j^2(\underline{k})\chi_\alpha(\ell|{}_j^{\underline{k}}) \tag{54}$$

The terms $\chi_\alpha(\ell|{}_j^{\underline{k}})$ are eigenvector terms with respect to the normal coordinates and are normalized as follows:

$$\sum_{\alpha\ell} m|\chi_\alpha(\ell|{}_j^{\underline{k}})|^2 = 1. \tag{55}$$

Since the characteristic frequency of the $({}_j^{\underline{k}})$ normal mode is $\omega_j(\underline{k})$, which is the same as the eigenfrequency of the matrix $[F]$, and since there is a one to one correspondence between these eigenvalues and the normal coordinates, the normal mode frequencies of the lattice can also be identified as $[\omega_j(\underline{k})]$ where the brackets indicate the complete set of lattice frequencies.

It can be seen from equations (42), (32) and (36), that out of the 3s solutions for each $\underline{k}$, three tend toward zero as $\underline{k}$ goes to zero. Such modes are called acoustic modes and are characterized by the condition.

$$\frac{[e(\kappa|{}_j^0)]}{\sqrt{m_\kappa}} = \frac{[e(\kappa'|{}_j^0)]}{\sqrt{m_{\kappa'}}} = \underline{u}({}_\kappa^\ell|{}_j^0) = \underline{u}({}_{\kappa'}^\ell|{}_j^0), \tag{56}$$

where the expression $\underline{u}({}_\kappa^\ell|{}_j^{\underline{k}})$ refers to the displacement from equilibrium of the κth atom in the ℓth unit cell when it is vibrating with frequency $\omega_j(\underline{k})$. Therefore, all s particles in each unit cell move in parallel and with equal amplitudes which is a characteristic of the displacement associated with an acoustic wave in an elastic continuum.

The remaining 3s - 3 modes whose frequencies do not vanish at $\underline{k} = 0$ are called optic modes. For diatomic crystals ($s = 2$), i.e., equation (43) for $\underline{k} = 0$ can be written in vector form as

50

$$[e(A|_j^0)] \cdot [e(A|_{j'}^0)] + [e(B|_j^0)] \cdot [e(B|_{j'}^0)] = 0 \quad (57)$$

where A and B refer to the positive and negative ions, respectively, j refers to any one of the acoustic branches and j' refers to any one of the optic branches. Equations (56) and (57) can be solved to obtain,

$$[e(A|_j^0)] \cdot \{[e(A|_{j'}^0)] + \frac{m_B}{m_A}[e(B|_j^0)]\} = 0 \quad (58)$$

Excluding the trival solutions, $[e(K|_j^k)] \equiv 0$, one gets

$$\sqrt{m_A}\,[e(A|_j^0)] = -\sqrt{m_B}\,[e(B|_j^0)]. \quad (59)$$

Therefore for the optic mode the two ions in each unit cell vibrate 180° out of phase, while the center of mass of the cell remains stationary.

For increasing values of $\underline{k}$, the ratio of the amplitudes of the lighter to heavier atom in the optic branch in general increases. The corresponding ratio in the branch eq. (56) decreases from its value to unity for $\underline{k} = 0$.

The dispersion of the lattice is expressible by the equation,

$$\omega = \omega_j(\underline{k}), \quad j=1, 2.....3s. \quad (60)$$

In diatomic crystals the number of atoms in each unit cell is two, therefore in general there are three acoustic and three optic branches of phonon dispersion.

The introduction of a substitutional impurity for one of the atoms of the host lattice modifies the dynamical behavior of the lattice in the region of the substitution. It is assumed in this analysis that the force constants remain unchanged from the perfect lattice in the vicinity of the defect and that only the mass parameter is changed. Due to the presence of a substitutional impurity, the mass m in eq. (29) will depend on l. Writing this in terms of its deviation from the perfect lattice value, the general equation of motion which gives the normal modes and frequencies of the perturbed lattice

51

can be written as

$$m(\ell)\ddot{u}_\alpha(\ell) + \sum_{\beta\ell'} \Phi_{\alpha\beta}(\ell\ell')u_\beta(\ell') = \Delta m(\ell)\ddot{u}_\alpha(\ell) \qquad (61)$$

The new normal modes for the perturbed lattice can be defined by a transform similar to eq. (53),

$$u_\alpha(\ell) = \sum_f \chi'_\alpha(\ell|f)df. \qquad (62)$$

These new normal modes are labeled by a quantum number, f, which takes 3Ns values. The new normal coordinates of the perturbed lattice, df, are similar to the normal coordinates, $Q(\frac{k}{j})$, of the perfect lattice and also include the time dependence. The $\chi'_\alpha(\ell|f)$ terms are the eigenvector terms corresponding to the normal coordinates of the perturbed lattice. Substitution of eq. (62), into eq. (63) yields,

$$-\omega'^2 m \, \chi'_\alpha(\ell|f) + \sum_{\beta\ell'} \Phi_{\alpha\beta}(\ell\ell') \, \chi'_\beta(\ell'|f)$$

$$= \sum_{\beta\ell'} S_{\alpha\beta}(\ell\ell') \, \chi'_\beta(\ell'|f), \qquad (63)$$

where $S_{\alpha\beta}$ now incorporates the change of mass and is given as,

$$S_{\alpha\beta}(\ell\ell') = -\Delta m(\ell)\omega'^2\delta_{\alpha\beta}\delta_{\ell\ell'} \qquad (64)$$

The eigenvectors $\chi'_\alpha(\ell|f)$ of the perturbed lattice, which correspond to the normal coordinates df, are normalized by a relation similar to that given in eq. (55), namely,

$$\sum_{\alpha\ell} (m(\ell) + \Delta m(\ell))|(\chi'_\alpha(\ell|f)|^2 = 1. \qquad (65)$$

In matrix notation the equations of the perfect lattice [eq. (54)], can be written as,

$$[L][\chi] = [[D] - \omega^2[I]][\chi] = 0, \qquad (66)$$

where [D] incorporates the particle masses, m, and the force constants $\Phi_{\alpha\beta}(\ell\ell')$. For the lattice with a

52

substitutional impurity, eq. (66) bocomos

$$[L][\chi'] = [[D] - \omega'^2[I]][\chi'] = [S][\chi'] \tag{67}$$

where ω'^2 and $[\chi']$ are the eigenvalues and the eigen-
vectors of the imperfect lattice and $[S]$ is the pertur-
bation matrix incorporating the change of mass.

A Green's function technique, introduced earlier
can be used to calculate the new normal mode frequencies
and the amplitude of the lattice with substitutional im-
purities. Eq. (66) is the perfect crystal equation while
(67) is identical to equation (6) with the symbol D re-
placed by F and χ by σ. Therefore, the Green's function
technique described before can be applied for the three
dimensional case. The Green's function matrix $[G]$ de-
fined as in eq. (7) may be written as,

$$-\omega^2 m \mathcal{E}_{\alpha\gamma}^{\omega}(l, l'') + \sum_{\beta l'} \Phi_{\alpha\beta}(l, l') \, \mathcal{E}_{\beta\gamma}^{\omega}(l', l'') = \delta_{\alpha\gamma}\delta_{ll''} \tag{68}$$

where $\mathcal{E}_{\alpha\gamma}^{\omega}(l, l'')$ are the elements of $[G]$. The explicit
representation of the elements, $g_{\alpha\gamma}^{\omega}$, of the Green's func-
tion matrix, as given by eq. (21) can be written as

$$\mathcal{E}_{\alpha\gamma}^{\omega}(l, l'') = \sum_{\underline{k}, j} \frac{\chi_{\alpha}^{*}(l|\frac{\underline{k}}{j}) \, \chi_{\beta}(l''|\frac{\underline{k}}{j})}{\omega_{j}^{2}(\underline{k}) - \omega'^2} \tag{69}$$

Eq. (9) describing the eigenvectors of the perturbed lat-
tice can be written as

$$\chi_{\alpha}'(l|f) = \sum_{\beta l' \gamma l''} \mathcal{E}_{\alpha\beta}^{\omega}(l, l'') S_{\beta\gamma}(l'', l') \chi_{\gamma}'(l'|f). \tag{70}$$

The eigenfrequencies of the perturbed lattice are deter-
mined by the secular equation,

$$\left| \sum_{\beta l''} \mathcal{E}_{\alpha\beta}^{\omega}(l l'') S_{\beta\gamma}(l'' l') - \delta_{\alpha\gamma}\delta_{ll'} \right| = 0. \tag{71}$$

If the cell containing the single substitutional im-
purity of the perturbed lattice is chosen to be at the
origin, eq. (64) can be written as,

53

$$S_{\alpha\beta}(\ell\ell') = -m\varepsilon\omega'^2 \, \delta_{\alpha\beta}\delta_{\ell 0}\delta_{\ell'0'} \tag{72}$$

where ε is the dimensionless mass defect parameter defined as

$$\varepsilon = \frac{m-m'}{m} . \tag{73}$$

m is the mass of the particle to be substituted for and m' is the mass of the substitutional impurity.

Using eq. (52) the element $g^\omega_{\alpha\beta}(0,0)$ of the Green's function matrix (69) can be written as

$$g^\omega_{\alpha\beta}(0,0) = \frac{1}{Nm} \sum_{\underline{k},j} \frac{e^*_\alpha(\frac{k}{j})e_\beta(\frac{k}{j})}{\omega_j^2(\underline{k})-\omega'^2} \tag{74}$$

Substitution of eq. (72) into eq. (71), reduces it to a 3 x 3 matrix

$$|m\varepsilon\omega'^2 \, \delta_{\alpha\beta}g^\omega_{\alpha\beta}(0,0) + \delta_{\alpha\beta}| = 0. \tag{75}$$

Due to the $\delta_{\alpha\beta}$ term, this equation contains only diagonal elements and the solution is triply degenerate. Substituting eq. (74) into eq. (75) one obtains

$$1 + \frac{\varepsilon(K)\omega'^2}{3N} \sum_{\underline{k},j} \frac{|\underline{e}(K|\frac{k}{j})'|^2}{\omega_j^2(\underline{k})-\omega'^2} = 0 \tag{76}$$

The above equation is used to calculate the impurity mode frequency due to a substitutional impurity replacing either the cation or the anion of the host lattice, where K refers to the ion which has been replaced by the impurity and $\varepsilon(K)$ is defined as

$$\varepsilon(K) = \frac{m(K) - m'(K)}{m(K)} .$$

It is also possible in the framework of this analysis to obtain an expression for the amplitude of vibration of the impurity. Substitution of eqs. (72) and (74) into eq. (70) yields the following expression for the amplitude of vibration in the imperfect lattice,

$$\chi_{\beta'}(\ell|f) = \frac{1}{N} \sum_{\alpha,\underline{k},j} \frac{e^*_\beta\binom{k}{j} \, e_\alpha\binom{k}{j}}{\omega_j^{\,2}(\underline{k}) - \omega'^2} \, \chi'_\alpha(0|f)\epsilon\omega'^2(f) \quad x$$

$$\exp[-i\pi\underline{k}\cdot\underline{r}(\ell)] \; . \tag{77}$$

The term $\chi_\beta^\iota(\ell|f)$ represents the modification of the amplitude of vibration of the particles in the lattice due to the defect mass. For the case $\ell = Q$, one gets $\chi_\beta^\iota(0|f)$ which corresponds to the amplitude of the defect atom itself.

The normalization condition given in eq. (65), can be written as

$$\sum_{\beta\ell} m|\chi_\beta^\iota(\ell|f)|^2 + \sum_\alpha \epsilon m|\chi_\alpha^\iota(0|f)|^2 = 1 \tag{78}$$

Substitution of eq. (78) along with the use of the orthonormality conditions given in eqs. (43) and (44) into eq. (77) yields the following equation for the amplitude of vibration for the impurity atom, $|\chi'(0|f)|^2$,

$$\frac{1}{m(k)|\chi'(0|f)|^2} = \frac{\epsilon^2(\kappa)\omega'^4(f)}{3N} \sum_{\underline{k}j} \frac{|e(\kappa|\frac{k}{j})|^2}{[\omega'^2(f)-\omega_j^{\,2}(\underline{k})]^2} \, \epsilon(\kappa). \tag{79}$$

Eqs. (76) and (79) therefore provide the basic description of the single mass defect problem in cubic crystals.

The eigenfrequencies and eigenamplitudes of the perfect lattice can be substituted into eq. (76) in order to determine the triply degenerate localized and gap modes. The local modes correspond to the condition that the substitutional impurity mass, $m'(k)$ is smaller than the corresponding host lattice atomic masses. Gap modes occur when $m'(k)$ may be heavier or lighter, than one or both of the host lattice masses.

Utilizing the modified rigid ion model[39] for the perfect lattice, calculations were performed for the impurity modes of zinc-blende type crystals. The variation of the local mode frequencies as functions of the mass defect parameter is presented in Figs. 4 and 5 for GaP and ZnSe, respectively.

55
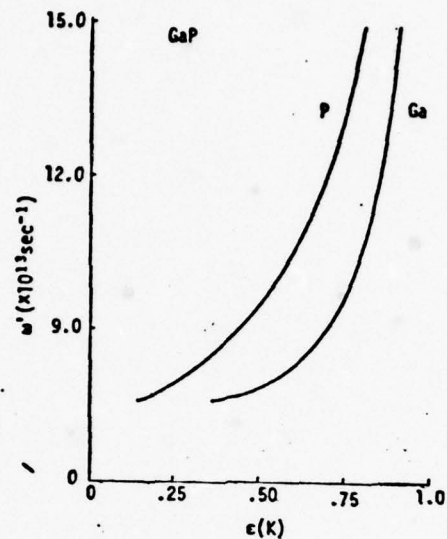
Fig. 4   Localized mode frequency, ω', as a function of the mass defect parameter, $\varepsilon(K)$, for GaP.

Fig. 5   Localized mode frequency, ω', as a function of the mass defect parameter, $\varepsilon(K)$, for ZnSe.

56

The variation of gap mode frequencies as a function of
mass defect parameter are presented in Figs. 6 and 7,
for GaP and ZnTe, respectively.

Fig. 6 Gap mode frequency, ω', as a function of the
mass defect parameter, $\varepsilon(K)$, for GaP. The gap in the
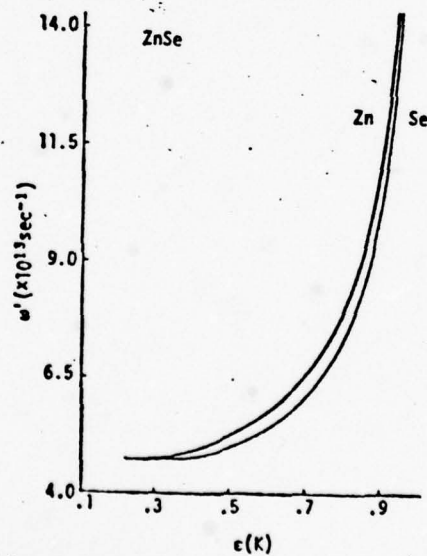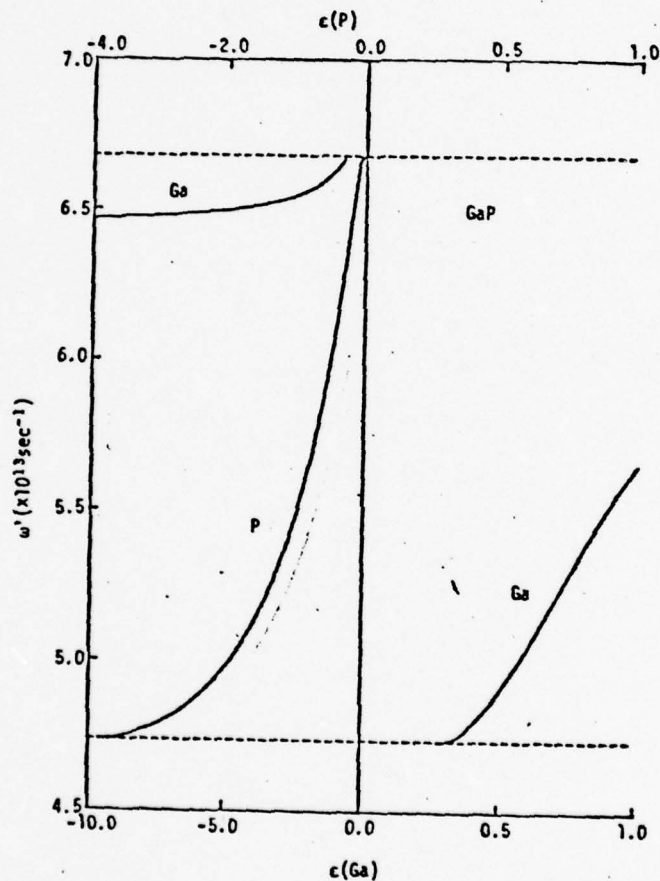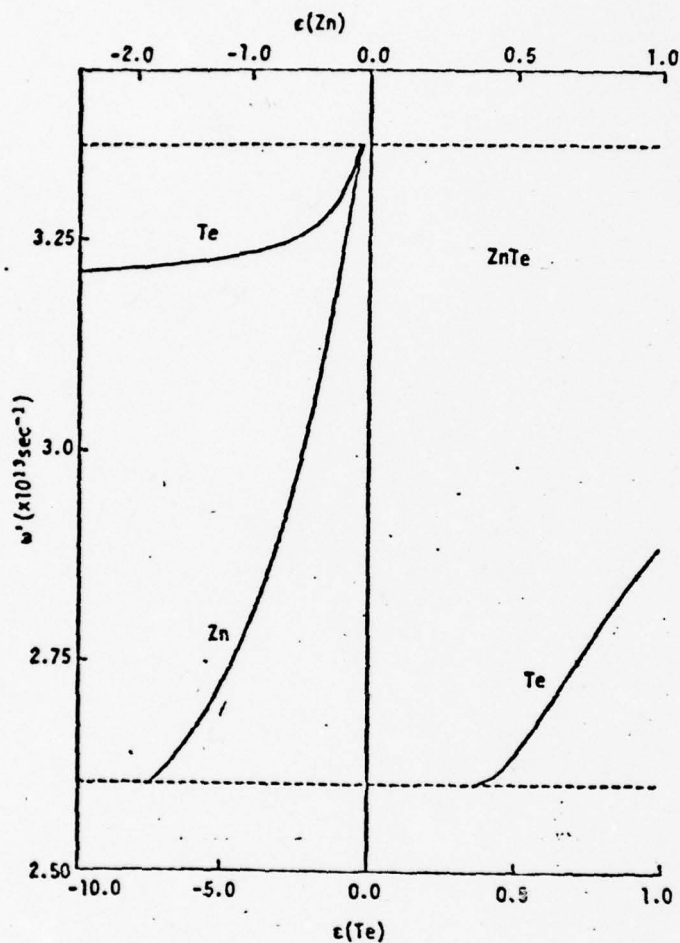frequency spectra is shown by the dotted lines.

57

FIG. 7 Gap mode frequency, ω', as a function of the mass defect parameter, $\varepsilon(K)$, for ZnTe. The gap in the frequency spectra is shown by the dotted lines.

The available experimental data are compared to some calculated values in Tables 1 and 2.

Table I: Comparison of calculated and experimental values of local mode frequencies (in cm^{-1}) for various zinc-blende compounds.

Compound[a]	Calculated local mode frequency	Experimental local mode frequency	Reference for experimental data
GaP:Si	437.4	453	31
GaP:^{11}B	611.6	569,571	31,15
GaP:^{10}B	636.6	592,594	31,15
GaP:Al	442.2	443	31
GaP:^{12}C	563.1	527,606.2	31,33
GaP:^{14}C	525.2	564	33
GaP:O	494.4	464	31
GaP:^{14}N	525.2	488	15
GaP:^{15}N	509	472	15
GaAs:Si	362.9	384	27
GaAs:Si	365	399	27
GaAs:P	351	355.4,351	25,29
GaAs:Al	368.9	362	24
GaAs:^{7}Li	685.9	422.2	22
GaAs:^{6}Li	739	451.4	22
GaSb:Al	333	316.7	21
GaSb:P	327.3	324	21
GaSb:As	248	240	16
InAs:Ga	244	240	30
InSb:Al	307	295.7	23,25
InSb:As	206.6	200	16
InSb:Ga	209.8	196	36
ZnS:Al	362.6	437.9	41
ZnS:Be	543	486	37
ZnSe:S	285.9	297	28
ZnSe:^{7}Li	563	383	26
ZnSe:^{6}Li	606.6	412	26
ZnSe:Al	301.9	359	42
ZnSe:Be	498	450	26
ZnSe:^{24}Mg	317.2	352	26
ZnSe:^{25}Mg	312	345	26
ZnSe:^{26}Mg	306.6	334	26
ZnTe:Al	274.5	312.6	41
ZnTe:S	266.5	269 to 272	35
ZnTe:Be	461.5	411	37
CdTe:Be	426	391	32
CdTe:Se	171.6	170	35
CdTe:Mg	266.3	248	34

a Underlined atom has been replaced.

59

Table 2: Comparison of calculated and experimental values of gap mode frequencies (in cm^{-1}) for impurities in GaP and SiC.

Compound[a]	Calculated gap mode frequency	Experimental gap mode frequency	Reference for experimental data
GaP:^{10}B	289.2	293.8	15
GaP:^{11}B	287.9	284.2	15
GaP:As	275	270	15
SiC:He(?)	676	670	38

a Underlined atom has been replaced.

III. MIXED CRYSTAL OR ALLOY SYSTEM

If the concentration of the substitutional impurity in a crystal increases significantly, the resulting lattice is defined as a mixed crystal system. Symbolically, a mixed crystal may be represented as $AB_{1-x}C_x$ where $0 \leq x \leq 1$. A successful lattice dynamical model for a mixed crystal system should predict the appropriate impurity modes for a substitutional impurity as x approaches either zero or unity.

The study of mixed crystals can be dated back to as early as 1928[43]. Since then several phenomenological models[44-49] have been proposed to study the vibrations of mixed crystal systems. It has been observed that the models[46,49] using the concept of a unit cell do provide some basic understanding of mixed crystals. Verleur and Barker[46] considered a cluster model to account for the two mode behavior of the mixed crystals, $GaP_{1-x}As_x$ and $CdS_{1-x}Se_x$. This model assumed that like negative ions clustered around positive ions or vice versa depending on whether the impurity was an anion or a cation. In the random element isodisplacement (REI) model, Chen, Shockley and Pearson[47] assumed that in a mixed crystal, $AB_{1-x}C_x$, the B and C atoms are distributed on the anion sublattice and the anions of like species vibrate in phase with identical amplitudes against the cations which also vibrate as a rigid unit. Later Chang and Mitra[48] modified the REI model to include the polarization field. Subsequently, Chang and Mitra[49] proposed the pseudo unit cell model and predicted the zone boundary phonons of systems exhibiting two mode behavior at the zone center.

Recently, Kutty[50] applied the Green's function technique
to derive the phonon dispersion relations in mixed crys-
tals as a function of wave vector. Sen and Hartman[51]
explained the switching from one mode to two mode type
behavior observed in some III-V mixed crystals by using
the coherent potential approximation technique in one
dimension. At present no adequate theory exists to des-
cribe the complete lattice dynamics of mixed crystal sys-
tems.

A natural "brute force" technique to calculate the
lattice dynamics of a mixed crystal is to start with a
finite chain and then permute the various number of ways
to configurationally orient the crystal depending up-
on the concentration, x. For each configuration, the
lattice dynamics would be performed and the resulting
ensemble would then be averaged to obtain the lattice
dynamics of the mixed crystal system. This technique
would however be very tedious, long and perhaps impos-
sible due to the number of configurational orientations,
and the violation of lattice periodicity in many of the
configurations. For values of x approaching either zero
or unity, the Green's function technique described before
could be applied. However, as the impurity concentration
increases, the impurity-impurity interactions become sig-
nificant. This causes the Green's function approach to
become very complicated.

In this presentation a pseudo unit cell model de-
veloped by Chang and Mitra[48,49] will be used to describe
the lattice configuration. The pseudo unit cell is formed
by the ions A, (1-x) B and xC. Although this unit cell
is simple it is obviously unphysical as far as the exact
representation of the lattice. The fact that it obeys
translational symmetry is a physical drawback. In spite
of these deficiencies, however, this model has proven[46-49]
to be a simple approach by which one can estimate general
features of the optical properties of mixed diatomic crys-
tals. In particular this model has theoretically veri-
fied[49] the experimental behavior of certain zone center
and zone boundary phonons in mixed diatomic crystals.
In view of the simplicity and previous success of this
model, it was decided to extend the calculations to all
wave vectors to see if the model has merit in mixed crys-
tal lattice dynamical calculations. In the linear chain
lattice and the mixed zinc-blende lattice, the modified
rigid ion (MRI) model[39] is used to predict the lattice
dynamics. The MRI model consists of short range central
and noncentral repulsive interactions and long range

61

Coulomb interactions among ions of appropriate effective
ionic charge. The model parameters of the mixed crys-
tal of the form $AB_{1-x}C_x$ are deduced from the elastic con-
stants, optical mode frequencies and impurity mode fre-
quencies of the host crystals. The model parameters
along with the lattice constant are assumed to vary lin-
early as a function of concentration. Explicit calcula-
tions have been performed for a hypothetical mixed lin-
ear chain and for $ZnS_{1-x}Se_x$ and $GaP_{1-x}As_x$. The phonon
dispersion in various symmetry directions and the fre-
quency distribution function are obtained as a function
of concentration.

A. Pseudo Unit Cell

The unit cell as defined in perfect crystals cannot
be uniquely defined for the mixed crystals. However, the
mixed crystal problem may be treated in a manner similar
to the pure crystal case, if certain assumptions are made
on the distribution of the ions in the lattice. In a
mixed crystal, $AB_{1-x}C_x$ where $0 \leq x \leq 1$, the B and C ions
are assumed to be distributed randomly in their corres-
ponding sublattice and to obey the law of statistics. A
corresponding pseudo unit cell is then formed by ions A,
$(1-x)$ B and xC. The resulting mixed crystal system can
be thought of as a repetition of such cells. Probabilis-
tically the pseudo unit cell may be thought of as a con-
figurational average unit cell. A schematic representa-
tion of the pseudo unit cell for a mixed crystal in one
dimension is given in Figure 8. The fractional amount
of the B and C ions located at the same lattice site is
proportional to the mixing ratio in the crystal. This
means that the corresponding forces involving these ions
are weighted by these factors.

B. Mixed Linear Diatomic Chain

The generalized equations of motion in a mixed di-
atomic linear chain may be written as,

$$m_A u_{2n}^A = (1-x) \sum_m (F_{AB}^m + \Phi_{AB}^m) (u_{2n+m}^B - u_{2n}^A)$$

$$+ x \sum_m (F_{AC}^m + \Phi_{AC}^m) (u_{2n+m}^C - u_{2n}^A)$$

$$+ \sum_\ell (F_{AA}^\ell + \Phi_{AA}^\ell) (u_{2n+\ell}^A - u_{2n}^\ell),$$

PSEUDO   UNIT CELL
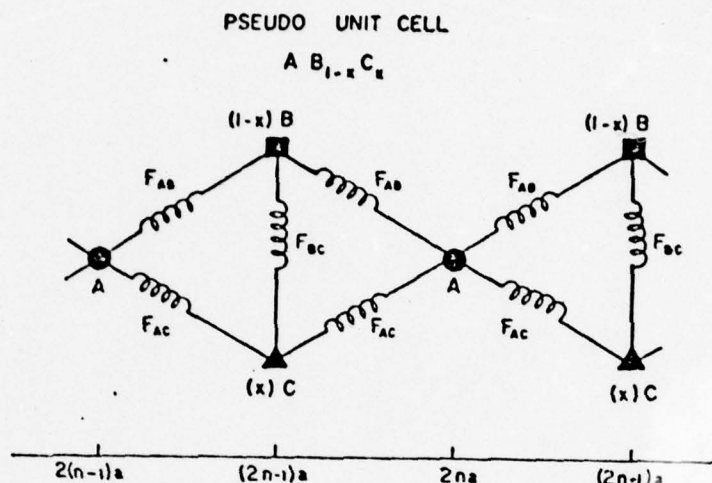
A $B_{1-x}C_x$

Fig. 8 Pseudo unit cell for a mixed linear diatomic chain, $AB_{1-x}C_x (0 \le x \le 1)$.

$$(1-x)m_B \ddot{u}^B_{2n+1} = (1-x) \sum_m (F^m_{AB} + \Phi^m_{AB})(u^A_{2n+1+m} - u^B_{2n+1})$$

$$+ (1-x)^2 \sum_\ell (F^\ell_{BB} + \Phi^\ell_{BB})(u^B_{2n+1+\ell} - u^B_{2n+1})$$

$$+ x(1-x) F_{BC} (u^C_{2n+1} - u^B_{2n+1})$$

$$+ x(1-x) \sum_\ell F^\ell_{BC} + \Phi^\ell_{BC})(u^C_{2n+1+\ell} - u^B_{2n+1})$$

$$(80)$$

and

$$(x)m_C \ddot{u}^C_{2n+1} = x \sum_m (F^m_{AC} + \Phi^m_{AC})(u^A_{2n+1+m} - u^C_{2n+1})$$

$$+ x^2 \sum_\ell (F^\ell_{CC} + \Phi^\ell_{CC})(u^C_{2n+1+\ell} - u^C_{2n+1})$$

$$+ x(1-x) F_{BC}(u^B_{2n+1} - u^C_{2n+1})$$

$$+ x(1-x) \Sigma (F^\ell_{BC} + \Phi^\ell_{BC})(u^B_{2n+1+\ell} - u^C_{2n+1}),$$

63

where $\ell = \pm 2, \pm 4, \pm 6 \ldots$ and $m = \pm 1, \pm 3, \pm 5 \ldots m_{A,B,C}$ are the atomic masses, and u_{2n}^A and $u_{2n+1}^{B,C}$ are the atomic displacements. The subscripts represent the ion's position. $F_{KK'}^j$ and $\Phi_{KK'}^j$ are the force constants representing the jth neighbor repulsive and the electrostatic (Coulomb) interactions respectively between the Kth and K'th ions.

The electrostatic force constants are defined as,

$$\Phi_{KK'}^j = - \frac{d^2}{dx^2} \left(\frac{e_K e_{K'}}{x} \right) \quad x = |r_j| \quad , \tag{81}$$

where

$$e_K = - e_{K'} = ze,$$

z is the effective ionic charge and r_j is the distance between the ions K and K'. The B and C ions are assumed to have the same effective ionic charge, therefore,

$$\Phi_{AB}^m = \Phi_{AC}^m = \Phi_{12}^m \tag{82}$$

and

$$\Phi_{AA}^\ell = \Phi_{BB}^\ell = \Phi_{CC}^\ell = \Phi_{BC}^\ell = \Phi_{11}^\ell .$$

Assuming a traveling wave solution of the form

$$u_{2n}^A = u_A e^{i(\underline{k}2na - \omega t)} \tag{83}$$

and

$$u_{2n+1}^{B,C} = u_{B,C} e^{i(\underline{k}(2n+1)a - \omega t)},$$

where ω is the angular frequency, k, the wave vector and a, the lattice spacing, eq. (80) reduces to the following matrix equation

$$[\underline{D} - \omega^2 \underline{I}][\underline{u}] = \underline{0}. \tag{84}$$

$\underline{I}$ is the identity matrix and $\underline{u}$ is the displacement matrix, the transpose of which is,

$$\underline{u}^T = [u_A \quad u_B \quad u_C]. \tag{85}$$

Tho dynamical matrix $\underline{D}$ is a 3 x 3 symmetrical matrix defined as,

$$\underline{D} =$$

$$
\begin{bmatrix}
m_{AA}[(1-x)T_{mAB} + xT_{mAC} & -\sqrt{1-x}\, m_{AB}[T'_{mAB} + F_{12}] & -\sqrt{x}\, m_{AC}[T'_{mAC} + F_{12}] \\
+ T_A + F_{11}] & & \\[2ex]
-\sqrt{1-x}\, m_{AB}[T'_{mAB} + F_{12}] & m_{BB}[T_{mAB} + (1-x)(T_B + F_{11}) & -\sqrt{x(1-x)}\, m_{BC}[F_{BC} + T'_{\ell BC} \\
& + x(F_{BC} + T_{\ell BC} - \Phi^\circ)] & -F_{11} - \Phi^\circ] \\[2ex]
-\sqrt{x}\, m_{AC}[T'_{mAC} + F_{12}] & -\sqrt{x(1-x)}\, m_{BC}[F_{BC} + T'_{\ell BC} & m_{CC}[T_{mAC} + x(T_C + F_{11}) \\
& -F_{11} - \Phi^\circ] & + (1-x)(F_{BC} + T_{\ell BC} - \Phi^\circ)]
\end{bmatrix}
$$

where

$$\Phi^\circ = -\frac{4z^2 e^2}{a^3}\left[\sum_m m^{-3} - \sum_\ell \ell^{-3}\right] = -3.6062 \frac{z^2 e^2}{a^3},$$

$$F_{12} = \frac{4z^2 e^2}{a^3} \sum_m m^{-3} \cos(kma),$$

$$F_{11} = -\Phi^\circ + \frac{4z^2 e^2}{a^3} \sum_\ell \ell^{-3} \cos(k\ell a),$$

$$m_{st} = (m_s m_t)^{-1/2},$$
(86)

$$T_{rst} = 2 \sum_r F_{st}^r,$$

$$T_s = 2 \sum_\ell F_{ss}^\ell (1 - \cos(k\ell a)),$$

and

$$s, t = A, B, C$$

$$r = \ell, m$$

The indices l and m are restricted to have only positive values. The normal modes of vibration are obtained by solving the secular equation

$$|\underline{D} - \omega^2 \underline{I}| = 0. \tag{87}$$

The three roots of eq. (87) give two optic modes and one acoustic mode. In the limit of infinite dilution (as $x \to 0$ and $x \to 1$), two of the above solutions become the acoustic and optic modes of the host lattice while the third mode becomes the impurity mode.

Explicit lattice dynamical calculations were performed considering nearest neighbor repulsive interactions and long range Coulomb interactions. It was assumed that the force constants vary linearly with concentration from one end member to the other as,

$$\frac{F_{AB}}{F_{ABO}} = \frac{F_{AC}}{F_{ACO}} = \frac{F_{BC}}{F_{BCO}} = 1 - \Theta x. \tag{88}$$

The solution of eq. (87) in the long wavelength limit gives three vibrational frequencies. One of these frequencies is zero and refers to the acoustic mode of the system. The remaining two modes pertain to the optic mode of the host lattice and the impurity mode. These solutions are given as,

at x=0

$$\omega^2_{LO,AB} = \frac{1}{\mu_{AB}} \left(2F_{ABO} + 4.2072 \frac{z_1^2 e^2}{a_1^3} \right)$$

and

$$\omega^2_{I,C} = \frac{1}{m_C} \left(2F_{ACO} + F_{BCO} + 3.6062 \frac{z_1^2 e^2}{a_1^3} \right.$$

$$= \text{Impurity mode of C in AB}, \tag{89}$$

66

at $x = 1$,

$$\omega^2_{LO,AC} = \frac{1}{\mu_{AC}} (2F_{ACO}(1-\theta) + 4.2072 \frac{z_2^2 o^2}{a_2^3})$$

and

$$\omega^2_{I,B} = \frac{1}{m_B}((2F_{ABO}+F_{BCO})(1-\theta)+3.6062 \frac{z_2^2 e^2}{a_2^3})$$

$$= \text{Impurity mode of B in AC.} \quad (90)$$

z_1 and a_1 refer to the AB system, z_2 and a_2 refer to the AC system and μ_{AB} and μ_{AC} are the reduced masses. The term $\frac{z^2 e^2}{a^3}$ is a force constant type term and is assumed to vary linearly with x, as,

$$\frac{z^2 e^2}{a^3} = F_Z = F_{ZO}(1-\theta x). \quad (91)$$

It was assumed that $z_1 = 1.0$. This enables the complete determination of the force constant parameters, F_{ABO}, F_{ACO}, F_{BCO}, F_{ZO} and θ.

The phonon dispersion curves can now be obtained by solving the secular eq. (87) at different points in the k space. Moreover, the phonon behavior can also be obtained for the entire composition range $0 \leq x \leq 1$.

The frequency distribution function as a function of the squared frequencies is defined as,

$$D(\omega^2) = \frac{dM(\omega^2)}{d(\omega^2)} , \quad (92)$$

where the integrated frequency spectrum, $M(\omega^2)$, is the fraction of phonon states the squares of whose frequencies are less than or equal to ω^2. This can be expressed for the mixed crystal case as,

$$M(\omega^2) = \frac{1}{N} \int_o^{\omega^2} \sum_{k,j} |\underline{e}(k|j)|^2 \delta(y-\omega_j^2 (k))dy, \quad (93)$$

67

where

$$|\underline{e}(k|j)|^2 = |u_A(k|j)|^2 + (1-x)|u_B(k|j)|^2$$
$$+ x|u_C(k|j)|^2.$$

$u_A(k|j)$, $u_B(k|j)$ and $u_C(k|j)$ are the eigenvectors for the frequency $\omega_j(k)$ and N is the total number of phonon states.

The model parameters were determined using the values of physical observables appropriate to $ZnS_{1-x}Se_x$. This was done so as to get physically realizable values for the results. The corresponding lattice dynamical results in no way are related to the actual results of the three dimensional mixed crystals but may provide insight into the actual three dimensional behavior. The physical observables used as input parameters and the resulting force constant parameters are summarized in Table 3. The phonon dispersion curves for the $ZnS_{1-x}Se_x$ case are presented in Figure 9. In general one expects three branches of

Table 3. Physical properties used and deduced force constant parameters for the $An_{1-x}Se_x$ case (ω in cm^{-1}, F in 10^5 dynes/cm.).

Physical Properties used	$\omega_{LO,AB}$	350^{52}
	$\omega_{LO,AC}$	252^{52}
	$\omega_{I,C}$	220^{52a}
	$\omega_{I,B}$	297^{52b}
Model Parameters	F_{ABO}	0.402950
	F_{ACO}	0.473864
	F_{BCO}	0.665076
	F_{ZO}	0.177979
	Θ	0.210241
	z_2	0.945792

a: Extrapolated gap mode

b: Local mode
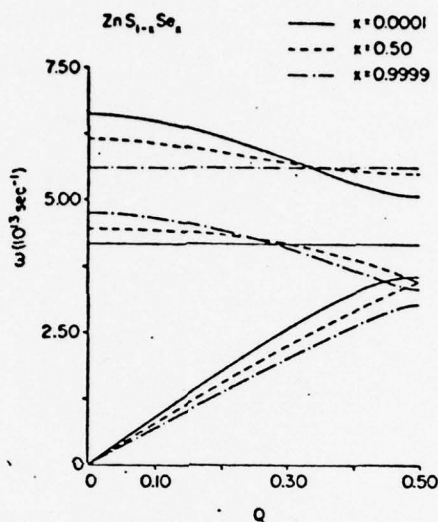
Fig. 9 Phonon dispersion for the $ZnS_{1-x}Se_x$ case at concentrations of x = 0.0001, x = 0.5 and x = 0.9999 as a function of reduced wave vector $(Q = ka/\pi)$.

phonon dispersion in the k-space for the mixed linear diatomic chain. One of these branches refers to the acoustic mode of the system. The two remaining branches are the optic mode of the host lattice and the impurity mode of the system. The mixed $ZnS_{1-x}Se_x$ type systems exhibits two mode behavior and indeed one observes the gap mode at x = 0.0001 and the local mode at x = 0.9999. At these values of concentration the nondispersive behavior of the impurity modes is quite evident. As the concentration departs from these limits of infinite dilution, the impurity mode starts to show dispersion while the optic mode becomes less and less dispersive.

The frequency distribution function for the $ZnS_{1-x}Se_x$ case are presented in Figs. 10 and 11. At x = 0.0001, which is a case of isolated impurities of Se in ZnS, the frequency distribution function is essentially that of the perfect ZnS system. But as x is increased, the impurities begin to play an increasing role in the
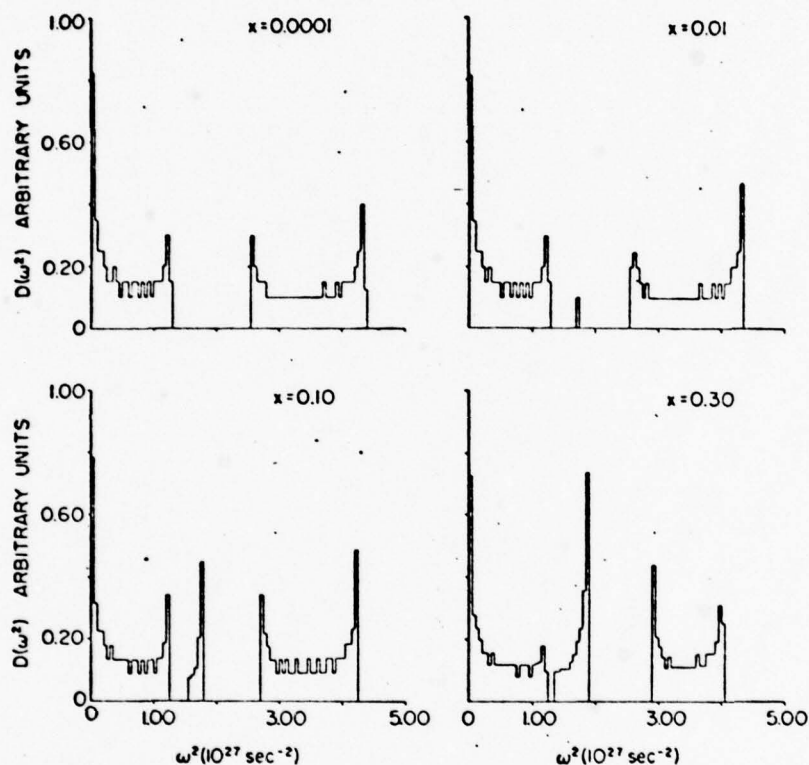
Fig. 10 Frequency distribution function for the $ZnS_{1-x}Se_x$ case at concentrations of $x = 0.0001$, 0.01, 0.10, and 0.30.

spectrum and consequently one notices a gradual emergence of the impurity frequency band in the gap of the optic and acoustic band. With increasing concentration, the frequency distribution in the impurity band increases while it goes on decreasing in the optic band. As x approaches unity one also notices the turning of the optic mode into the impurity mode and vice versa. And finally, at $x = 0.9999$, the frequency distribution function is essentially that of the pure ZnSe system.
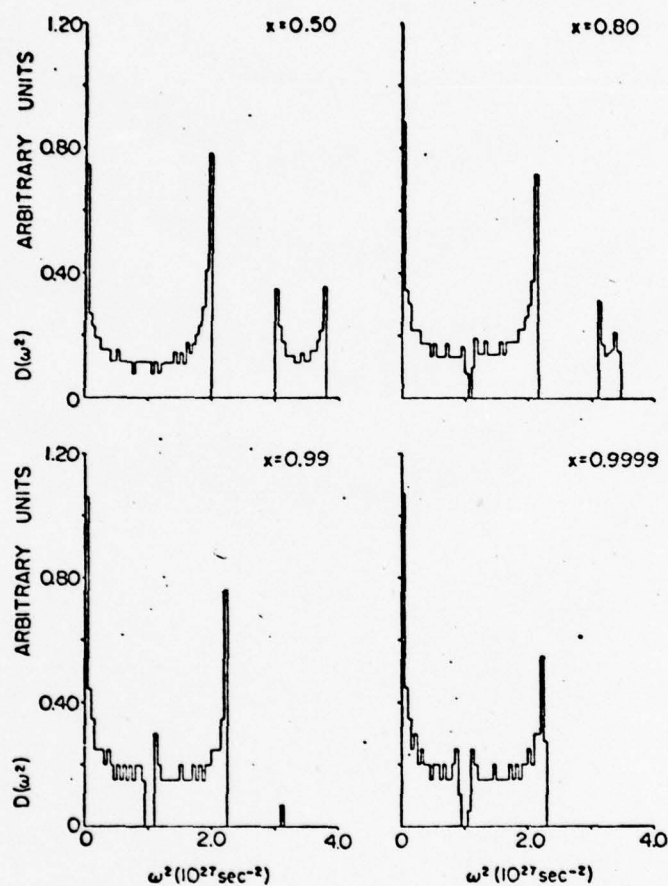
Fig. 11 Frequency distribution function for the
$ZnS_{1-x}Se_x$ case at concentration of x = 0.50, 0.80, 0.99
and 0.9999.

C. Three Dimensional Mixed Crystal System

In order to fully appreciate the mathematical complexity in describing a three dimensional mixed crystal system in the framework of the pseudo unit cell model, it is necessary to present the details of the three dimensional lattice dynamical model used. In these lectures the details of the lattice dynamical model will not be given, but rather the general approach will be outlined. Those who are interested in the details of the lattice dynamical model for the perfect crystal may refer to the appropriate literature[39].

, The explicit calculations described herein utilized a modified rigid ion model[39] for the perfect lattice. Corresponding calculated results are presented for various zinc-blende crystals. The modified rigid ion model consists of short-range central and non-central interactions and long-range Coulomb interactions among ions of appropriate effective ionic charge. The complete details of the three dimensional calculation may be found elsewhere[53].

The equation of motion for a three dimensional mixed crystal may be written as

$$[\underline{D} - \omega^2 \underline{I}][\underline{u}] = 0 \tag{94}$$

$[\underline{I}]$ is the familiar identity matrix and ω, the eigenfrequencies. $[u]$ is a nine by one column eigenvector matrix defined as

$$[u] = \begin{bmatrix} u_x(1) \\ u_x(2) \\ u_x(3) \\ u_y(1) \\ u_y(2) \\ u_y(3) \\ u_z(1) \\ u_z(2) \\ u_z(3) \end{bmatrix} \tag{95}$$

where particles A, B and C are designated by the numbers 1, 2 and 3 respectively. The matrix D is the nine by

nine dynamical matrix of the form given in eq. (40) re-
lating to the substitutional impurity systems. In this
analysis[53] "s" may take the values 1, 2 or 3. The mixed
crystal coupling coefficient matrices are similar to
those of the perfect three dimensional crystal with the
appropriate concentration weighting factors. A similar
sort of reasoning applies for the Coulomb coupling coef-
ficients. The force constant parameters, the ionic charge
and the lattice constant are assumed to vary in a linear
fashion from one end member to the other.

The model parameters are determined from the two
optic mode frequencies, the local, gap or resonant mode
frequency and the three elastic constants evaluated at
$x = 0$ and $x = 1$. This gives a total of twelve equations.

Examples of the three dimensional phonon dispersion
for the system $ZnS_{1-x}Se_x$ are presented in Figs. 12 and
14, for various values of concentration and wave vector
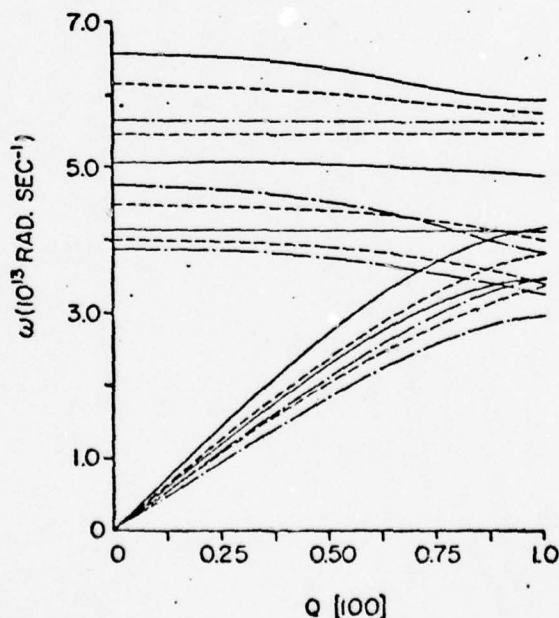
Fig. 12   Phonon dispersion for $ZnS_{1-x}Se_x$ in the [100] di-
rection.   Solid line, $x = 0.0001$; dotted line, $x = 0.50$;
dot-dash line, $x = 0.9999$.
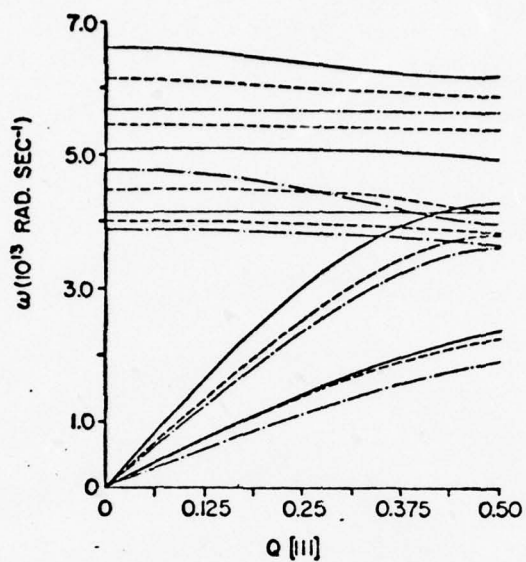
Fig. 13 Phonon dispersion for $ZnS_{1-x}Se_x$ in the $[111]$ direction. Solid line, $x = 0.0001$; dotted line, $x = 0.50$; dot-dash line, $x = 0.9999$.
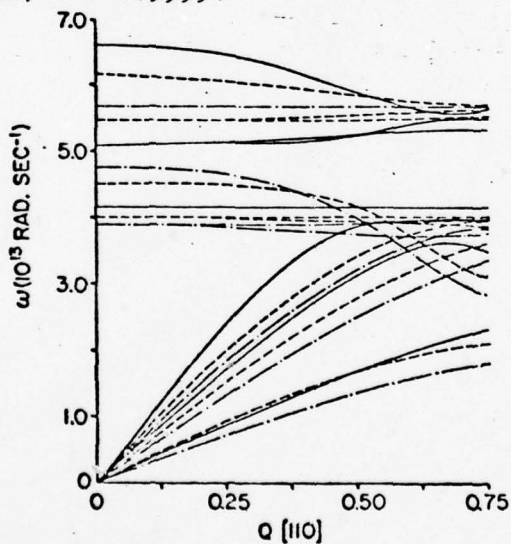
Fig. 14 Phonon dispersion for $ZnS_{1-x}Se_x$ in the $[110]$ direction. Solid line, $x = 0.0001$; dotted line, $x = 0.50$; dot-dash line, $x = 0.9999$.

74

direction. Appropriate distribution functions are pre-
sented for $ZnS_{1-x}Se_x$ and $GaP_{1-x}As_x$ in Figs. 15 - 18. It
is observed that $GaP_{1-x}As_x$ contains local and gap modes
at $x = 1$ and $x = 0$ respectively, while $ZnS_{1-x}Se_x$ has a
local mode at $x = 1$ but no gap mode at $x = 0$.
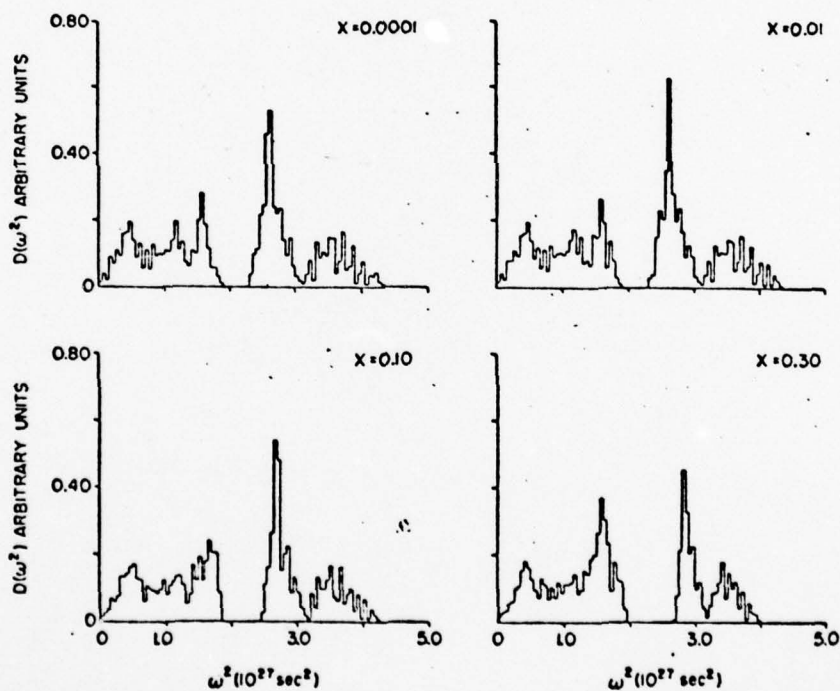
Fig. 15 Frequency distribution function for $ZnS_{1-x}Se_x$
for various values of concentration, $x_1 = 0.0001$, 0.010,
0.10, 0.30.
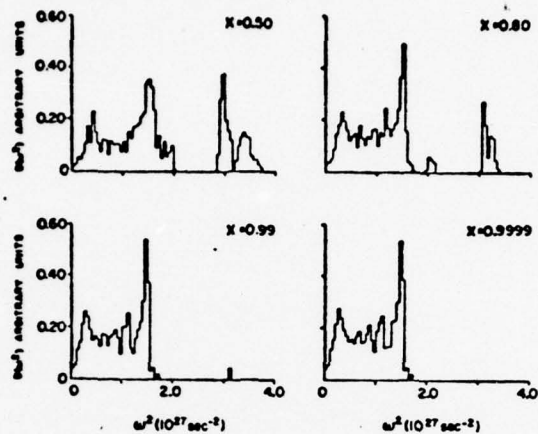
Fig. 16 Frequency distribution function for $ZnS_{1-x}Se_x$ for various values of concentration , x = 0.50, 0.80, 0.99, 0.9999.
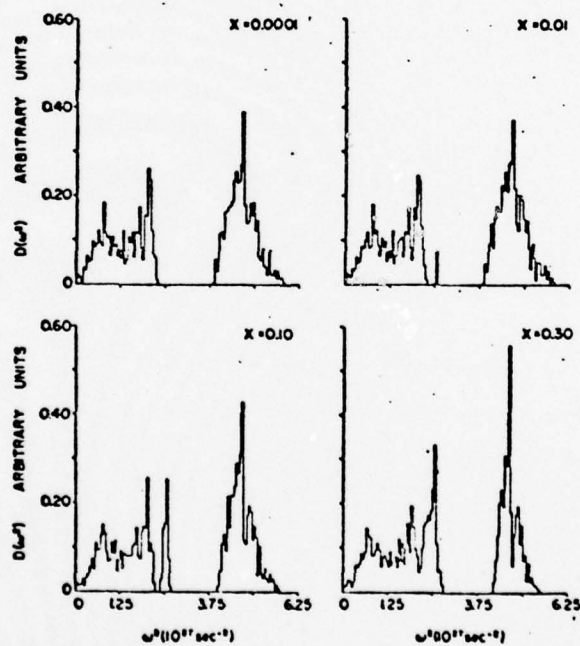
Fig. 17 Frequency distribution function for $GaP_{1-x}As_x$ for various values of concentration, x = 0.0001, 0.010, 0.10, 0.30.

76
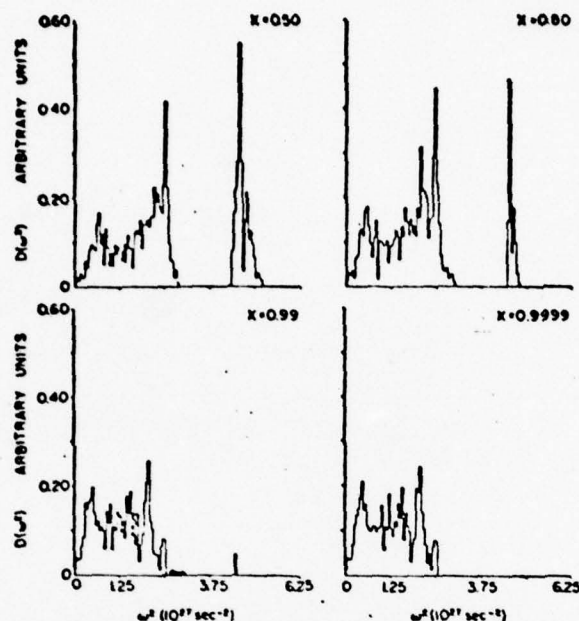
Fig. 18 Frequency distribution function for $GaP_{1-x}As_x$ for various values of concentration, $x = 0.50$, 0.80, 0.99, 0.9999.

IV. AMORPHOUS SYSTEMS

A. Brief Background

The lack of lattice periodicity greatly complicates the mathematics involved in calculating the dynamical properties of amorphous materials. The complexity increases with randomness in atomic type and geometry. Theoretically, if one knows the exact structure of an amorphous material, one can in principle study the dynamical properties in direct space. However, this technique becomes mathematically cumbersome as the size of the lattice increases.

The majority of the work done on amorphous materials has been in tetrahedrally bonded semiconductors[54] such as germanium and silicon. These materials have been studied by both experimental measurements and by theoretical model simulations. Shevchik and Paul[55,56] have examined the structure of amorphous Ge using small angle X-ray scattering along with the analysis of the radial

77

distribution function (RDF) which is defined as the number of atoms at different radii in three dimensional space. The RDF is obtained by a Fourier transform of the coherently scattered radiation measured by diffraction experiments. Moss and Graczyk[57] have investigated the structure of Si by the scanning electron diffraction technique. The proposed theoretical models for amorphous Ge and Si[58] might be classified as being microcrystallite models[59], dense random packed models[60], random network models[61] and amorphous cluster models[62].

Comparing the theoretical model RDF with the corresponding experimental data, it is found that the structure of amorphous Ge and Si is a random network lattice[58] with short-range order (SRO) and long-range disorder. The tetrahedral bond, with a coordination number of four, characteristic of the perfect crystal, is retained in the amorphous phase. The bond lengths and bond angles vary slightly from the corresponding perfect crystalline values. The atomic density of amorphous Ge and Si[58] is a few percent lower than the corresponding crystalline value.

Much of the early work[63-68] in the lattice dynamics of structurally disordered solids was done in one and two dimensional glasses which are essentially amorphous compounds. In 1964, Dean[63] was the first to compute the vibrational density of states for a glass-like disordered linear chain. The disorder is introduced by a continuous probability distribution function for interatomic distances, hence for interatomic force constants. The resulting phonon spectra showed a broad feature which not only smeared out the spectral singularities but extended the frequency range of the related ordered chain. Bell[65] has calculated the vibrational spectrum in a topologically disordered chain and examined the mode localization associated with it. All the atomic masses and force constants were taken to be equal, but the neighbors interacting with each atom were randomly selected to produce topological disorder. The calculated spectrum is essentially a smoothed-over version of the corresponding crystal. Bell et al[69] have investigated the vibrational spectra in a two dimensional glass-forming model. The influence of topological disorder and geometrical disorder was discussed separately.

Lattice dynamical calculations in three dimensions becomes much more difficult due to the complexity of the structure. Bell et al[70] have calculated the lattice dynamics of glasses from the three dimensional random net-

work models built by Bell and Dean[71]. Weaire and
Alben[72-74] have calculated the phonon spectra of amor-
phous Ge and Si. In their work, the calculation was done
for a 61-atom random network constructed by Henderson[75].
The model was obtained by perturbating the atoms in a
distorted diamond lattice. Thorpe[76] has calculated the
phonon density of states for a 5-atom single tetrahedron
to show the effect of local order on the frequency spec-
tra. Bell[77] also indicated the effect of topological
disorder alone on the vibrations of three dimensional
systems. It was pointed out[69] that, in amorphous SiO_2,
topological disorder mainly alters the detailed spectral
profile whereas geometrical disorder extends the frequency
range. Very recently, Alben et al[78] have extensively re-
viewed the vibrational properties of amorphous Ge and Si.
In their work, the vibrational densities of states of
tetrahedrally bonded amorphous semiconductors have been
calculated for various physical models. These models how-
ever have a finite size of about 90 atoms only.

Experimental data[79-84] on the vibrational density
of states of amorphous Ge and Si have been obtained by
optical spectroscopy such as Raman scattering and infra-
red absorption measurements. The phonon spectra of crys-
talline and amorphous forms are found to be similar re-
lative to their qualitative feature. Inelastic neutron
scattering experiments[85] have also been used to measure
the vibrational density of states. Additionally, tun-
neling spectroscopy[86] and electron-energy-loss spectro-
scopy[87] have recently been employed to obtain the phonon
spectra of amorphous Ge and Si. At the present time,
only the low-energy spectra can be obtained due to the
intensity limitation[78,85].

To date, it is impossible to obtain all the phonon
frequencies present in a three dimensional amorphous
solid. Theoretically, the reason is the inadequate model
representation of the amorphous structure. Experimental-
ly, the phonon spectra cannot be obtained simply by Raman
or infrared measurement because of the uncertainties in
the matrix elements. Although, the neutron scattering
method avoids the dependence of matrix elements, it can
only supply the low-frequency part of the phonon spectra
in amorphous materials.

In order to calculate the physical properties as-
sociated with an amorphous material, one must have a
physical model for the structure. In the last few years,
the random network model has been generally accepted[58,88]

79

for representing tetrahedrally bonded amorphous semicon-
ductors. This approach has more physical appeal than the
approach based on a perturbation of the perfect crystal.
In the simulation of the real amorphous structure, a model
with numerous atoms is usually desirable[78]. However, a
large amount of work is required to generate a truly ran-
dom network of any significant size. Most of the exist-
ing networks are not truly random in nature, but rather
a perturbation of the perfect crystalline structure.
Even though the RDF of the resulting network agrees fair-
ly well with the experimental RDF, the resulting struc-
tural representation, itself, might not be truly indica-
tive of the real amorphous structure[88,89]. Also, the use
of a finite size random network along with the invocation
of the periodic boundary condition is at best an approxi-
mation to the actual amorphous system.

In this work, the lattice dynamics of amorphous ma-
terials is calculated using a statistical method in which
the lattice dynamics is performed at various lattice spac-
ings and the ensemble is statistically averaged. Statis-
tical models have often been used[90] in describing disor-
dered systems. A phenomenological model was utilized by
Tsay et al[91] to statistically calculate the electronic
spectra for tetrahedrally bonded amorphous semiconductors.
Mitra et al[92] have also developed a statistical approach
to calculate the Raman scattering intensity for amorphous
Ge and Si. The calculated results agree quite well with
experimental values and indicate that the dynamical dis-
order, as manifested by the change in lattice spacing is
almost entirely responsible for the Raman spectrum[92].
The experimental results[79,80,82,84] on the phonon spec-
trum show that the general features of the crystalline
and amorphous materials are not too different.

To illustrate the application of the statistical
averaging technique, the lattice dynamics of an amorphous
chain is calculated. This is followed by the calculation
of the lattice dynamics of amorphous germanium and sili-
con. The density of phonon states of the corresponding
crystal with different neighbor distances was statistical-
ly averaged. The weighting function in the lattice spac-
ings is determined by the experimental RDF[55-57], which
consists of two Gaussian distributions corresponding to
the nearest and next-nearest neighbor distances centered
around the crystalline values. The calculations are com-
pared to experimental data obtained by Raman and infrared
measurements and other theoretical calculations.

B. Linear Monatomic Chain Model

In a one dimensional linear monatomic chain with periodicity, the dispersion relation is given by

$$\omega = 2 \sqrt{\frac{\beta}{m}} \sin \frac{ka}{2} , \tag{96}$$

where

m = particle mass
β = interatomic first neighbor force constant
a = interparticle spacing

and

k = wave vector.

In order to determine a value for the force constant β, eq. (96) is evaluated in the long wavelength limit, therefor ka<<1. The dispersion relation reduces to the following,

$$\omega = \sqrt{\frac{\beta}{m}} \ ak \tag{97}$$

In the long wavelength case or for a continuum the disperison relation is given as

$$\omega = \sqrt{\frac{c}{\rho}} \ k \tag{98}$$

where

c = elastic constant

and

ρ = mass density.

Comparison of eqs. (97) and (98) yields the following expression for the force constant,

$$\beta = ca \tag{99}$$

For a one dimensional chain of N atoms with the end points fixed, the phonon frequencies, ω_i may be written as

$$\omega_i = \sqrt{\frac{2}{m}} \ \sqrt{ca} \ \sin\frac{i\pi}{2N} , \tag{100}$$

where

i = 1--------N - 1.

The elastic constant, c, is a function of the lattice spacing in the crystal. Intuitively one would expect the chain to become stiffer when the atoms are closer together.

81

In order to get an order of magnitude result, the physical constants associated with germanium are used.

The dependence of the elastic constants on lattice spacing is deduced from the pressure dependence of the elastic constants, which is known experimentally. The relationship between the lattice spacing and the elastic constants can be expressed in terms of Murngahan's equation given as

$$a = a_o[1 + \frac{(dB/dp)o}{B}]^{-\frac{1}{3(dB/dp)o}} \tag{101}$$

where a_o = lattice constant at atmospheric pressure and

B = bulk modulous = $\frac{1}{3}(C_{11} + 2C_{12})$

The lattice dynamics may now be determined for a particular value of lattice spacing. In particular for each different lattice constant the Murngahan's equation is used to get the pressure and hence the appropriate elastic constant value.

The lattice constant values are weighted according to the radial distribution function. This is given in terms of a Gaussian distribution function as

$$p(a) = \frac{1}{2\pi\sigma} e^{-[\frac{(a-a_o)^2}{2\sigma^2}]}, \tag{102}$$

where σ^2 = mean square deviation.

The calculation was performed for 50 different lattice spacings. The phonon density of states of the amorphous material was obtained by associating the appropriate weighting factor with the density of states at each lattice spacing.

Figure 19, depicts the phonon density of states in a perfect and amorphous material. Qualitatively the phonon density of states in the amorphous chains is just a smoothed over version of the phonon density of states in the perfect crystal.
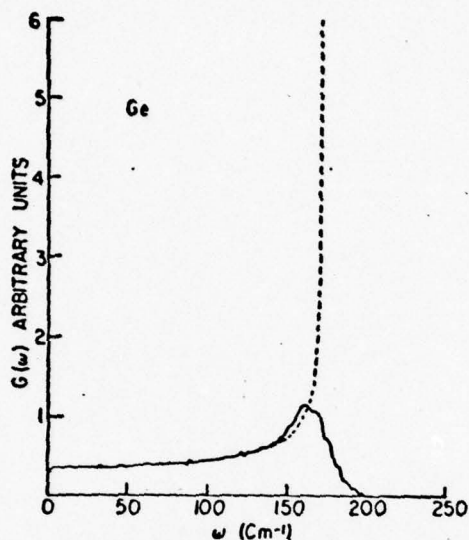
Fig. 19 Density of phonon states of Ge. Solid line -
amorphous; dashed line - crystal.

C. Lattice Dynamics of Amorphous Germanium and Silicon

Experimental studies on the radial distribution func-
tion have shown that some sort of short-range order
exists in amorphous germanium and silicon. Owing to the
short range order in these materials plus the fact that
they do not have appreciable Coulomb interactions, a
short range model is not a bad approximation. A modified
rigid ion model[39] is used as the lattice dynamical model.
The lattice dynamics of a perfect crystal is performed
for various values of radial distance and then statisti-
cally weighted according to the radial distribution func-
tions in order to obtain the frequency distribution func-
tion.

The phonon frequencies, $(\omega_1...\omega_n)_i$, corresponding
to the i-th lattice spacing are given by the solution of
the following determinantal equation,

$$|D - \omega^2 I|_i = 0, \qquad (103)$$

where D is the dynamical matrix and I, the identity matrix. The model parameters needed in the D matrix can be expressed in terms of the elastic constants and the Raman frequency as follows,

$$C_{11} = \frac{\alpha}{a} + \frac{8\mu}{a'} \qquad (104)$$

$$C_{12} = \frac{1}{a} (-\alpha + 2\beta) + \frac{4\mu}{a'} , \qquad (105)$$

$$C_{44} = \frac{1}{a} (\alpha - \beta^2/\alpha) + \frac{4\mu}{a'} , \qquad (106)$$

and

$$f_R = \frac{1}{2\pi C} \sqrt{\frac{8\alpha}{m}} . \qquad (107)$$

α and β are near neighbor force constants and μ is a central second neighbor force constant. a is the lattice constant appropriate to near neighbor interaction while a' is appropriate to second neighbor interactions. Obviously a = a' in a perfect crystal.

In order to obtain the model parameters at each lattice spacing, it is necessary to know the values of the physical observables at the spacing. The input physical observables, which include the elastic constants and the Raman frequency, are known[93-95] experimentally for both Ge and Si. They are simply linear functions of the pressure for reasonable pressure ranges. Figure 20 shows the pressure dependence of the elastic constants and the Raman frequency for Ge. Similar results are known[94] for Si. The pressure dependence of the physical observables can be written as,

$$C_{ij}(p) = C_{ij}(p=0) + (dC_{ij}/dp) p, \qquad (108)$$

$$B(p) = B(p = 0) + (dB/dp) p, \qquad (109)$$

and

$$f_R(p) = f_R(p = 0) + (df_R/dp) p, \qquad (110)$$

where the permutation of the indices i and j is understood to indicate C_{11}, C_{12} and C_{44}. The elastic constants and Raman frequency at each lattice constant can be evaluated if the corresponding pressure at this lattice constant is known. This is done by using Murnaghan's
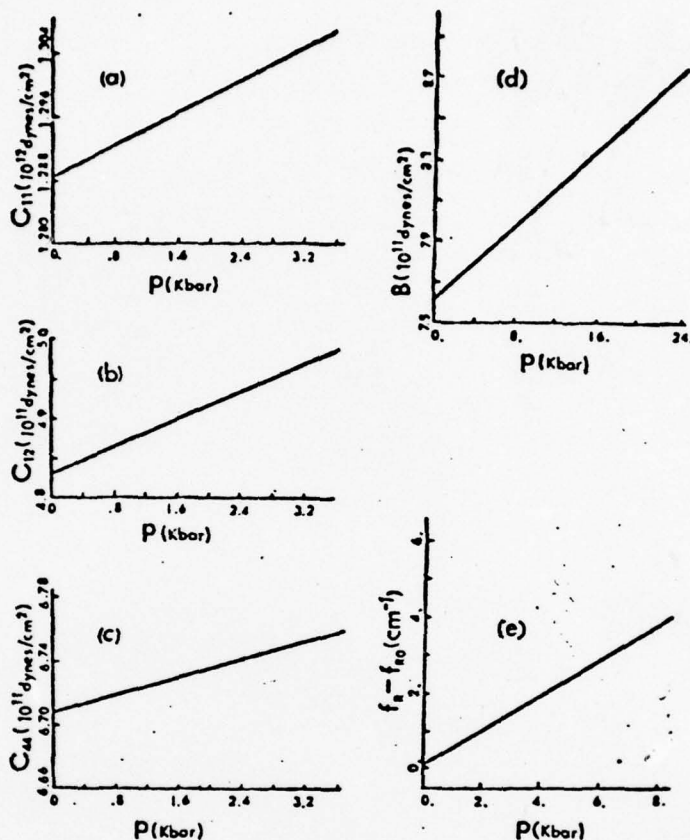
Fig. 20 Pressure dependence of the elastic constants and the Raman frequency for Ge. (a) C_{11} (ref. 93); (b) C_{12} (ref. 93); (c) C_{44} (ref. 93); (d) B (ref. 93) and (e) f_R (ref. 95).

equation,

$$p = \left[(a_0/a)^{3(dB/dp)} - 1 \right] \frac{B_0}{(dB/dp)} \cdot \tag{111}$$

so as to give a pressure corresponding to each lattice constant.

The first and second near neighbor distances, x and y, are known experimentally from the RDF data,

85

Table 4: Summary of Structural Data of Germanium and Silicon

	Ge[*]	Si[**]
r_1^c (Å)	2.45	2.35
r_1^a (Å)	2.46 ± 0.02[+] 2.47 ± 0.01	2.35
σ_1^c (Å)	0.080 ± 0.008	0.141
σ_1^a (Å)	0.088 ± 0.008	0.167
σ_1 (Å)	0.037 + 0.026 − 0.037	0.09
r_2^c (Å)	4.00[++]	3.84[++]
r_2^a (Å)	4.00 ± 0.04	3.86
σ_2^c (Å)	0.12 ± 0.02	0.200
σ_2^a (Å)	0.28 ± 0.01	0.319
σ_2 (Å)	0.25 ± 0.02	0.25

[*] Experimental data due to Temkin et al. (Ref. 96)

[**] Moss and Graczyk (Ref. 57).

[+] Shevchik and Paul (Ref. 55)

[++] Calculated from nearest neighbor distance

$$(r_1^c), \quad r_2^c = \sqrt{8/3} \ r_1^c$$

$$P(x,y) = \exp\left\{-0.5\left[\left(\frac{x-x_0}{\sigma_1}\right)^2 + \left(\frac{y-y_0}{\sigma_2}\right)^2\right]\right\} \quad (112)$$

where

$$x = \sqrt{3}\, a/4$$

and

$$y = a/\sqrt{2}\; .$$

x_0, y_0 and σ_1, σ_2 are the mean and standard deviation respectively of the first and second neighbor distance and K is a proportional constant. The means are chosen to be the corresponding crystalline values. The standard deviation used in this context is the static deviation, σ_1 derived[96] from the experimental crystalline and amorphous deviations, $\sigma_i{}^C$ and $\sigma_i{}^a$ respectively, according to

$$\sigma_i = \left[(\sigma_i{}^a)^2 - (\sigma_i{}^C)^2\right]^{1/2}\; . \qquad\qquad (113)$$

It is assumed that thermal broadening is the same for both the crystalline and amorphous forms. The values of the means and standard deviations of Ge and Si are presented in Table 4. Since the lattice constant is known from x and y, the corresponding value for the pressure is obtained from eq. (111). The value of the elastic constants and Raman frequency for the appropriate lattice spacing is then deduced from the pressure dependence of these quantities which is presented in Table 5. Since there is an unbalance in the number of physical observables and model parameters, the model parameters are deduced by solving equations (104) - (107) in a least square sense[39].

To avoid the complexity of performing lattice dynamical calculations at many lattice spacings, a linear approximation which calculates the lattice dynamics only three times is used. The linear Taylor expansion used to obtain the phonon frequencies at each i-th spacing is

$$\omega_i(x,y) = \omega(x_0, y_0) + \frac{\partial\omega(x,y)}{\partial x}\Big|_{x_0,y_0}(x-x_0)$$

$$+ \frac{\partial\omega(x,y)}{\partial y}\Big|_{x_0,y_0}(y-y_0)\; ,$$

Table 5: Summary of Physical Observables * of Germanium and Silicon

Material	C_{110}**	C_{120}**	C_{440}**	B_o**	ν_o***	$\dfrac{dC_{11}}{dp}$	$\dfrac{dC_{12}}{dp}$	$\dfrac{dC_{44}}{dp}$	$\dfrac{dB}{dp}$	γ	$\dfrac{d\omega}{dp}$****
Ge	1.2886	0.4829	0.6710	0.7515	301	4.99	4.32	1.25	4.51	0.89[69]	0.356
Si	1.65779	0.639365	0.796246	0.9788	520	4.33	4.19	0.80	4.24	0.90[70]	0.478

* Experimental data due to Mcskimin (ref. 93,94) except otherwise indicated

** Elastic constants and bulk moduli are in units of 10^{12} dyne/cm^2.

*** Raman frequencies (ref. 97) are in units of cm^{-1}.

**** Raman shifts, as calculated from Grüneisen constant in this paper,

$\gamma = B/\nu$ ($d\nu/dp$), are in units of cm^{-1}/kbar.

where

$$\frac{\partial \omega(x,y)}{\partial x}\Big|_{x_o,y_o} = \frac{\omega(x_1,y_o) - \omega(x_o,y_o)}{x_1-x_o} \, , \qquad (114)$$

$$\frac{\partial \omega(x,y)}{\partial y}\Big|_{x_o,y_o} = \frac{\omega(x_o,y_1) - \omega(x_o,y_o)}{y_1-y_o}$$

and

$$x_1 = x_o + 0.01$$
$$y_1 = y_o + 0.02$$

In the present calculation, the variation of x around x_o is chosen to be about $\pm 5^o/o$, whereas the y variation a-round y_o is about $\pm 12.5^o/o$. These spreads are about twice the Gaussian spread for both amorphous Ge and Si. The phonon frequencies are calculated at the perfect lattice spacing (x_o,y_o) and at the slightly different spacings (x_1,y_o), $x_o,y_1)$. This was done by calculating the force constant set $[\alpha,\beta,\mu]$ from the physical observables determined at the average value of two pressures corresponding to the first and second neighbor distances. Using eq. (114), the phonon frequencies at various lattice spacings for first and second neighbors are then obtained.

The density of phonon states, $G(\omega)$, is defined as the following,

$G(\omega)d\omega$ = number of phonon states whose frequencies
are located between $\omega = d\omega/2$ and
$\omega + d\omega/2$.   (115)

The $G(\omega)$ of a crystal is obtained by categorizing all the allowed phonon frequencies in the first Brillouin zone. According to the symmetry of the Brillouin zone associated with the diamond structure, the $\underline{k}$ points need only be confined to a region in which

$$16 > k_x > k_y > k_z > 0. \qquad (116)$$

This region, named the irreducible Brillouin zone, is only 1/48th of the first Brillouin zone. Since the phonon states are uniformly distributed in $\underline{k}$ space, it is reasonable to select an equally distributed mesh of points

in the irreducible Brillouin zone so that the phonon den-
sity of states will be obtained. In this work, 149 in-
dependent $\underline{k}$ points along with their degeneracy factors[98]
were used for the frequency calculations. A total of
24,576 frequencies were used to calculate phonon density
of states for the crystalline structure.

The phonon density of states for the amorphous ma-
terial was calculated by statistically averaging each
$g_i(\omega)$ for the i-th lattice spacing according to the weight-
ing function appropriate to the RDF. Mathematically,
this can be represented as

$$G(\omega) = \sum_{i=1}^{n} P_i(x,y) \, g_i(\omega) \tag{117}$$

$P_i(x,y)$ is the associated RDF weighting function defined
by eq. (112) and n is the number of lattice spacings used.
In the present calculation, n was equal to 1250. The
resulting densities of phonon states for both crystalline
and amorphous Ge and Si are presented in Figs. 21 and 22
respectively.

Experimental data for the density of phonon states
of various amorphous materials can be obtained by Raman
and infrared measurements. Due to the lack of long-range
order, the $\underline{k}$-selection rules break down in amorphous
solids. Therefore, all the vibrational modes can take
part in the Raman or infrared process. Under the assump-
tion that all vibrational modes couple equally to the
light, the Raman or infrared spectrum can then be used
as a measure of the density of phonon states in an amor-
phous material[79,80]. Fig. 23 and Fig. 24 present the
optical and phonon spectra for Ge and Si respectively[84].
Fig. 23a is the reduced Raman and infrared spectra ob-
tained by experimental measurements for amorphous Ge.
Fig. 23b shows the density of phonon states. The dashed
line is the crystalline spectrum obtained by Dolling and
Cowley[99] using an eleven-parameter model to fit the neu-
tron inelastic scattering data. The solid line for amor-
phous Ge[84] is a Gaussian-broadened version of the crystal-
line density of states. This is done by convoluting the
crystalline density of states with a Gaussian distribu-
tion. The Gaussian spread was chosen[79] by comparing the
reduced Raman spectrum in the amorphous case with the
corresponding crystalline Raman frequency. Fig. 24 shows
the equivalent results for Si. However, to be more phys-
ically plausible, one should really determine the
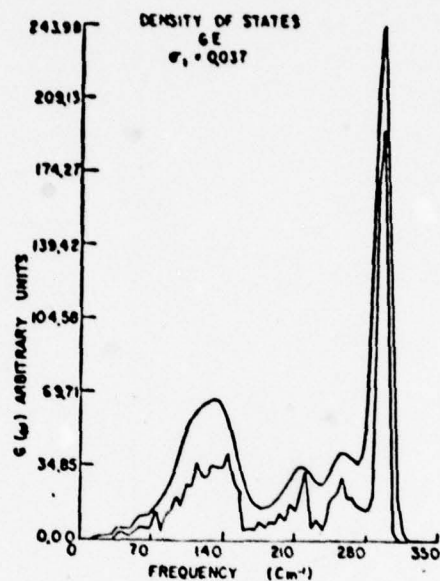
Fig. 21 Density of phonon states of Ge. Top curve - amorphous; bottom curve - crystal.
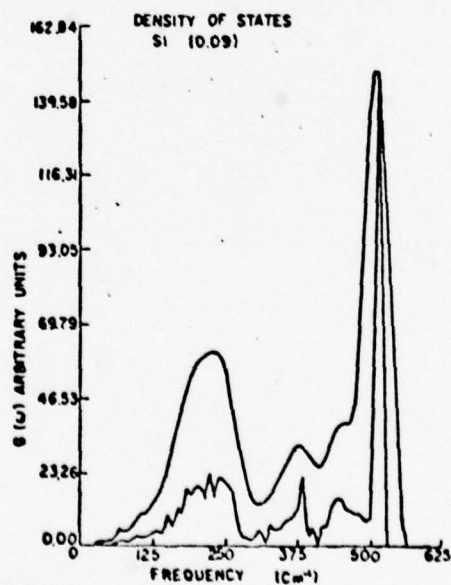
Fig. 22 Density of phonon states of Si. Top curve - amorphous; bottom curve - crystal.
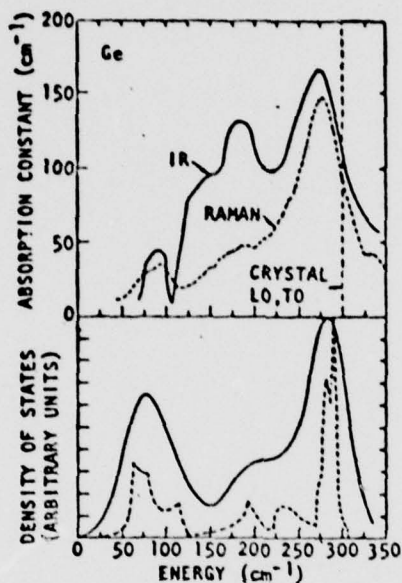
Fig. 23 (a) The infrared and Raman spectra for amorphous
Ge. Solid line - infrared absorption constant (ref. 84).
Dashed line - Raman spectrum (ref. 82). (b) The density
of phonon states for Ge. Solid line - amorphous (ref.
84); Dashed line - crystal (ref. 99).

amorphous density of states from a lattice dynamical model
rather than just use a broadening of the crystalline den-
sity of states[84].

Figs. 25 and 26 compares the phonon density of states
of Ge and Si calculated using the statistical method, to
the results of other work. The present results, as well
as the previous results, indicate that the amorphous
phonon density of states is a smoothed over version of
the crystalline density of states. The singularities in
the crystalline density of states are smeared out by the
disorder in the amorphous state. The similarity between
the crystalline and amorphous spectra is due to the fact
that the short-range model used for the lattice dynamical
calculations is essentially the same in both the amor-
phous and crystalline phases. Comparing this work to
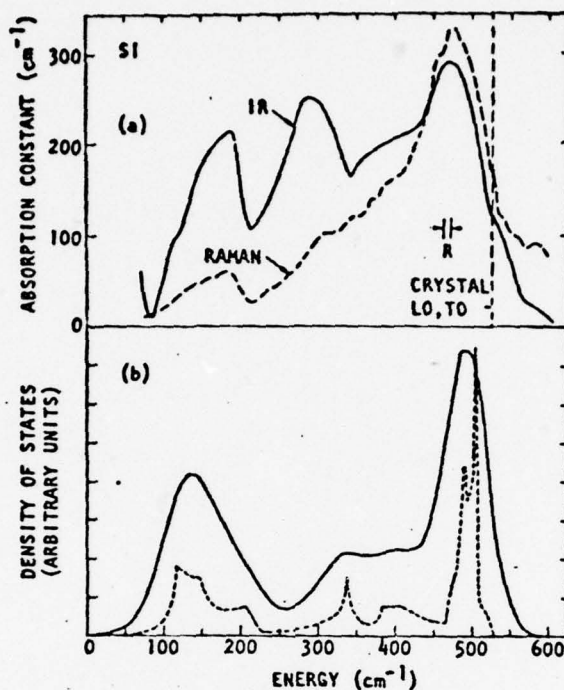
Fig. 24　(a) The infrared and Raman spectra for amorphous
Si.　Solid line - infrared absorption constant (ref. 84);
Dashed line - Raman spectrum (ref. 79).　(b) The density
of phonon states for Si.　Solid line - amorphous (ref.
84); Dashed line - crystal (ref. 99).

Brodsky's results[84], the agreement is fairly good.　How-
ever, the frequency associated with our first peak is
slightly higher.　This is because the rigid ion model was
used in our calculation whereas Dolling's model[99] was
used in the other work.　Our work also compares favorably
to Alben's theoretical calculation[73] using a 61-atom ran-
dom network[75].　The finite size of the model along with
the periodic boundary conditions might be the reason that
the phonon density of states in Alben's work is not as
smooth as the others.

In Figure 27, the calculated phonon density of
states of Ge is compared to various experimentally ob-
tained Raman and infrared data[83,84].　It may be pointed

93
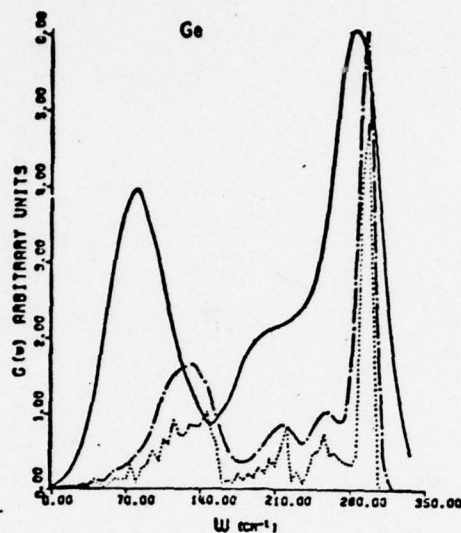
Fig. 25 Density of phonon states for Ge. Dash-dotted
line - amorphous form as calculated in this work; Dotted
line - crystalline form as calculated in this work;
Solid line - Brodsky's result (ref. 84).
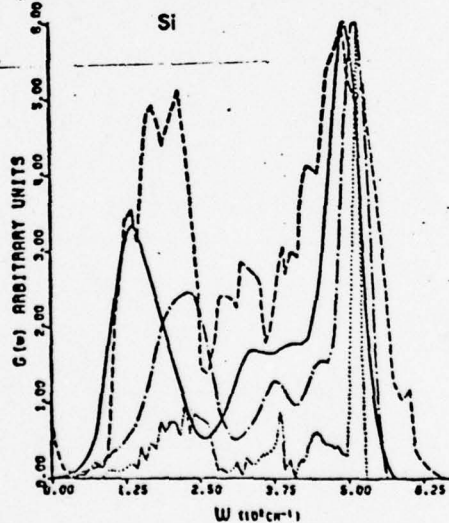
Fig. 26 Density of phonon states for Si. Dash-dotted
line - amorphous form as calculated in this work; Dotted
line - crystalline form as calculated in this work; Dashed
line - Alben's calculation (ref. 73); Solid line -
Brodsky's result (ref. 84).
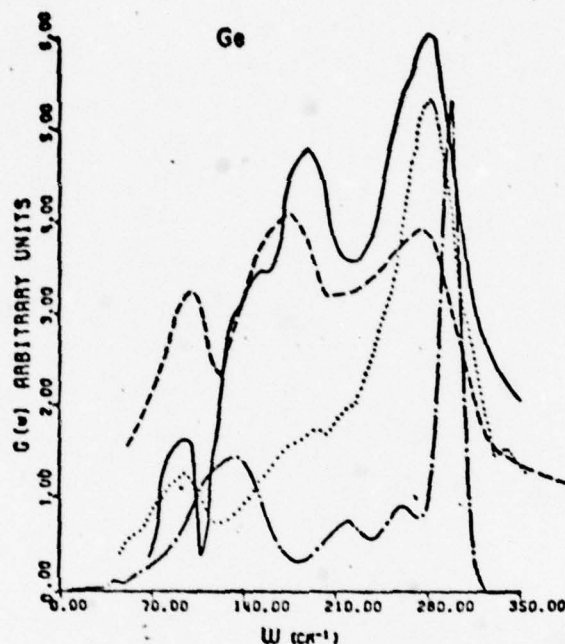
Fig. 27 Comparison of calculated density of phonon
states to infrared and Raman measurements for amorphous
Ge.   Dash-dotted line - calculated density of phonon
states; Dotted line - Raman spectrum (ref. 84); Solid
line - infrared spectrum (ref. 84); Dashed line - infra-
red spectrum (ref. 83).

out that the density of states should represent the fea-
tures observed in the Raman and infrared spectra. How-
ever, they are not expected to be identical because of
the matrix element effects.   It is particularly worth
noting that the high frequency peak in the Raman spec-
trum is much stronger than that in the infrared spectrum,
and compares well with the present calculated result.
This becomes even more obvious from the infrared results
of Stimets et al[83].   This is to be expected since in crys-
talline Ge, the first order Raman spectrum for the long-
wavelength optical phonon is allowed whereas it is forbidden for the infrared spectrum. It has been pointed
out before[92] that the allowed Raman spectrum in the crys-
talline case, although somewhat broadened, persists in
the amorphous phase.

V. ONE-PHONON INFRARED AND RAMAN SPECTRA OF TETRAHEDRALLY BONDED AMORPHOUS SEMICONDUCTORS

A. Introduction

Most existing works[73,82,100] on the optical properties of amorphous solids emphasize the role of k-selection rule breakdown, and what is consequently expected to be a strong similarity between densities of states and optical spectra of such solids. Recently, the role of crystalline-allowed analogue (CAA) processes in tetrahedrally bonded amorphous semiconductors (TBAS) was pointed out by Tsay et al[91] for electronic spectra, and by Mitra et al[92] for lattice spectra. In this section, we develop a statistical approach to the interpretation of lattice spectra in amorphous solids, which accounts in a natural way for the role of CAA processes. The formalism is then applied to interpret available experimental first-order infrared and Raman spectra of TBAS.

We view[101] the properties of an amorphous solid as derived from an ensemble of atomic (structural) configurations (labeled by "n") with probabilities p_n, rather than from a single unique structural entity. Then for a particular property Θ we require the configurational average

$$\langle \Theta \rangle = \sum_n p_n \, \Theta(n) \tag{118}$$

where $\Theta(n)$ is the expectation value of Θ in configuration n. Clearly, for any relistic system, it is difficult if not impossible to evaluate $\langle \Theta \rangle$ from first principles. Rather, for the statistical approach to be useful one must be able to identify a restricted class of configurations which elicit the principal features of the properties concerned; moreover, of course, one must be able to calculate the corresponding $\Theta(n)$'s for these configurations. We here propose to parameterize TBAS in terms of two classes of principal configurations, namely those possessing (a) both short and long range order [denoted by $(n)_{SL}$] and (b) just short range order [denoted by $(n)_S$]. The motivation for this parameterization for TBAS is that the experimental evidence[83,102,103] indicates that to a large extent they are "nearly crystalline"; i.e., spectral features that are prominent in the crystal remain prominent in the corresponding amorphous solid, and are expected to arise from the $(n)_{SL}$. Features which are weak or absent for the crystal are generally also weak in the amorphous counterpart, and are expected to

96

arise principally through the non-crystalline configurations $(n)_S$. Each of the configurations in the set $(n)_{SL}$ will lead individually to features obeying crystalline $\underline{k}$-selection rules, i.e., $\theta^{SL}(n) = 0$ for forbidden processes. The final spectra will in general however, be broadened out because of the averaging process. If, on the other hand, the p_n possess a considerable spread, then the crystalline features may be largely washed out. The configurations $(n)_S$, on the other hand, are not subject to crystalline selection rules, and always contribute to the spectrum. In addition to broad, featureless contributions arising from the breakdown of the $\underline{k}$-selection rule, various peaks evident in the crystalline density of states, but suppressed by selection rules in optical spectra, will reappear for the amorphous solid.

In quantum mechanical terms, this is equivalent to the introduction of a perturbation Hamiltonian in an otherwise ordered solid such that,

$$H_{disord} = H_{ord} + (H_{disord} - H_{ord}) = H_{ord} + H'$$

$$(119)$$

When the solid is disordered, such a perturbation will introduce changes in the reststrahlen frequencies, ω_{TO}, or ω_{LO} and also in the frequency-dependent matrix elements for dipole moment, $M(\omega)$ and induced polarizability, $\alpha(\omega)$. For ordered solids, $M(\omega)$ and $\alpha(\omega)$ depend purely on the structural symmetry. For example, for the rock-salt and zinc-blende structures $M(\omega) = 0$ for all ω except $\omega = \omega_{TO}$, where it is large. On the other hand, for $NaC\ell$-type crystals $\alpha(\omega) = 0$ for all ω, and for the diamond structure $\alpha(\omega) \neq 0$ for $\omega = \omega_{LO}$. In the structurally disordered solids $M(\omega)$ is now finite for all ω because of the removal of the translational symmetry, and probably small, except for $M_a(\omega_{TO})$, corresponding to the allowed transition in the case of an ordered solid, which is still large. Similar remarks hold for $\alpha(\omega)$. If the perturbation limit is valid, we shall expect differences between the perturbed and unperturbed cases to be finite and small, which is indeed observed in many cases, for example, mixed crystals systems[49] where translational symmetry is substantially disturbed. We shall demonstrate later that the viewpoint described here does indeed provide a basis for a consistent interpretation of observed spectra of TBAS.

With the above prescriptions, one may write,

97

$$\langle \Theta \rangle = \langle \Theta \rangle^{SL} + \langle \Theta \rangle^{S}$$

$$= \sum_{n} \left[\rho^{SL} p_n^{SL} \Theta^{SL}(n) + \rho^{S} p_n^{S} \Theta^{S}(n) \right] \quad (120)$$

$$\sum_{n} p_n^{SL} = \sum_{n} p_n^{S} = 1, \quad \rho^{SL} + \rho^{S} = 1$$

where we have chosen a convenient normalization for the p_n's. The parameters $\eta \equiv \rho^{S}/\rho^{SL}$, which we here deduce from experiments, is the fraction of disordered relative to ordered configurations, and thus provides a measure of the amorphicity of the solid ($\eta = 0$ for a crystal; $\eta \gg 1$ for a highly disordered system). In order to proceed, one must specify the $(n)_{SL}$ and $(n)_{S}$ to be employed above. Among the configurational parameters n suggestive for TBAS, are the interatomic spacings, local densities and bond angles, all known to deviate from those of their crystalline analogues and to display characteristic spreads as well. As a first step in the calculation of $\langle \Theta \rangle^{SL}$ we here restrict n to correspond to variations in local density ρ alone. While the calculation of $\langle \Theta \rangle^{SL}$ for a given value of ρ will be relatively straight forward, this is not the case for $\langle \Theta \rangle^{S}$. A reasonable, but not unique, possibility is to employ just a nearest neighbor (nn) unit immersed in a continuum to calculate the $(n)_{S}$. This would account for the principal features representative of short-range order, yet suppress those features characteristic of the periodic lattice structure beyond the nn cell. In this paper, we calculate only $\langle \Theta \rangle^{SL}$ for IR and Raman spectra; analogous calculations for $\langle \Theta \rangle^{S}$ will be reserved for future work.

B. Local Density Distribution in TBAS

One of the most important quantitative data on the structure of amorphous semiconductors is the RDF which is defined as

$$F(r) = 4\pi r^2 \rho(r) \quad (121)$$

where $\rho(r)$ is the density of atoms at a distance r from an arbitrarily chosen central atom ($r = 0$). The experimental data on the RDF of amorphous tetrahedrally-bonded semiconductors indicate the following:

(i) The RDF for both the crystalline and amorphous forms of the same material are very similar, at least up to the second neighbor distance, implying that the short-

98

range order is preserved for the amorphous material.

(ii) The positions of the first and second peaks of the amorphous RDF are slightly shifted (a few percent) toward higher values as compared with the crystalline counterparts. This is consistent with the fact that the amorphous form of a material usually has lower density than that of the crystalline form.

(iii) Aside from thermal broadening, there are intrinsic widths, σ_i^s, of the peaks in the amorphous RDF. This is due to the introduction of static distortions in bond lengths and/or angles resulting in the amorphous structure. The first and second peaks of the RDF of an amorphous material are fairly well-defined, and may normally be expressed as a Gaussian of the form

$$\exp\left[-\frac{(r-r_i^a)^2}{2\sigma_i^a{}^2}\right], \quad i = 1, \text{ or } 2 \tag{122}$$

where r_i^a and σ_i^a are the position and width, respectively, of the ith peak. The spreads σ_i^a, however, include thermal as well as disorder-induced effects. In order to consider disorder-induced effects only, the static spread, σ_i^s, should be obtained from σ_i^a after correcting for the thermal spread.

If one regards the spreads in the first and second peaks in the amorphous RDF as distributions of the first and second nn distances which exist in an amorphous material, the "local" density at a point is expected to depend on the extent of the distortions of the local environment from the crystalline case. We define local density as the number of atoms per unit volume, for a volume whose linear dimension is of the order of a few multiples of the nn distances. Given the statistical distributions in the local distortions, (i.e., the spreads in first and second nn distances), the distribution in local density can be approximately calculated.

In crystalline semiconductors where the distance between any pair of atoms is fixed, the local density should be uniform throughout the crystal. For diamond and zincblende crystals, there are two particles per unit cell. The cell volume is $a^3/4$, where a is the lattice constant. Defining the nearest neighbor distance as

$$r_1 = \frac{\sqrt{3}}{4} a \tag{123}$$

99

the density in terms of this distance is

$$\rho = \frac{3\sqrt{3}}{8} \left(\frac{1}{r_1^3}\right) \tag{124}$$

In amorphous solids, both r_1 and r_2 have spreads about their respective mean values, r_1^a, r_2^a. In order to include the second neighbor atoms in defining the local density, one may write

$$\rho(r_1, r_2) = \frac{3\sqrt{3}}{8} \left[\frac{1}{r_1^3} + C \frac{k^3 - 1}{r_2^3 - r_1^3}\right]/(1 + C) \tag{125}$$

where $k = r_2^a / r_1^a$ and C is a weighting factor determining the relative importance of the contribution of the second nn to the local density. The reasons for defining the local density in the form of eq. (125) are: (a) The terms

$\dfrac{1}{r_1^3}$ and $\dfrac{k^3 - 1}{r_1^3 - r_1^3}$ define a correct density in the crystal-

line case; and(b) If an amorphous semiconductor is such that its first nn distance, r_1^a, and the next neighbor distance, r_2^a do not have any spread, eq. (125) reduces to eq. (124).

In order to calculate the distribution in local density, a range of r_1 (or r_2) about $3\sigma_1$ (or $3\sigma_2$) from $r_1^a(r_2^a)$ is considered. The probability distributions of r_1 and r_2 in these ranges are assumed to be independent. Therefore,

$$p(r_1, r_2) \propto \exp\{-0.5[(\frac{r_1 - r_1^a}{\sigma_1})^2 + (\frac{r_2 - r_2^a}{\sigma_2})^2]\} \tag{126}$$

From eq. (124) and (125), the distribution of local density, $p(\rho)$ can be determined, provided the value of C is known. A reasonable value of C may be $\dfrac{r_1^a{}^2}{r_2^a{}^2}$.

In the crystalline case, this value of C is equal to 0.375. This definition for C implies that the relative importance of atoms in contributing to the local density is inversely proportional to the distance from the origin. Fig. 28, shows the local density distribution for various values of C. It is seen that for $C \leq 0.5$, the curve does

100
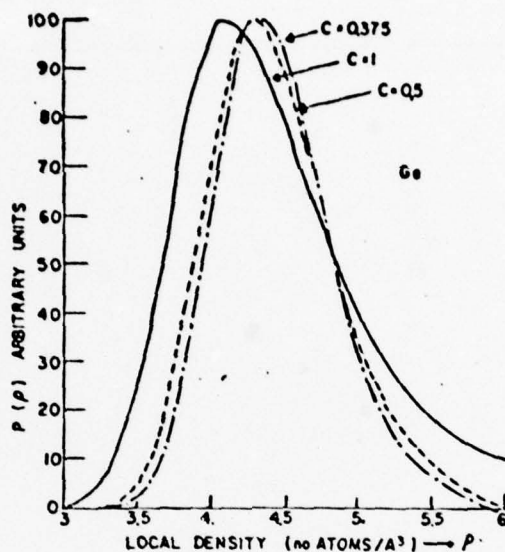
Fig. 28 Changes in the distribution of local density, $p(\rho)$, due to variations in C. (see text).

not depend strongly on C, and has a Gaussian shape except for a slight asymmetry on the high density side. The local density distribution for various values of σ_2, as shown in Fig. 29 are not affected appreciably, indicating that the local density is most likely determined by σ_1, the spread in the nearest neighbor distance. The most reasonable value for local density in this analysis seems to be for C = 0.375.

C. Method of Calculation

To calculate the contribution of $<\varrho>^{SL}$ to infrared absorption we take for the imaginary part of the lattice susceptibility of a crystal with a single reststrahlen frequency ω_{TO}

$$\varepsilon_2^c \propto \frac{\Gamma\omega}{(\omega_{TO}^2 - \omega^2)^2 + \Gamma^2\omega^2} \qquad (127)$$

with $\Gamma\sim$ constant in the vicinity of the reststrahlen spectrum. Then the SL contribution to the amorphous solid is
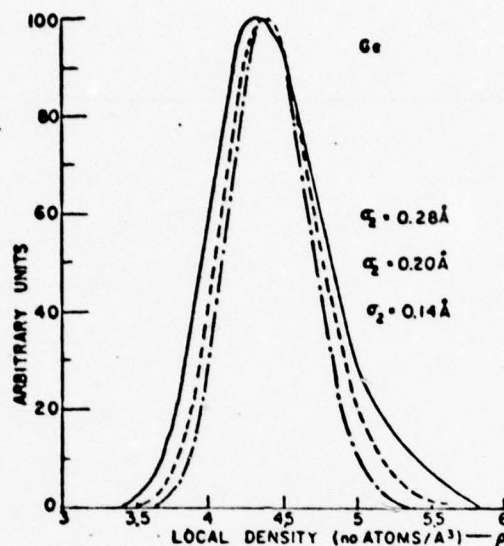
Fig. 29 Changes in the distribution of local density, $p(\rho)$, due to variations in σ_2 (see text).

$$\epsilon_2^{SL} = \rho^{SL} \int_0^\infty d\rho \; p(\rho) \; \epsilon_2^c(\rho) \tag{128}$$

In the simplified calculations carried out here we assume that ϵ_2^c depends on ρ only through ω_{TO}, and that the distribution $p(\rho)$ is a Gaussian. This spread will be relatively narrow, and is taken to be peaked around the equilibrium nn distance r_0 of the amorphous solid. Such assumptions seem reasonable in view of the local density distribution as discussed in the previous section. Values of $\omega_i(\rho)$ may be inferred directly from the Grüneisen approximation, which should be adequate for small departures in ρ_0 from crystalline values. Thus[104]

$$\omega_i(\rho) = \omega_i(\rho_0)(\rho/\rho_0)^{\gamma_i} \tag{129}$$

where γ_i is the mode Grüneisen parameter[105,95]. An obvious analogous calculation yields the SL contribution to the Raman intensity for an amorphous solid.

102

D. Results and Discussions

The spread in $p(\rho)$ has been adjusted to provide a best fit with experiment. In Fig. 30a and 30b we display the first order Raman and infrared spectra of amorphous Ge. If one chooses $\eta = 0$ a good fit is obtained for the principal Raman peak, with the remaining features presumably arising from $(n)_S$. The infrared one-phonon spectrum, which is forbidden in the crystal, arises entirely from $(n)_S$; i.e., $\varepsilon_2 = \varepsilon_2^S$. Apart from matrix element effects, this spectrum should be proportional to the $(n)_S$ contribution to the Raman spectrum, which may be determined by first choosing η and then subtracting the calculated (SL) portion of the Raman spectrum from the
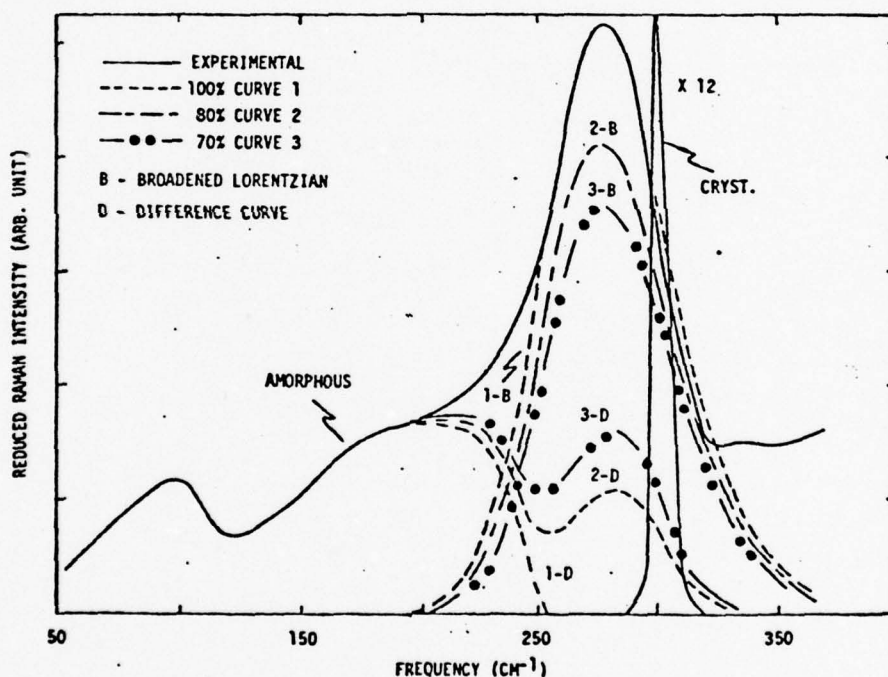
Fig. 30a   Comparison of calculated crystalline like contribution and experimental Raman spectrum of amorphous Ge. Experimental data (ref. 82). The difference curves represent the $(n)_S$ contributions similar to the vibrational density of states.

103
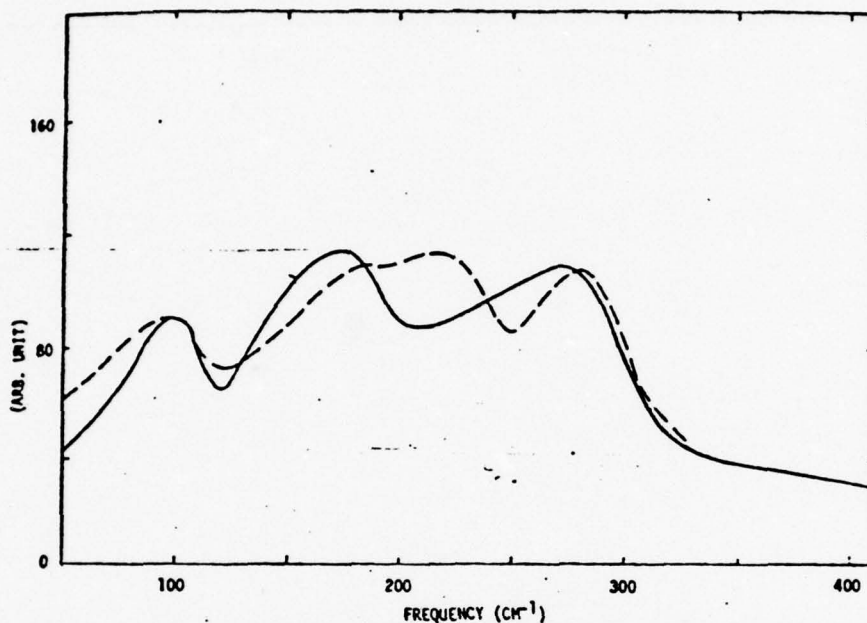
Fig. 30b Infrared data (solid curve) of ref. 83 is com-
pared to the $(n)_S$ contribution (dashed curve) correspond-
ing to $\eta = 0.7$ [curve 3-D of (a) above].

experimental one. Comparison of the infrared data with
ϵ_2^S corresponding to $\eta = .7$ is indicated in Fig. 30b. Si-
milar results may be shown to follow for the case of Si
as well. It appears that the peak positions and shapes
of the Raman spectra of these solids are well represent-
ed by a simple sum of $(n)_{SL}$ and $(n)_S$ contributions, and
infrared spectra by $(n)_S$ contributions. For binary TBAS
the crystalline counterparts display allowed spectra both
for infrared and first order Raman. Fig. 31 displays the
$\eta = 0$ fit to the IR spectrum for amorphous GaAs; Fig.
32 shows the same for SiC, but for a geometry where both
TO and LO were excited (Berreman effect[106]). Very simi-
lar results were also obtained for the infrared spectra
of amorphous GaP, GaSb and InAs. The conclusion reached
is that the $(n)_S$ contribute very little to the spectrum
of typical binary TBAS; the principal features arise from
just $(n)_{SL}$ alone.
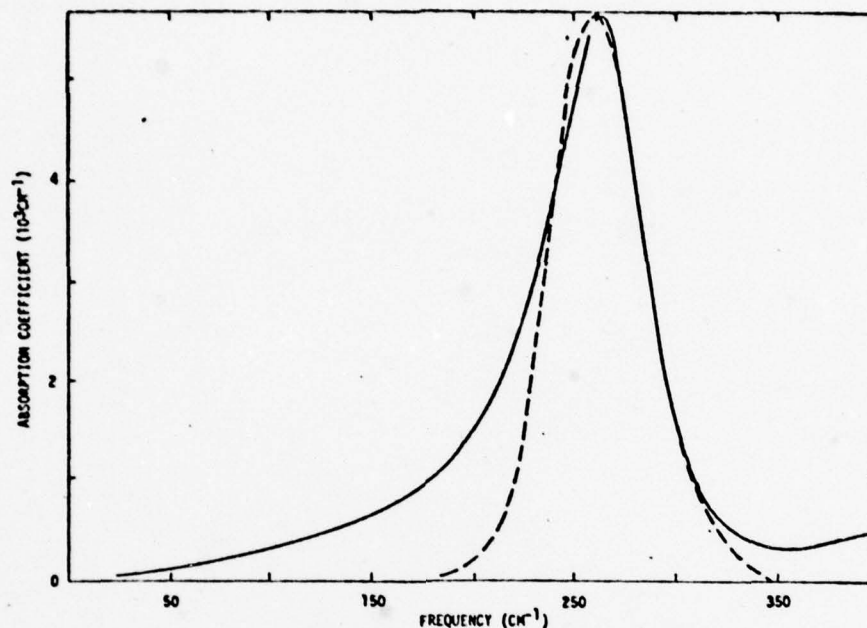
Fig. 31 Infrared absorption in amorphous GaAs. Solid curve: experimental (from ref. 102); dashed curve: broadened Lorentizian calculated in this work with $\sigma_\rho^a = 0.076\ \rho_{ao}$, and $\rho_{ao}/\rho_c = 0.96$, where σ_ρ^a is the Gaussian spread in local density, ρ_{ao}/ρ_c is the ratio of mean density of the amorphous phase to the crystalline density.

The present results thus suggest that CAA processes play an important role in the spectra of TBAS, and that a statistical approach incorporating such processes can account successfully for the principal features of measured spectra.

ACKNOWLEDGMENTS
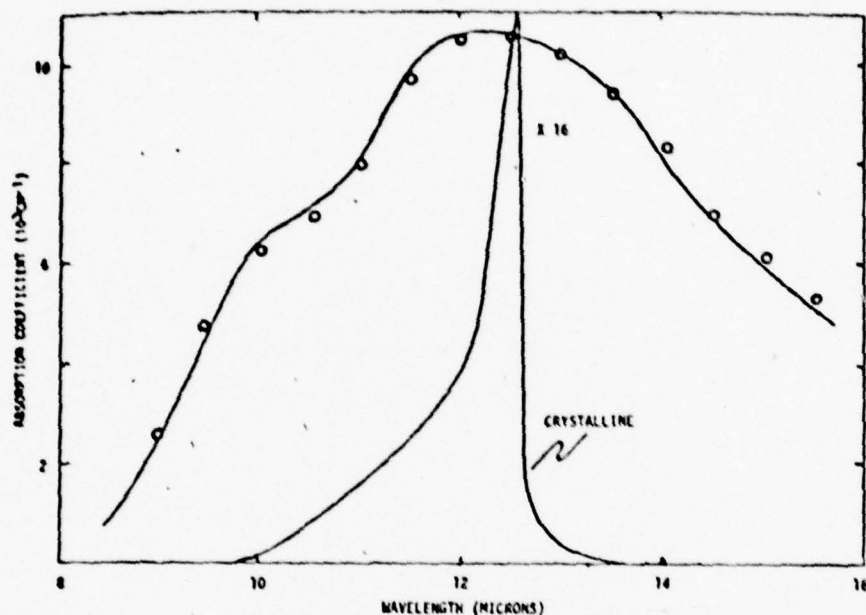
Fig. 32 Infrared absorption in amorphous SiC. Solid
curve: calculated in this work. Relevant crystalline
Lorentz oscillator parameters were taken from D. W.
Feldman, et al, Phys. Rev. 170, 698 (1968); 173, 787
(1968); and mode Grüneisen parameters from ref. 105;
Circles: experimental data from ref. 103.

REFERENCES

*Work supported in part, by Air Force Cambridge Research
 Laboratories (AFSC), Contract No. F19628-72-C-0286.

1.   I. M. Lifshitz, J. Phys. USSR, 7, 215 (1943); 7,
      249 (1943); 8, 89 (1944).
2.   E. W. Montroll and R. B. Potts, Phys. Rev. 100, 525
      (1955); ibid, 102, 72 (1965).
3.   P. Mazur, E. W. Montroll and R. B. Potts, J. Wash.
      Acad. Sci. 46, 2 (1956).
4.   G. Schaefer, Phys. Chem. Solids 12, 233 (1960).
5.   See for example, L. Genzel, "Optical Properties of
      Solids", ed. S. Nudelman and S. S. Mitra (Plenum,
      N. Y., 1969), p. 453.

6. P. G. Dawber and R. J. Elliott, Proc. Roy. Soc. A273, 222 (1963).

7. I. M. Lifshitz, Nuovo Cimento Suppl. 3, 716 (1956).

8. P. G. Dawber and R. J. Elliott, Proc. Phys. Soc. 81, 521, 453 (1963).

9. S. S. Jaswal, Phys. Rev. 140, 2A, 687 (1965).

10. N. Krishnamurthy and T. M. Haridasan, Indian J. Pure Appl. Phys. 4, 255 (1966).

11. J. B. Page and D. Strauch, Phys. Stat. Sol. 24, 469 (1967).

12. A. P. Zhernov and G. R. August, Soviet Physics, Solid State 9, 8, 1724 (1968).

13. N. Krishnamurthy and T. M. Haridasan, Indian J. Pure Appl. Phys. 7, 89 (1969).

14. J. Govindarajan and T. M. Haridasan, Phys. Letters 29A, 387 (1969).

15. W. Hayes, H. F. MacDonald and C. T. Sennet, J. Phys. C (Solid State Phys.), 2 2402 (1969).

16. G. Lucovsky, M. H. Brodsky and E. Burstein, Phys. Rev. B, 2, 3295 (1970).

17. See for example, F. B. Hilderbrand, Methods of Applied Mathematics, 2nd edition, Sec. 1.12 and 1.17, Prentice Hall Inc., New Jersey.

18. K. F. Renk, Z. Physik 201, 445 (1967).

19. R. Weber, Ph. D. Thesis, Physikalisches Institut der Universität, Freiburg im Breisgau (1967).

20. J. F. Vetelino, Ph. D. Dissertation, University of Rhode Island (1969), (unpublished).

21. W. Hayes, Phys. Rev. Letters 13, 275 (1964).

22. W. Hayes, Phys. Rev. 138, 1227 (1965).

23. A. R. Goodwin and S. D. Smith, Phys. Letters 17, 203 (1965).

24. O. G. Lorimor, W. G. Spitzer and M. Waldner, J. Appl. Phys. 37, 2509 (1966).

25. S. D. Smith, R. E. V. Chaddock and A. R. Goodwin, Proc. Intern. Conf. Phys. Semicond., Kyoto, 67 (1966).

26. A. Mitsuishi, A. Manabe, H. Yoshinaga, S. Ibuki and H. Komiya, Progress of Theoretical Phys., Supp. 45, 21 (1970).

27. O. G. Lorimor and W. G. Spitzer, J. Appl. Phys. 37, 3687 (1966).

28. O. Brafman, I. F. Chang, G. Lengyel and S.S. Mitra, Phys. Rev. Letters 19, 1120 (1967).

29. W. G. Spitzer, J. Phys. Chem. Solids 28, 33 (1967).

30. M. H. Brodsky and G. Lucovsky, Phys. Rev. Letters, 21, 990 (1968).

31 W. G. Spitzer, W. Allred, S. E. Blum and R. J. Chicotka, J. Appl. Phys. 40, 2589 (1969).

32.   C. T. Sonnet, D. R. Bosomworth, W. Hayes and A. R.
       L. Sray, J. Phys. C. (Solid State Phys.), $\underline{2}$, 1137
       (1969).

33.   W. Hayes, M. D. K. Wiltshire, P. J. Dean, J. Phys.
       C. (Solid State Phys.), $\underline{3}$, 1762 (1970).

34.   D. T. F. Marple, unpublished.

35.   M. Balkanski, R. Beserman and L. K. Vodopianov,
       Localized Excitation in Solids, edited by R. F.
       Wallis, (Plenum, N. Y., 1968). p. 154.

36.   M. H. Brodsky, G. Lucovsky, M. F. Chen and T. S.
       Plaskett, Phys. Rev. B $\underline{2}$, 3303 (1970).

37.   A. Mitsuishi, unpublished.

38.   W. J. Choyke and L. Patrick, Bull. Am. Phys. Soc.
       $\underline{16}$, 397 (1971).

39.   J. F. Vetelino and S. S. Mitra, Phys. Rev. $\underline{178}$,
       1349 (1969).

40.   S. P. Gaur, J. F. Vetelino and S. S. Mitra, J. Phys.
       Chem. Solids $\underline{32}$, 2737 (1971).

41.   S. Ibuki, H. Komiya, A. Mitsuishi, A. Manabe and
       H. Yoshinaga, International Conference on Semicon-
       ductors, Moscow, (1968), p. 1047.

42.   S. Ibuki, H. Komiya, A. Mitsuishi, A. Manabe and
       H. Yoshinaga, II-VI Semiconductor Compounds (Edit.
       by D. G. Thomas) (Benjamin, New York, 1967), p. 1140.

43.   F. Krueger, O. Reinkober and E. Koch-holm, Annln.
       Phys. $\underline{85}$, 110 (1928).

44.   F. Matossi, J. Chem. Phys. $\underline{19}$, 161 (1951).

45.   P. Dean, Proc. Phys. Soc. $\underline{73}$, 413 (1959); ibid Proc.
       Roy. Soc. $\underline{254A}$, 507 (1960); ibid Proc. Roy. Soc.
       $\underline{260A}$, 263 (1961).

46.   H. W. Verleur and A. S. Barker, Phys. Rev. $\underline{149}$, 715
       (1966); ibid Phys. Rev. $\underline{155}$, 750 (1967).

47.   Y. S. Chen, W. Shockley and G. L. Pearson, Phys.
       Rev. $\underline{151}$, 648 (1966).

48.   I. F. Chang and S. S. Mitra, Phys. Rev. $\underline{172}$, 924
       (1968).

49.   I. F. Chang and S. S. Mitra, Adv. in Phys. $\underline{20}$,
       359 (1971).

50.   A. P. G. Kutty, Solid St. Commun., $\underline{14}$, 213 (1974).

51.   P. N. Sen and W. M. Hartmann, Phys. Rev. $\underline{B9}$, 367
       (1974).

52.   O. Brafman, I. F. Chang, G. Lengyel, S. S. Mitra
       and E. Carnall, Phys. Rev. Letters $\underline{19}$, 1120 (1967);
       Proc. Intl. Conf. on Localized Excitations in Solids
       (New York, Plenum Press, 1968), p. 602.

53.   S. C. Varshney, J. F. Vetelino and S. S. Mitra,
       Phys. Rev. (to be published).

54.   See for example, "AIP Proc. No. 20 on, Tetrahedrally
       Bonded Amorphous Semiconductors", ed. M. H. Brodsky,

S. Kirkpatrick and D. Weaire (1974).

55. N. J. Shevchik and W. Paul, J. Non-Cryst. Sol.
     8-10, 381 (1972).
56. N. J. Shevchik and W. Paul, J. Non-Cryst. Sol.
     13, 1 (1973/74).
57. S. Moss and J. Graczyk, "Proc. Tenth Intern. Conf.
     on the Physics of Semiconductors, Cambridge, Mass.,
     1970, ed. S. P. Keller et al, Conf.-700801 (USAEC
     Division of Technical Information, Springfield, Va.,
     1970), p. 658.
58. D. Turnbull and D. E. Polk, J. Non-Cryst. Sol.
     8-10, 19 (1972).
59. M. L. Rudee, Thin Solid Films 12, 207 (1972).
60. J. D. Bernal, Proc. Roy. Soc. 280A, 299 (1964).
61. W. H. Zachariasen, J. Am. Chem. Soc. 54, 384 (1932).
62. R. Grigorovici and R. Manaila, J. Non-Cryst. Sol.
     1, 371 (1969).
63. P. Dean, Proc. Phys. Soc. 84, 727 (1964).
64. P. Dean, Rev. Mod. Phys. 44, 127 (1972).
65. R. J. Bell, J. Phys. C5, L315 (1972).
66. R. J. Bell, P. Dean and D. C. Hibbins-Butler, J.
     Phys. C3, 2111 (1970).
67. J. Hori, "Spectral Properties of Disordered Chains
     and Lattices", Intern. Series of Monographs in
     Natural Philosophy, Vol. 16, Pergamon Press, (1968).
68. M. Goda, J. Phys. C6, 3047 (1973).
69. R. J. Bell, N. F. Bird and P. Dean, J. Phys. C7,
     2457 (1974).
70. R. J. Bell, N. F. Bird and P. Dean, J. Phys. C1,
     299 (1968).
71. R. J. Bell and P. Dean, Nature 212, 1354 (1966).
72. D. Weaire and R. Alben, Phys. Rev. Letters 27,
     1505 (1972).
73. R. Alben, J. E. Smith, Jr., M. H. Brodsky and D.
     Weaire, Phys. Rev. Letters 30, 1141 (1973).
74. R. Alben, "Tetrahedrally Bonded Amorphous Semicon-
     ductors", AIP Proc., No. 20 (1974).
75. D. Henderson and F. Herman, Jr. J. Non-Cryst. Sol.
     8-10, 359 (1972); D. Henderson, "Computational
     Solid State Physics", ed. F. Herman (Plenum, N.Y.
     1972), p. 175.
76. M. F. Thorpe, Phys. Rev. B8, 5352 (1973).
77. R. J. Bell, J. Phys. C7, L265 (1974).
78. R. Alben and D. Weaire, J. E. Smith and M. H.
     Brodsky, Phys. Rev. B11, 2271 (1975).
79. J. E. Smith, Jr., M. H. Brodsky, B. L. Crowder, M.
     I. Nathan and A. Dinczyk, Phys. Rev. Letters, 26,
     642 (1971).

80.   J. E. Smith, Jr., M. H. Brodsky, B. L. Crowder, M. I. Nathan and A. Dinczyk, J. Non-Cryst. Sol. 8-10, 179 (1972).

81.   M. Wihl, M. Cardona and J. Tauc, J. Non-Cryst. Sol. 8-10, 172 (1972).

82.   J. E. Smith, Jr., M. H. Brodsky, B. L. Crowder and M. I. Nathan, "Proc. of the 2nd Intern. Conf. on Light Scattering in Solids", ed. M. Balkanski (Flammarion, Paris, 1971) p. 330.

83.   R. W. Stimets, J. Waldman, J. Lin, T. S. Chang, R. J. Temkin and G. A. N. Connell, Solid St. Commun. 13, 1485 (1973).

84.   M. H. Brodsky and A. Lurio, Phys. Rev., B9, 1646 (1974).

85.   J. D. Axe, D. T. Keating, G. S. Cargill, III and R. Alben, AIP Proc., No. 20 (1974), p. 279.

86.   F. R. Ladan and A. Zylberstein, Phys. Rev. Letters 29, 1198 (1973).

87.   B. Schröder and J. Geiger, Phys. Rev. Letters 28, 301 (1972).

88.   D. E. Polk, J. Non-Cryst. Sol. 5, 365 (1971).

89.   R. J. Temkin, Solid St. Commun. 15, 1325 (1974).

90.   R. Grigorovici, J. Non-Cryst. Sol. 1, 303 (1969).

91.   Y. F. Tsay, D. K. Paul and S. S. Mitra, Phys. Rev. 138, 2827 (1973).

92.   S. S. Mitra, D. K. Paul, Y. F. Tsay and B. Bendow, "Tetrahedrally Bonded Amorphous Semiconductors," AIP Proc. No. 20 (1974), p. 284.

93.   H. J. McSkimin, J. Acous. Soc. of Am. 30, 314 (1958).

94.   H. J. McSkimin and P. Andreatch, Jr., J. Appl. Phys. 35, 2161 (1964).

95.   C. J. Buchenauer, F. Cerdeira and M. Cardona, "Proc. of the 2nd Intern. Conf. on Light Scattering in Solids", ed. M. Balkanski (Flammarion, Paris, 1971) p. 280.

96.   R. J. Temkin, W. Paul and G. A. N. Connell, Adv. in Phys. 22, 581 (1973).

97.   S. S. Mitra, "Optical Properties of Solids", ed. S. Nudelman and S. S. Mitra (Plenum, N.Y. 1969), p.333.

98.   S. P. Gaur, M.S. Thesis, University of Maine (1971).

99.   G. Dolling and R. A. Cowley, Proc. Phys. Soc., London, 88, 463 (1966).

100.   H. Shuker and R. W. Gammon, Phys. Rev. Letters 25, 222 (1970).

101.   S. S. Mitra, Y. F. Tsay, D. K. Paul, B. Bendow, Phys. Stat. Solidi, to be published.

102.   W. Prettl, N. J. Shevchik and M. Cardona, Phys. Stat. Sol. (b) 59, 241 (1973).

J. F. VETELINO AND S. S. MITRA

103.   E. A. Fagan, in Proc. of the Fifth Intl. Conf. on
        Amorphous and Liquid Semiconductor (Garmisch-
        Partenkirchen, West Germany, September 1973),
        pp. 601-7.
104.   See for example, S. S. Mitra in "Optical Properties
        of Solids", ed. S. Nudelman and S. S. Mitra, Plenum
        Press, New York (1969).
105.   S. S. Mitra, O. Brafman, W. B. Daniels and R. K.
        Crawford, Phsy. Rev. 186, 942 (1969).
106.   D. W. Berreman, Phys. Rev. 130, 2193 (1963).

3.2
STATISTICAL INTERPRETATION OF RAMAN SPECTRA OF AMORPHOUS SOLIDS

S. S. Mitra *+
Electrical Engineering Department
University of Rhode Island
Kingston, RI 02881, USA

Bernard Bendow and Y.F. Tsay
Air Force Cambridge Research
Laboratories (AFSC)
Hanscom AFB, MA 01731, USA

1. INTRODUCTION

Until recently, most investigations of the optical properties of amor-
phous solids emphasized the role of $\vec{k}$-selection rule breakdown, and what is
consequently expected to be a strong similarity between densities of states
and optical spectra of such solids. In various recent papers, however, the
present authors have pointed out (1-4) that the principal features of opti-
cal spectra of tetrahedrally bonded amorphous semiconductors (TBAS) are well
explained in terms of a statistical approach emphasizing the role of crys-
talline analog processes. Essentially, the solid is parametrized by a set
of crystalline analog configurations, which preserve short and long range
order, and a set of non-$\vec{k}$-conserving configurations on which just short
range order is maintained. Although Alben et al (5) have demonstrated that
detailed cluster calculations provide a good account of observed IR and
Raman spectra of Ge and Si, it is highly desirable to provide a simpler ap-
proach, which can more readily provide an interpretation of TBAS spectra
without the lengthy and detailed calculations required in the cluster ap-
proach. We have previously discussed the application of the present method
to the analysis of Si and Ge spectra, and to IR spectra of selected III-V
TBAS. The purpose of the present paper is to extend the present concepts to
an analysis of Raman spectra of selected III-V amorphous semiconductors.

II. METHOD OF CALCULATION

For the statistical approach to be useful one must be able to identify
a restricted class of configurations which elicit principal features of the
properties concerned. Furthermore one should be able to calculate the phys-
ical properties of interest for these configurations. We have parameterized
TBAS in terms of two classes of principal configurations, viz., (a) both
short and long range order (SL) and (b) just short range order (S). Among
the configurational parameters suggestive for TBAS, are interatomic spacings,
local densities and bond angles, all known to deviate from those of their
crystalline analogs and to display characteristic spreads as well. For sim-
plicity of calculation we had restricted this configurational parameter to
correspond to variations in local density ρ alone. It was assumed that the
local density fluctuation results only from the static spreads of the first
and second nearest neighbor distances. The results of such an analysis (6)
indicated that the distribution of local density in TBAS is nearly Gaussian
represented by $P(\rho)$ with two adjustable parameters ρ_a and σ_ρ.

In the case of crystalline Si and Ge the first order Raman spectrum is
allowed, and consists of a single resonance, whereas the IR spectrum is for-
bidden. Therefore Raman spectra of their amorphous phases have contribu-
tions from both SL and S configurations, whereas for IR spectra only the S
configuration. For the crystalline III-V compound semiconductors both IR
and Raman spectra are permitted. IR spectrum consists of a single resonance
at the long wavelength transverse optic mode frequency, ω_{TO}. Raman spectrum
on the other hand, consists of two resonances corresponding to both $\vec{k} \sim 0$
transverse and longitudinal optic mode frequencies, ω_{TO} and ω_{LO}. Thus ac-
cording to the crystal analog model the SL contribution to the amorphous
phase should be significantly different for IR and Raman spectra, which in-
deed is what one observes experimentally (see Figs. 1 and 3).

To calculate the SL contribution to IR absorption in the III-V com-
pounds the imaginary part of the dielectric constant, ε_2^c is represented (7)
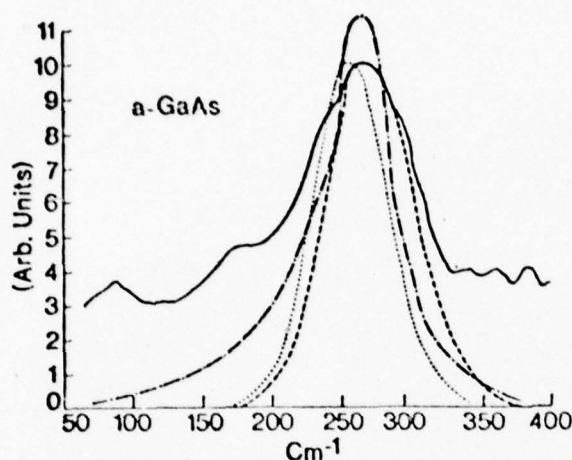
113

Fig. 1 Spectra of amorphous GaAs.
— Raman (experimental);
-·- IR (experimental);
··· Raman (calcd.) with TO only;
--- Raman (calcd.) with TO and LO.
$c_{LO}/c_{TO} = 1.5$

by a damped Lorentzian in ω_{TO}, $\mathcal{L}(\omega_{TO}, \Gamma_{TO})$. For the Raman scattering inten-
sity, S_{Raman}^c one likewise uses two damped Lorentzians, viz., in ω_{TO} and ω_{LO}:

$$S_{Raman}^c \propto [c_{TO} \mathcal{L}(\omega_{TO}, \Gamma_{TO}) + c_{LO} \mathcal{L}(\omega_{LO}, \Gamma_{LO})][n(\omega) + 1] \qquad (1)$$

$n(\omega)$ is the phonon occupation number and c corresponds to the relative
strength of the TO and LO resonances. Then the SL contribution to amorphous
solid is

$$\varepsilon_2^{SL} = \int_0^\infty d\rho \; P(\rho) \; \varepsilon_2^c(\rho) \qquad (2)$$

and

$$S_{Raman}^{SL} = \int_0^\infty d\rho \; P(\rho) \; S_{Raman}^c(\rho) \qquad (3)$$

ε_2^c and S_{Raman}^c are assumed to depend on ρ only through ω_{TO} (and ω_{LO}). Values
of $\omega_i(\rho)$ may be calculated in the Grüneisen approximation (7) in terms of
measured mode Grüneisen parameters (8).

First the IR spectra of amorphous III-V semiconductors are fitted with
eq. (2) using ρ_u and σ_ρ as adjustable parameters. The values of ρ_u and σ_ρ
thus obtained agree reasonably well with an approximate calculation involv-
ing the first and second neighbor radial distribution functions (6). Such
calculated spectra agree (3) extremely well with experimental spectra ex-
cept for slight deviations in the low frequency region where S contributions
become significant. In this paper we calculate Raman spectra of amorphous
GaAs, InAs and GaP by means of eqs (1) and (3), and using ρ_u and σ_ρ as

114

derived from the fitting of IR spectra. Additional parameters needed are c_{TO} and c_{LO} of eq. (1), which were also used as adjustable parameters.

111. RESULTS AND CONCLUSIONS

The IR and Raman spectra of amorphous GaAs are shown in Fig. 1. It should be noted that there is an additional feature in the high frequency side of the Raman spectrum, which we believe correspond to the crystal-analog LO contribution. The calculated Raman spectra using TO alone, and both TO and LO are also shown in this figure. The former gives poor agreement. The best fit for the high frequency side of the spectrum is obtained by choosing $c_{LO}/c_{TO} \approx 1.5$. The relative intensity of LO and TO modes depends, among other things, on the excitation frequency. However, the LO resonance for the zincblende type crystals is expected (9) to be relatively more intense than the TO resonance. The difference between the experimental and calculated curves in the low frequency region is attributed to the S contribution. Results for amorphous InAs and GaP are shown in Figs. 2 and 3. The position of the principal peak of both infrared and Raman spectra of the amorphous phase are shifted slightly to lower frequencies as compared to the corresponding crystalline case. The present model accounts for this shift by choosing ρ_a slightly lower than ρ_c, which is reasonable because both the first and second nn distances in TBAS are known to be smaller than the corresponding crystalline case.

We have utilized a statistical approach to interpret the broadening and shifting of peaks in the lattice spectra of TBAS induced by disorder. The present analysis thus suggests that the Raman and IR spectra of amorphous semiconductors are dominated by crystalline analog processes, and do not merely represent a broadened version of the crystalline density of states.
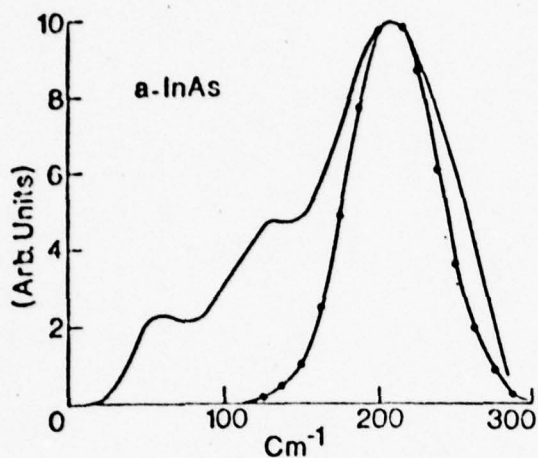
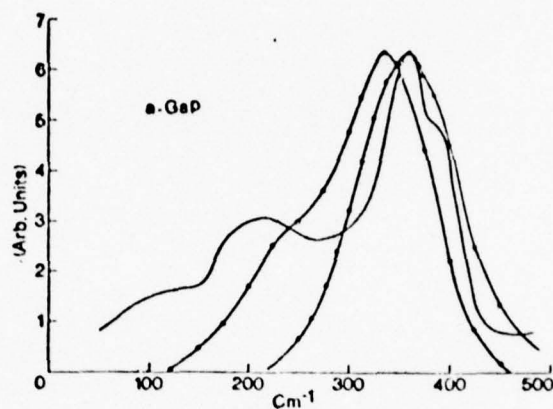Fig. 2 Raman spectrum of amorphous InAs. ____ experimental; ──•── calculated with $c_{LO}/c_{TO}=1.5$.

Fig. 3 Spectra of amorphous GaP. ____ Raman (exptl.); -o- IR (exptl.) ──•── Raman (calcd.) with $c_{LO}/c_{TO}=9$.

REFERENCES

[1] Y. F. Tsay, D. K. Paul and S. S. Mitra, Phys. Rev. B8, 2827 (1973).

[2] S. S. Mitra, D. K. Paul, Y. F. Tsay and B. Bendow, in "Tetrahedrally Bonded Amorphous Semiconductors", "M. H. Brodsky, S. Kirkpatrick and D. Weaire", [Amer. Inst. Phys., New York, USA, 1974], "284".

[3] S. S. Mitra, Y. F. Tsay, D. K. Paul and B. Bendow, Phys. Stat. Sol., to be published.

[4] Y. F. Tsay, B. Bendow and S. S. Mitra, J. Electronic Mat., to be published.

[5] R. Alben, D. Weaire, J. E. Smith, Jr. and M. H. Brodsky, Phys. Rev. B11, 2271 (1975).

[6] J. F. Vetelino and S. S. Mitra, in "Physics of Structurally Disordered Solids", "S. S. Mitra", [Plenum Press, New York, USA, to be published].

[7] See for example, S. S. Mitra, in "Optical Properties of Solids", "S. Nudelman and S. S. Mitra", [Plenum Press, New York, USA, 1969], "358".

[8] S. S. Mitra, O. Brafman, W. B. Daniels and R. K. Crawford, Phys. Rev. 186, 942 (1969); C. J. Buchenauer, F. Cerdeira and M. Cardona, in "Proc. Second Intntl. Conf. on Light Scattering in Solids", "M. Balkanski", [Flammarion, Paris, France, 1971], "280".

[9] R. Loudon, Advs. in Phys. 13, 423 (1964).

VIBRATIONAL PROPERTIES OF A THREE-FOLD COORDINATED TWO DIMENSIONAL RANDOM LATTICE

J. Y. Chen and J. F. Vetelino
Department of Electrical Engineering
University of Maine
Orono, Maine 04473

and

S. S. Mitra
Department of Electrical Engineering
University of Rhode Island
Kingston, Rhode Island 02881

ABSTRACT

A two-dimensional amorphous lattice has been constructed using the generalized random walk technique. The bond lengths and angles were obtained from the random number generation functions. The lattice sites were assumed to have a coordination number of three and were connected to form closed polygons. The lattice and the associated structural properties are calculated. A lattice dynamical calculation is then performed using this network as a two-dimensional amorphous structural representation. The explicit vibrational spectra are obtained for the random network and the corresponding three-fold-coordinated honeycomb lattice.

I. INTRODUCTION

The random network concept was first introduced by Zachariasen[1] in the description of a two-dimensional lattice for a glass. Using this concept Ordway[2], Evans and King[3], and Bell and Dean[4] have constructed random models for vitreous silica. In the last few years, this concept has been extensively studied in the modelling of an amorphous structure[5,6].

Most of the previous models, however, are either perturbations of crystalline structures or rough hand-built models consisting of tetrahedral units. The tetrahedral units were distorted in order to achieve the connectivities. The randomness and the statistics of the bond lengths and bond angles were not considered in the connecting process. Further adjustments were therefore necessary to make the model radial distribution function (RDF) match well with the experimental one. The adjusting procedure obviously improves the model geometry but does not change the topological structure[7]. The nonrandomness introduced by using crystalline structural units as a starting point may still exist after adjust-

ments. It might be more realistic to use random numbers rather than any perturbated crystalline units as a basis for the random model construction. The resulting model certainly should have real amorphous topology and geometry, hence further adjustment is no longer needed.

The purpose of this paper is to present an approach which utilizes the random walk concept to construct a truly random network. The use of the random walk technique was first suggested by Axe[8] in his work on a one dimensional random network. As an example to illustrate the application of the random walk technique, a two dimensional random network with coordination number three was constructed in this work. The assumption of a constant coordination number complies with the short-range order (SRO) characteristic of amorphous materials[6,8]. The corresponding crystalline lattice exhibits the honeycomb structure. This kind of amorphous network might serve as a two-dimensional analogy for certain planes in three-dimensional diamond, zincblende or wurtzite structures. It can also be used as a basis to develop the random models for layer-like amorphous materials such as amorphous graphite, amorphous arsenic and chalcogenide glasses.

In the present approach, random numbers for bond lengths and bond angles are first generated from a random number generation function. A two-dimensional amorphous lattice is then drawn by using these random numbers under the constraint of a coordination number of three.

II. MODEL CONSTRUCTION

In the present work, experimental data appropriate to amorphous silicon was used for the bond length[9]. The data used for the bond angle spread and cut off was according to the RDF analysis of amorphous germanium and silicon[10]. The random numbers for bond lengths were generated from a random number generation function having Gaussian distribution with a mean at 2.35Å and a standard deviation of 0.09Å. Since there are only two linearly independent angles associated with one lattice site, two sequences of Gaussian distributed random numbers were generated having a 120° mean and 10° standard deviation. In order to obtain a cutoff angle of 20° from the mean angle, only those angles between 100° and 140° were retained. Also, a pair of angles whose sum was outside the interval of $[220^\circ - 260^\circ]$ was rejected to ensure that the third angle had a cutoff of $\pm 20^\circ$ from the mean.

Next, a two-dimensional amorphous lattice was drawn using the random numbers generated for the bond lengths and bond angles. The assumption of three nearest neighbors for each lattice site implies that no interior broken bonds exist and no bonds cross each other. In

other words, the lattice sites when connected form crossed polygons. In the process of connecting the last two bonds on a polygon, two random bond lengths and one random bond angle were chosen simultaneously. In order to achieve perfect connectivity in the polygon, the random bond lengths and angles were allowed to vary up to a few percent about the value given by the random number generation procedure. The bond angle variation usually was higher than the bond length variation. This is due to the fact that the bond lengths should maintain a Gaussian form whereas the bond angle distribution is not necessarily an exact Gaussian.

The individual polygon construction was time consuming in that if a polygon could not be closed, the bonds had to be erased and new bonds drawn to attempt to close the polygon. Finally, a lattice consisting of 233 interior atoms and 39 boundary atoms was obtained. A total of 369 random numbers have been used for the bond lengths and 699 for the bond angles. From the coordinates of all the sites, the corresponding lattice was drawn. Figure 1 presents the resulting two dimensional random lattice. No crystallinity appears in the lattice, however short range order (SRO) does exist in the immediate neighborhood of each lattice site. Every bulk atom has three nearest-neighbors and six next nearest-neighbors.
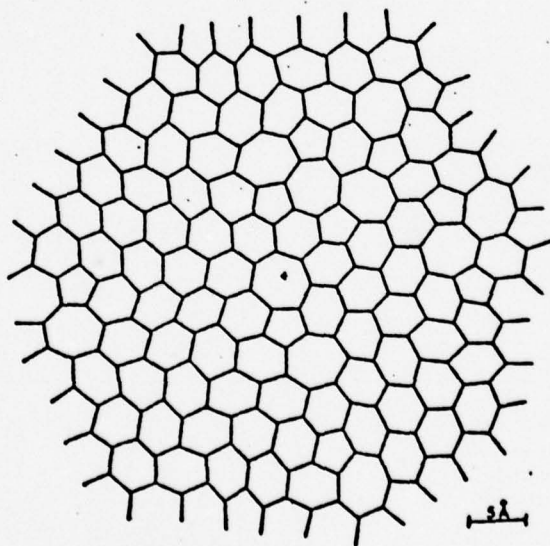

Fig. 1. A two dimensional random network of coordination number three.

119

III. STRUCTURAL PROPERTIES

Several interesting properties associated with this random lattice are discussed below.

The number of sides in the polygon can be expressed as

$$n = 360°/(180° - \bar{\theta}) \qquad (1)$$

n is the number of polygon sides and $\bar{\theta}$ is the average internal angles of the polygon. Since $\bar{\theta}$ lies between 100° and 140°, the polygon could have only 5, 6, 7, 8 or 9 sides. By referring to the angular distribution, it can be seen that the probability of having a nine or eight sided polygon with average internal angles of 140° and 135° respectively is quite low. Among the 98 polygons in the random lattice, there are 10 pentagons, 11 septagons and the remaining 77 are all hexagons. The average number of polygon sides is 6.0102. This result agrees well with Euler's theorem[11] which states that in an infinite two dimensional lattice with a coordination number of three, the average number of polygon sides is exactly six. Another interesting fact is that the pentagons and septagons in the lattice always locate together. The reason for this is that for any random two dimensionally connected array, the distortion of the internal angle inside a polygon has to be compensated by the variation of a corresponding external angle. A relation between the number of sides (n) in a polygon and the average number of sides (m) of the neighboring polygons was originally proposed by Aboav[12] and then modified by Weaire[13] as

$$m \approx 5 + 6/n \qquad (2)$$

The above equation has served as an independent check for the present lattice and the agreement is very good.

Figure 2 presents the RDF of this model. The calculations were based on the method described by Polk and Boudreaux[14] for a finite size model. The 40 atoms around the lattice centroid (Fig. 1) were selected as central atoms. The radius r = 14.3Å was used as an upper limit to keep the calculations within the model. The distribution up to about six bond lengths was plotted. The preservation of SRO in this lattice produces the distinct first and second peak under which the area is exactly three and approximately six, respectively. As a consequence of the two dimensional model, the RDF increases linearly with distance instead of the parabolic variation observed in three dimensions.
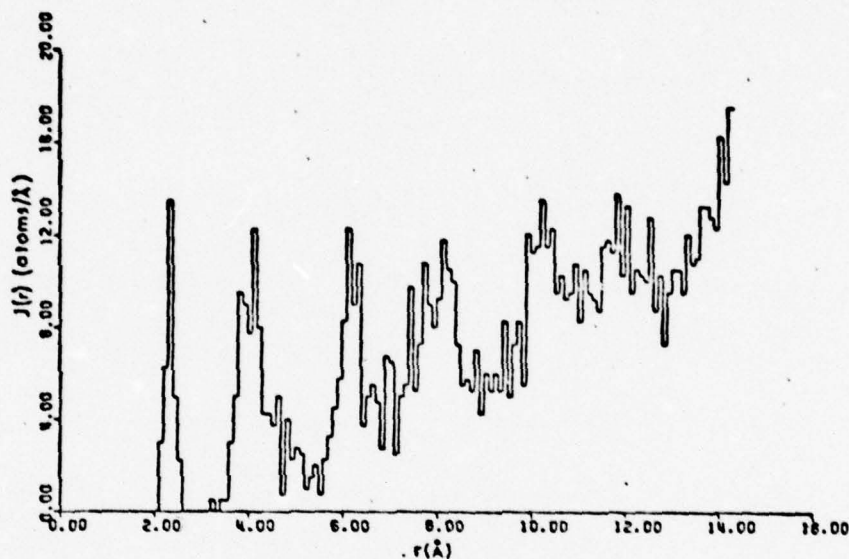
Fig. 2. The RDF of the model. The histogram is
calculated with radius intervals, $\Delta r = 0.1$Å.

IV. VIBRATIONAL PROPERTIES

In the lattice dynamical calculation, each atom was
assumed to be subject to a simple force field[16] with
central and non-central nearest-neighbor interactions.
The free end boundary conditions which are physically
realistic for the actual solid surface[15] are imposed on
the lattice boundaries. The dynamical matrix (D) in this
calculation is 544 by 544 and of band[16] form which means
all the non-zero elements are within an interval around
the main diagonal. The half-bandwidth is 80 and the
number of non-zero elements in each row is no more than
8. Those elements are placed according to the neighbor
relationships. Their positions were not regular because
of the topological disorder in the lattice. The matrix
elements, which are a function of force constants, hence
the bond length and bond angle are different due to the
geometrical disorder associated with the variation of
bond lengths and angles. The force constants were deter-
mined by relating them to the pressure dependences of the
elastic constants and the optical mode frequency[16].
Dean and Bacon's method[17] based on the negative eigen-
value theorem[18] is then used to find the frequency dis-
tribution.

121

A simple force field with nearest-neighbor central and non-central force constants is used for the perfect honeycomb lattice.[19] The details of this calculation may be found elsewhere[19]. The resulting phonon density of states of both the perfect honeycomb and the random lattice is presented in Fig. 3. In the amorphous material the phonon spectrum becomes broader due to the amorphous disorder in the lattice. The geometric disorder induced by force constant variations extends the spectrum to a higher frequency range, hence reducing the height of the high frequency peak.
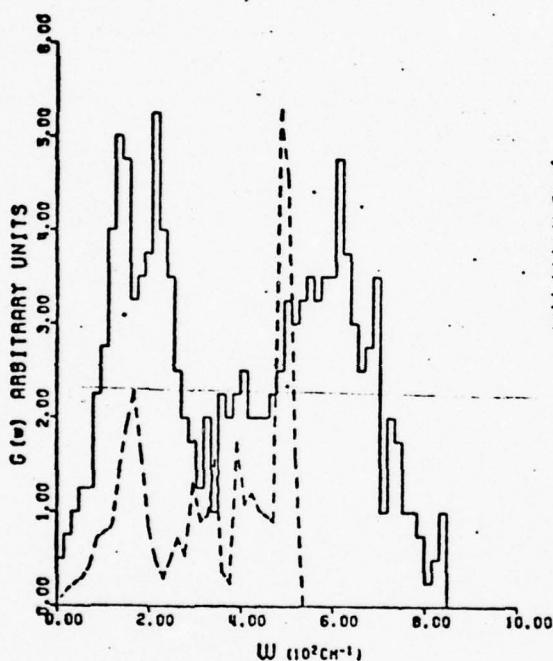

Fig. 3.
Vibrational Spectra.
Solid Line: the random network lattice.
Dashed Line: the perfect honeycomb lattice.

A random lattice of the type discussed here, can be successfully utilized for the calculation of electronic and vibrational properties since there is no broken bond inside the model. Two dimensional random networks of higher coordination numbers e.g., four (quadratic) and six (triangular) can also be constructed using this technique. An extension of this random walk technique to a three dimensional tetrahedrally bonded lattice is under consideration. Such a model is expected to be a better simulation of amorphous Ge, Si and the III-V compounds than any of the restricted models so far presented.

ACKNOWLEDGMENTS

REFERENCES

1. W. H. Zachariasen, J. Amer. Chem. Soc. 54, 3841 (1932).
2. F. Ordway, Science 143, 800 (1964).
3. D. L. Evans and S. V. King, Nature 212, 1353 (1966).
4. R. J. Bell and P. Dean, Nature 212, 1354 (1966).
5. D. E. Polk, J. Non-Cryst. Solids 5, 365 (1971).
6. N. J. Shevchik and W. Paul, J. Non-Cryst. Solids 8-10, 381 (1972).
7. W. Paul, in Physics of Structurally Disordered Solids, ed., S. S. Mitra (Plenum Press, New York, in press).
8. J. D. Axe, ibid (ref. 7).
9. S. Moss and J. F. Graczyk, in Proc. Tenth Int'l. Conf. on Phys. of Semiconductors, ed., S. P. Keller, et al., Conf. 700801 (USAEC, Div. of Tech. Info., Springfield, Va., 1970) p. 658.
10. N. J. Shevchik and W. Paul, J. Non-Cryst. Solids 3, 1 (1973/74).
11. C. S. Smith, Revs. Mod. Phys. 36, 524 (1964).
12. D. A. Aboav, Metallography 4, 425 (1971).
13. D. Weaire, Metallography, to be published.
14. D. E. Polk and D. S. Boudreaux, Phys. Rev. Letters 31, 92 (1973).
15. R. J. Bell and P. Dean, J. Inst. Math. Applics. 4, 375 (1968).
16. J. Y. Chen, J. F. Vetelino and S. S. Mitra, Solid State Commun. 16, 1313 (1975).
17. P. Dean and M. D. Bacon, Proc. Roy. Soc. A283, 64 (1965).
18. P. Dean and J. L. Martin, Proc. Roy. Soc. A259, 404 (1960).
19. J. Y. Chen, M.S. Thesis, University of Maine at Orono (1975). Also J. Y. Chen, J. F. Vetelino and S. S. Mitra, Phys. Rev. B, in press.

IV

OPTICAL AND ELECTRONIC

PROPERTIES OF SEMICONDUCTORS

124

4.1 ELECTRONIC STRUCTURE AND OPTICAL PROPERTIES OF CUBIC BN*

Y. F. Tsay,[+] A. Vaidyanathan[++] and S. S. Mitra[+]
Departments of Electrical Engineering[+] and Physics[++]
University of Rhode Island
Kingston, Rhode Island 02881

ABSTRACT

The electronic energy band structure of cubic BN is calculated using a non-local empirical pseudopotential method (NEPM). The electronic density of states, imaginary part of the dielectric constant and soft X-ray emission spectra are also calculated and compared with available experimental and theoretical results.

I. INTRODUCTION

The energy band structure of cubic BN has not been well studied experimentally, even though a few theoretical calculations of its band structure exist in the literature. The results of these calculations are at variance with each other and with available experimental data.

The first energy band structure calculation of this crystal was performed by Kleinman and Phillips[1] in which they treated, in a self-consistent manner, the antisymmetric pseudopotential as a first order perturbation to the crystal Hamiltonian of diamond. The width of the valence bands in the calculation was 17.95 eV and there were no energy gaps, direct or indirect of about 7 eV. Bassani and Yoshimine[2] using the OPW method, predicted a direct gap at Γ point of about 8.5 eV. One shortcoming of this calculation is that it perdicts an indirect gap ($\Gamma_{15,v} \rightarrow X_{1,c}$) of about 3 eV

125

which is smaller than the corresponding gap in diamond. In general this gap increases in going from group IV to the corresponding III-V compound[3]. In a different approach, Stocker[4] calculated the band structure using linear combinations of band orbitals as basic functions. A valence band width of 12.6 eV was obtained in this calculation. An APW calculation of the band structure of cubic BN was carried out by Wiff and Keown[5]. This predicted a valence band width of 17.8 eV, in fair agreement with the value of Kleinman and Phillips[1]. Hemstreet and Fong[6] performed a non-local empirical pseudopotential calculation and obtained a value of 7.6 eV for the indirect energy gap $\Gamma_{15,v} \rightarrow X_{1,c}$; a value of 27.5 eV was obtained for the valence band width. Aleshin and Smirnov[7] calculated the transition probabilities from the valence bands to the core states of cubic BN, using the OPW method. Nemoshkalenko and Aleshin[8] calculated the electronic density of states of cubic BN and obtained a width of the upper sub-valence-band of about 12 eV and the entire valence band width of about 24 eV.

On the experimental side, Philipp and Taft[9] made crude reflectance measurements on a small BN sample and found structure in the region 9-10 eV and a peak near 14.5 eV. Gielisse[10], in his ultraviolet absorption measurements on cubic BN, found that the absorption has a sharp rise in the vicinity of 7 eV. This presumably arises from the onset of the lowest interband transition. Fomichev and Rumsh[11] measured the K-band X-ray emission spectra of boron and nitrogen

in cubic BN and deduced a value of about 6 eV as an upper
estimate of the indirect gap and a value of about 15.4 eV
as a lower estimate of the valence band width. Chrenko[12]
measured the ultraviolet absorption spectra of cubic BN
crystals and deduced a value of about 6.4 eV as the minimum
value of the indirect gap.

In order to clarify the values of bandgaps and valence
band widths we carry out a non-local pseudopotential calcu-
lation of the band structure and soft X-ray emission spectra
of cubic BN. Our treatment of the non-local part of the
pseudopotential is similar to that of Hemstreet and Fong[6],
although the local pseudopotentials used in the present work
are obtained, in our opinion, from a better physical con-
sideration.

II. METHOD

The empirical pseudopotential method (EPM) of calcula-
ting the electronic energy band structure of crystalline
solids is well known in the literature[13]. The usual pre-
cedure is to treat the pseudopotential as a local potential.
This is justified as long as there is cancellation due to
the core states[14]. However, when the atomic core does not
contain electrons of a particular angular momentum quantum
number l, the Coulomb potential felt by the valence elec-
trons of the same angular momentum quantum number l is not
cancelled in the core region by the repulsive term. In this
case, one should add to the local pseuodpotential $V_L(\vec{r})$, a
non-local potential $V_{NL}(\vec{r})$ which acts only on the states

with angular momentum quantum number ℓ. In BN, since there are no p electrons in the ionic cores, a non-local pseudo-potential term should be added for $\ell = 1$. Following the analysis of Lee and Falicov[14] for potassium and the analysis of Fong and Cohen[15] for KCℓ, we write for $V_{NL}(\vec{r})$

$$V_{NL}(\vec{r}) = \sum_j \hat{P}_1^+ \, U\,(|\vec{r}-\vec{R}_j|)\hat{P}_1 \tag{1}$$

In the above equation $\hat{P}_1$ is the projection operator which operates only on the states with $\ell = 1$ and $\hat{P}_1^+$ is the Hermitian conjugate of $\hat{P}_1$. $U(|\vec{r}-\vec{R}_j|)$ is the potential of the jth ion core centered at $\vec{R}_j$. Following Hemstreet et al[16], we choose $U(r)$ to be of the form

$$U(|r-R_j|) = A_j r e^{-\alpha_j r} \qquad r \leq r_{cj}$$

$$\qquad\qquad\qquad = 0 \qquad\qquad r > r_{cj} \tag{2}$$

where A_j and α_j are to be treated as parameters and r_{cj} is the radius of the jth core. This form of $U(r)$ is chosen because it was found[16] to yield the best results in the non-local pseudopotential calculations of the band structure of diamond.

Our treatment of the non-local component of the pseudo-potential of cubic BN follows that of Hemstreet and Fong[6]. Specifically, we choose r_c for B and N to have an average value of 0.2 Å, the same as the free atom value of carbon. We set $A_{boron} = A_{nitrogen} = -0.16$ Ry so that the symmetric

non-local form factors of BN and diamond[16] are the same while the antisymmetric non-local form factors of BN vanish. Since the lattice constants of cubic BN and diamond are very nearly the same, the parameter α for BN is set equal to that of diamond[16], viz., 1.25 A^{-1}. The non-local parameters are treated in the approximate manner due to the lack of relevant experimental data on cubic BN. Hemstreet and Fong[6] chose the local symmetric form factors of cubic BN to be the same as those of diamond, and obtained the local antisymmetric form factors from those of BP by scaling the latter by the ratio of the volumes of the unit cells of the two crystals. While the former approximation seems to be reasonable, the latter approximation is perhaps too drastic. Lattice reflectivity measurements[17] indicate that BN is the most ionic of all the III-V compounds, while BP is the least ionic solid in this class. It is unlikely that the scaling procedure could wholly reflect this difference. In our calculation we obtain the local antisymmetric form factors of BN by taking the corresponding form factors for GaAs and scaling them by the ratio of the heteropolar energy gaps of the two crystals. Since the heteropolar energy gap is obtained by an averaging of the antisymmetric form factors over all the reciprocal lattice vectors, in the first approximation, the two quantities are directly proportional to each other[18]. Hence we believe our approximation for the antisymmetric form factors is a more reasonable one to start with. We obtain the local symmetric form factors of cubic BN by

scaling those of diamond by the ratio of the volumes of the unit cells of the two crystals.

In order to obtain the electronic density of states, we sample a uniform bcc mesh of 240 points in the irreducible wedge of the Brillouin zone, followed by linear interpolation, which generates eigenvalues and eigenfunctions of more than 100,000 $\vec{k}$-points in the Brillouin zone.

We next calculate the imaginary part of the dielectric constant, $\varepsilon_2(\omega)$, due to direct interband transitions. By time-dependent perturbation, one can show that[19]

$$\varepsilon_2(\omega) \sim \frac{1}{\omega^2} \sum_{c,v} \int \delta\{E_c(\vec{k}) - E_v(\vec{k}) - \hbar\omega\} M_{v,c}(\vec{k}) d\vec{k} \tag{3}$$

where

$$M_{v,c}(\vec{k}) = |<u_{\vec{k},v}|\nabla|u_{\vec{k},c}>|^2 \tag{4}$$

$u_{\vec{k},v}$ and $u_{\vec{k},c}$ are, respectively the periodic parts of the valence and conduction band wave functions.

The intensity of the soft X-ray emission at energy E is given by the formula[20]

$$I(E) = CE^2 \sum_v \int d\vec{k} \, M_{\alpha,v}(\vec{k}) \, \delta(E_{v\alpha}(\vec{k})-E) \tag{5}$$

In eq. (5), the sum is over all occupied valence states and

$$M_{\alpha,v}(\vec{k}) = |<\alpha|\vec{p}|v,\vec{k}>|^2 \tag{6}$$

is the squared momentum matrix element between the Bloch valence band state $|v,k>$ at wave vector $\vec{k}$ and a core state

$|\alpha>$, with energy difference $E_{v\alpha}(\vec{k})$. With $C = e^2 \Omega o/6c^3\hbar^2 m^2$, and Ωo equal to the volume of the unit cell, eq. (5) gives the total emitted intensity per core hole in the crystal. To evaluate $M_{\alpha,v}(\vec{k})$ given by eq. (6), we need the core wave functions of B and N and the true valence wave functions of the BN crystal. The former are taken from Hübner[21]. The latter are obtained by recalling that the true valence wave functions are related to the pseudo wavefunctions $|\Psi_{pseudo}>$ obtained in our EPM calculations, by[22]

$$|v,k> = |\Psi_{pseudo}> - \sum_{\alpha} |\alpha> <\alpha|\Psi_{pseudo}> \qquad (7)$$

where the summation is over all the core states $|\alpha>$ of the crystal. The energies of B and N cores in the crystal are assumed to be the same as the core energies of the isolated atoms as given in Ref. 23. Using eqs. (5 to 7), the K X-ray emission spectra of B and N in cubic BN are calculated.

III. RESULTS

The E-$\vec{k}$ diagram along several high symmetry directions is shown in Fig. 1. In Table 2, we compare some of the important energy gaps and the widths of the valence bands obtained in our calculation, with the results of other calculations and with available experimental data. In Fig. 2 the electronic density of states obtained in our calculation is compared with the result of the calculations of Nemoshkalenko and Aleshin[8]. The overall agreement is seen to be satisfactory, even though the peak positions differ by as much as

2.8 eV. The structure in the EDOS between 0 and 14 eV is due to the upper valence bands while that between 21 and 28 eV is due to the lower valence band. The two valence subbands are separated by about 7 eV in our result and by about 6 eV in the result of Nemoshkalenko and Aleshin[8]. In Fig. 3a the imaginary part of the dielectric constant $\varepsilon_2(\omega)$ is plotted as a function of energy. In Fig. 3b our $\varepsilon_2(\omega)$ is compared with that obtained in the calculation of Hemstreet and Fong[6] for the energy range 9 - 17 eV. The agreement between the two results is seen to be good. Our theoretical $\varepsilon_2(\omega)$ begins with a M_0 type transition at Γ_1, corresponding to the $\Gamma_{15,v} \rightarrow \Gamma_{1,c}$ energy gap of 8.8 eV. The peak at 11.3 eV is due to the transition $\Gamma_{15,v} \rightarrow \Gamma_{15,c}$ The main peak is at 13.7 eV and is due to the transition $X_{5,v} \rightarrow X_{3,c}$. This agrees reasonably well with the value of 14.5 eV reported by Philipp and Taft[9] for the peak in the reflectivity. It is worth mentioning that their measurement was crude, and that the peak in the reflectivity is generally 0.1 - 0.5 eV higher than the corresponding peak in $\varepsilon_2(\omega)$. The peak at 14.8 eV is due to the transition $L_{3,v} \rightarrow L_{3,c}$.

In Figures 4a and 4b, we compare the K X-ray emission spectra of B and N in cubic BN obtained in our calculation with the experimental result of Fomichev and Rumsh[11]. The agreement is seen to be good regarding both the shape of the spectra and the peak positions. The sharp maxima A and A' are due to transitions from the non-degenerate valence band,

while the principal maxima C and C' are due to transitions from the degenerate part of the valence band.

REFERENCES

*Supported by U.S. Air Force, under contract No. F19628-75-C-0163.

1. L. Kleinman and J. C. Phillips, Phys. Rev. $\underline{117}$, 460 (1960).

2. F. Bassani and M. Yoshimine, Phys. Rev. $\underline{130}$, 20 (1963).

3. M. L. Cohen and T. K. Bergstresser, Phys. Rev. $\underline{141}$, 789 (1966).

4. D. Stocker, Proc. Roy. Soc. (London) $\underline{A270}$, 397 (1962).

5. D. R. Wiff and R. Keown, J. Chem. Phys. $\underline{47}$, 3113 (1967).

6. L. A. Hemstreet and C. Y. Fong, Phys. Rev. B$\underline{6}$, 1464 (1972).

7. V. G. Aleshin and V. P. Smirnov, Soviet Physics Solid State, $\underline{11}$, 1621 (1970).

8. V. V. Nemoshkalenko and V. G. Aleshin, Soviet Physics Solid State, $\underline{12}$, 46 (1970).

9. H. R. Philipp and E. A. Taft, Phys. Rev. $\underline{127}$, 159 (1962).

10. P. J. Gielisse, Dept. of Chemical Engineering, University of Rhode Island, Kingston, R. I. (private communication).

11. V. A. Fomichev and M. A. Rumsh, J. Phys. Chem. Solids $\underline{29}$, 1015 (1968).

12. R. M. Chrenko, unpublished research, G.E. Research and Development Center (1971).

13. M. L. Cohen and V. Heine, Solid State Physics $\underline{24}$, 37 (Academic Press, New York, 1970).

14. M. J. G. Lee and L. M. Falicov, Proc. Roy. Soc. (London) $\underline{A304}$, 319 (1968).

15. C. Y. Fong and M. L. Cohen, Phys. Rev. $\underline{185}$, 1168 (1969).

16. L. A. Hemstreet, C. Y. Fong and M. L. Cohen, Phys. Rev. B2, 2054 (1970).

17. P. J. Gielisse, S. S. Mitra, J. N. Plendl, R. D. Griffis, L. C. Mansur, R. Marshall and E. A. Pascoe, Phys. Rev. 155, 1039 (1967).

18. J. A. VanVechten, Phys. Rev. 182, 891 (1969).

19. D. L. Greenaway and G. Harbeke, Optical Properties and Band Structure of Semiconductors, (Pergamon Press, New York, 1968), p. 36.

20. A. S. Davydov, Quantum Mechanics, (Pergamon Press, Oxford, 1965), p. 294-297.

21. K. Hübner, Phys. Stat. Sol. 38, K17 (1970).

22. V. Heine, Solid State Physics 24, 11 (Academic Press, New York, 1970).

23. J. A. Bearden, X-ray Wavelengths and X-ray Atomic Energy Levels, (National Bureau of Standards, Washington, D. C., 1967), p. 52.

FIGURE CAPTIONS

Fig. 1 E-$\vec{k}$ diagrams for cubic BN along three high symmetry directions.

Fig. 2 Electronic density of states of cubic BN. Dashed line is our result. Solid line is due to Nemoshkalenko and Aleshin (Ref. 8). The zero of the energy scale is chosen to be at the highest valence band at the zone center (Γ_{15}). The energy axis of Ref. 8 is accordingly shifted.

Fig. 3a Imaginary part of the dielectric constant $\varepsilon_2(\omega)$ obtained in our calculation plotted as a function of photon energy.

Fig. 3b Our result for $\varepsilon_2(\omega)$ (dashed curve) compared with that (solid curve) of Hemstreet and Fong (Ref. 6), for the energy range 9 - 17 eV.

Fig. 4a K X-ray emission spectrum of B in cubic BN. Solid line is our result. ----line is the experimental result of Fomichev and Rumsh (Ref. 11).

Fig. 4b K X-ray emission spectrum of N in cubic BN. Solid line is our result. ----line is the experimental result of Fomichev and Rumsh (Ref. 11).

TABLE 1

Pseudopotential parameters used in our calculation

$$V_L^s(3) \quad = \quad -0.755 \text{ Ry}$$

$$V_L^s(8) \quad = \quad 0.182 \text{ Ry}$$

$$V_L^s(11) \quad = \quad 0.133 \text{ Ry}$$

$$V_L^a(3) \quad = \quad 0.1755 \text{ Ry}$$

$$V_L^a(4) \quad = \quad 0.125 \text{ Ry}$$

$$V_L^a(11) \quad = \quad 0.0251 \text{ Ry}$$

$$r_{cB} = r_{cN} = 0.2 \text{ A}$$

$$A_s = \frac{A_B + A_N}{2} = -0.16 \text{ Ry}$$

$$A_a = \frac{A_B - A_N}{2} = 0.0 \text{ Ry}$$
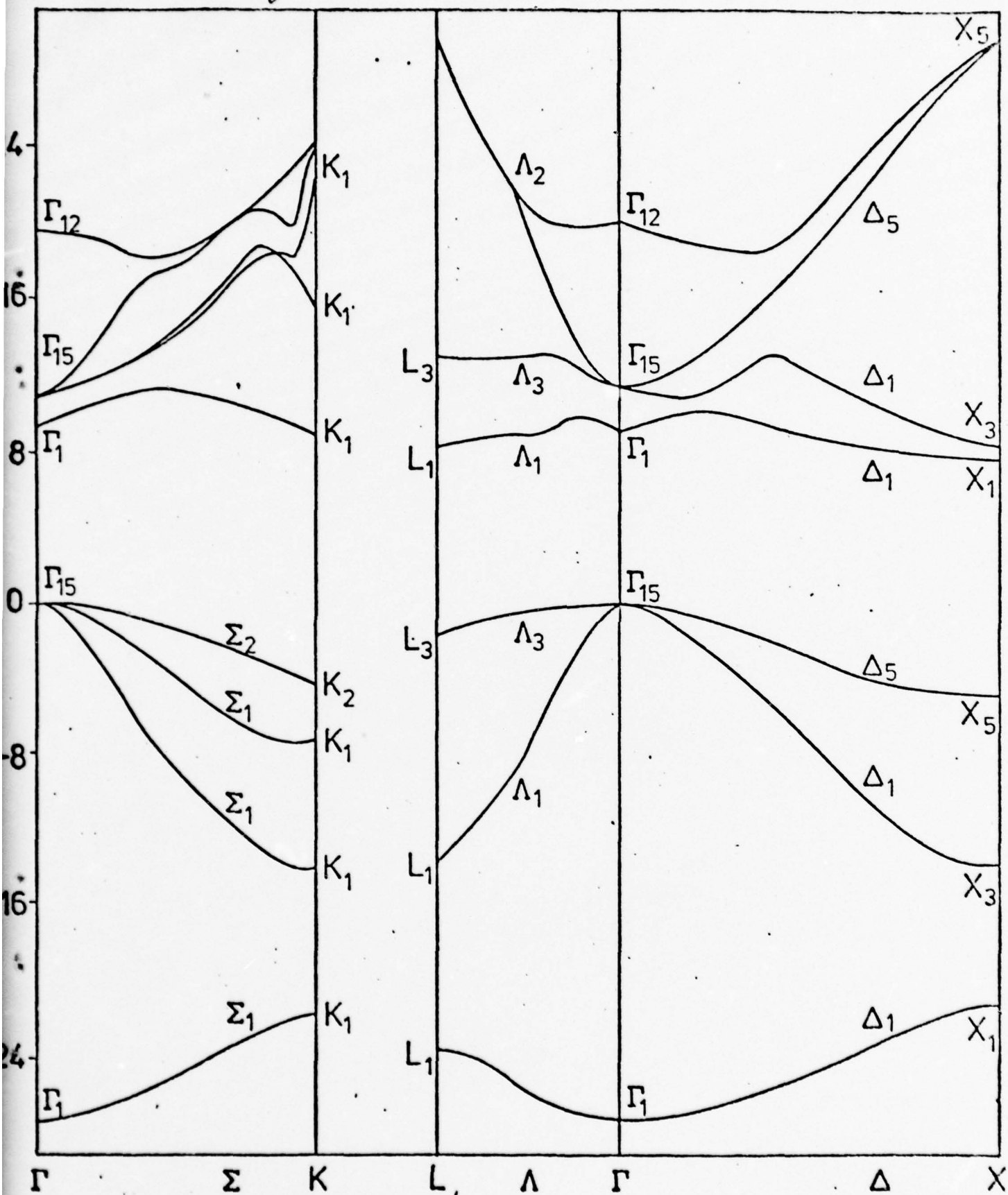
$$\alpha = 1.25 \text{ A}^{-1}$$

TABLE 2

Comparison of some important energy gaps and valence band widths obtained in different calculations and experiments. (All the energies are in eV's).

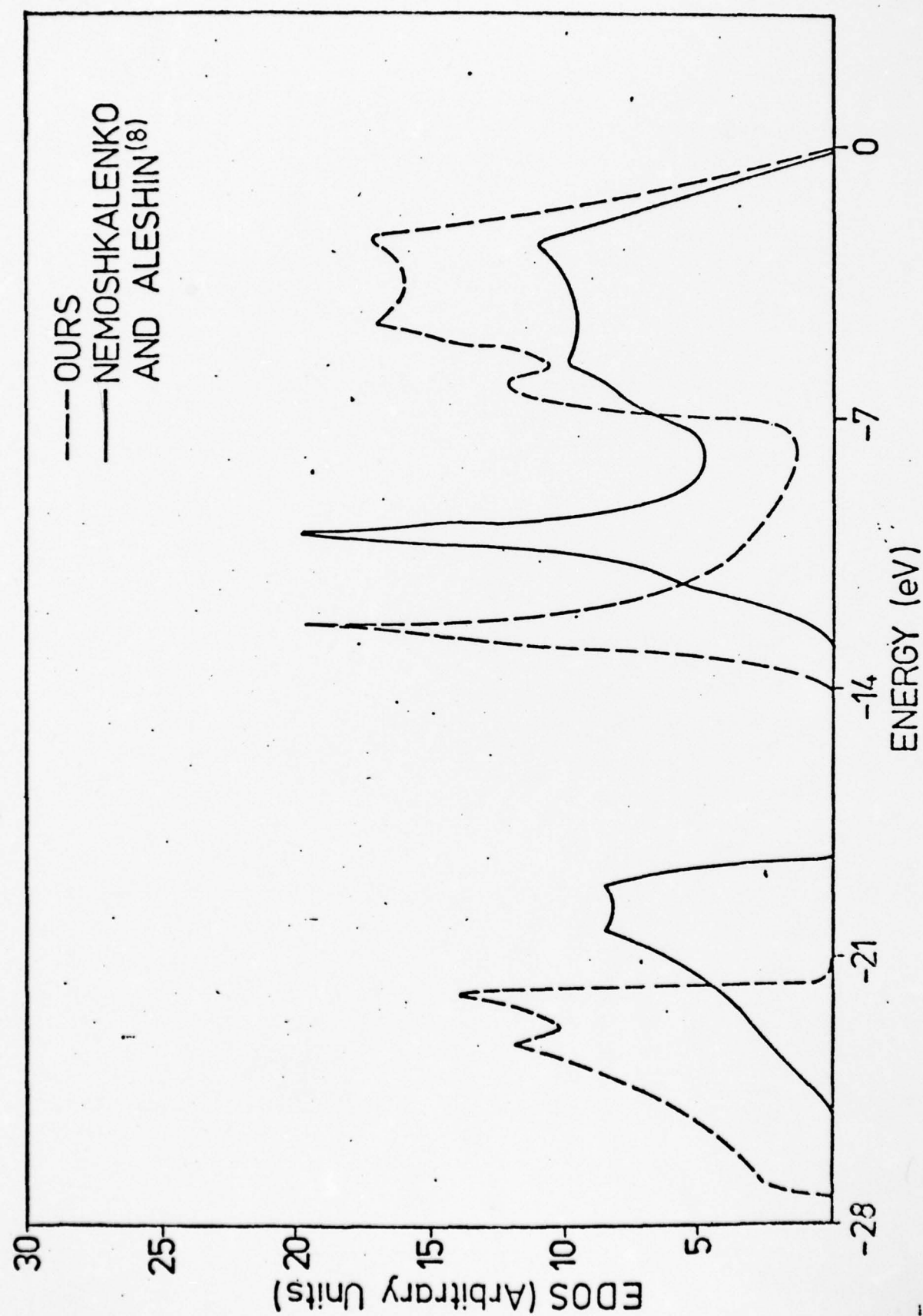| Author	$\Gamma_{15,v} \to$ $\Gamma_{1,c}$	$\Gamma_{15,v} \to$ $\Gamma_{15,c}$	$X_{5,v} \to$ $X_{1,c}$	$X_{5,v} \to$ $X_{3,c}$	$L_{3,v} \to$ $L_{1,c}$	$L_{3,v} \to$ $L_{3,c}$	$\Gamma_{15,v} \to$ $X_{1,c}$	$\Gamma_{15,v} \to$ $L_{1,c}$	Width of upper valence subbands	Full Width of all the valence bands
Theoretical										
Present calculation	8.8	11.3	13.2	13.7	10.0	14.8	8.0	8.0	14.0	27.36
Kleinman and Phillips[1]	19.99	14.28	13.33	14.68	14.42	15.37	10.47	13.06	3.54	17.95
Bassani and Yoshimine[2]	8.43	7.7	9.0	13.6	13.37	11.84	2.84	8.24	12.3	23.5
Wiff and Keown[5]	9.6	8.9	10.8	14.5	11.2	11.7	7.2	9.9	8.0	17.5
Hemstreet and Fong[6]	8.36	10.83	12.69	13.75	9.88	14.95	7.6	7.62	16.5	27.5
Nemoshkalenko and Aleshin[8]	----	----	----	----	----	----	----	----	~12.0	~24.0
Experimental										
Gielisse[10]			indirect gap ~7.0							
Fomichev and Rumsh[11]			indirect gap ≤6.0						≥15.4	≥22.0
Chrenko[12]			indirect gap ~7.0							

Footnote: The interband transition energies obtained in the calculations of Kleinman and Phillips[1] and Bassani and Yoshimine[2] as reported here are obtained from the original references and are different from the values quoted by Wiff and Keown[5] (we believe the latter to be incorrect). A value of 8.0 eV for an experimentally measured gap in Refs. 5 and 6 has been attributed to Gielisse[10]. However, discussions by the present authors with Giclisse indicated that his ultraviolet absorption data (unpublished) showed increased absorption close to 7 eV.
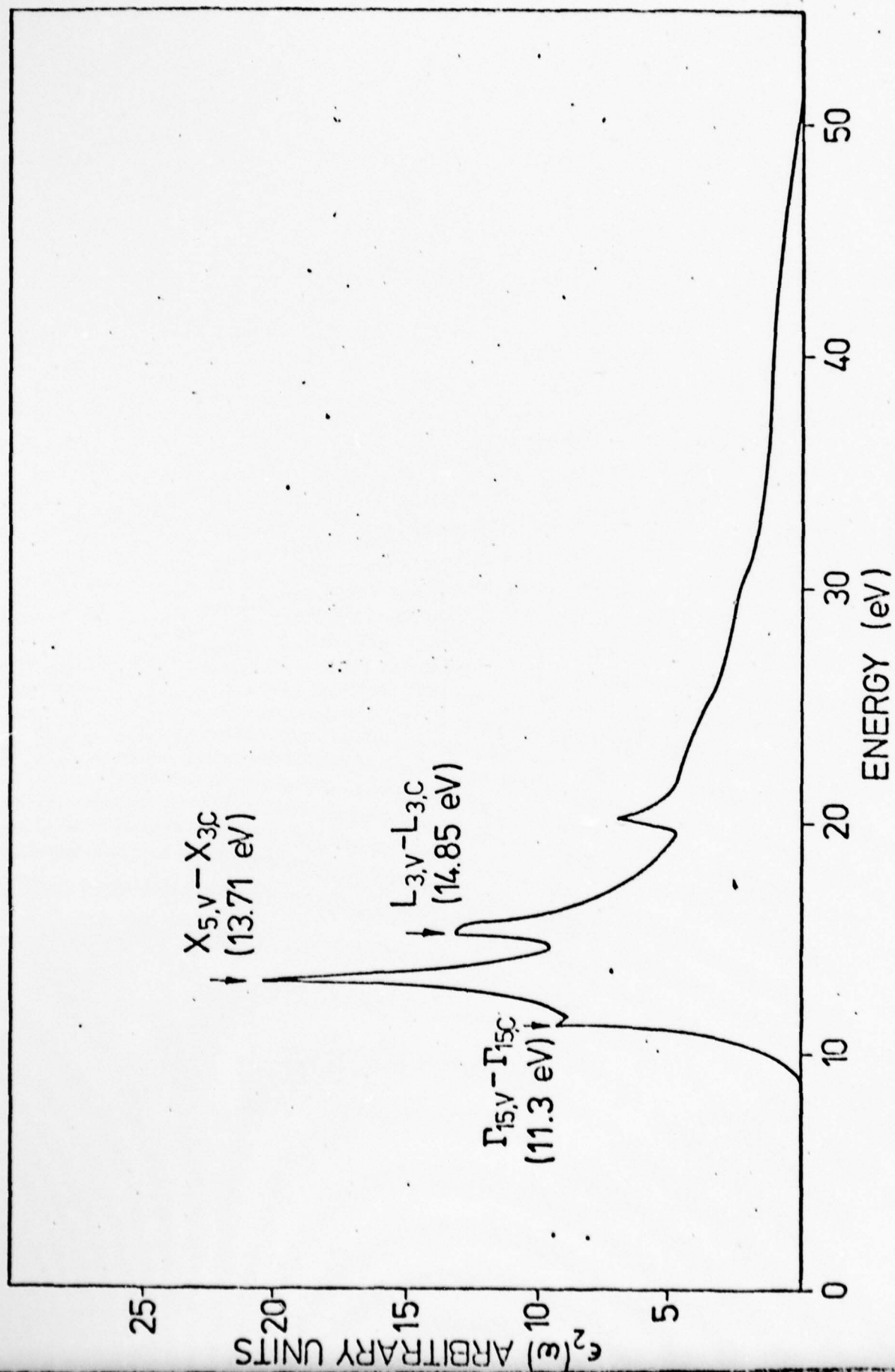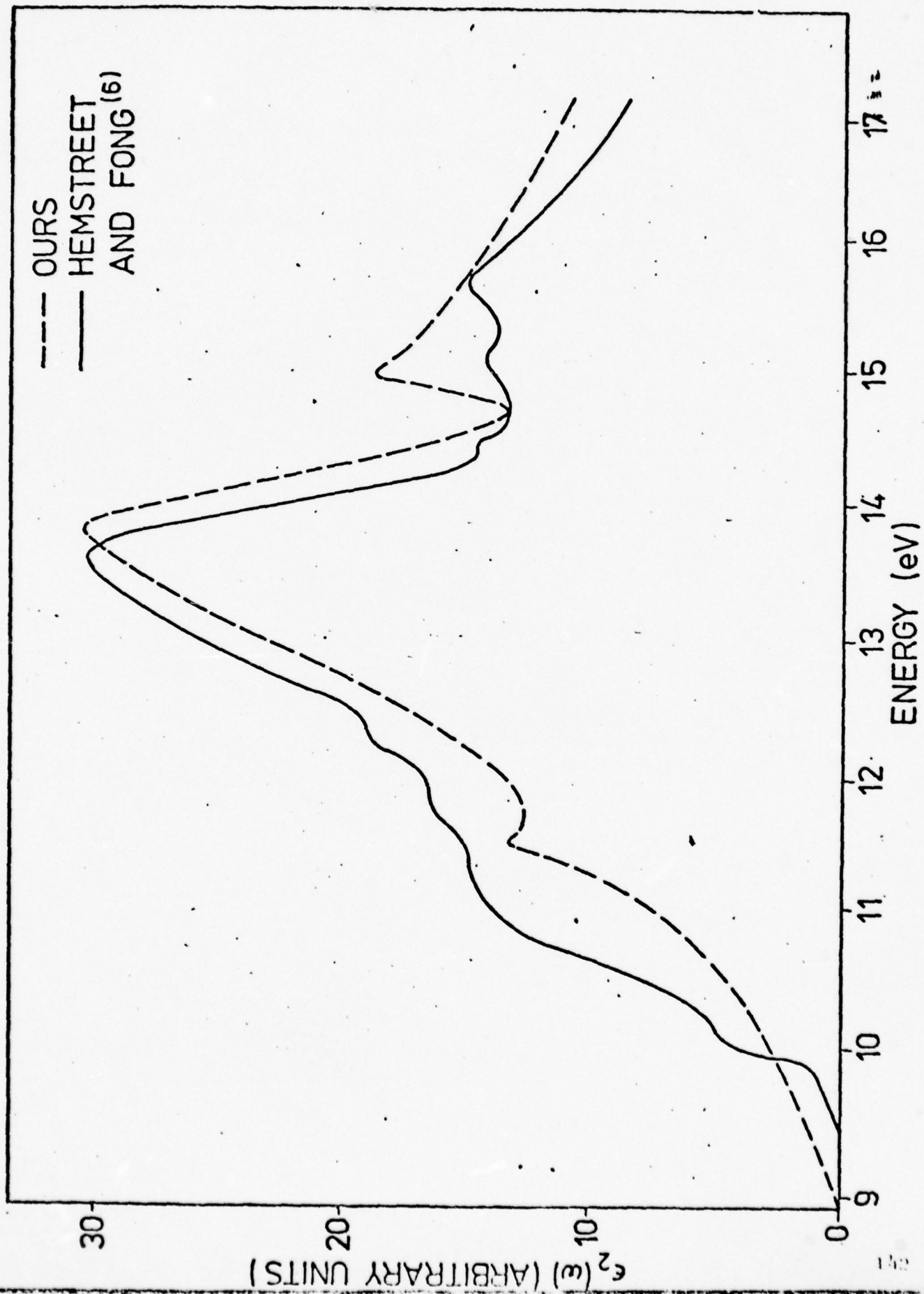
Kacy, et al Fig 13

Legend:
- - - OURS
——— NEMOSHKALENKO AND ALESHIN[8]

ENERGY (eV)

EDOS (Arbitrary Units)

Yang, et al. Fig 3a. Phys Rev B.

Kray, et al   Fig 36   Phys Rev 13

Tang, et al. Fig 4a

X RAY INTENSITY (ARBITRARY UNITS)

ENERGY (eV)

- - - Experimental[11]
—— Calculated

144
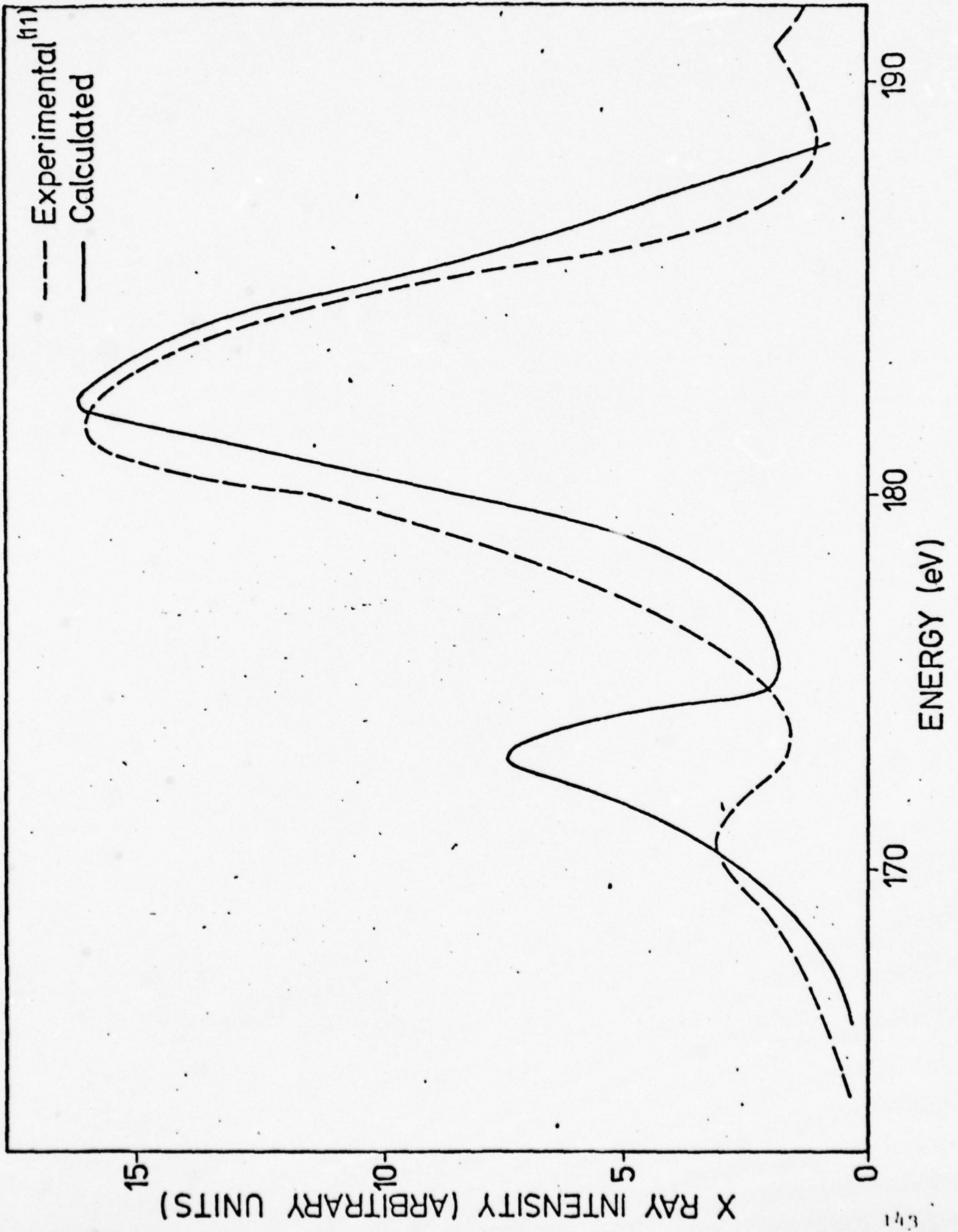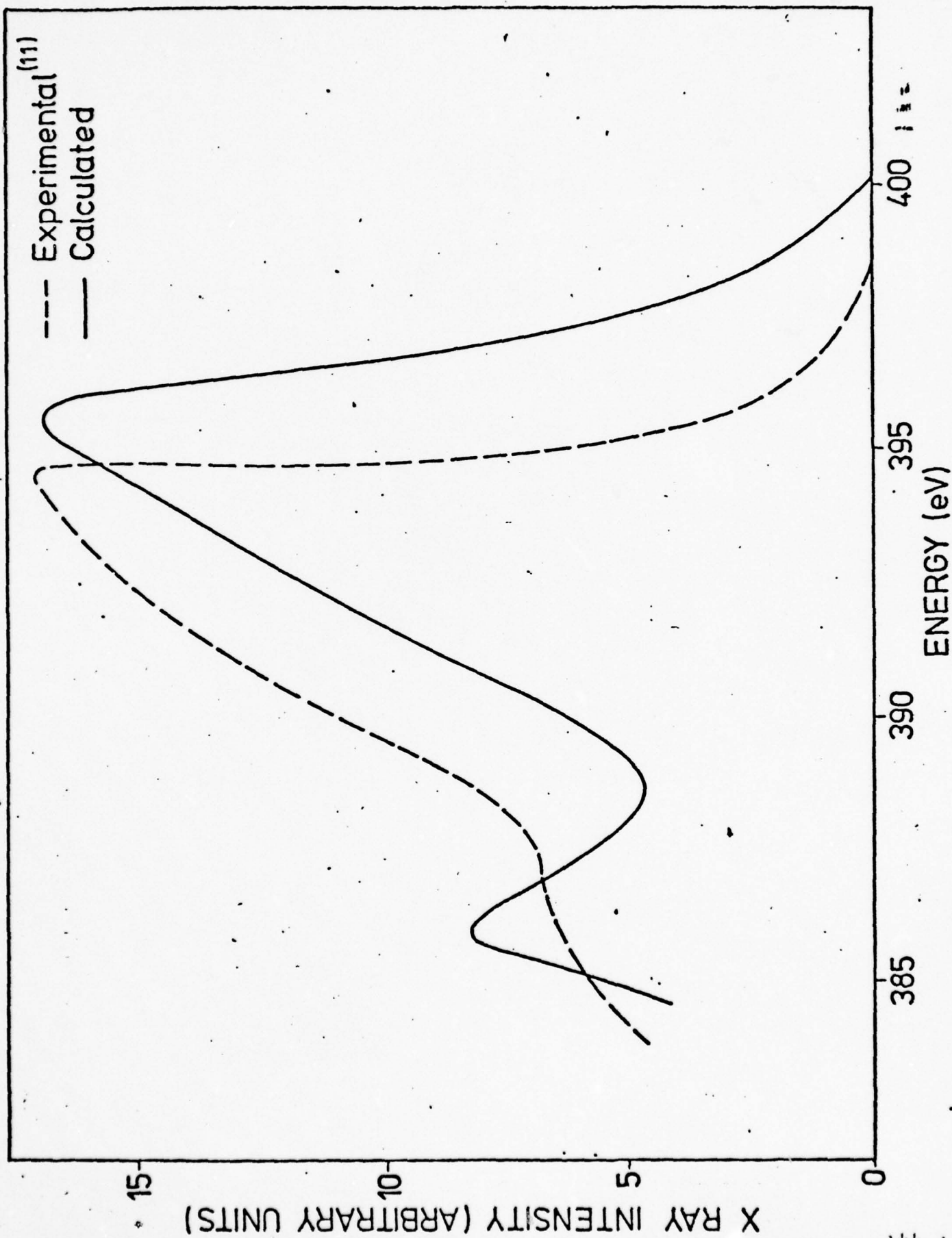
4.2 ELECTRONIC DENSITY OF STATES AND OPTICAL SPECTRUM OF TETRAHEDRALLY-BONDED AMORPHOUS III-V SEMICONDUCTORS[*]

Y. F. Tsay,[+] D. K. Paul[‡] and S. S. Mitra
Department of Electrical Engineering
University of Rhode Island
Kingston, Rhode Island 02881

Abstract

The disorder in an amorphous III-V semiconductor is described in terms of spatial variation in local density. The electronic density of states for the amorphous semiconductors are then simulated by a weighted sum of the crystalline electronic density of states (EDS) with a variation in local density. It is shown that the amorphous electronic density thus obtained is equivalent to its crystalline counterpart with the energy of each electronic state broadened by an individual broadening parameter, which is related to the degree of disorder of the amorphous semiconductor considered and the "sensitivity" of the energy of the particular state to variations in local density. The result of our phenomenological model is similar to that of Kramer's complex band structure calculation based on Green's function formalism. The optical spectra for the corresponding materials are also calculated using the theoretical EDS, along with the non-direct transition model with an energy dependent matrix element. The results are compared with available experimental data.

I. INTRODUCTION

Recent investigations on the physics of amorphous materials, particularly semiconductors, have generally focused on two related questions: Firstly, how different is the structure of an amorphous material as compared with its crystalline counterpart; and secondly, how are the electronic and vibrational properties of an amorphous material modified by such structural changes if the latter do exist. To find possible answers to the first question, numerous X-ray diffraction experiments[1] have been performed in order to determine the radial distribution function (RDF), which up to date provides the major experimental observable for a semi-quantitative description of the structure of an amorphous semiconductor. A comparison of the amorphous and crystalline RDF's of the same tetrahedrally bonded semiconductor indicates the following:

(i) The RDF's for both the crystalline and amorphous phases are very similar, at least, up to the second nearest neighbor (nn) distance, implying that, at least the short-range order is preserved in the amorphous phase.

(ii) The position of the first peak of the amorphous RDF appears to shift slightly toward higher values (a few percent) as compared with those of the crystalline peak.

(iii) The first and second peaks of the amorphous RDF are fairly well-defined, and are usually described, respectively, as a Gaussian of the form

$$\exp\left[-\frac{(r-r_{ia})^2}{2\sigma_{ia}^2} \right], \quad i = 1, \text{ or } 2 \tag{1}$$

where r_{ia} and σ_{ia} denote the position and the width, respectively.

Table I lists the relevant structural parameters of the amorphous (subscript a) semiconductors of interest. Corresponding crystalline (subscript c) values are also given for comparison. It appears that in general the width of a peak in the amorphous RDF is consistently larger than that in the crystalline phase. This is particularly true for the second peak of the RDF. The difference, which presumably may result from the structural distortions of bond lengths and/or angles, as well as wrong bond formation, is the static width (or spread) and is given as

$$\sigma_i^2 = \sigma_{ia}^2 - \sigma_{iT}^2 \approx \sigma_{ia}^2 - \sigma_{ic}^2, \quad i = 1,2. \tag{2}$$

Here it is assumed that the thermal width, σ_{iT}, of a peak in the amorphous phase is equal to the width in the crystalline phase, as the latter does not have a static width.

It must be pointed out, that the RDF may not uniquely determine the microscopic structure of an amorphous material. For instance, in the case of Si and Ge, both the continuous random network (CRN) model and the microcrytallite model[2] which consists of a mixture of microcrystallites with various crystalline structures, are capable of giving RDF's in close agreement with the experimental results. Although the CRN

model for amorphous Si and Ge seems to be favored, it is not clear, however, that the same is true for amorphous III-V compounds.

Because of the loss of the long range order, many theoretical works on the electronic and vibrational properties of amorphous materials have stressed the importance of the breakdown of the $\underset{\sim}{k}$-selection rule. This results in the belief that in the calculation of the electronic[3] and vibrational[4] properties of an amorphous material, use should be made of the aspects of its structure which is independent of the $\underset{\sim}{k}$-selection rules, and therefore requires an approach that is distinctly different from that used for the crystalline phase.

Recently, we have questioned the sole importance of the breakdown of the $\underset{\sim}{k}$-selection rule in explaining the basic optical properties of amorphous semiconductors. We have demonstrated[5] that the first order infrared and Raman spectra of a tetrahedrally bonded amorphous semiconductor (TBAS) can be interpreted as consisting primarily of a crystalline-like spectrum, whenever the optical process concerned is allowed in the crystalline phase. The residual difference is then interpreted as that arising from configurations in which only short range order is maintained. It is our contention that the electronic structure of a TBAS can also be calculated using its crystalline analog as a starting point, but with certain modifications to take account of the structural disorders.

Thoro aro soyoral previous calculations of the electronic structure of TBAS based on the same philosophy. Herman and Van Dyke[6] simulated the electronic density of states (EDS) of amorphous Ge by that of a dilated (an overall expansion of the lattice constant by $10^{\circ}/o$) Ge crystal. In order to calculate the imaginary part of the corresponding dielectric constant, they adopted the non-direct transition (NDT) model with constant matrix elements. Brust, on the other hand, calculated[7] the ε_2-spectrum of a crystalline Ge with density equal to that of the amorphous phase. A substantial red shift of the spectrum was obtained, in agreement with the experimental observation[8]. However, in order to produce the single humped structure of the experimental ε_2-spectrum, a life-time broadening of the order of 2 eV had to be used, which is about ten times as large as the crystalline value. Kramer et al[9] using the Green's function formalism, have developed a method for calculating the electronic energy spectrum of a disordered system. By approximating the n-body spatial correlation function as products of two-body correlation functions, they obtained a complex band structure (CBS) for several TBAS. The electronic energy states with the reduced wave vector $\underset{\sim}{k}$, which in the case of crystalline solids consist of a set of δ-functions, are now broadened into damped Lorentzians, the widths of which depends on $\underset{\sim}{k}$, as well as the two-body correlation function. The latter, in turn, reflects the structural disorders in amorphous solids. According to the CBS results,

the valence band density of states (VBDS) is relatively less distrubed by disorder, and retains most of the features of its crystalline counterpart. The conduction band density of states (CBDS), on the other hand, is profoundly changed, and is devoid of crystalline features.

In a previous paper[10], we obtained the EDS of amorphous Si and Ge by calculating the weighted average of the densities of states of the corresponding crystal with slightly different nn distances. The weighting function is taken to be a Gaussian. In the present paper the EDS for several amorphous III-V compounds will be calculated following a similar approach. However, for reasons to become apparent below, the averaging is taken over local density distributions. The ε_2-spectrum will also be calculated using the EDS obtained in this paper, together with the NDT model[11] with energy dependent transition matrix elements[12].

II. LOCAL DENSITY AND ITS DISTRIBUTION IN AN AMORPHOUS TBAS

Material inhomogeneity, voids, local strains, bond length and bond angle variations[13] are known to exist in most amorphous semiconductor films. As a consequence, the local density in the material is not expected to be uniform. By local density we mean the number of atoms per unit volume averaged over a volume whose linear dimensions are of the order of several multiples of the bond length. As mentioned above, the static spread in the first and second peak of the RDF of a TBAS, may by themselves result in a spatial fluctuation of the local density. A quantitative analysis of

the spatial variation of local density, including inhomogeneity, void structure, local strains, as well as bond length and angle distortions, is a formidable task. However, if one assumes that the local density variation results principally from the spreads of the first and second nn distances then a distribution in local density can be estimated, in the following way: First a reasonable definition[14] for local density in terms of the first and the second nn distances, r_1 and r_2 is made:

$$\rho(r_1, r_2) = 3\sqrt{3/8}\ (1/r_1^3 + C\frac{K^3 - 1}{r_2^3 - r_1^3})/(1+C) \tag{3}$$

where $K = r_{2a}/r_{1a}$ and C is a weighting factor determining the relative importance of the second nn's in contributing to the local density. The rationale for such a definition is discussed in detail elsewhere[14]. In order to calculate the distribution of the local density, a deviation of $r_1(r_2)$ by about $\sigma_1(\sigma_2)$ from its mean value $r_{1a}(r_{2a})$ is considered. If it is assumed that for these ranges of r_1 and r_2, their respective probability distributions are independent, then their joint probability distribution is given by

$$P(r_1, r_2) \propto \exp\{-0.5[(\frac{r_1 - r_{1a}}{\sigma_1})^2 + (\frac{r_2 - r_{2a}}{\sigma_2})^2]\} \tag{4}$$

In eq. (4), σ_1 and σ_2, are respectively the _static_ spread of the first and the second peaks in the amorphous RDF, as given in Table I. From eqs. (3) and (4), the local density distri-

151

bution of amorphous Ge, and its dependence on σ_2 and C, respectively. Results for III-V compounds are similar. It is seen that, except for a slight asymmetry, the local density distribution is approximately Gaussian. We point out, however, that the approach outlined above should be regarded as only a preliminary attempt to calculate the local density distribution. It is believed, however, that although the peak position and width may not be accurately predicted, as there is no physical guidance to fix the value of C, the general shape of the local density distribution may be correct. Therefore, before a better method for calculating the local density distribution, including bond and dihedral angles, becomes available, one may for practical purposes, take it as a Gaussian of the following form:

$$P(\rho) = \exp\left[-\frac{(\rho - \rho_a)^2}{2\sigma_\rho^2}\right] \tag{5}$$

with the mean, ρ_a, and the variance, σ_ρ, as adjustable parameters.

In this work ρ_a and σ_ρ have been obtained in two different ways. Firstly, $P(\rho)$ is determined from eqs. (3) and (4) with $C = 0.375$. Secondly, these two quantities are used as adjustable parameters in eq. (5) in fitting[15] the main features of infrared and/or Raman spectra of TBAS[5]. The values of ρ_a and σ_ρ obtained by these two methods along with the experimental values[16] of ρ_a are compared in Table I. In general the agreement is remarkably good.

III. CALCULATION OF ELECTRONIC DENSITY OF STATES

In analogy with the point of view adopted for interpreting the lattice spectra of a TBAS, as discussed in the last section, we make the following assumption that

$$N_a(E) \approx \int N_c(E,\rho) \exp\left[- \frac{(\rho-\rho_a)^2}{2\sigma_\rho^2} \right] d\rho \tag{6}$$

where $N_a(E)$ stands for the electronic density of states at energy E of a TBAS. $N_c(E,\rho)$ is the corresponding crystalline density of states for the local density ρ. The above assumption amounts to neglecting the contribution arising from highly disordered structural configurations. Next, if $N_c(E,\rho)$ is written as

$$N_c(E,\rho) = \sum_n \sum_k \delta(E-E_{n,k}(\rho)) \tag{7}$$

then

$$N_a(E) \approx \sum_n \sum_k \int \delta(E-E_{n,k}(\rho)) \exp\left[- \frac{(\rho-\rho_a)^2}{2\sigma_\rho^2} \right] d\rho \tag{8}$$

In the last two equations, the subscript, k, should not be regarded as carrying the usual meaning of wave vector, which is a good quantum number for an electronic state in a perfect crystal. Instead it is just an index by which electronic states are enumerated.

In general, we expect the local density distribution to be sharply peaked around its mean value, ρ_a. Therefore most contribution to the integral in eq. (8) comes from ρ, for

which $|\rho - \rho_a| \sim \sigma_\rho \ll \rho_a$; in this range of ρ, $E_{n,k}(\rho)$ can be expanded as

$$E_{n,k}(\rho) = E_{n,k}(\rho_a) + \gamma_{n,k}(\rho - \rho_a) + \ldots \qquad (9)$$

where

$$\gamma_{n,k} \equiv \partial(E_{n,k}(\rho))/\partial\rho \Big|_{\rho = \rho_a} \qquad (10)$$

Eq. (8) can then be rewritten as

$$N_a(E) \propto \sum_{n,k} \frac{1}{\gamma_{n,k}} \exp\left[-\frac{(E - E_{n,k}(\rho_a))^2}{2\sigma_{n,k}^2}\right] \qquad (11)$$

where

$$\sigma_{n,k} \equiv \gamma_{n,k}\sigma_\rho \qquad (12)$$

It is seen therefore, that the δ-functions in eq. (7) for the crystalline phase are now replaced by a series of Gaussians. The width of the Gaussian is given by $\sigma_{n,k}$, which is the product of the density spread parameter, σ_ρ, and $\gamma_{n,k}$, the derivative of the electronic energy $E_{n,k}$ with respect to the local density.

To calculate $\gamma_{n,k}$ use can be made of the following equation.

$$\gamma_{n,k} \equiv \partial E_{n,k}/\partial\rho \Big|_{\rho = \rho_a} = \frac{1}{\rho_a K} \partial E_{n,k}/\partial P \Big|_{P = P_a} \qquad (13)$$

provided the pressure (P) coefficient of $E_{n,k}$ is known. In eq. (13), K is the isothermal compressibility. The problem

154

then reduces to finding $\partial E_{n,k}/\partial P$. This latter quantity can, in principle, be estimated from high pressure data. Unfortunately, most experimental data are related to the pressure coefficients of a few optical transitions, which actually consists of the relative pressure induced shifts of the energy levels of the initial and final states. We therefore resort to a pressure-dependent band structure calculation[17]. Specifically, the calculation uses only the compressibility and the empirical pseudopotential form factors appropriate for describing the crystalline band structure at normal pressure as input data. The predicted pressure coefficients at several critical point band gaps are in good agreement with the available experimental data in the cases of elemental and III-V compound semiconductors. In the above-mentioned calculation, it is assumed, as in most previous calculations[18], that the energy of the top valence states (Γ_{15} in the zinc blende type, and Γ_{25} in the diamond type crystals) does not change with pressure, since it is only the relative shifts of the initial and final states defining the band gap (optical transition) that are of interest. We believe that such a method is also adequate for estimating the pressure shift of $E_{n,k}$'s, provided that the pressure coefficient of the energy, $E(\Gamma_{15})$, of the top valence states is known. The pressure coefficient $dE(\Gamma_{15})/dP$, in fact, can be obtained from the appropriate volume deformation potential, which occurs in the theory of electron-phonon interaction. Unfortunately, experimental values of $dE(\Gamma_{15})/dP$ are scarce

and somewhat controversial. For example, Herring and Vogt[19] gave a value of -3.6×10^{-6} eV/bar for Ge, based on transport properties of the crystal. Whereas Bagguley et al[20] from cyclotron resonance measurement, estimated the value to be $\sim +4 \times 10^{-6}$ eV/bar, which agrees, in sign, with the theoretical prediction of Kleinman[21] for Si. To our knowledge, no appropriate values exist for III-V semiconductors. In the present work, we shall assume that the shift of the topmost valence state, with pressure is negligible, i.e., $dE(\Gamma_{15})/dP \approx 0$. The final results of the calculation, however, do not depend sensitively on the exact value of $dE(\Gamma_{15})/dP$, as long as its absolute value remains small, which seems to be the case.

In actual calculation, whenever available, use has been made of the modified pseudopotential form factors due to Chelikowsky et al[22], which agree well with the energy of the low-lying valence bands recently determined from X-ray photoemission data[23a,b]. The effect of mean density deficiency in the amorphous state as compared with its crystalline counterpart is accounted for in an approximate way by scaling the pseudopotential form factors according to density, as was previously done by Brust[7].

To obtain the EDS, we calculate $E_{n,k}(\rho_o)$ and $\gamma_{n,k}$ at 1500 different $\underline{k}$ values in the Brillouin zone. A linear interpolation is then used to sample a finer $\underline{k}$-mesh of about a quarter million points in order to suppress the statistical "noise" in the histogram. The sampling procedure

is capable of generating the crystalline EDS in excellent

agreement in details of fine spectral features with those

obtained recently by Chelikowsky et al[22].

The imaginary part of the dielectric constant, $\varepsilon_2(\omega)$,

in the one-electron approximation may be written as

$$\varepsilon_{2,a} \sim \frac{1}{\omega^2} \, |M(\omega)|_a^2 \, N_{conv.}(\omega) \tag{15}$$

where $|M(\omega)|_a^2$ is the amorphous matrix element and $N_{conv}(\omega)$

is the convoluted densities of states of the valence and

conduction bands for which energy is conserved. $|M(\omega)|_a^2$

is obtained from that of the crystalline phase by smoothing

the unklapp peak[24], which often originates from long range

order.

IV. RESULTS AND DISCUSSIONS

Fig. 2(a) shows the crystalline E-$\underset{\sim}{k}$ diagram (full line)

along the [100] and [111] directions. The bars indicate

the relative magnitude of $Y_{n,k}$. GaP is taken as an illus-

trative example. Results for other materials considered in

this paper are similar. It is observed that the conduction

states, in general, have larger $Y_{n,k}$ than the valence states.

This, of course, is expected because the conduction band

wave functions are extended in space and therefore are more

sensitive to the change of the local atomic volume due to

the local density fluctuation. The calculated crystalline

density of states for GaP is shown in Fig. 2(b).

Figure 3 shows the calculated EDS for GaP with various values of the "disorder parameter", σ_ρ/ρ_a. Curve A of Fig. 3 is the least disordered. The VBDS is essentially the same as its crystalline counterpart except for some smoothing-out of the fine structures in the upper most valence band. The CBDS, on the other hand, has already shown substantial departure from the crystalline density of states although the broad profiles remain. For Curves B and C, the values of σ_ρ/ρ_a are 0.13 and 0.20, respectively. The changes in the VBDS and CBDS with the degree of disorder are clearly shown by the trend manifested by these curves. Several points are particularly worth mentioning: (i) the widths of peaks of the VBDS are very little affected by disorder except for the tailing of density of states into the crystalline gaps, (ii) higher degrees of disorder produce larger tailings. This is particularly significant regarding the crystalline optical gap, as is vividly shown in Fig. 3. (iii) for higher degrees of disorder, e.g., Curves B and C in Fig. 3, the structures in the crystalline density of states have all but disappeared, and in its place, is a single hump followed by a flat plateau. Similar single-hump CBDS has recently been reported by Eastman et al[25] for amorphous Ge, which is significantly different from the totally flat CBDS previously deduced by Donovan et al[26] from ultraviolet photoemission data. Although no experimental data on the CBDS of III-V amorphous semiconductors are available at the present, such a one-hump structure for amorphous III-V compounds

is highly possible, because of the similarity of their electronic structures to that of Ge. Fig. 4 shows the EDS for the other amorphous solids considered in the present paper. In all cases, the changes due to disorder in the VBDS are much less significant as compared with the corresponding changes in the CBDS. The VBDS for several crystalline[23a,b] and amorphous[23a] III-V and II-VI semiconductors have been determined by Shevchik et al from X-ray photoemission experiment. They concluded that the VBDS of an amorphous compound is essentially a broadened version of its crystalline counterpart. The results of the present calculation indicate the same, although the extent of broadening is not significant except in the tailing parts of VBDS. However, we would like to point out that in the experimental results of Shevchik et al, the crystalline VBDS themselves are also greatly broadened when compared with theoretically calculated VBDS. We feel that since the amorphous VBDS are determined by the same experimental setup, a significant part of their broadening might have the same origin as their crystal counterpart and therefore does not result from the effects of disorder.

The imaginary part of the dielectric constant $\varepsilon_2(\omega)$ for the amorphous III-V compounds as obtained from the present calculated density of states are compared in Figs. 5(a) to 5(d) with those of Kramer et al[9] and experimental data[16]. The energy dependence of the matrix elements (shown

as inserts in Figs. 5(a) to 5(d)) gives better agreement.
The agreement between the calculated and experimental $\varepsilon_2(\omega)$
is quite good for GaAs, GaP and InAs. For GaSb, the calcu-
lated result is less satisfactory, in that the predicted
peak position of $\varepsilon_2(\omega)$ is shifted from that of experimental
data by more than 1 eV. The shape of $\varepsilon_2(\omega)$ curve, however,
is fairly well predicted. Presumably the calculated peak
position can be shifted to coincide with the experimental
one by using a different energy dependent matrix element
or by using a significantly different value of ρ_a, which
would reduce the "pseudo" optical band gap, so as to cause
stronger absorption at lower energies, i.e., a red shift of
the absorption peak to lower energies.

REFERENCES

1. See for example, N. J. Shevchik and W. Paul, J. Non-Crystalline Solids 13, 1 (1974) and references therein.

2. G. P. Betteridge, J. Phys. C., 6, L427 (1973).

3. See for example, D. Weaire and M. Thorpe, Phys. Rev. B 4, 2508 (1971); M. F. Thorpe and D. Weaire, Phys. Rev. B 4, 3518 (1971); B. Y. Tong, pp. 145, AIP Conf. Proc. No. 20, "Tetrahedrally Bonded Amorphous Semiconductors", M. H. Brodsky et al, Eds., AIP (1974).

4. See for example, R. Alben, pp. 249, AIP Conf. Proc. No. 20, "Tetrahedrally Bonded Amorphous Semiconductors", M. H. Brodsky, et al, Eds., AIP (1974).

5. S. S. Mitra, D. K. Paul, Y. F. Tsay and B. Bendow, pp. 284, AIP Conf. Proc. No. 20, "Tetrahedrally Bonded Amorphous Semiconductors", M. H. Brodsky, et al, Eds., AIP (1974); Phys. Stat. Solidi (b), 72, 475 (1975); Proc. Third International Conference on Light Scattering in Solids, p. 646, ed. by M. Balkanski, et al, Flammarion, Paris (1976).

6. F. Herman and J. P. Van Dyke, Phys. Rev. Letters, 21, 1575 (1968).

7. D. Brust, Phys. Rev. 186, 768 (1969) and Phys. Rev. Letters 23, 1232 (1969).

8. T. M. Donovan, W. E. Spicer and J. M. Bennett, Phys. Rev. Letters 22, 1058 (1969).

9. B. Kramer, K. Maschke and P. Thomas, Phys. Stat. Sol. (b) 48, 635 (1971).

10. Y. F. Tsay, D. K. Paul and S. S. Mitra, Phys. Rev. B **8**, 2827 (1973).

11. J. Tauc, Mater. Res. Bull., **3**, 37 (1968); also in "Optical Properties of Solids", edited by S. Nudelman and S. S. Mitra (Plenum Pub., N. Y., 1969), p. 123.

12. K. Maschke and P. Thomas, Phys. Stat. Sol. **41**, 743 (1970).

13. See for example N. J. Shevchik and W. Paul, J. of Non-Crystalline Solids **16**, 55 (1974).

14. J. F. Vetelino and S. S. Mitra, in "Physics of Structurally Disordered Solids", edited by S. S. Mitra (Plenum Pub., N.Y., 1976), in press.

15. Y. F. Tsay, B. Bendow and S. S. Mitra, J. Electronic Materials, **5**, 995 (1975).

16. J. Stuke and G. Zimmerer, Phys. Stat. Sol. B **49**, 513 (1972).

17. Y. F. Tsay, S. S. Mitra and B. Bendow, Phys. Rev. B **10**, 1476 (1974).

18. See references given in Ref. 17.

19. C. Herring and E. Vogt, Phys. Rev. **101**, 941 (1956).

20. D. M. S. Bagguley, D. W. Flaxen and R. A. Stradling, Phys. Rev. Letters, **1**, 111 (1962).

21. L. Kleinman, Phys. Rev. **130**, 2283 (1963).

22. J. Chelikowsky, D. J. Chadi and M. L. Cohen, Phys. Rev. B **8**, 2786 (1973).

23a. N. J. Shevchik, J. Tejeda and M. Cardona, Phys. Rev. B **9**, 2627 (1974).

23b. D. E. Eastman, W. D. Grobman, J. L. Freeouf and M. Erbudak, Phys. Rev. B 2, 3473 (1974).

24. J. C. Phillips, Solid State Physics, edited by H. Ehrenreich, F. Seitz and D. Turnbull (Academic Press, N. Y., 1966), Vol. 18, p. 55.

25. D. E. Eastman, J. L. Freeouf and M. Erbudak, pp. 95, AIP Conf. Proc. No. 20, "Tetrahedrally Bonded Amorphous Semiconductors", M. H. Brodsky, et al, Eds., AIP (1974).

26. T. M. Donovan and W. E. Spicer, Phys. Rev. Letters 21, 1572 (1968); Phys. Rev. B 2, 397 (1970).

TABLE I

Relevant Structural Parameters for Amorphous III-V Semiconductors

	GaAs	GaP	GaSb	InAs
$r_{1c}(\text{Å})$	2.45	2.36	2.65	2.63
$r_{1a}(\text{Å})^*$	2.48±0.03	2.44±0.1	2.67±0.03	2.69
$\sigma_{1c}(\text{Å})^*$	0.085	0.015	0.079	0.075
$\sigma_{1a}(\text{Å})^*$	0.085±0.01	0.18±0.01	0.14±0.01	0.09±0.01
$\sigma_1(\text{Å})^+$	~0.0	~0.16	~0.12	~0.05
$r_{2c}(\text{Å})$	4.0	3.86	4.33	4.3
$r_{2a}(\text{Å})^*$	4.1±0.05	3.9±0.05	4.3±0.05	4.0±0.05
$\sigma_{2c}(\text{Å})^*$	0.109	0.1	0.105	0.114
$\sigma_{2a}(\text{Å})^*$	0.3±0.05	0.35±0.05	0.4±0.05	0.3±0.05
$\sigma_2(\text{Å})^+$	~0.28	~0.34	~0.39	~0.28
ρ_a/ρ_c				
Calcd. eqs.(3) and (4)	0.92	0.90	0.81	0.77
eq.(5)++	0.96	0.89	0.87	0.91
exptal.**	0.96	0.90	0.98	0.93

FIGURE CAPTIONS

Fig. 1   (a) The distribution of local density for various
           values of σ_2 (see text).
           (b) The distribution of local density for various
           values of C (see text).

Fig. 2   (a) E-$\vec{k}$ diagram of crystalline GaP along the
           [100] and [111] directions. The vertical bars
           indicate the relative magnitude of $\gamma_{n,k}$.
           (b) The electronic density of states of crystal-
           line GaP.

Fig. 3   The calculated electronic density of states of
           amorphous GaP with various values of disorder
           parameter, σ_ρ/ρ_a. Curve A: $\sigma_\rho/\rho_a = 0.05$;
           Curve B: $\sigma_\rho/\rho_a = 0.13$; Curve C: $\sigma_\rho/\rho_a = 0.20$.

Fig. 4   The calculated electronic density of states for
           amorphous GaAs, GaSb and InAs. σ_ρ/ρ_a values used
           for these curves are those obtained from the fit-
           ting of first order infrared and Raman spectra
           (see Table I).

Fig. 5   The imaginary part of the dielectric constant
           versus photon energy for amorphous III-V compounds.
           (a) GaP: Curve 1 - experimental (Ref. 16);
           Curve 2 - calculated by Kramer et al (Ref. 9);
           Curve 3 - calculated in this paper using EDS with
           $\sigma_\rho/\rho_a = 0.13$; Curve 4 - calculated in this paper
           using EDS with $\sigma_\rho/\rho_a = 0.20$; Curve 5 - calculated
           using EDS with $\sigma_\rho/\rho_a = 0.13$ and with constant
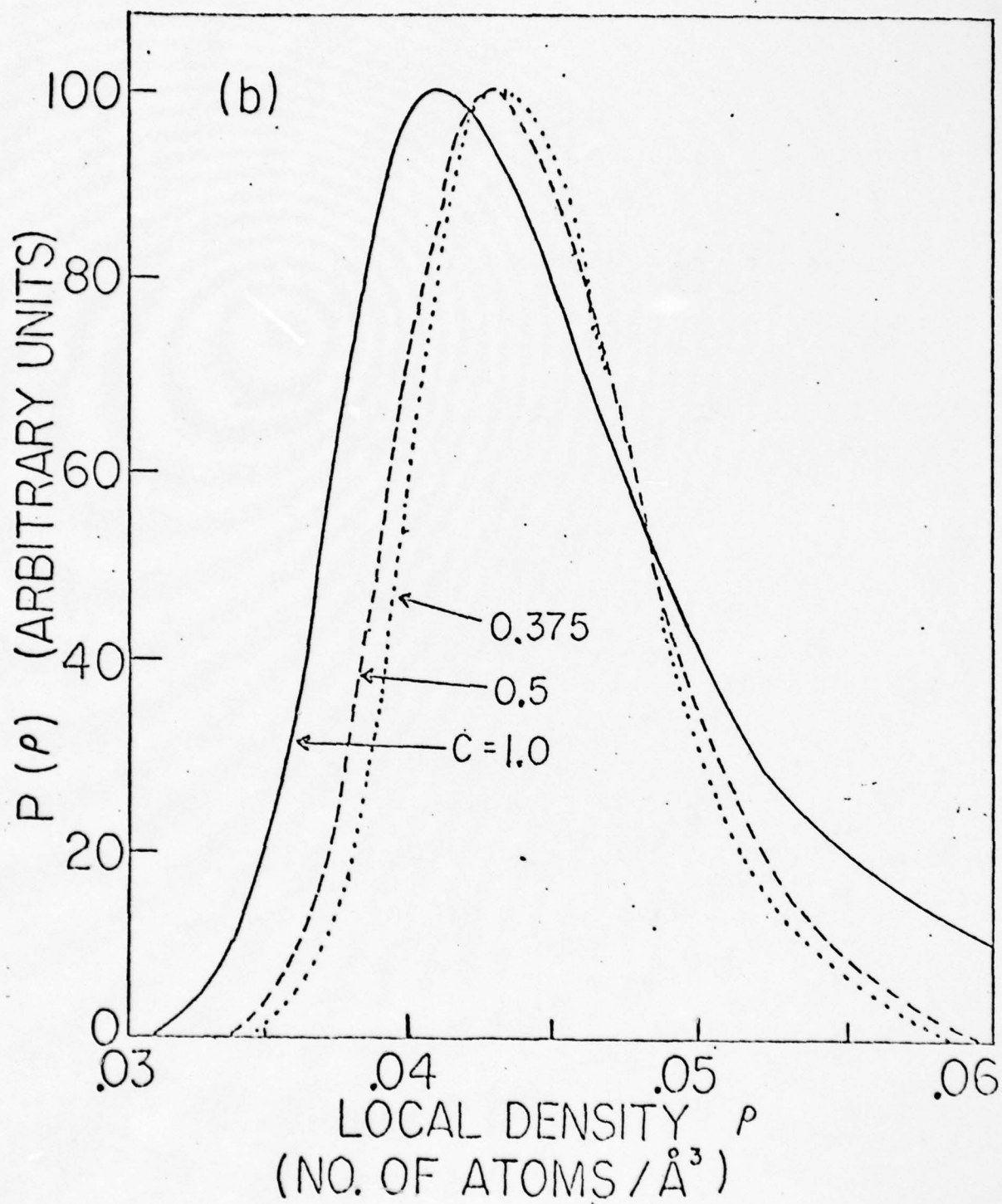   matrix element.

FIGURE CAPTIONS cont.

Fig. 5   (b) GaAs: Curve 1 - experimental (Ref. 16);

Curve 2 - calculated in this paper using the EDS

of Fig. 4; Curve 3 - calculated by Kramer et al

(Ref. 9); Curve 4 - the same as Curve 2 except

for the use of constant matrix element.

(c) GaSb: for legends, see Fig. 5 (b).

(d) InAs: for legends, see Fig. 5 (b).

Inserts to figs. a-d: Curve 1 - crystalline

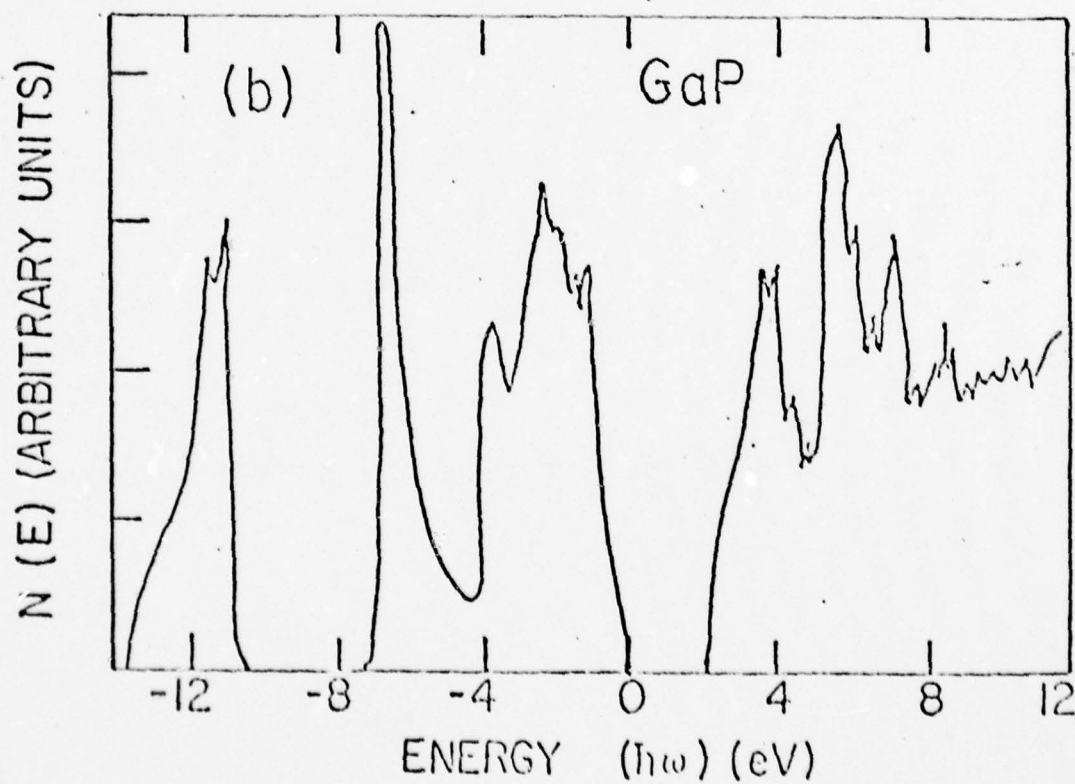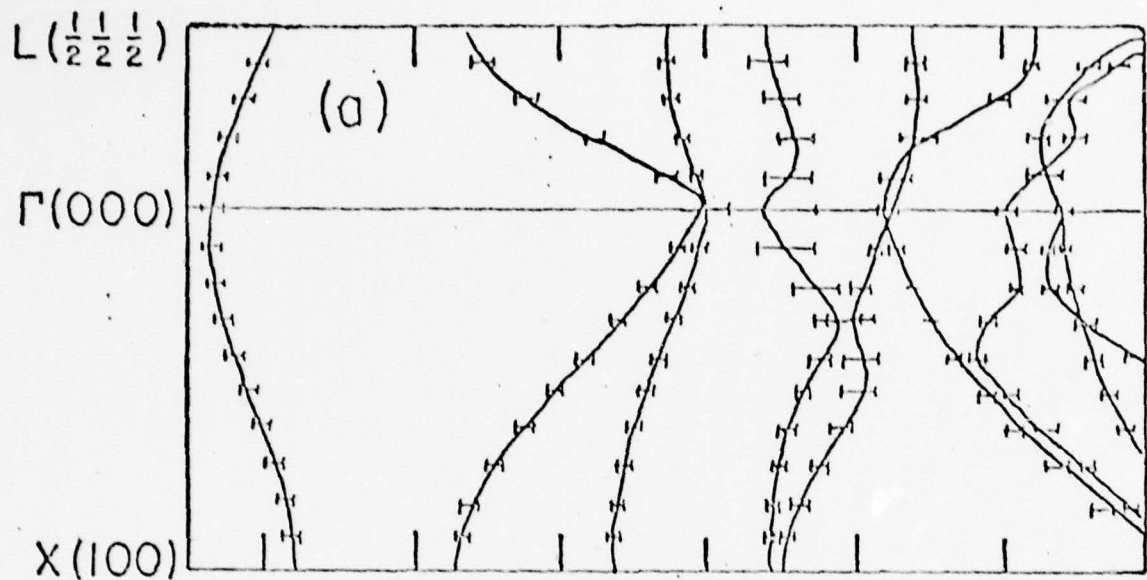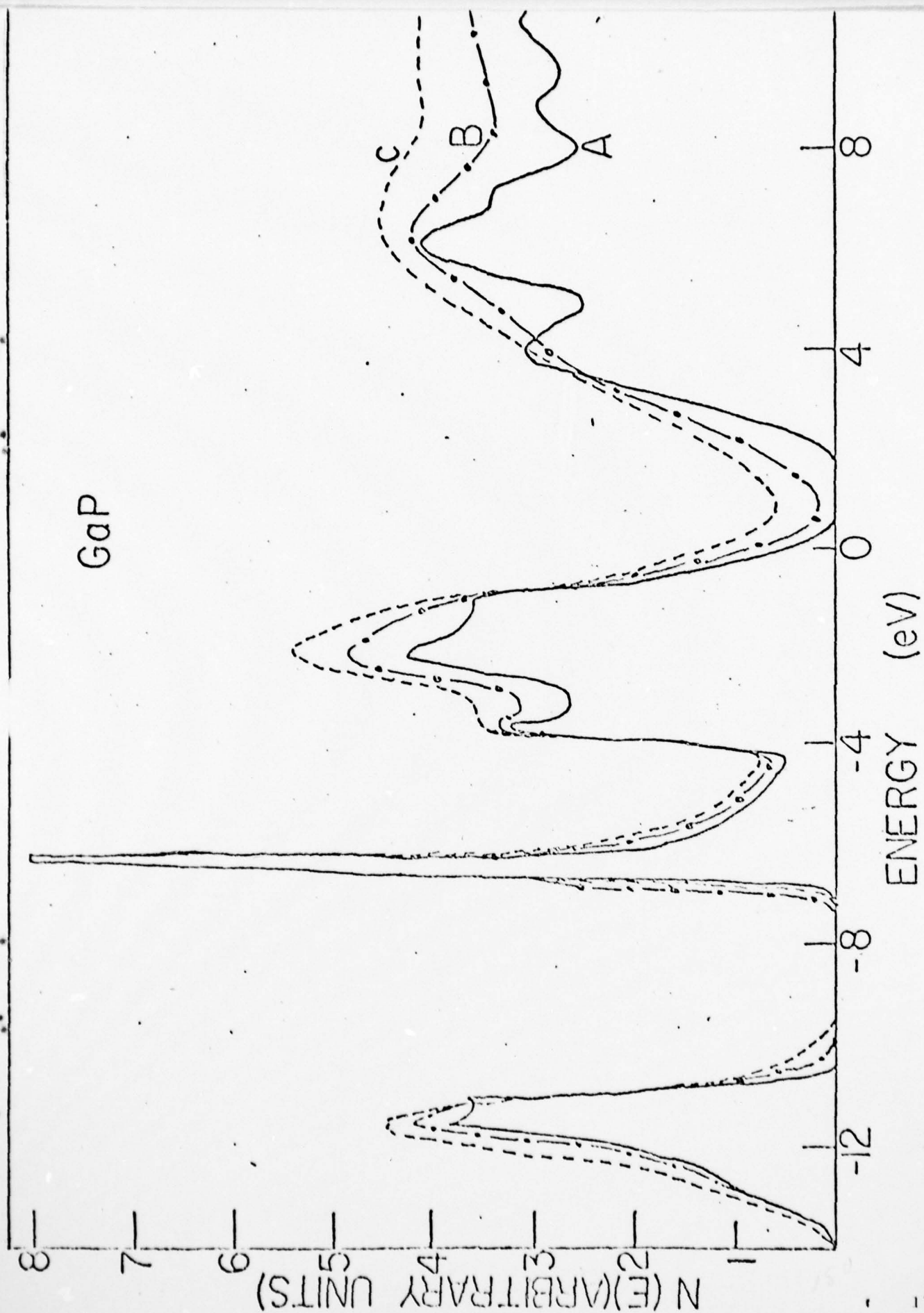$|M(\omega)|^2$; Curve 2 - amorphous $|M(\omega)|^2$ used in

the present calculation.
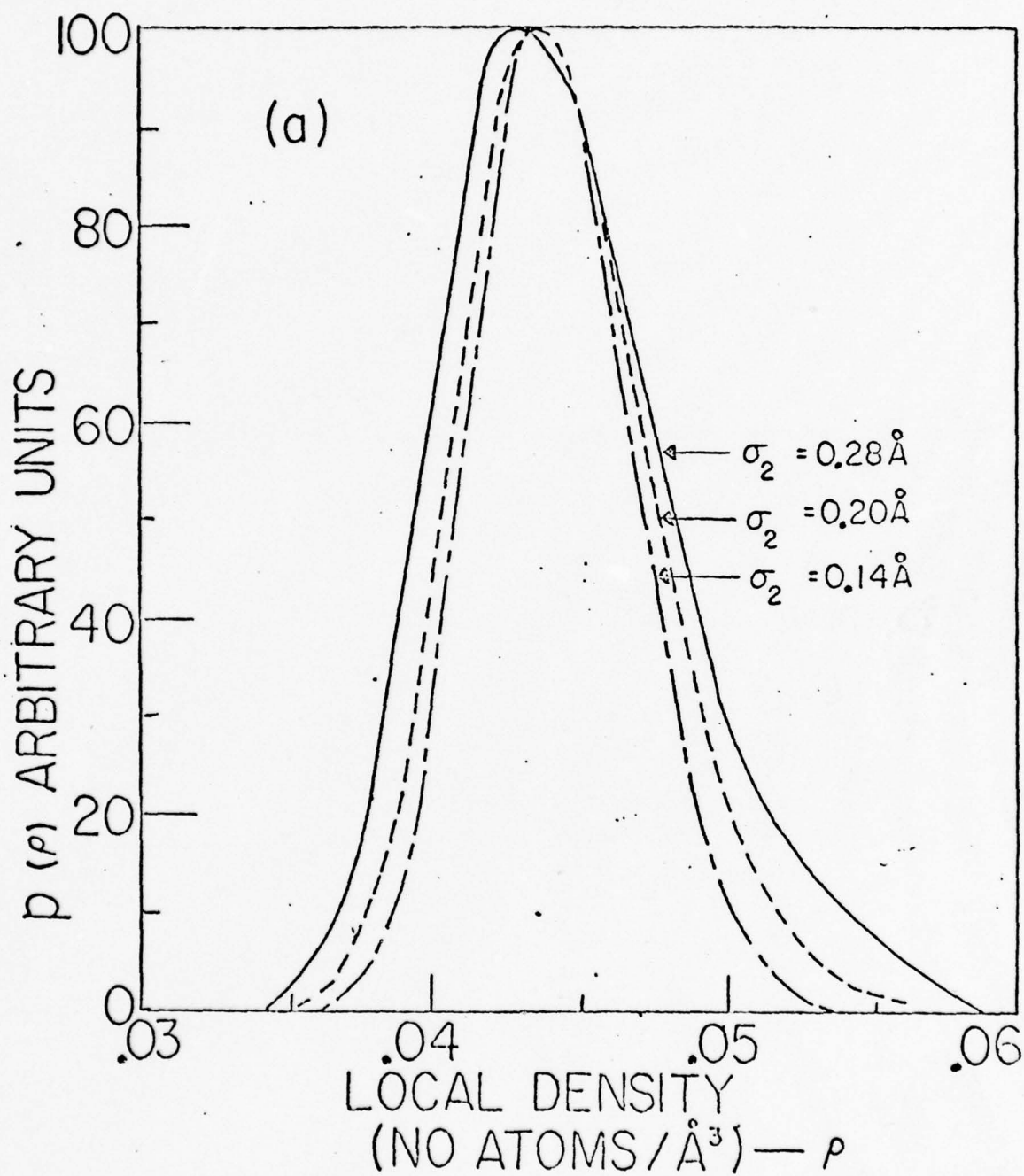
(a)

σ₂ = 0.28 Å
σ₂ = 0.20 Å
σ₂ = 0.14 Å

$\sigma_2 = 0.28$ Å
$\sigma_2 = 0.20$ Å
$\sigma_2 = 0.14$ Å

p (ρ) ARBITRARY UNITS

LOCAL DENSITY
(NO ATOMS/Å³) — ρ

(b)

P (P) (ARBITRARY UNITS)

100
80
60
40
20
0

0.375
0.5
C = 1.0

LOCAL DENSITY ρ
(NO. OF ATOMS / Å³)

.03   .04   .05   .06

169

GaP

Tans et al Phys. Rev. D. B. Cin 2 ......

170

Trayest et. Chapter B. Fig 4. Bm665

171

Trudy et al.

(a)

GaP

$\epsilon_2(\omega)$ (ARBITRARY UNITS)

PHOTON ENERGY (eV)

IMI2 (ARBITRARY UNITS)

PHOTON ENERGY (eV)

172

GaAs

(b)

PHOTON ENERGY (eV)
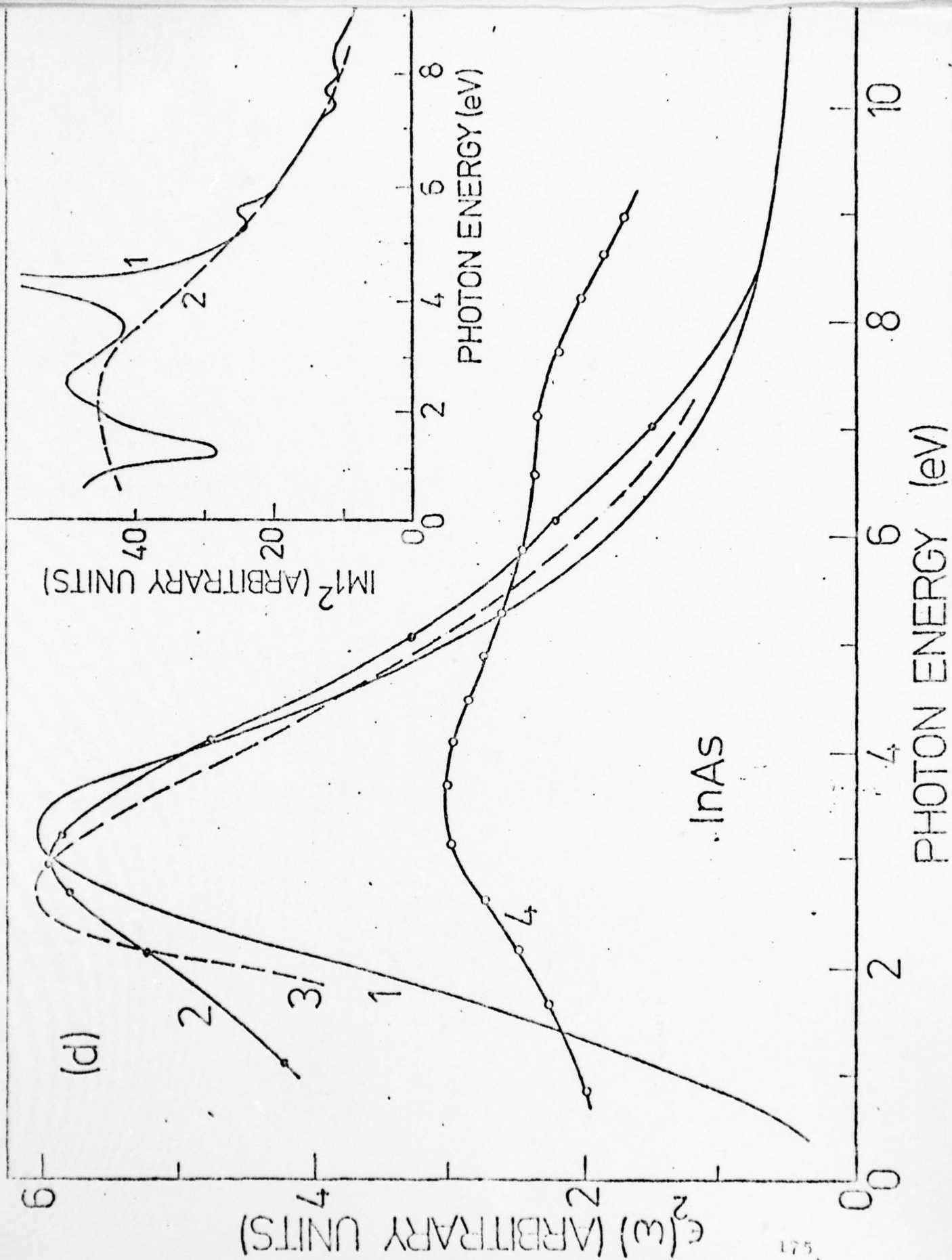
$\varepsilon_2(\omega)$ (ARBITRARY UNITS)

Inset: |M|² (ARBITRARY UNITS) vs PHOTON ENERGY (eV)

Tsay, et al. Phys Rev. B, Fig. 5(c), BM 679

(c)

GaSb

3

1

2

4

$\varepsilon_2(\omega)$ (ARBITRARY UNITS)

PHOTON ENERGY (eV)

|M|² (ARBITRARY UNITS)

PHOTON ENERGY (eV)

174
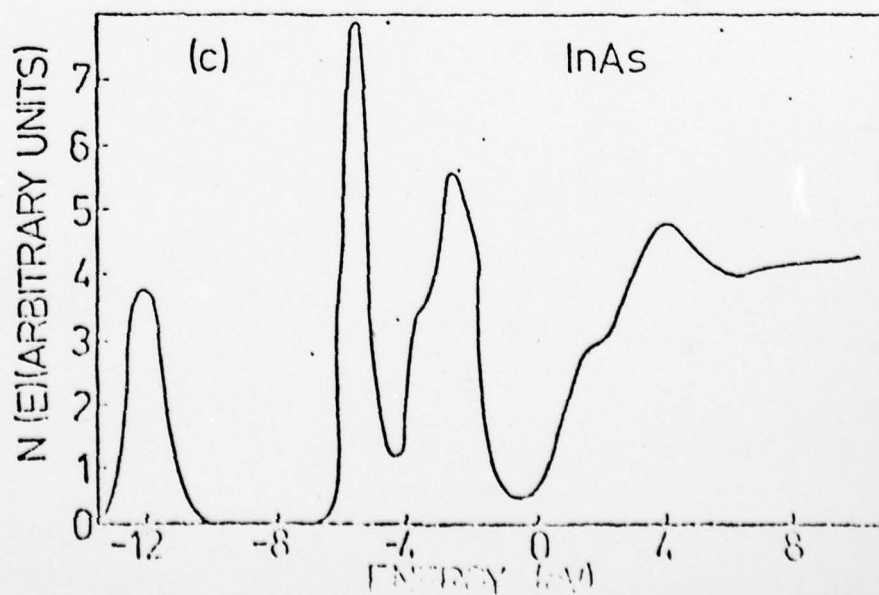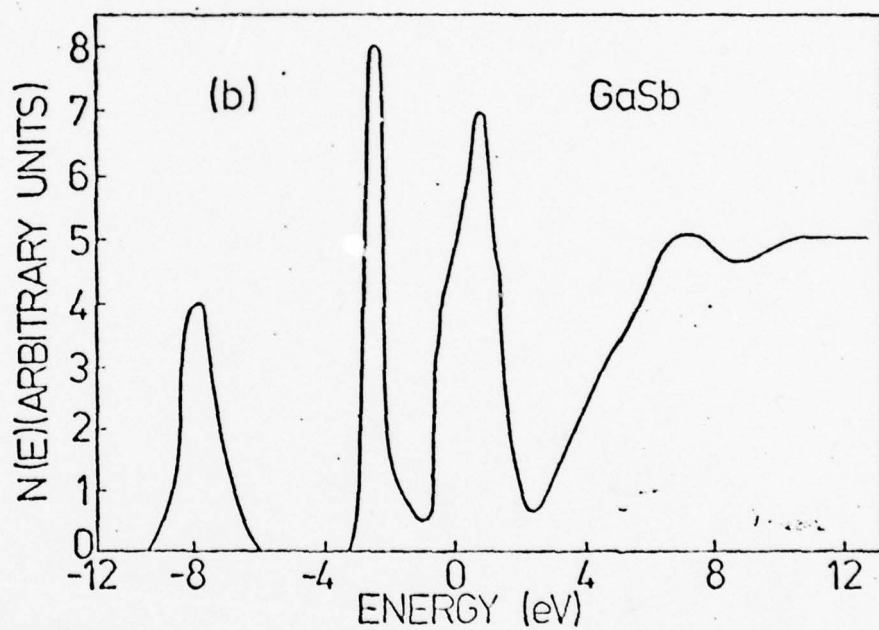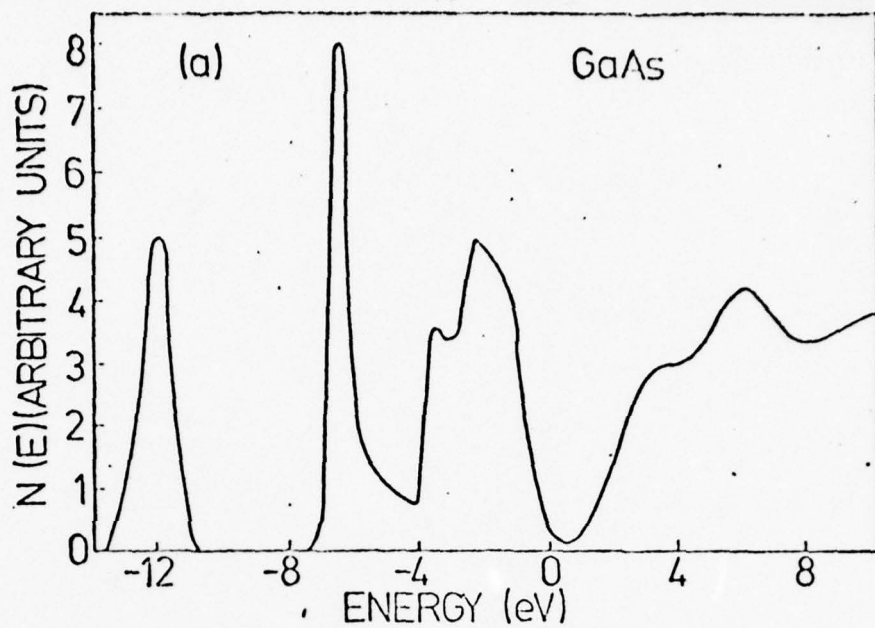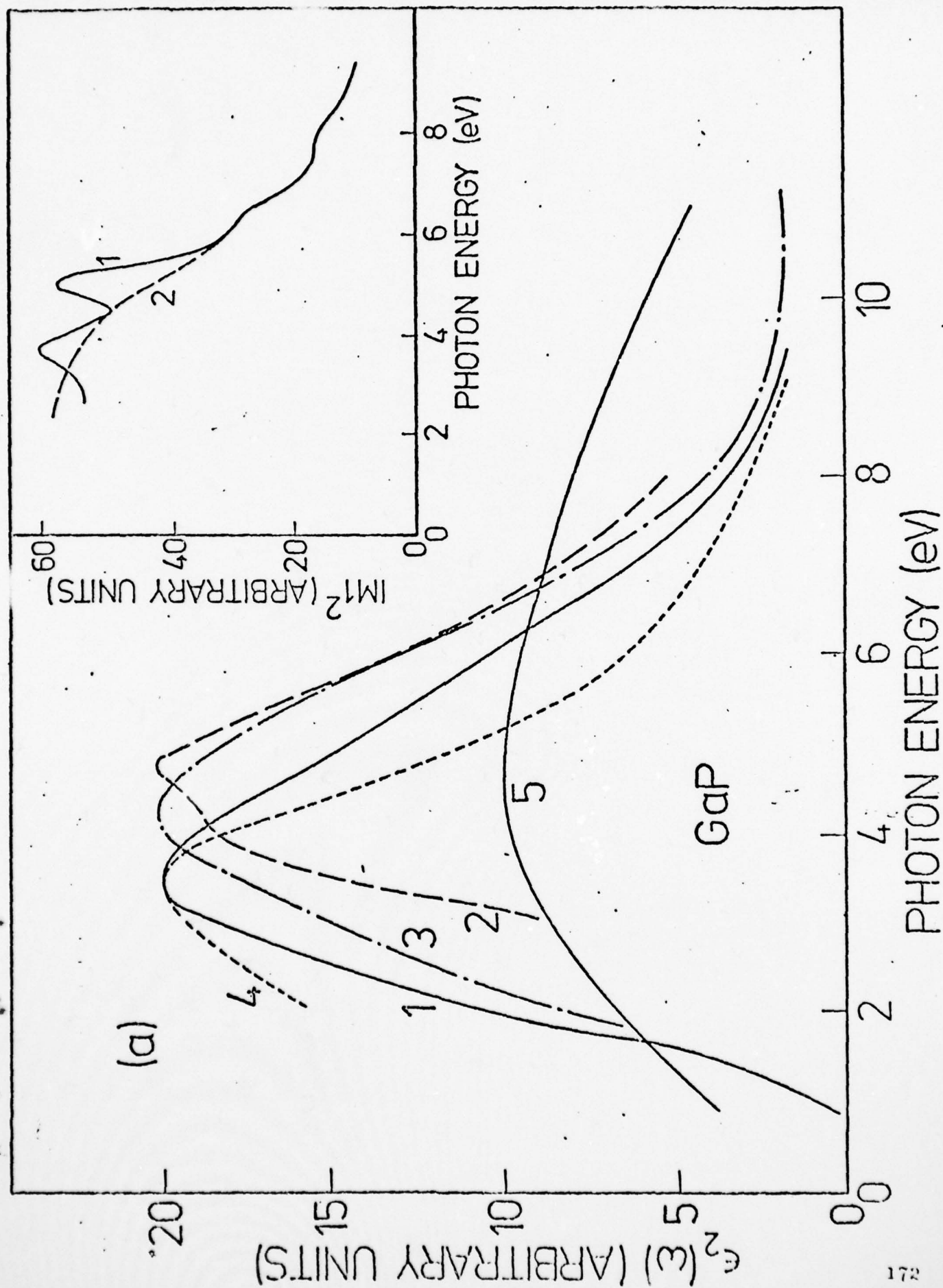
InAs

PHOTON ENERGY (eV)

$\epsilon_2(\omega)$ (ARBITRARY UNITS)

|M|² (ARBITRARY UNITS)

PHOTON ENERGY (eV)
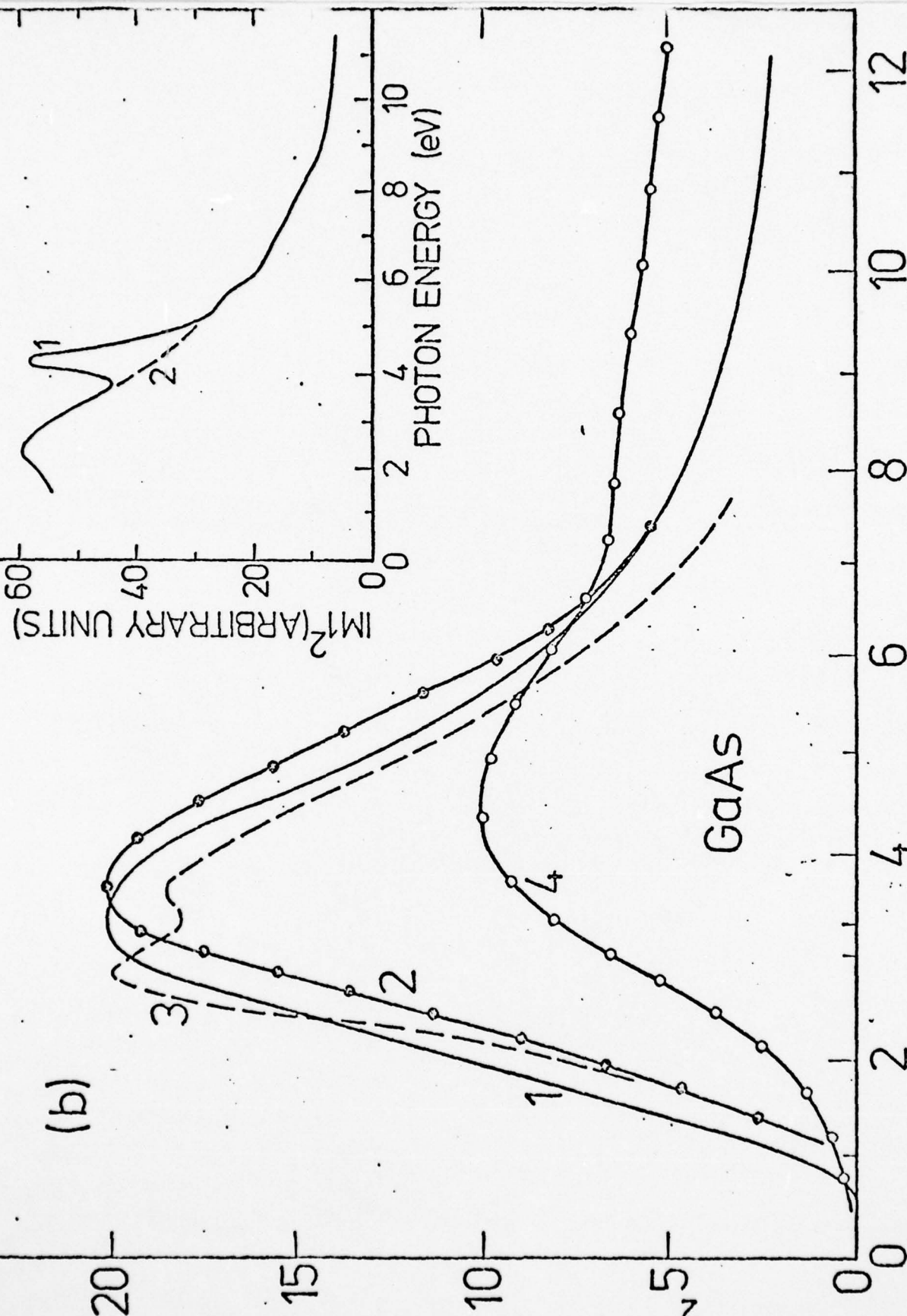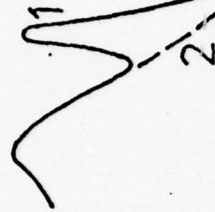
175
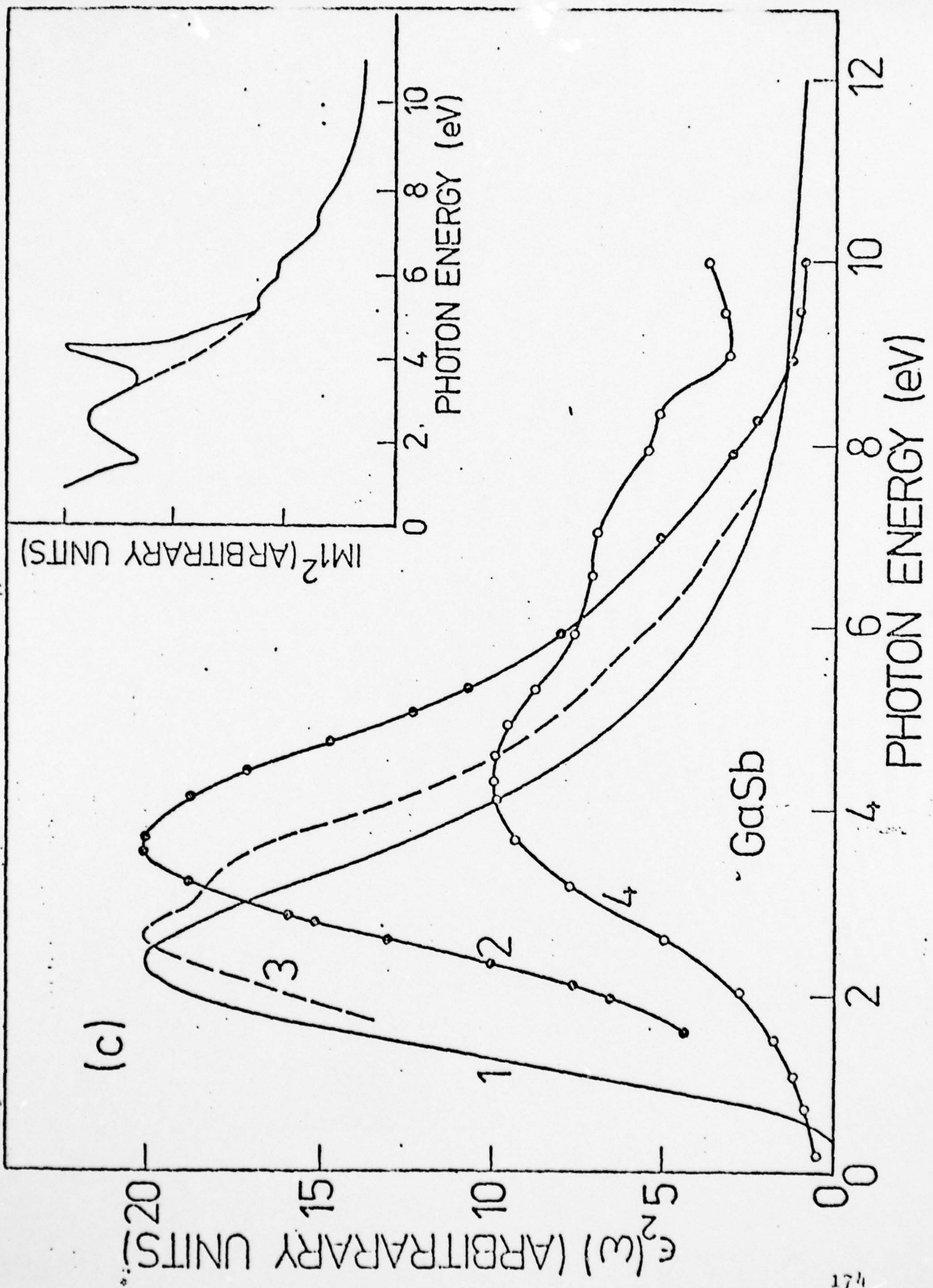
4.3 OPTICAL PROPERTIES OF DENSITY-DISORDERED SOLIDS

Yet-Ful Tsay* and Bernard Bendow
AF Cambridge Rsch Labs(AFSC), Hanscom AFB, MA 01731 .

Shashanka S. Mitra+
Dept of Elec. Engr., U/Rhode Island, Kingston, R.I. 02881

A statistical theory of the optical response in solids with
a small degree of microscopic density disorder is formulated,
in which the properties of the disordered solid are related
to those of its crystalline counterpart. Both the elec-
tronic and lattice response are treated, by determining the
changes in band structure and phonon spectrum as functions
of local density. As an application of the theory, we de-
duce the optical properties of amorphous semiconductors
such as Si, Ge, GaAs and InAs and compare them to those of
their crystalline counterparts. Good agreement with ex--
periment is obtained for the predicted optical and infra-
red absorption spectra, and for the Raman scattering spec-
trum. The analysis provides a quantitative gauge of the
departure from crystallinity in the optical spectrum, i.e.,
the relative contribution of processes which do not con-
serve crystal momentum.

I. Introduction

Most existing works (1-3) on the optical properties
of amorphous or structurally disordered solids emphasize
the role of k-selection rule breakdown, and what is con-
sequently expected to be a strong similarity between den-
sities of states and optical spectra of such solids. Re-
cently, the role of crystalline-allowed analogue (CAA)
processes in tetrahedrally bonded amorphous semiconductors
(TBAS) was pointed out by Tsay et al (4) for electronic
spectra, and by Mitra et al (5) for lattice spectra. In
this paper we develop a statistical approach to the in-
terpretation of optical spectra of disordered solids, and
comparison is made with available experimental data for
TBAS.

Statistical descriptions have long served as a basis
for investigations of disordered systems. (6). For our pur-
poses, we view the properties of an amorphous solid as de-
rived from an ensemble of atomic (structural) configura-
tions (labeled by "n") with probabilities p_n, rather than
from a single unique structural entity. Then for a par-
ticular property θ we require the configurational aver-
age (7)

$$\langle\theta\rangle = \sum_n p_n \theta(n) \tag{1}$$

where $\theta(n)$ is the expectation value of θ in configuration
n. Clearly, for any realistic system it is difficult, if
not impossible, to evaluate $\langle\theta\rangle$ from first principles.
Rather, for the statistical approach to be useful one must
be able to identify a restricted class of configurations
which elicit the principal features of the properties con-
cerned; moreover, of course, one must be able to calculate
the corresponding $\theta(n)$'s for these configurations. We
here propose to parameterize disordered solids in terms of
two classes of principal configurations, namely those
possessing (a) both short and long range order (denoted by
$[n]^{SL}$) and (b) just short range order (denoted by $[n]^S$).
The motivation for this parametrization for various amor-
phous solids such as TBAS is that the experimental evi-
dence (8,9,10) indicates that, to a large extent, they are
"nearly crystalline"; i.e., spectral features that are
prominent in the crystal remain prominent in the corres-
ponding amorphous solid, and are expected to arise from

2

Bendow

the $[n]^{SL}$. Features which are weak or absent for the crystal are generally also weak in the amorphous counterpart, and are expected to arise principally through the non-crystalline configurations $[n]^S$. Each of the configurations in the set $[n]^{SL}$ will lead individually to features obeying crystalline-like $\underline{k}$-selection rules, i.e., $\theta^{SL}(n) = 0$ for forbidden processes. The final spectra will in general however, be broadened out because of the averaging process. If the principal p_n peaks strongly about a single configuration $\bar{n}$, then the analogue crystalline features characteristic of $\bar{n}$ will be prominent. If, on the other hand, the p_n possess a considerable spread, then the crystalline features may be largely washed out. The configurations $[n]^S$, on the other hand, are not subject to crystalline selection rules, and always contribute to the spectrum. In addition to broad, featureless contributions arising from the breakdown of $\underline{k}$-selection, various peaks evident in the crystalline density of states, but suppressed by selection rules in optical spectra, will reappear for the amorphous solid. We shall demonstrate below that the viewpoint described here does indeed provide a basis for a consistent interpretation of observed spectra of TBAS.

With the above prescriptions, one may write

$$\langle\theta\rangle = \langle\theta\rangle^{SL} + \langle\theta\rangle^S$$

$$= \sum_n [n_{SL} \, p_n^{SL} \, \theta^{SL}(n) + n_S \, p_n^S \, \theta^S(n)] \, . \qquad (2)$$

$$\sum_n p_n^{SL} = \sum_n p_n^S = 1, \; n_{SL} + n_S = 1 \qquad (3)$$

where we have chosen a convenient normalization for the p_n's. The parameters n_{SL} and n_S which we here deduce from experiments are, respectively, the fractions of ordered and disordered configurations, and thus provides a measure of the amorphousness of the solids ($n_S = 0$ for a crystal, $n_S \approx 1$ for a highly disordered system). In order to proceed, one must specify the $[n]^{SL}$ and $[n]^S$ to be employed above. Among the configurational parameters n suggestive for TBAS, for example, are the interatomic spacing, local densities and bond angles, all known to deviate from those of their crystalline analogues and to display characteristic spreads as well. As a first step in the calculation of $\langle\theta^{SL}$ we

3

Bendow

here restrict n to correspond to variations in local density ρ alone. While the calculation of $<0>^{SL}$ for a given value of ρ will be relatively straightforward, this is not the case for $<0>^S$. A reasonable, but not unique, possibility is to employ just a nearest-neighbor (nn) unit immersed in a continuum to calculate the $[n]^S$. This would account for the principal features representative of short-range order, yet suppress those features characteristic of the periodic lattice structure beyond the nn cell.

The plan of the paper is as follows: In Section II we calculate the first order IR and Raman spectra of disordered solids, and in Section III the electronic density of states and optical absorption spectrum are determined. In every instance, comparison with available experimental results for TBAS is carried out. In Section IV we utilize the present theory to predict the multiphonon response in the highly transparent regime of amorphous solids, with specific application to TBAS. Conclusions are given in Section V.

II. First Order Infrared and Raman Spectra

In this section we describe a new interpretation of the first order infrared and Raman spectra of amorphous solids. For definiteness, we concern ourselves mainly with TBAS, such as Si, Ge, and the III-V compounds.

The photon-phonon interaction in crystalline solids may be characterized, to a first approximation, in terms of damped Lorentz oscillators. The IR absorption is related to the imaginary part of the lattice dielectric function (11), $\varepsilon_2(\omega)$, which takes the form

$$\varepsilon_2(\omega) \sim \sum_i |M(\omega_i)|^2 L(\omega_i, \Gamma_i) \tag{4}$$

with

$$L(\omega_i, \Gamma_i) = \frac{\Gamma_i \omega}{(\omega_i^2 - \omega^2)^2 + \Gamma_i^2 \omega^2} \tag{5}$$

where $|M(\omega_i)|^2$ is the square of the dipole matrix element[*] for mode ω_i and $L(\omega_i, \Gamma_i)$ is a Lorentzian oscillator with

------

[*]for instance, $|M(\omega_{TO})|^2 = (\varepsilon_0 - \varepsilon_\infty)\omega_{TO}^2$.

frequency ω_j and damping Γ_j. In diamond-type crystals, $M(\omega_{TO}) = 0$, and in the lowest order there are no contributions to the imaginary part of the dielectric constant (higher order photon-phonon interactions contribute the entire absorption). For the Raman scattering intensity (e.g., the Stokes component), the corresponding expression (12) may be written as

$$I_R(\omega) = \sum_i |\alpha_i(\omega)|^2 L(\omega_i, \Gamma_i)[n(\omega_i) + 1] \qquad (6)$$

where $|\alpha(\omega)|^2$ represents the matrix element of the induced polarizability, and $n(\omega)$ is the Bose-Einstein factor. In Eqs. (4) and (6), the summation is to be performed over the lattice modes which are excited in a particular experimental configuration. In what follows, we shall assume, as is generally the case, that only a single transverse optical (TO) mode is active. The generalization to situations in which more than one mode is excited is straightforward.

Adopting the statistical approach discussed above, one splits the lattice response in an amorphous solid into

$$\varepsilon_{2a}(\omega) \sim \eta_{SL} <\varepsilon_2(\omega)>^{SL} + \eta_S <\varepsilon_2(\omega)>^S \qquad (7)$$

The second term in the right-hand side of Eq. (7) is the contribution of those structural configurations {S} which possess short-range order only, and do not obey crystalline $\underline{k}$-selection rules. This term should, in principle, involve contributions from all the vibrational modes originating from the {S} configurations (although they may have substantially different strengths); it will thus be intimately related to the density of phonon states of TBAS. The first term in the right-hand side of Eq. (7), on the other hand, results from configurations which possesses both short-range and long-range orders, and thus, individually obey crystalline $\underline{k}$-selection rules.

As discussed in the Introduction, calculation of the lattice response requires enumeration and/or parametrization of the structural configurations of the solid, and specification of their associated probabilities. Among the configurational parameters n suggestive for TBAS are bond lengths, bond angles, and local density, all of which are known to deviate from those of the corresponding crystal,

and to display characteristic spreads about some mean value (13). In the present calculation of $<\theta>^{SL}$, we shall restrict n to local density variation alone and moreover, approximate this density as being uniform throughout the solid. While such a procedure is admittedly crude, we will here demonstrate that it nevertheless successfully accounts for the principal features of a variety of experimental data.

It is assumed that the dependence of the lattice response, i.e., $\varepsilon_2(\omega)$ on the local density is mainly through ω_i, the oscillator frequency, which, for small variation of the local density, can be obtained from the crystalline value by the Gruneisen approximation (14)

$$\omega_i(\rho) = \omega_i(\rho_c)(\rho/\rho_c)^{\gamma_i} \tag{7'}$$

where ρ_c is the crystalline density. γ_i is the Gruneisen parameter for mode ω_i. The {SL} contribution then is given by

$$<\varepsilon_2(\omega)>^{SL} \sim \int_0^\infty d\rho P(\rho)\, \varepsilon_2(\omega,\rho) \tag{8}$$

where $P(\rho)$ is the distribution of the local density, which for convenience is taken to be Gaussian,

$$P(\rho) = \exp\left[-\frac{(\rho-\rho_a)^2}{2\sigma^2}\right] \tag{9}$$

where ρ_a is the mean density in a TBAS, and σ is the corresponding spread. Such a form, i.e., Eq. (9), for the local density distribution, can be partially justified by considering the effects of the spreads of the nearest and the second nearest interatomic spacings on the local density. The details of this procedure will be given elsewhere (15).

Calculation of the short-range {S} terms is considerably more difficult. As suggested above, one might simply choose these to be proportional to the crystalline density of phonon states (possibly with minor modifications). However, since the crystalline density of states includes both short and long range features, its use for the {S} terms is therefore not, strictly speaking, consistent with the present break-up. As alluded to previously in the Introduction, a possible

181

6

Bendow

alternative is the calculation of the modes and associated response of a small cluster of atoms, viewed as immersed in a continuum (acoustic bath). Calculations along this line have recently been pursued by various authors (16). In the present work, we will calculate just the {SL} terms, and content ourselves with pursuing a consistent interpretation of the {S} and {SL} contributions manifested in experimental data.

As an application of the above prescriptions, we analyze in the following the first order IR and Raman spectra of several TBAS, including Ge, Si and III-V's. Figs. 1-3 display results of calculations, employing the above recipe, as compared with the experimental spectra. The mean density, ρ_a, and the spread, σ, in $P(\rho)$ have been adjusted to provide a best fit to experimental spectra. Fig. 1a and 1b show the first order Raman and IR spectra of amorphous Ge. If one sets $\eta_S = 0$ in Eq. (7), one obtains a good fit for the principal Raman peak, with the remaining lower frequency features, presumably arising from the {S} configurations. The IR one-phonon spectrum, which is forbidden for Ge in the crystalline phase should arise entirely from the {S}, i.e., $\varepsilon_2 = \varepsilon_2^S$. Apart from matrix element effects, this spectrum should be roughly proportional to the {S} contributions to the Raman spectrum, which may be determined by first choosing an η_{SL} and then subtracting the calculated {SL} contribution to the Raman spectrum from the experimental one. Comparison of the IR data with $\langle\varepsilon_2\rangle^S$ with $\eta_{SL} = 0.7$ is shown in Fig. 1b. Similar results may be obtained for amorphous Si as well. It appears that the peak positions and shapes of the Raman spectra of these amorphous solids are well represented by a simple sum of the {SL} and {S} contributions, and the IR spectra by just the {S} contribution. Fig. 2 displays a similar fit to the IR spectrum for amorphous GaAs with $\eta_{SL} = 1$. Fig. 3 shows the same for amorphous SiC, but for a geometry in which both TO and LO are excited (Berreman effect) (17). Very similar results are also obtained for the infrared spectra of amorphous GaP, GaSb and InAs and are shown in Figs. 4-6. The conclusion reached is that {S} contribute very little to the first order spectra of a typical binary TBAS; the principal features arise from just the {SL} alone.

In Table 1, we list the relevant structural data of the TBAS. The σ and ρ_a characterizing the local density distribution are also given. The local density parameters are
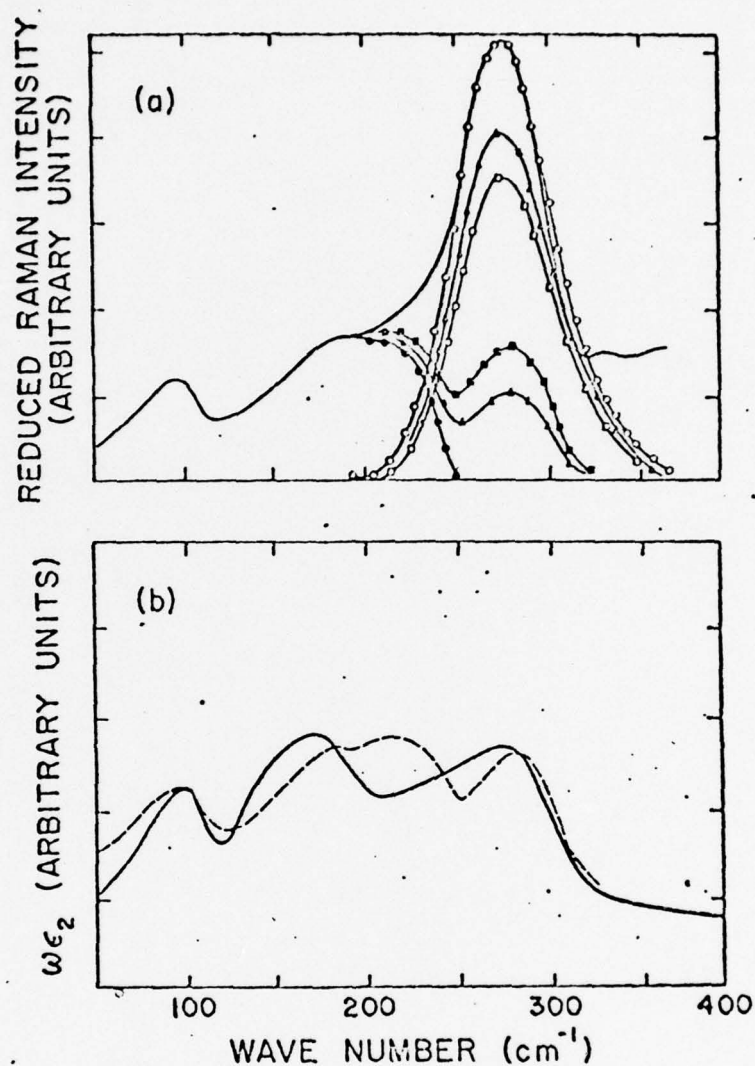
7

Bendow
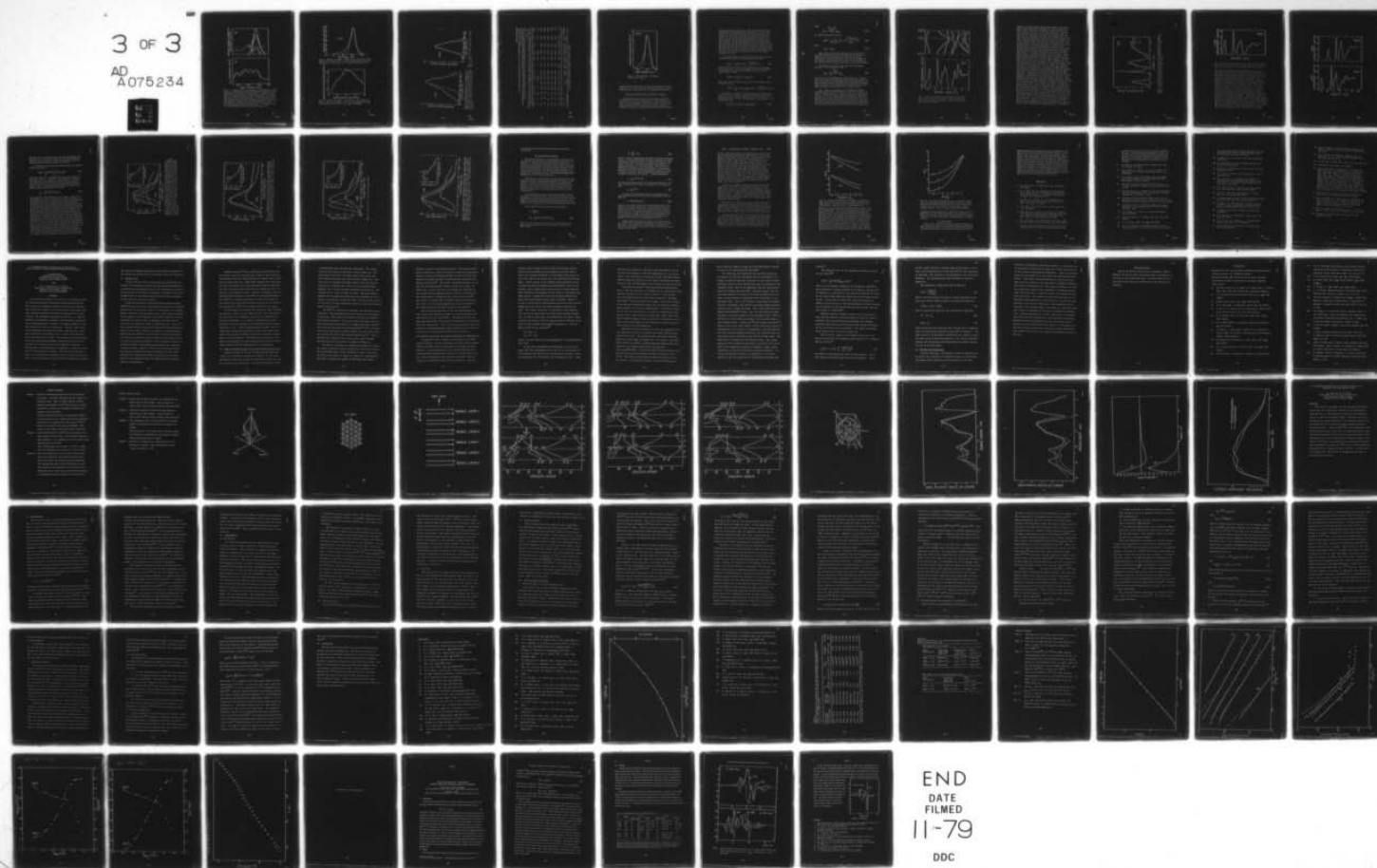
Fig. 1. (a) Comparison of calculated crystalline-like contribution and experimental Raman spectrum of amorphous Ge. Line: experimental data (Ref. 2), open circles: calculated with $\eta_{SL} = 1.0$, open triangles: calculated with $\eta_{SL} = 0.8$, open squares: calculated with $\eta_{SL} = 0.7$. The difference between the experimental and calculated curves are represented by full circles, full squares, and full triangles, respectively. The difference curves represent the $(n)^S$ contribution. (b) Infrared data (solid curve) of Ref. 9 is compared with the $(n)^S$ contribution (dashed curve) for $\eta_{SL} = 0.7$.
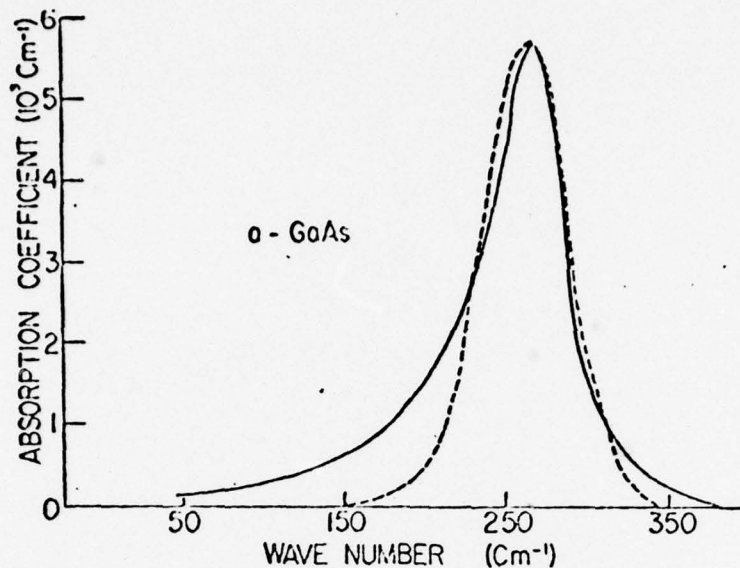
183

8

Bendow

Fig. 2. IR abs. in a-GaAs. Solid curve: experimental data from Ref. 8, dashed curve: result calculated in this paper with $\rho_a/\rho_c = 0.96$, $\sigma/\rho_a = 0.77$ (see text and Table I).
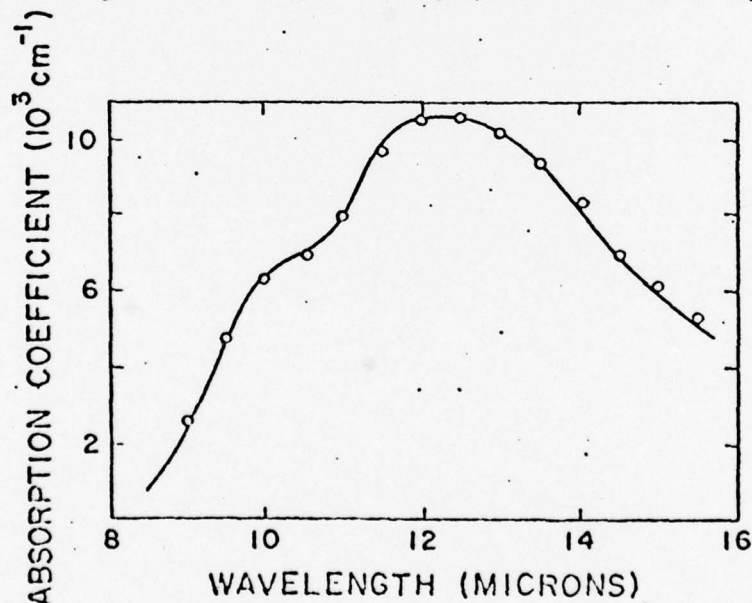

Fig. 3. IR abs. in a-SiC. Solid curve: calc. with parameters taken from Feldman et al, P.R. 170, 698(1968); 173, 787 (1968) and Mitra et al, P.R. 186, 942 (1969).
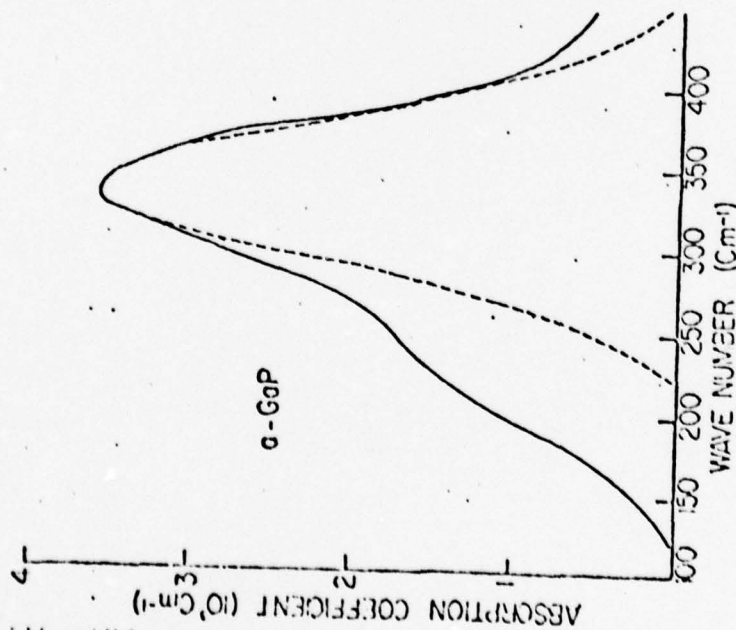
9

Bendow

Fig. 4. Infrared absorption in amorphous GaP. Solid curve: experimental data from Ref. 8, dashed curve: result calculated in this paper with $\rho_a/\rho_c = 0.69$, $\sigma/\rho_a = 0.15$ (see text and Table I.)
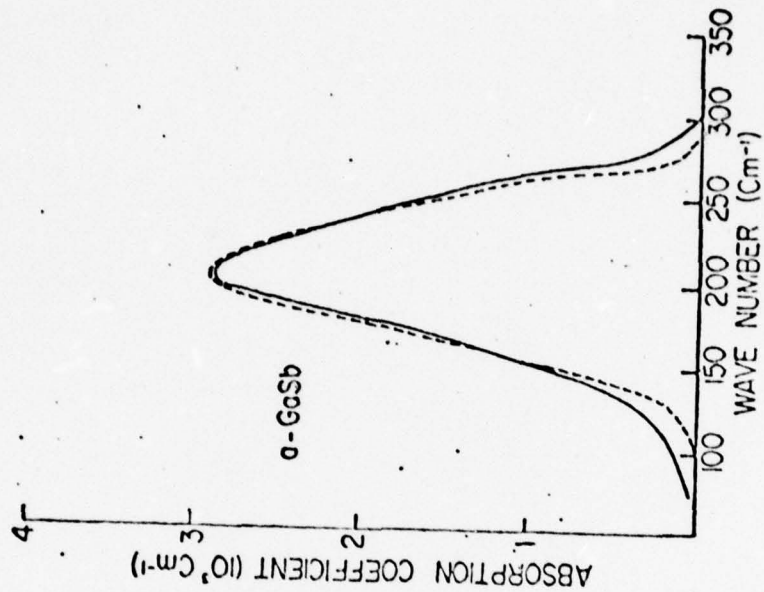
Fig. 5. Same for GaSb, with $\rho_a/\rho_c = 0.87$, $\sigma/\rho_a = 0.15$.

10a

Bendow

TABLE I. Relevant Structure Parameters of Some TBAS

Material	r_{1c} (Å)	r_{1a} (Å)	σ_{r1} (Å)	r_{2c} (Å)	r_{2a} (Å)	σ_{r2} (Å)	ρ_a/ρ_c A	B	C	$c/\rho_a \times 100\%$ A	B	C
Si	2.35	2.37–2.41	0.09	3.84	3.84$^\Delta$	0.25	0.95	0.91	0.89	11.5	8.2	7.6
Ge	2.45	2.46	0.037	4.0	4.0	0.28	0.99	0.94	0.96	4.5	7.5	7.0
GaP	2.36	2.44	0.16	3.86	3.9	0.34	0.90	0.89	0.90	2.0	13.	13.4
GaAs	2.45	2.48	0.02	4.0	4.0	0.28	0.96	0.96	0.92	2.2	7.7	6.8
GaSb	2.65	2.67	0.12	4.33	4.3	0.38	0.98	0.87	0.81	13.	15.	11.
InAs	2.63	2.69	0.05	4.3	4.0	0.28	0.93	0.91	0.77	5.6	9.9	
InP	2.54	--	0.09$^\Delta$	4.15	--	--	0.95$^\Delta$	--	--	12$^\Delta$	--	--
InSb	2.81	2.86	0.10	4.59	4.5	0.43	0.94	--	0.75	9.9	--	10.7

+All experimental data taken from Ref, N.J.Shevchik and W.Paul, J.Non-Cryst. Solids 13, 1 (1974), except those of Si, which were taken from R. Grigorovici, J. of Non-Cryst Solids 1, 303 (1969).

*Column A represents values estimated from data for nearest neighbor distance only.
Column B gives values obtained from absorption (or Raman for Si and Ge) spectrum, as discussed in the text.
Column C gives values obtained from a local density calculation (Ref. 15).
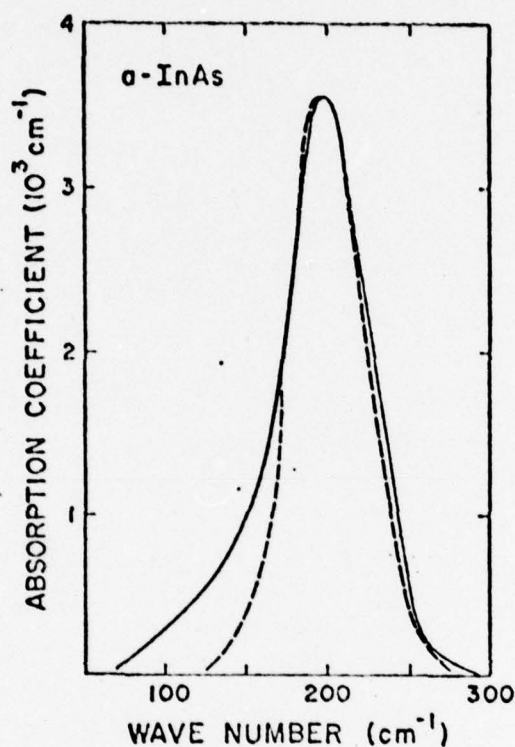
ΔEstimated values.

Bendow

Fig. 6.   Same for InAs, with ρ_a/ρ_c = 0.91, σ/ρ_a = 0.099.

compatible with the results of various experimental measurements, if one realizes that the structural properties of a TBAS film are very dependent on the preparation conditions.

III. Electronic Structure and Optical Spectra

Most theoretical works on the electronic properties of TBAS have stressed the importance of the breakdown of the k-selection rules associated with a loss of long-range order. As a consequence, it has often been suggested (18) that calculation of the electronic properties of TBAS should take explicit account of structural disorder, thereby

Bendow

II

dictating approaches which are widely different from those used for the crystalline phase. However, as we have demonstrated above in connection with the lattice response, the disorder in TBAS does not result in catastrophic effects. In fact, as was shown above, the principal features in the latter spectra can still be described by crystalline-like contributions. In our calculation of the electronic structure, particularly the electronic density of states of TBAS, we shall follow a philosophy similar to that taken by Herman and Van Dyke (19), Brust (20), and Kramer et al (21). Namely, the electronic density of states of a TBAS are calculated by using its crystalline counterpart as the starting point with, however, certain modifications which take account of the structural disorder.

We start with the following prescription for $n_a(E)$, the electronic density of states at energy E, of TBAS:

$$n_a(E) \simeq \int n_c(E,\rho) \exp\left[- \frac{1}{2}\left(\frac{\rho-\rho_a}{o}\right)^2 \right] d\rho \qquad (10)$$

where $n_c(E,\rho)$ is the crystalline counterpart corresponding to local density ρ. Eq. (10) amounts to neglecting the {S} contribution to $n_a(E)$, which should be useful as a first approximation. Since

$$n_c(E,\rho) = \sum_n \sum_k \delta(E - E_{n,k}(\rho)) \qquad (11)$$

where n is the band index, and k is the wave vector of the electronic states

$$n_a(E) \simeq \sum_n \sum_k \int \delta(E-E_{n,k}(\rho)) \exp\left[- \frac{1}{2} \left(\frac{\rho-\rho_a}{o}\right)^2 \right] d\rho \qquad (12)$$

In general, we expect the local density distribution to be fairly sharply peaked, and therefore that the largest contribution to the integral in Eq. (12) will come from ρ's for which $|\rho-\rho_a| \simeq o \ll \rho_a$. In this range of ρ, $E_{n,k}(\rho)$ can be expanded in $\rho-\rho_a$,

$$E_{n,k}(\rho) \simeq E_{n,k}(\rho_a) + \gamma_{n,k}(\rho-\rho_a) + \ldots \qquad (13)$$

12

Bendow

where

$$\gamma_{n,k} \equiv \frac{\partial E_{n,k}(\rho)}{\partial \rho}\Big|_{\rho=\rho_a} \tag{14}$$

Eq. (12) can then be written as

$$n_a(E) \propto \sum_{n,k} \frac{1}{\gamma_{n,k}} \exp\left[-\frac{1}{2} \left(\frac{E-E_{n,k}(\rho_a)}{\sigma_{n,k}}\right)^2\right] \tag{15}$$

where

$$\sigma_{n,k} \equiv \gamma_{n,k}\sigma \tag{16}$$

Thus, within the present approach, the δ-functions in Eq. (11) representative of the crystalline phase are now replaced by a series of Gaussians. The widths of the Gaussians are given by the $\sigma_{n,k}$, which are the products of the density spread parameter σ and $\gamma_{n,k}$, the derivative of the electronic energy $E_{n,k}$ with respect to the local density.

To calculate $\gamma_{n,k}$ use can be made of the following equation. If P is pressure, then

$$\gamma_{n,k} = \frac{1}{\rho_a K} \frac{\partial E_{n,k}}{\partial P}\Big|_{P=P_a} \tag{17}$$

In Eq. (17), K is the isothermal compressibility. The problem then reduces to finding $\partial E_{n,k}/\partial P$. This latter quantity can, in principle, be estimated from high pressure data, or obtained from a pressure dependent band structure calculation. Such calculations are available; the details have been discussed elsewhere (22) and need not be repeated here.

Fig. 7 shows a crystalline E-k diagram (full lines) along the [100] and [111] directions. The bars indicate the relative magnitude of $\gamma_{n,k}$. GaP is taken as an illustrative example. Results for other solids considered in this paper are similar. It is observed that the conduction states, in general, have larger $\gamma_{n,k}$ than the valence states. This is not unexpected, because the conduction states wave functions are more extended in space and therefore are more "sensitive" to the change of the local density resulting from structural
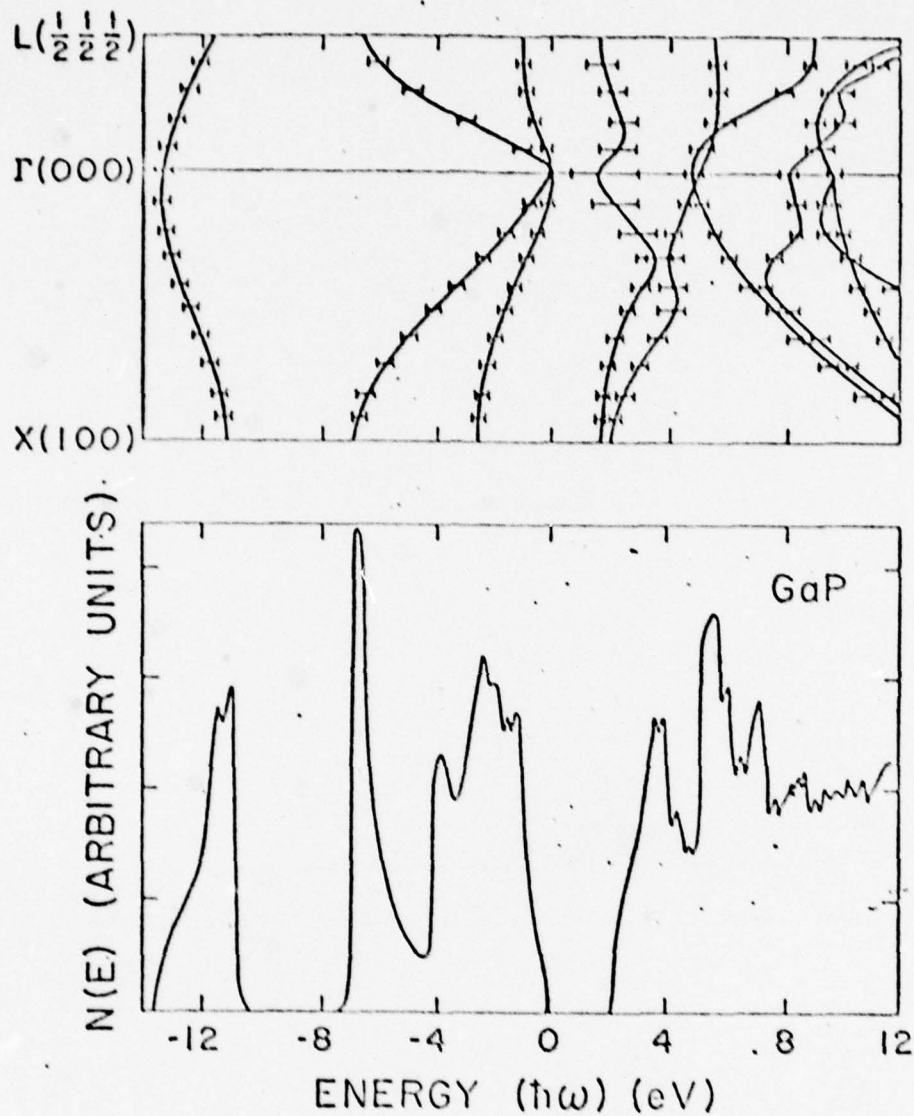
13

Fig. 7. Upper: crystalline E-k diagram (full curves)
along [100] and [111] directions. The bars indicate
the relative magnitude of $\gamma_{n,k}$'s. Lower: the crystal-
line density of states.

disorder. Figure 8 shows the calculated density of valence states (DVS) and density of conduction states (DCS) for GaP with various values of a "disorder parameter" defined as σ/ρ_a. Curve A of Fig. 8 is the least disordered. The DVS is essentially the same as its crystalline counterpart except for some smoothing-out of the fine structures in the upper-most valence band. The DCS, on the other hand, already shows substantial departure from the crystalline density of states, although the broad profiles remain. For Curve B and C, the values of σ/ρ_a are 0.13 and 0.2, respectively. The changes in DVS and DCS with the degree of disorder are vividly indicated by the trends manifested in these curves. Several points are particularly worth noting: (a) the widths of peaks of the DVS are very little affected by disorder except for the tailings of density of states into the crystalline "gap", i.e., regions of energies with no states; (b) higher degrees of disorder produce larger tailings. This is particularly significant regarding the crystalline optical gap, as shown in Fig. 8; (c) for a higher degree of disorder, (e.g. Curve B and C in Fig. 8) the fine structures in the crystalline DCS all but disappear, and is replaced by a single big hump followed by a flat plateau. Results of similar calculations for amorphous Ge and Si also show some hump-like structures in their DCS (4). A single-hump structured DCS has recently been reported by Eastman et al (23) for amorphous Ge, which is in contrast to the totally flat DCS previously deduced by Donovan et al (24) from UV photo-electron emission data. Although no experimental data on the DCS for III-V amorphous semiconductors are available at the present, such a one-hump structure appearing at the lower energy part of the conduction band of these materials is highly possible, because of the general similarity of their electronic structure to that of Ge. Fig. 9 shows the electronic densities of states for several III-V TBAS. In all cases, the changes induced in the DVS by disorder are much less significant in comparison with the corresponding changes in the DCS. Similar results were obtained for Ge and Si (4). A controversy regarding the structures of the lower energy part of the amorphous DVS is worthy of some discussion: For elemental TBAS, i.e., Ge and Si, the calculated results (4) for the present approach, show two distinct peaks (at $E \approx -8$ eV and -10 eV) in the lower-energy part of the DVS. This is in contrast to the experimental results of Ley et al (25), where it was found that the two distinct lower-energy peaks in the crystalline phase coalesced into a single big hump in the amorphous phase. Joannopoulos
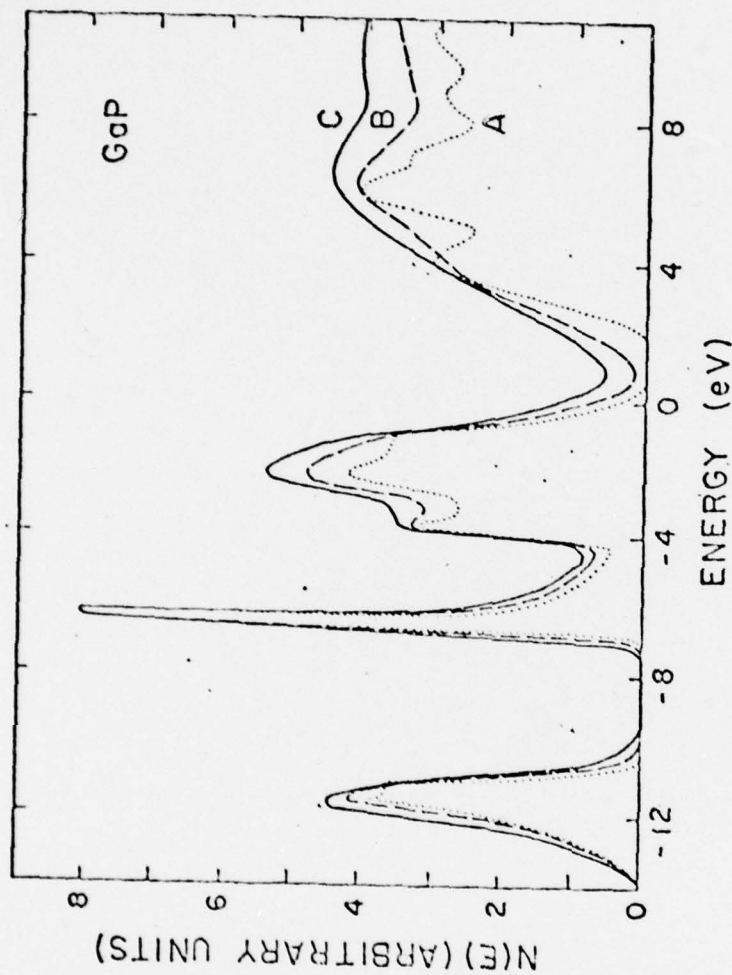
15

Bendow

191

Fig. 6. Electronic density of states for amorphous GaP calculated
with various values of disorder parameter σ/ρ_a, Curve A: $\sigma/\rho_a = 0.05$,
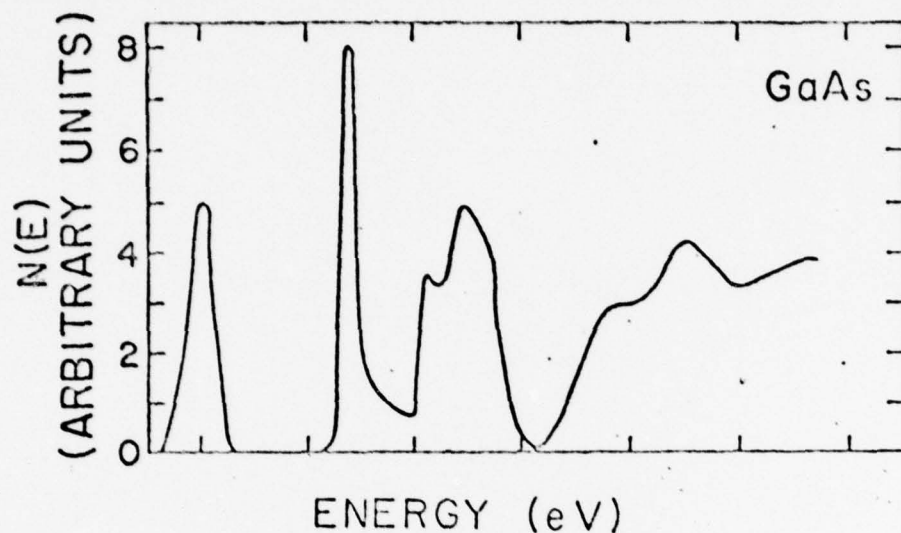Curve B: $\sigma/\rho_a = 0.13$, Curve C: $\sigma/\rho_a = 0.20$.

Fig. 9. Electronic densities of states for amorphous TBAS. (a) GaAs, with $\sigma/\rho_a = 0.077$, (b) GaSb, with $\sigma/\rho_a = 0.15$, (c) InAs, full curve: $\sigma/\rho_a = 0.1$, dashed curve: $\sigma/\rho_a = 0.06$.

and Cohen (26) argued that the possible existence of the five-fold rings in amorphous Ge and Si would introduce eigenstates with energies in between these two peaks, thus resulting in their apparent mixing. The argument based on five-fold rings has been disputed, for example, by Tejeda et al (27) and Treusch and Kramer (28). In fact, Treusch and Kramer demonstrated that the fluctuations in the second-neighbor distance leads to an additional effective potential $V(2,0,0)$ in amorphous TBAS. While this effect is small in compound semiconductors, it is large enough in amorphous Si and Ge to cause coalescence of the two low energy peaks in the amorphous phase. The DVS for several crystalline (29,30) and amorphous (29) III-V and II-VI semiconductors have recently been determined from x-ray photo-emission measurements. It was found (29) that the DVS of an amorphous compound is essentially a broadened version of its crystalline counterparts. The results of the present calculation indicate the same, although the extent of broadening is small except in the tailing parts. However, note that in the experimental results of Shevchik et al (29), the crystalline DVS is also greatly broadened as compared with theoretical results (31). We feel that since the

17a

Bendow

17b
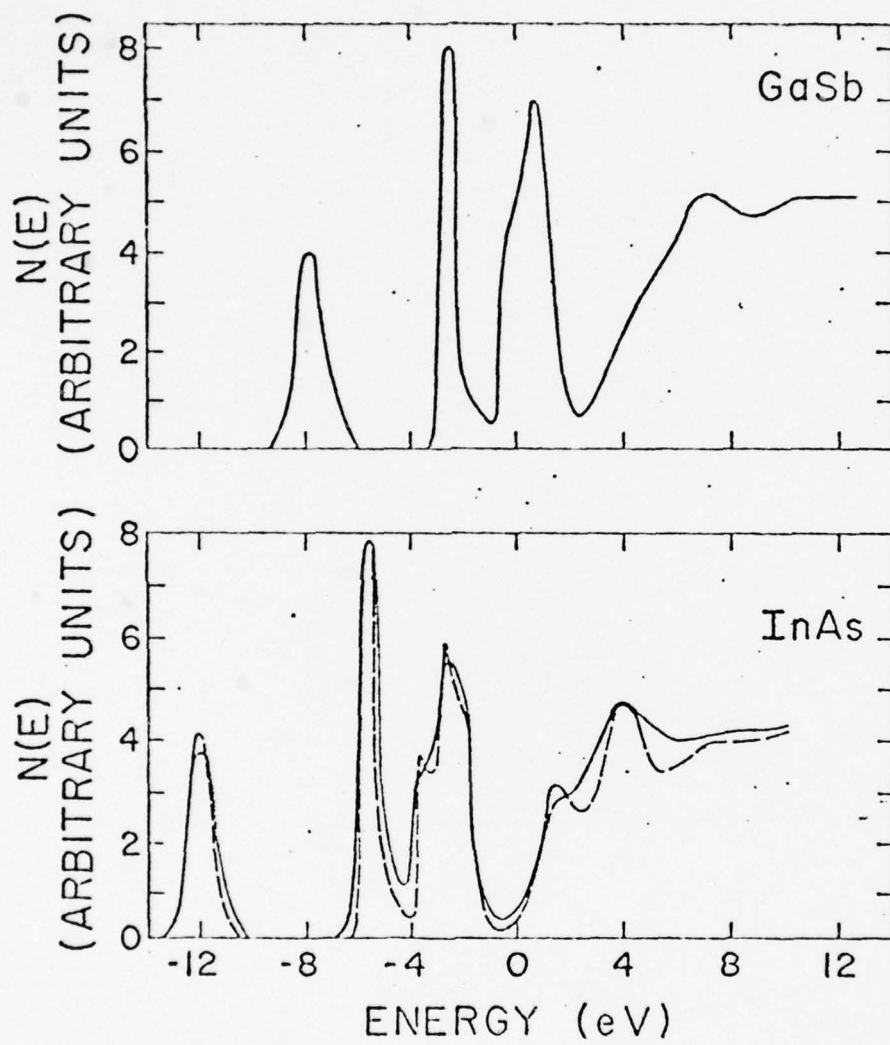
amorphous DVS are determined with the same experimental set-up (e.g. same resolution), much of the observed broadening might be similar in origin to that observed in the crystalline counterparts and not a result of disorder.

The imaginary part of the electronic dielectric constant, $\epsilon_2(\omega)$, is given by

$$\epsilon_2(\omega) \sim \frac{1}{\omega^2} |M(\omega)|^2 \sum_{i,f} \delta(E_f - E_i - \hbar\omega) \tag{18}$$

where the summation is performed over all initial states, i, and final states, f. $|M(\omega)|^2$ is the arithmetic average of the transition matrix element at photon energy ω. In the crystalline case, both momentum and energy are conserved, the summation in Eq. (18) can be represented by the joint density states. For the amorphous phase, we adopt the non-direct transition model (31a), for which

$$\epsilon_{2,a} \sim \frac{1}{\omega^2} |M(\omega)|_a^2 \, n_{con}(\omega) \tag{18'}$$

where $|M(\omega)|_a^2$ is the amorphous matrix element, which is obtained from that of the crystalline phase by smoothing out the umklapp peak (32) (a feature resulting specifically from crystalline long range order); $n_{con}(\omega)$ is the convoluted density of states of the DVS and DCS corresponding to energy ω. The imaginary part of the dielectric function $\epsilon_2(\omega)$ for several III-V compounds obtained in the above manner are compared with experimental data (33) in Figs. 10 to 13; the energy dependent matrix elements are shown as insets. For Si and Ge, (for which results are given elsewhere (4)) the agreement with experiment, regarding both peak position and shape of the calculated $\epsilon_2(\omega)$, is good. For III-V compounds, the agreement is good for GaP, GaAs and InAs; for GaSb, the calculated result is less satisfactory, in that the predicted position is shifted by more than 1 eV below the experimental data. In Fig. 10, we also show clearly how the disorder parameter affects the ϵ_2 spectrum of amorphous GaP. We note, in particular, that disorder will produce large density of states tailing into the crystalline optical gap, which in turn contributes to higher absorption at lower energies (i. e., a red shift of the peak). The discrepancy in the case of GaSb may in part result from inaccuracies in the tail of
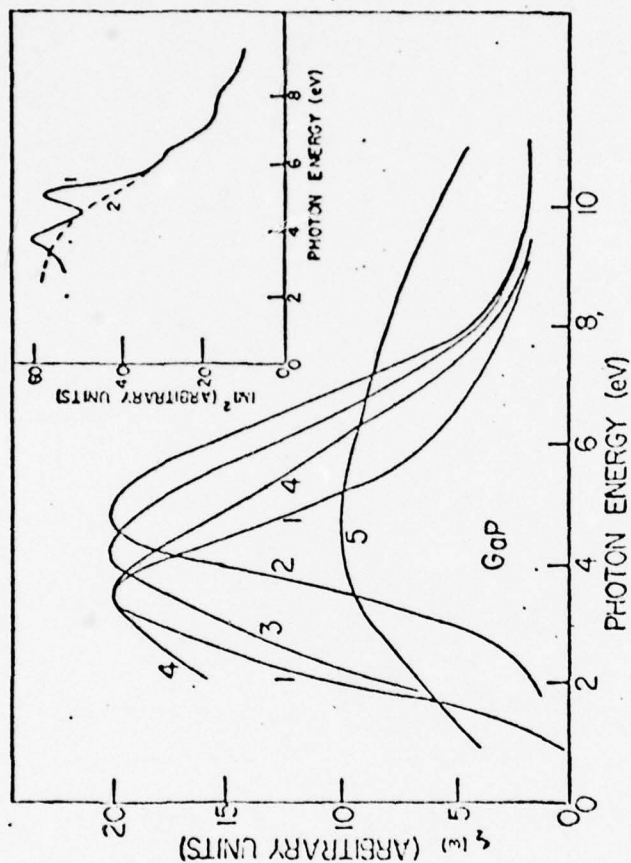
18

Bendow

Fig. 10. Imaginary part of dielectric constant versus photon energy for amorphous GaP. Curve 1: experimental data (Ref. 33). Curve 2: calculated in the present paper with $\sigma/\rho_a = 0.05$. Curve 3: same as Curve 2, but with $\sigma/\rho_a = 0.13$. Curve 4: same as Curve 2 but with $\sigma/\rho_a = 0.20$. Curve 5: same as Curve 2 but with $\sigma/\rho_a = 0.13$ and constant matrix element. Curve 1: crystalline matrix element. Curve 2: amorphous matrix element used in the present calculation.
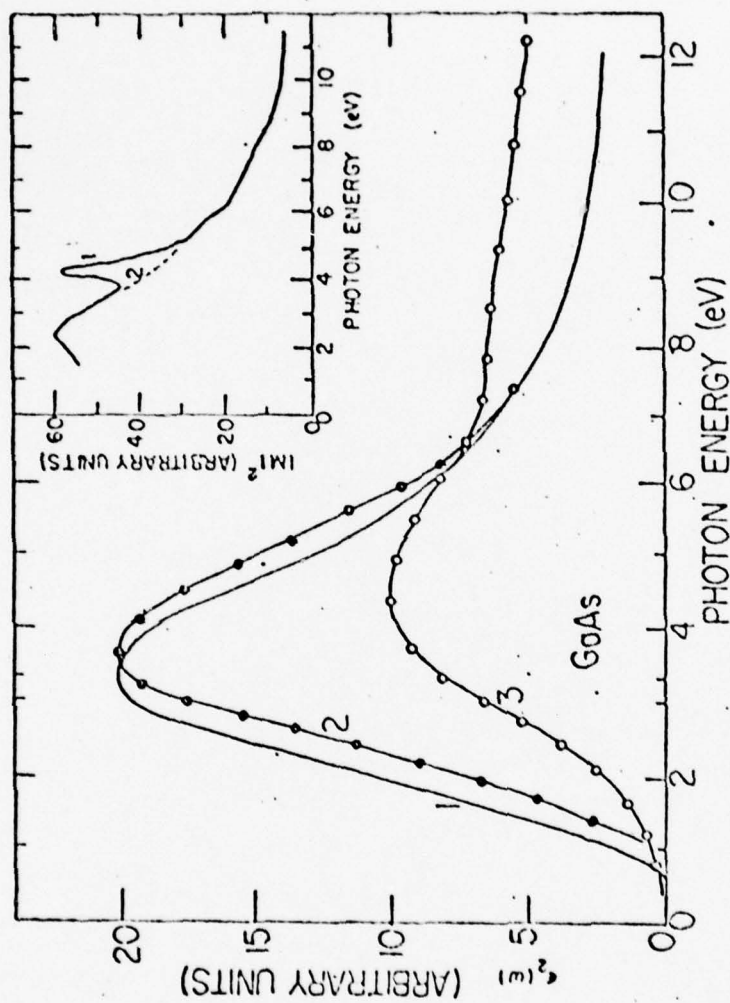
Fig. 11. Imaginary part of dielectric constant versus photon energy for amorphous GaAs. Curve 1: experimental data (Ref. 53). Curve 2: calculated in the present paper with $\sigma/\sigma_a = 0.077$. Curve 3: same as Curve 2, but with constant matrix element. Insert: same as in Fig. 10.
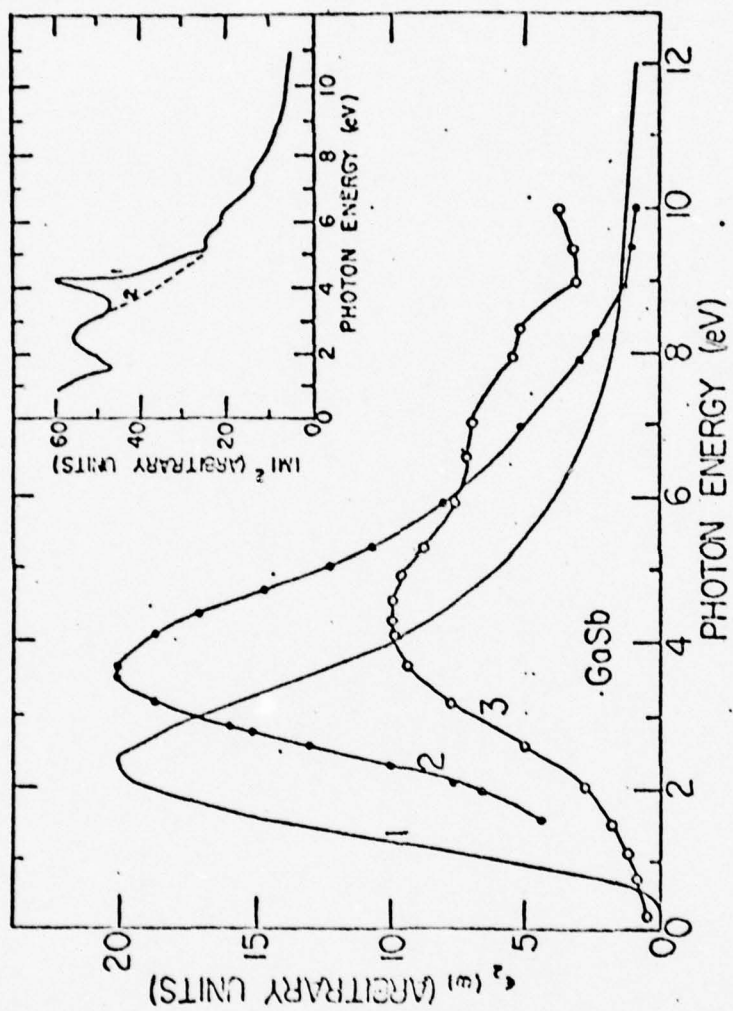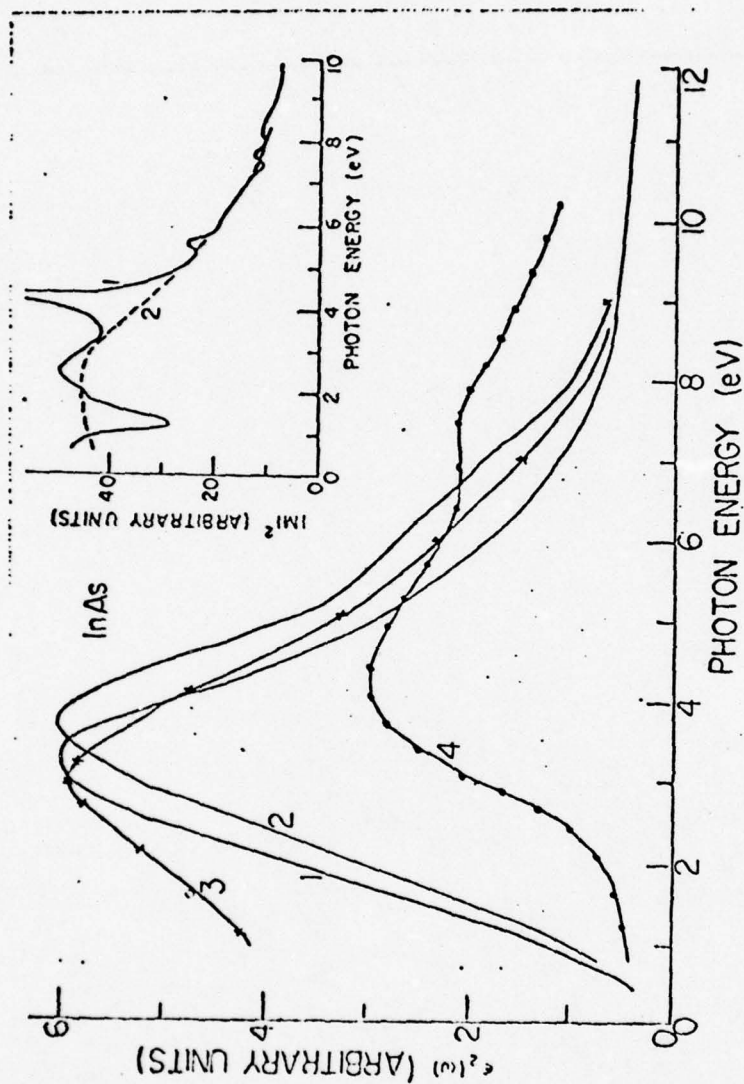
Fig. 12. Same as Fig. 11, but for amorphous GaSb.

Fig. 13. Imaginary part of dielectric constant versus photon energy for amorphous InAs. Curve 1: experimental data (Ref. 33). Curve 2: calculated in the present paper with $\sigma/\rho_a = 0.06$. Curve 3: same as Curve 2 but with $\sigma/\rho_a = 0.10$. Curve 4: same as Curve 2 with constant matrix element. Insert: same as in Fig. 10.

199

the density of states function predicted by the present calculation.

IV. Multiphonon Absorption

Multiphonon absorption is the principal loss mechanism limiting the transparency of infrared optical materials (34). Recently, a wide variety of theoretical and experimental studies of multiphonon absorption have been carried out (35). For certain applications, especially those requiring coatings or a thin-film geometry, the use of amorphous materials has been contemplated (36). The purpose of this section is to investigate the properties of the multiphonon absorption coefficient $\alpha(\omega)$ in amorphous solids, and to contrast them with predictions for the crystalline case.

To calculate α, we will utilize the single-particle (sp) model (37) which, although rather artificial, allows an exact treatment accounting for both anharmonicity and nonlinear moments. Although the absolute values predicted for α may not be reliable, trends in the frequency and temperature dependence, and trends in the ratio of the amorphous to the crystalline value for α are expected to be at least qualitatively correct.

Our calculations for α for the III-V's will be restricted to the {SL} portion alone. This is motivated by two considerations: (a) the S terms are small overall in these solids, and (b) the greatest modifications in the density of states appear at the lower frequencies which have a relatively minor effect on multiphonon processes in the transparent regime (35).

The absorption in the sp model is given by (37)

$$\alpha = \frac{4\pi\omega}{\mu c} \, \text{Im}\chi$$

$$\text{Im}\chi = \sum_{n} \left| <0|m(r)|n> \right|^{2} \delta(\omega - \omega_{no}) \tag{19}$$

where μ is the refractive index; $|n>$'s are eigenstates and ω_{no}'s eigenergies measured from the ground state of the Hamiltonian

23

Bendow

$$H = \frac{p^2}{2M} + \nu(r) \tag{20}$$

where ν is the sp (anharmonic) potential; m is the (nonlinear) moment. Various schemes (38) have been introduced to extract a continuous spectrum mimicking a crystal from the line spectrum of Eq. (19). For the present qualitative purposes it will be sufficient to merely interpolate between peaks to provide a continuous α. The justification for such procedures stems from more detailed calculations, which indicate substantial smoothing of the multiphonon absorption spectrum at higher frequencies (35) and from the considerations described at the end of this section. The Morse potential,

$$\nu = \nu_o(e^{-2\xi r} - 2e^{-\xi r}) \tag{21}$$

has been utilized previously in various sp calculations, and will be employed here as well; the moment will be chosen as (39)

$$m = m_o e^{-2\xi_1 r}. \tag{22}$$

If $\omega_o(\rho)$ is the harmonic frequency associated with a given value of density ρ, then α for the amorphous solid is given by

$$\alpha = \int d\rho P(\rho)\alpha(\omega_o(\rho)) \tag{23}$$

where we again employ a Gaussian distribution for the local density as discussed previously. We assume that the range parameters ξ and ξ_1 are the same in the amorphous solid as in the crystal, and account for changes in ω_o vs ρ through variations in ν_o. Since we do not account for changes in m_o (i.e., effective charge), the absolute magnitude of α will be unreliable, although the frequency and temperature dependence of α will not be substantially affected.

Before proceeding to the computed results for III-V's, it is instructive to indicate the general trends anticipated for $\alpha(\omega,T)$. For purposes of illustration it suffices to utilize an approximate result for α, valid for a crystal with a linear moment (34).

24

Bendow

$$\alpha(\omega) = \alpha_1 \exp[\ln\{(n_0+1)-B\}\omega/\omega_0 - \ln(n(\omega) + 1)] \qquad (25)$$

where α_1 and B depend relatively weakly on ω_0, and n_0 is the Bose-Einstein function for $\omega=\omega_0$; typically, $B \sim 4$ for zinc-blende semiconducting crystals (39). In the vicinity of the crystalline density ρ_c, the Gruneisen approximation, i.e., Eq. (5) is valid. Thus if $\rho_a/\rho_c \equiv \eta<1$, ω_0 decreases and $\alpha(\omega)$ falls more rapidly, while the reverse is true if $\rho_a/\rho_c>1$. The averaging procedure, on the other hand, always tends to broaden $\alpha(\omega)$. While the two effects act in the same direction for $\eta>1$, they oppose each other for $\eta<1$, which is the case for III-V TBAS. The determining factor is the extent of the spread in local density, as measured by the parameter σ in $P(\rho)$. A similar situation prevails regarding temperature dependence. For $\eta<1$, for example, the absorption at fixed ω involves more phonons and thus would be more highly temperature dependent; however, this tendency is counteracted by the averaging procedure which tends to reduce the overall dependence.

Examples of calculated results for $\alpha(\omega)$ obtained utilizing values of $n_0\xi$ and ξ_1 are taken from Ref. 39, and are illustrated in Fig. 14. Computations for GaSb, GaP, InAs and GaAs all predict that amorphous spectra display a lower rate of decrease as a function of ω than do the corresponding crystalline ones. Moreover, departures from exponential behavior are more evident than in the crystalline case. While the changes are relatively small in GaAs, they are very substantial in GaSb and GaP.

The effects of amorphousness on temperature dependence of multiphonon absorption are indicated in Fig. 15. The temperature dependence at fixed ω is suppressed substantially in the highly amorphous limit. Note that while amorphousness has a significant effect at quantum temperatures ($T/\omega_c<1$), the effect on α at high T ($T\omega_c>>1$) becomes relatively minor.

We have here found that it is possible for the decrease in α vs ω to be greater or less in an amorphous solid than in the crystalline counterpart, depending on the mean density and the spread in the density distribution. For the amorphous III-V's investigated, $\alpha(\omega)$ was always broadened relative to the crystal, and displayed greater departures from exponential behavior. The temperature dependence of α was
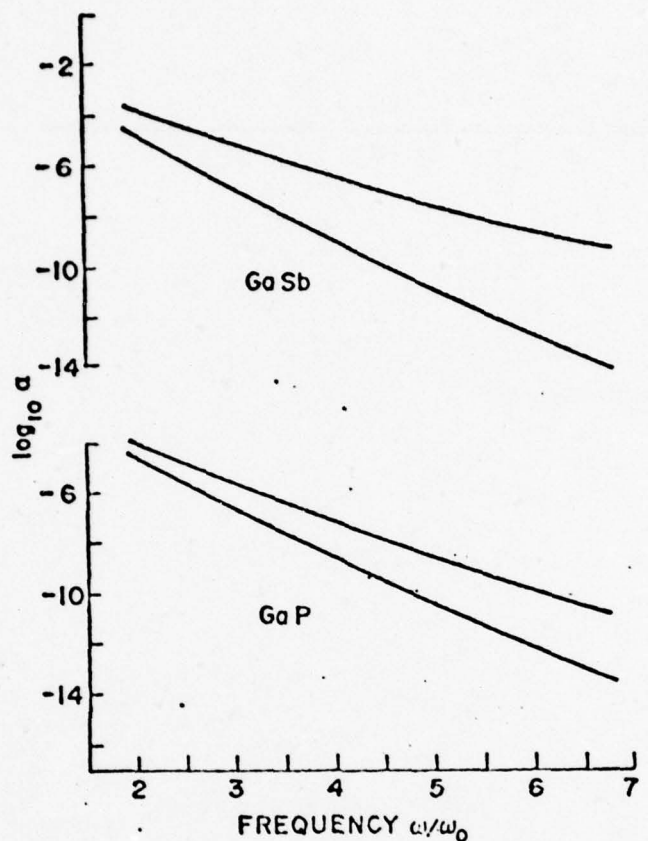
25

Bendow

Fig. 14. Log$_{10}$ of absorption coefficient vs. frequency ω/ω_0, where ω_0 is the crystalline harmonic frequency, for GaSb and GaP. The upper curves in each pair is the amorphous result, while the lower is the crystalline.

found to be suppressed in the amorphous solid, especially in the quantum regime. The III-V's investigated display a wide range of behavior; e.g., the effects of amorphousness are predicted to be relatively minor for GaAs, but substantial for GaSb. Since n_s is larger for amorphous Si and Ge than for III-V's, it is reasonable to surmise that α will be even more enhanced and broadened in these solids. Thus various potential infrared materials may, in their amorphous forms, incur inacceptable losses in applications requiring high transparency in the amorphous states. However, some qualification of the present results is in order. The calculations rely on rather limited amounts of input data, deduced from particular samples. Given the well-known fact that the
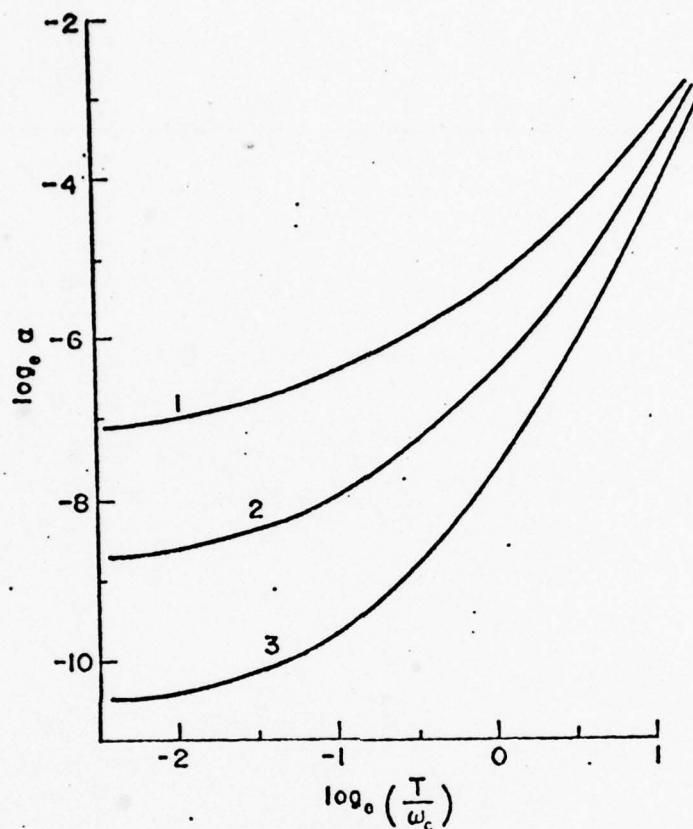
76

Bendow

Fig. 15. Log$_e$ absorption coefficient vs log$_e$(T/ω_c), where ω_c is the crystalline harmonic frequency at ω/ω_c = 3. Parameters characteristic of GaSb are used, except that σ/ρ_a is varied. Curve 1: σ/ρ_a = 0.22. Curve 2: σ/ρ_a = 0.15 (amorphous GaSb). Curve 3: σ/ρ_a = 0 (crystalline GaSb).

structural characteristics of an amorphous film are very dependent on its preparation conditions, the quantitative details of the present calculation may be unreliable, although we believe that the qualitative trends predicted are indeed correct.

V. Conclusions

We have here shown how microscopic density disorder affects the optical properties of solids, leading to shifting and broadening of spectral features, and to modifications of temperature dependence, as compared to crystalline solids.

27

Bendow

Such phenomena may be accounted for by considering the effects of density variation on crystalline spectra. A parameterization in terms of two classes of configurations, namely those conserving $\underline{k}$ and those which do not, appears useful. For solids which are only "slightly disordered", a prescription in terms of just the former is sufficient to describe the principal features of their spectra. Application of the method to tetrahedrally bonded amorphous semiconductors provides an interpretation of lattice and electronic spectra which is in overall good agreement with experiments. Moreover, it provides predictions of the intrinsic optical properties of disordered solids in regimes where they are not yet available experimentally, such as in the regime of high transparency in the mid-IR.

References

1. H. Shuker and R. W. Gammon, Phys. Rev. Letters 25, 222 (1970).

2. J. E. Smith, Jr., M. H. Brodsky, B. L. Crowder and M. I. Nathan, in Proc. Second Intl. Conf. on Light Scattering in Solids, ed. M. Balkanski (Flammarion Sciences, Paris, 1970), p. 330.

3. R. Alben, J. E. Smith, Jr., M. H. Brodsky and D. Weaire, Phys. Rev. Letters, 30, 1141 (1973); also, Phys. Rev. B11, 2271 (1975).

4. Y. F. Tsay, D. K. Paul, and S. S. Mitra, Phys. Rev. B 8, 2827 (1973).

5. S. S. Mitra, D. K. Paul, Y. F. Tsay and B. Bendow in "Tetrahedrally Bonded Amorphous Semiconductors" eds. M. H. Brodsky, S. Kirkpatrick and D. Weaire (Amer. Inst. Phys., New York, 1974), pp. 284-289.

6. See, for example, R. Grigorovici, J. Non-Cryst. Solids 1, 303 (1969), ibid 1, 571 (1969); ibid 4, 27 (1970).

7. Strictly speaking, such averages are meaningful only when taken over a complete set of configurations Ψ_n,

and when the 0's are operators in the space spanned by the Ψ_n's. For more approximate purposes, however, it is useful to relax these prescriptions to include the average values of arbitrary physical quantities 0 for which the set of values of 0(n), now viewed simply as the value of 0 corresponding to configuration n, are available.

8. W. Prettl, N. J. Shevchik and M. Cardona, Phys. Stat. Sol. (b) 59, 241 (1973).

9. R. W. Stimets, J. Waldman, J. Lin, T. S. Chang, R. J. Temkin and G. A. N. Connel, Solid State Commun. 13, 1485 (1973).

10. E. A. Fagan, in Proc. Fifth Intl. Conf. on Amorphous and Liquid Semiconductors, Garmisch-Partenkirchen, West Germany, 1973, pp. 601-607

11. See, for example, B. Donovan and J. F. Angress, in "Lattice Vibrations", (Chapman and Hall, London, 1971) p. 143.

12. See, for example, A. S. Barker in "Far Infrared Properties of Solids" edited by S. S. Mitra and S. Nudelman (Plenum Press, NY, 1970), p. 272.

13. For review of the structure of TBAS, see W. Paul in Proceedings of Nato Adv. Inst. on Physics of Structurally Disordered Solids, (Plenum Press, NY, to be published)

14. See, for example, S. S. Mitra in "Optical Properties of Solids", ed. S. Nudelman and S. S. Mitra, (Plenum Press, NY, 1969).

15. S. S. Mitra, Y. F. Tsay, D. K. Paul and B. Bendow, to be published.

16. See, for example, M. F. Thorpe, Phys. Rev. B 8, 5352 (1973).

17. D. W. Berreman, Phys. Rev. 130, 2193 (1963).

18. See, for example, D. Weaire and M. Thorpe, Phys. Rev. B 4, 2508 (1971); M. F. Thorpe and D. Weaire, Phys. Rev.

29

Bendow

B 4, 3518 (1971); and B. Y. Tong, AIP Conf. Proc. No.
20 "Tetrahedrally Bonded Amorphous Semiconductors",
M. H. Brodsky et al, eds.: AIP (1974)

19. F. Herman and J. P. Van Dyke, Phys. Rev. Letters 21,
1575 (1968).

20. D. Brust, Phys. Rev. 186, 768 (1969) and Phys. Rev.
Letters 23, 1232 (1969).

21. B. Kramer, K. Maschke and P. Thomas, Phys. Stat. Sol.
(b) 48, 635 (1971).

22. Y. F. Tsay, S. S. Mitra and B. Bendow, Phys. Rev. B
10, 1476 (1974).

23. D. E. Eastman, J. L. Freeouf and M. Erbudak, in
"Tetrahedrally Bonded Amorphous Semiconductors" eds.
M. H. Brodsky, S. Kirkpatrick and D. Weaire (Amer.
Inst. Phys., NY, 1974).

24. T. M. Donovan and W. E. Spicer, Phys. Rev. Letters,
21, 1572 (1968); Phys. Rev. B 2, 3971 (1970).

25. L. Ley, S. Kowalczyk, R. Polk and D. A. Shirley,
Phys. Rev. Letters 29, 1088 (1972).

26. J. D. Joannopoulos and M. L. Cohen, Solid State Commun.
11, 549 (1972); Phys. Rev. B 7, 2644 (1973).

27. J. Tejeda, N. J. Shevchik and M. Cardona, in Proc.
Fifth Intl. Conf. on Amorphous and Liquid Semicon-
ductors, Garmisch-Partenkirchen, W. Germany, 1973.

28. J. Treusch and B. Kramer, Solid State Commun. 14,
169 (1974).

29. N. J. Shevchik, J. Tejeda and M. Cardona, Phys. Rev.
B 9, 2627 (1974).

30. D. E. Eastman, W. D. Grobman, J. L. Freeouf and M.
Erbudak, Phys. Rev. B 9, 3473 (1974).

31. J. Chelikowsky, D. J. Chadi and M. L. Cohen, Phys.
Rev. B 8, 2786 (1973).

31a. See, for example, J. Tauc in "Optical Properties of Solids" edited by S. Nudelman and S. S. Mitra (Plenum, NY, 1969).

32. J. C. Phillips, in "Solid State Physics", eds. H. Ehrenreich, F. Seitz and D. Turnbull (Academic Press, NY, 1966), Vol. 18, p. 55.

33. J. Stuke and G. Zimmer, Phys. Stat. Sol. B 49, 513(1972).

34. B. Bendow, J. Elec. Mats. 3, 101 (1974).

35. Some theory papers: B. Bendow, S. C. Ying and S. P. Yukon, Phys. Rev. B 8, 1679 (1973); D. L. Mills and A. A. Maradudin, ibid, 1617 (1973); M. Sparks and L. J. Sham, ibid, 3037 (1973); K. V. Namjoshi and S. S. Mitra, Phys. Rev. B 9, 815 (1974); H. B. Rosenstock, ibid, 1973 (1974); T. C. McGill, R. W. Hellwarth, M. Mangir and H. V. Winston, J. Phys. Chem. Sol. 34, 2105 (1973). Some experimental papers: T. F. Deutsch, J. Phys. Chem. Sol. 34, 2091 (1973); J. A. Harrington and M. Hass, Phys. Rev. Letters 31, 710 (1973); L. H. Skolnik, H. G. Lipson and B. Bendow, Appl. Phys. Lett. 25, 442 (1974); K. V. Namjoshi, S. S. Mitra, B. Bendow, J. A. Harrington and D. L. Stierwalt, ibid, 26, 41 (1975).

36. "Proceedings 3rd Conference on IR Laser Windows", C. A. Pitha et al, eds. (AFCRL, Bedford, MA 1974).

37. See, for example, D. L. Mills and A. A. Maradudin, and T. C. McGill et al, op. cit, Ref. 35; Also, B. Bendow and S. P. Yukon, in "Proc. of Conf. on Optical Properties of Highly Transparent Solids", S. S. Mitra and B. Bendow, eds. (Plenum, NY, in press).

38. See, for example, H. B. Rosenstock, op. cit., Ref. 35, and L. L. Boyer et al, in Proceedings, op. cit., Ref 37.

39. B. Bendow, S. P. Yukon and S. C. Ying, Phys. Rev. B 10, 2286 (1974).

4.4 PSEUDOPOTENTIAL CALCULATION OF ELECTRONIC BAND STRUCTURE OF CRYSTALLINE AND AMORPHOUS ARSENIC[*]

A. Vaidyanathan
Department of Physics
University of Rhode Island
Kingston, Rhode Island 02881

and

Y. F. Tsay[+] and S. S. Mitra
Department of Electrical Engineering
University of Rhode Island
Kingston, Rhode Island 02881

ABSTRACT

The electronic density of states of crystalline arsenic is calculated using the empirical pseudopotential method. The structure of amorphous arsenic is believed to preserve the double-layer nature of its crystalline counterpart, but with randomly distributed interlayer separations, or equivalently, the internal displacement parameter, u. Thus to simulate the amorphous situation, the electronic density of states corresponding to values of u slightly different from the crystalline value are calculated. Finally, these electronic densities of states are added, weighted with a Gaussian probability distribution in u to yield the amorphous electronic density of states. The nondirect transition model along with the energy dependent matrix elements is used to evaluate the imaginary part of the dielectric constant. A Kramers-Kronig transformation is performed to obtain the real part of the dielectric constant. The electronic density of states of crystalline and amorphous As are compared with each other and with available theoretical and experimental results.

The real and imaginary parts of the dielectric constants and the absorption coefficient of amorphous As are also reported.

I. INTRODUCTION

In the last few years, there has been considerable interest[1] in studying the structural and optical properties of crystalline and amorphous forms of the same material in order to understand the effects of disorder; especially the changes brought about in the above properties due to the relaxation of the momentum conservation rule.

After the successful empirical pseudopotential method (EPM)[2] and self-consistent orthogonalised plane wave (SCOPW)[3] calculations of the energy bands of crystalline As of rhombohedral structure, various workers have turned their attention to the study of the structural and optical properties of As. Van Dyke[4] has used the EPM to calculate the densities of states of two different forms of crystalline As. Ley et al[5] have experimentally obtained the X-ray photoelectron spectra (XPS) of the valence bands of crystalline and amorphous As. Bishop and Shevchik[6] have measured the valence band density of states of crystalline and amorphous As using high resolution photoemission experiments. Kelly And Bullett[7] have calculated the EDOS of crystalline and amorphous As using the recursion method. Raisin et al[8] have measured the reflectivity and absorption spectra of amorphous As. Krebs and Steffen[9] have obtained the radial distribution functions (RDF) for two different forms of glassy As from X-ray diffraction measurements.

Greaves and Davis[10] have constructed a continuous random network model for amorphous As, based on the threefold coordination and bond angles found in the double-layer structure of crystalline As. Breitling[11] showed, from X-ray diffraction measurements of three different forms of amorphous As, that the double-layer structure of crystalline As is retained in the amorphous state. Further, he deduced that the shortest layer distance is 4.05 $\AA$ in precipitated amorphous As, 3.66 $\AA$ in evaporated amorphous As and 3.15 $\AA$ (same as the crystalline value) in precipitated amorphous As that has been annealed at 250°C and in high vacuum for five hours.

In this paper we calculate the electronic band structure and density of states of As using the EPM. The calculations are performed for 5 different values of the internal displacement parameter, u, in order to understand the role played by the above parameter in determining the electronic structure of As. Using a phenomenological model, that incorporates a Gaussian distribution of the inter-layer distance, the density of states and optical constants of amorphous As are calculated. The densities of states of crystalline and amorphous As are compared and the effect of disorder arising from the variation in u, is discussed.

II. BAND STRUCTURE AND DENSITY OF STATES OF CRYSTALLINE As

Arsenic belongs to group V of the periodic table and exists in two different crystalline forms[4]. In the black phosphorous structure, As has an orthorhombic unit cell and is a narrow gap semiconductor. In the A7 structure, As has

a rhombohedral unit cell and is a semimetal. The latter, which is considered in this work, is the normal As. The rhombohedral unit cell of normal crystalline As has two atoms associated with each lattice point (Figure 1a). The two atoms are located along the trigonal axis and are separated by a distance 2ud, where d is the trigonal body diagonal and u is the internal displacement parameter. For crystalline As, u has a value of 0.226. The point midway between the two adjacent atoms along the trigonal axis is a center of inversion for the unit cell, and is usually chosen as the origin of the coordinate system, so that the structure factor becomes real[2].

The EPM[12] is employed to calculate the electronic band structure. The pseudopotential form factors P1 of reference 2 were used, since they were found by Falicov and Golin[2] to successfully reproduce the data on band structure obtained from experimental measurements of deHaas-Van Alphen effect[13]. Following the procedure described by Brust[14], 20 to 30 plane waves are treated exactly and a further 70 to 80 plane waves are included by first order Löwdin perturbation[15]. The resulting band structure for electron wave vector $\vec{k}$ along several important directions, is shown in Figure 2a.

In order to calculate the crystalline density of states, the energy eigenvalues were calculated at 191 evenly distributed sampling points in the irreducible part of the first Brillouin zone, shown in Figure 3. Quadratic interpolation was used to extend the results to 349 finer mesh points

closest to each of the sampling points. The resulting density of states is compared in Figure 4 with the experimental density of states obtained from XPS by Ley et al[5] and that obtained from high resolution photoemission experiments by Bishop and Shevchik[6]. The overall agreement between our result and the experimental results is seen to be good. We would like to point out that even though the structure in the p-like valence subbands between 4 and 5 eV obtained in our calculation is missing in the results of Ley et al[5], the results of Bishop and Shevchik[6] confirm the structure. Our result is also in good agreement with the results of the calculations of Van Dyke[4] and Kelly and Bullett[7].

Our calculated splitting of the low energy peaks in the valence band density of states is more pronounced than that observed in the experiments. The bottom of the valence band according to the present calculation, is at 15.2 eV below the Fermi level. This is in better agreement with the results of tight-binding and SCOPW calculations as reported in reference 5, than with the experimental results.

III. DENSITY OF STATES AND OPTICAL CONSTANTS OF AMORPHOUS As

As mentioned above, arsenic crystallizes in a double layer structure. In the following, we discuss those aspects of the structure which are relevent to our model of amorphous As. As mentioned above, two interpenetrating face-centered rhombohedral lattices form the crystal lattice of As. Thus the primitive cell contains two atoms, each belonging to a different rhombohedral sublattice. Any par-

ticular atom is sited on one of the [111] planes and has
three nearest neighbors on the adjacent parallel plane;
three next nearest neighbors lie on another [111] plane on
the other side of the given atom, but substantially further
away. Planes normal to the trigonal [111] direction occur
in pairs in which the atoms are comparatively close to one
another, while these double layers are more widely spaced.
Three different arrangements of the atoms on the planar net-
works exist. A projection onto the xy-plane (Figure 1b)
shows the relationship between these networks, labeled A,
B, and C, which follow sequentially along the z-axis and are
separated by the short and long interplanar spacings in
turn. The crystal structure is described by the sequency
123 123 123 of three types of double layer network (Figure
1c). It can be shown that the separation of a plane, along
the [111] direction, from its adjacent planes depends on the
value of the internal displacement parameter u. In fact,
these distances are given by[16]

$$w_o = 6ru - r$$
$$v_o = 2r - 6ru$$

where r is one third of the body diagonal of the rhombohedral
unit cell.

In our model calculation for amorphous As, it is as-
sumed that the rhombohedral unit cell of the crystalline As
is unchanged, but the internal displacement parameter u has
a distribution of $\sim 10^\circ/o$ about its crystalline value. This

changes the values of v_o and w_o by the same amount, but in opposite directions, so that the separation $v_o + w_o$ is constant. Our model allows variations in the first and second nearest neighbor distances, while still preserving the rhombohedral unit cell and double layer nature of crystalline As.

Breitling has shown[11] from X-ray diffraction measurements that the structure of amorphous As is crystalline-like, and that amorphous As is found to exist in three different forms with different inter-layer distances. Williams and Weaire[17] have calculated the change in the total energy of As when the rhombohedral angle and the internal displacement parameter are varied independently. From these results we see that for the changes in u that we consider here the change in the total energy is indeed very small, (~ 0.1 eV). These findings suggest that our model is a reasonable one to start with in the study of the electronic structure and optical properties of amorphous As.

Band structure and density of states are calculated for five different values of u within the limits $\pm 10^o/o$ of the crystalline value. The band structure for three different values of u are shown in Figures 2a, 2b, and 2c. The amorphous density of states is approximated by summing the five densities of states weighted with the function: $\exp[-(u_o-u)^2/(2o^2)]$. Greaves and Davis[10] have estimated the Gaussian spread in the nearest neighbor distance o to be 0.1 Å. From this we estimated the Gaussian spread in u to be 0.00975. The resulting density of states of amorphous

As is shown in Figure 5 along with the experimental results of Ley et al[5], and Bishop and Shevchik[6].

On comparing our crystalline and amorphous densities of states, we note the following: most of the features are common to both of them; the structure in the p-like valence sub-bands noticed in the crystalline case is retained in the amorphous form. This is in agreement with the experimental results of Biship and Shevchik[6]. The splitting in the valence band between 10 eV and 14 eV below the Fermi level becomes less pronounced in going from the crystalline to the amorphous form. Ley et al[5] however, found from X-ray photoemission experiment, that the two low energy peaks virtually coalesce into a single big hump. More recent experiments by Bishop and Shevchik[6] indicate that the pronounced two peak structure is greatly reduced in the amorphous form. This is believed to result from the presence of five-fold rings in the amorphous form. Tejeda et al[18] and Treusch and Kramer[19], however, have shown that similar effects observed in group IV semiconductors may also be a consequence of the fluctuations in second nearest neighbor positions, and therefore does not necessarily arise exclusively from the five-fold rings. Our model does not assume any odd membered rings. The slight mixing of the two peaks in our model is caused by the variation in the internal displacement parameter, which causes variations in the first and second neighbor distances. Our calculated density of states of amorphous As is in fair agreement with the result of the calculation by Kelley and

Bullett[7].

The imaginary part of the dielectric constant is given by the formula[20]

$$\varepsilon_2(\omega) \sim \frac{1}{\omega^2} \, |M(\omega)|^2_{amorp} \, n_c(\omega) \tag{1}$$

where ω is the angular frequency of the photon, $|M(\omega)|^2$ is the arithmetical average probability of dipole transitions[21] at frequency ω, and $n_c(\omega)$ is the convoluted density of states of the valence and conduction bands for which energy is conserved. In the above formula the convoluted density of states is used instead of the joint density of states because, in the amorphous solid the $\vec{k}$-selection rule breaks down and only energy is conserved[20].

Amorphous matrix elements as used in this paper have been obtained from the energy dependent crystalline matrix elements, which we calculated by smoothing out umklapp-enhanced transitions and retaining as much energy dependence of the crystalline case as possible. The $\varepsilon_2(\omega)$ calculated using equation (1) is shown in Figure 6a.

The real part, $\varepsilon_1(\omega)$, of the complex dielectric constant is related to the imaginary part, $\varepsilon_2(\omega)$, by the Kramers-Kronig relation[22]

$$\varepsilon_1(\omega) = 1 + \frac{2}{\pi} \, P \int_0^\infty \frac{\varepsilon_2(\omega')\omega'd\omega'}{\omega'^2 - \omega^2} \tag{2}$$

in which P is the principal value of the integral. To use this formula one needs $\varepsilon_2(\omega)$ over all frequencies. Since

we have $\varepsilon_2(\omega)$ only for a limited range of frequency, we attach a structureless tail of the form A/ω^2 to the calculated ε_2 spectrum. The constant A is determined by the continuity relation. The $\varepsilon_1(\omega)$ spectrum thus obtained is shown in Figure 6b.

The absorption coefficient $\alpha(\omega)$ is given by

$$\alpha(\omega) = \frac{\varepsilon_2(\omega)\ \omega}{c\ n(\omega)} \tag{3}$$

where c is the velocity of light in vacuum and $n(\omega)$ is the real part of the complex index of refraction, defined by

$$n^*(\omega) = n(\omega) + ik(\omega) \tag{4}$$

$n(\omega)$ is calculated using the two simultaneous equations

$$n^2 - k^2 = \varepsilon_1 \tag{.5}$$

$$2nk = \varepsilon_2 \tag{6}$$

$\alpha(\omega)$ calculated using equation (3), (5) and (6) is compared with the experimental absorption spectrum[8] in Figure 7. The peak value of our absorption coefficient was scaled to equal the peak value of the experimental α. The overall agreement between the theoretical and experimental absorption spectra is seen to be quite good.

IV. SUMMARY AND CONCLUSIONS

We have presented a calculation of EDS of amorphous As. We regard the structure of amorphous arsenic as preserving the double layer structure of crystalline As, but with

interlayer separations distributed randomly. The latter can be described conveniently in terms of a random distribution of the internal displacement parameter u. Such a structural model for amorphous As is consistent with experimental data of RDF. This model is also plausible in view of the fact that the total energy of the structure is slightly different from that of crystalline As. The slight deviation of u from the crystalline value can be regarded as a random perturbation, which broadens, to various extents the energy of each and every state. The extent of the broadenings due to u is determined approximately by calculating the crystalline band structure with various values of u. The amorphous EDS is obtained in the present paper, by summing up crystalline EDS with various u weighted by a Gaussian probability distribution. Such a procedure is, in fact, equivalent to broadening each individual energy level with different broadening parameters which is determined by how sensitively the individual energy levels shift with respect to the change in u. Our model predicts electronic density of states and absorption coefficient that are in reasonable agreement with existing data.

ACKNOWLEDGMENTS

One of us (SSM) is grateful to Professor S. Robin-Kandare for many helpful discussions and communicating to us some of her unpublished data. We also thank Dr. N. J. Shevchik for bringing our attention to his experimental results.

REFERENCES

*Supported in part by Air Force Cambridge Research Laboratories, Contract No. F19628-75-C-0163.

+Present address: NRC Post-Doctoral Resident Research Associate at AFCRL, Hanscom Air Force Base, Bedford, Mass. 01731.

1. See for example, Y. F. Tsay, D. K. Paul and S. S. Mitra, Phys. Rev. B $\underline{8}$, 2827 (1973) and references therein.

2. L. M. Falicov and Stuart Golin, Phys. Rev. $\underline{137}$, A871 (1965).

3. Stuart Golin, Phys. Rev. $\underline{140}$, A993 (1965).

4. J. P. Van Dyke, J. Non-Cryst. Solids $\underline{12}$, 263 (1973).

5. L. Ley, R. A. Pollak, S. P. Kowalczyk, R. McFeely and D. A. Shirley, Phys. Rev. B $\underline{8}$, 641 (1973).

6. S. G. Bishop and N. J. Shevchik, Phys. Rev. B $\underline{12}$, 1567 (1975).

7. M. J. Kelly and D. W. Bullett, Solid State Commun., $\underline{18}$, 593 (1976).

8. C. Raisin, S. Robin and J. Robin, C. R. Acad. Sci., Paris B $\underline{274}$, 555 (1972). Also personal communication from S. Robin-Kandare.

9. H. Krebs and R. Steffen, Z. anorg. alg. chem. $\underline{327}$, 224 (1964).

10. G. N. Greaves and E. A. Davis, Phil. Mag. $\underline{29}$, 1201 (1974).

11. G. Breitling, J. Vacuum Sci. Technol. $\underline{6}$, 628 (1969).

12. M. L. Cohen and Volker Heine, Solid State Physics, edited by H. Ehrenreich, F. Seitz and D. Turnbull, (Academic Press, New York, 1970), vol. 24, p. 37.

13. T. G. Berlincourt, Phys. Rev. 99, 1716 (1955).

14. D. Brust, Phys. Rev. 134, A1337 (1964); 139, A489 (1965).

15. P. Lowdin, J. Chem. Phys. 19, 1396 (1951).

16. J. C. Slater, Quantum Theory of Molecules and Solids (McGraw-Hill, New York, 1965), vol. 2, p. 47.

17. See for example, V. Heine and D. Weaire, Solid State Physics, edited by H. Ehrenreich, F. Seitz and D. Turnbull, (Academic Press, New York, 1970), vol. 24, p. 416.

18. J. Tejeda, N. J. Shevchik, and M. Cardona, Proc. of the Fifth Intl. Conf. on Amorphous and Liquid Semi-conductors, Garmisch-Partenkirchen, ed. J. Stuke and W. Brenig (Taylor and Francis, 1974), p. 557.

19. J. Treusch and B. Kramer, Solid State Commun. 14, 169 (1974).

20. J. Tauc, Optical Properties of Solids, edited by S. Nudelman and S. S. Mitra (Plenum Press, New York, 1969), p. 123.

21. (a) K. Maschke and P. Thomas, Phys. Status Solidi 41, 742 (1970); (b) B. Kramer, K. Maschke, P. Thomas and J. Teusch, Phys. Rev. Letters 25, 1020 (1970).

22. M. Cardona, Optical Properties of Solids, edited by S. Nudelman and S. S. Mitra (Plenum Press, New York, 1969), p. 137.
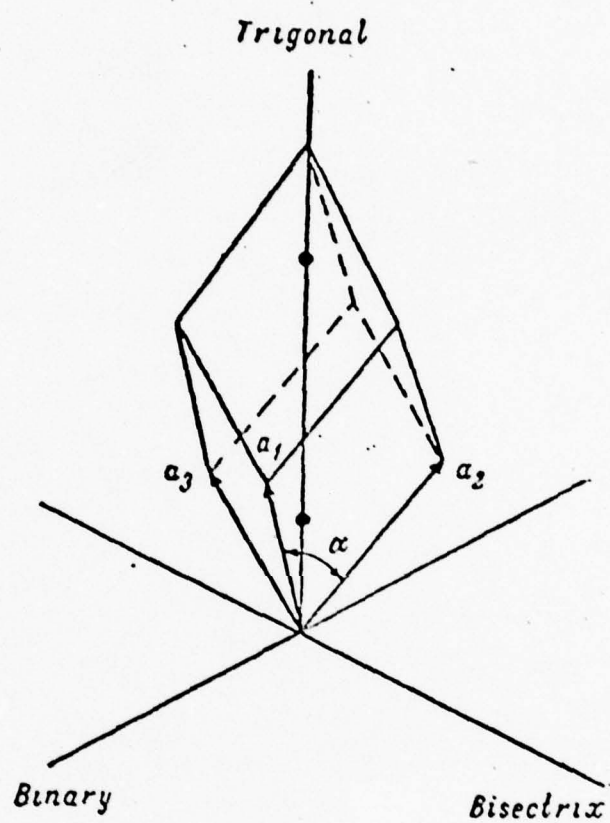
FIGURE CAPTIONS

Figure 1 (a).The rhombohedral unit cell of As in the A7 structure. The dots represent the two atoms in the unit cell. $|\vec{a}| = 4.1318$ A and $\alpha = 54^{\circ}13'$.

(b).The arrangement of the three types of atomic networks A, B and C in crystalline arsenic projected on the xy plane.

(c).The sequential nature of the planes normal to the z-axis in As. Single planes are separated alternately by $v_o(=2.2531$ A) and $w_o(=1.2529$ A) and are arranged in the sequence ABCABC. The double layer planes follow the order 123123123.

Figure 2 (a).E-$\vec{k}$ diagrams for crystalline As along a few high symmetry directions. The internal displacement parameter u is assumed to be the normal crystalline value of 0.226.

(b). E-$\vec{k}$ diagrams for As with u = 0.95 x 0.226.

(c). E-$\vec{k}$ diagrams for As with u = 1.05 x 0.226.

Figure 3 The first Brillouin zone of As (A7 structure). The zone bounded by the interior planes ΓLL', ΓLUT, ΓL'XT and the surface planes constitutes the irreducible part of the Brillouin zone and its volume is one-twelfth of the volume of the Brillouin zone. For a more detailed description of the Brillouin zone, please see reference 2.
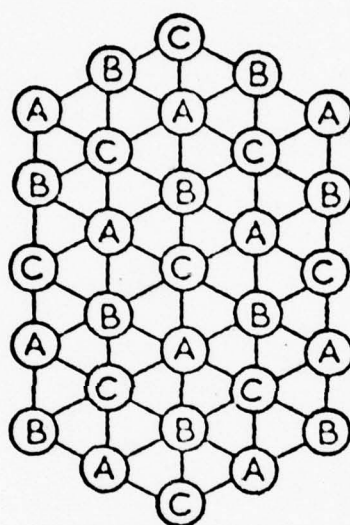
Figure captions cont.

Figure 4   Electronic density of states of crystalline As.
Solid line is our result. ooooo is due to
Loy et al[5], xxxxx is due to Bishop and Shevchik[6].

Figure 5   Electronic density of states of amorphous As.
Solid line is our result. ooooo is due to
Ley et al[5], xxxxx is due to Bishop and Shevchik[6].

Figure 6   (a). Imaginary part of the dielectric constant,
$\epsilon_2(\omega)$, of amorphous As plotted as a function of
energy.

(b). Real part of the dielectric constant, $\epsilon_1(\omega)$,
of amorphous As obtained by performing a Kramers-
Kronig transformation of $\epsilon_2(\omega)$.

Figure 7   Absorption coefficient of amorphous As, as a
function of energy. The experimental result
is due to Raisin et al[6].
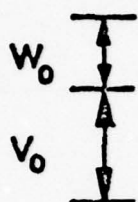
225

x-y plane

231

DENSITY OF STATES (Arbitrary Units)
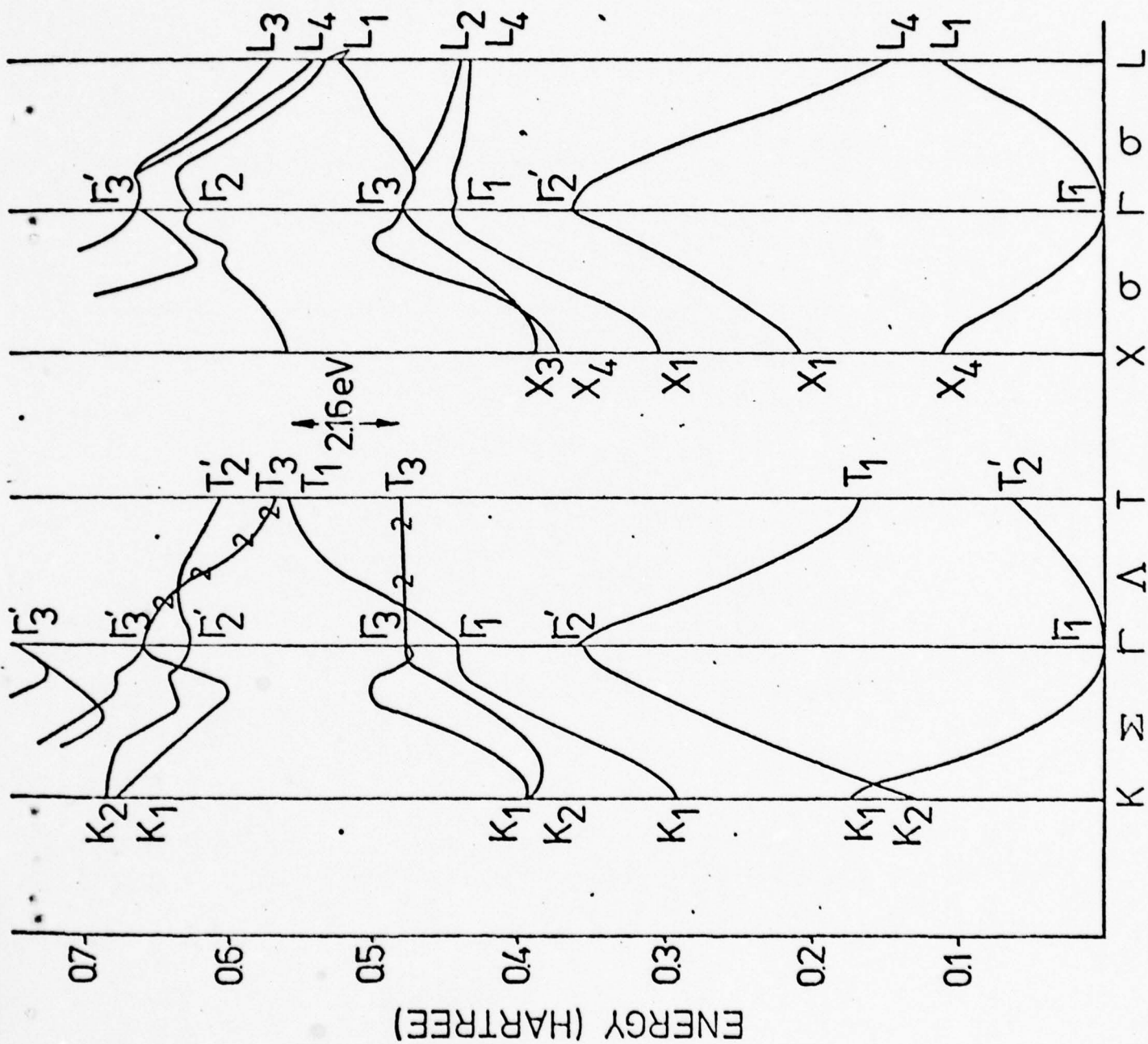
BINDING ENERGY (eV)

DENSITY OF STATES (Arbitrary Units)

BINDING ENERY (eV)

234

ABSORPTION COEFFICIENT (10^5 cm^{-1})
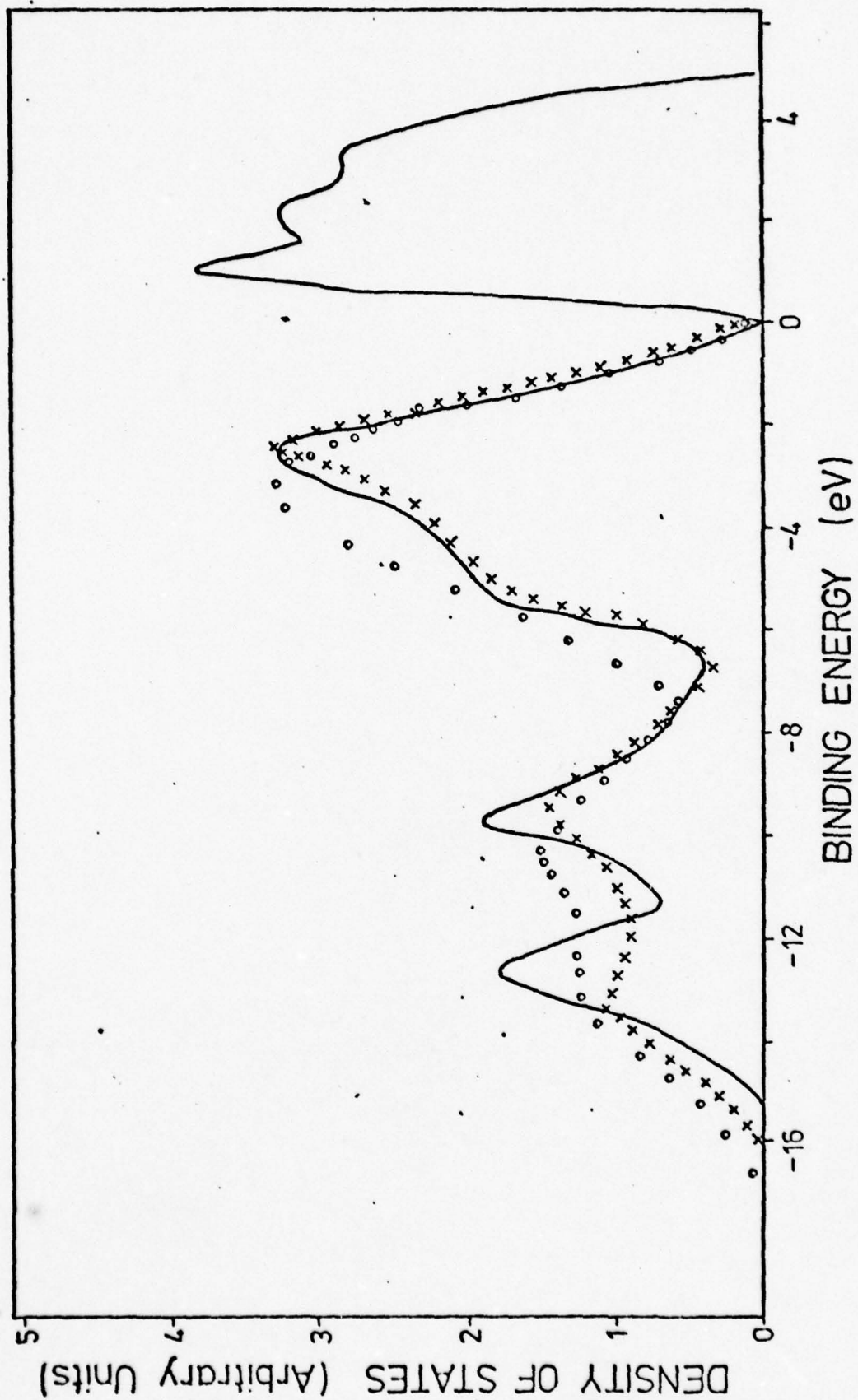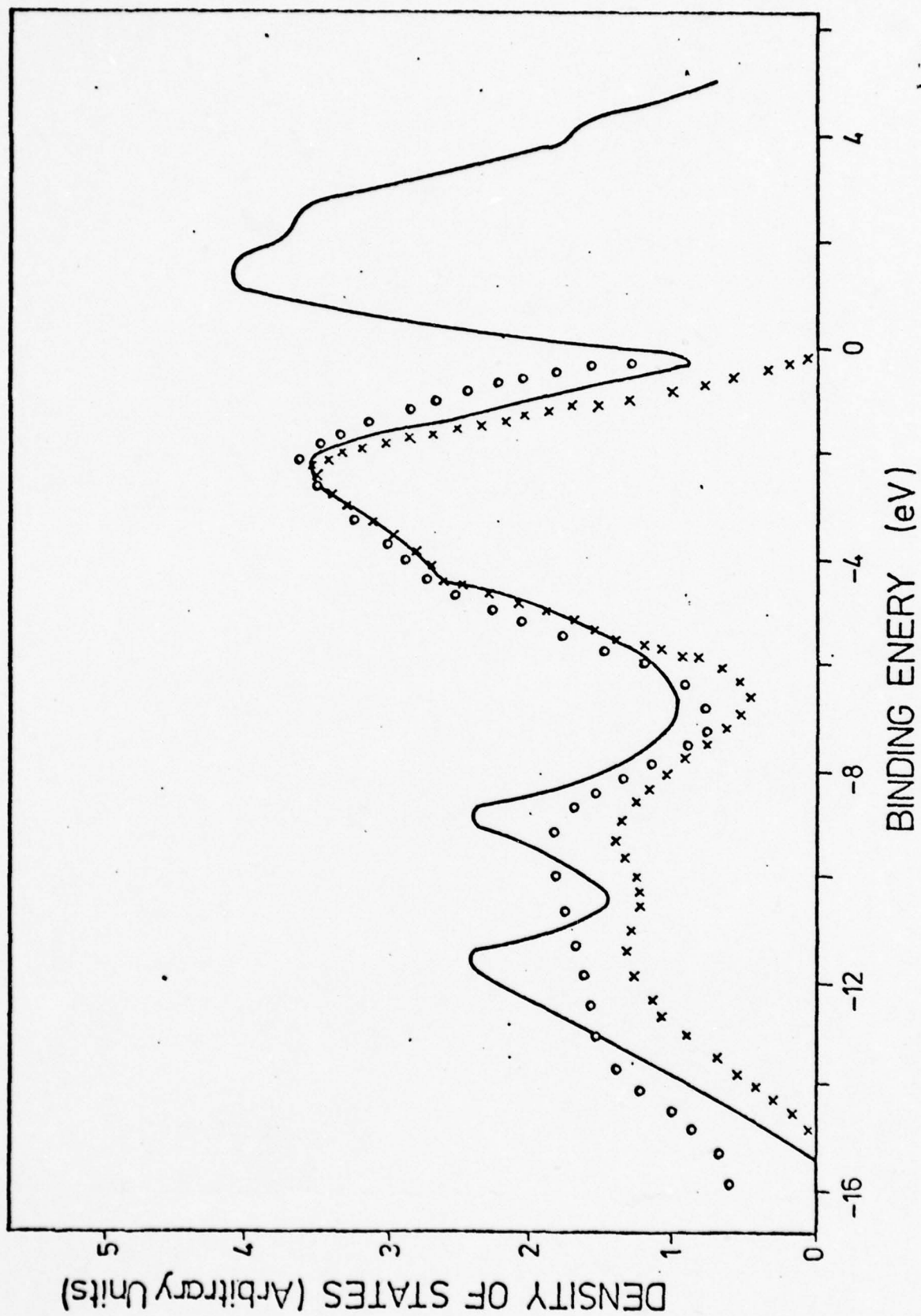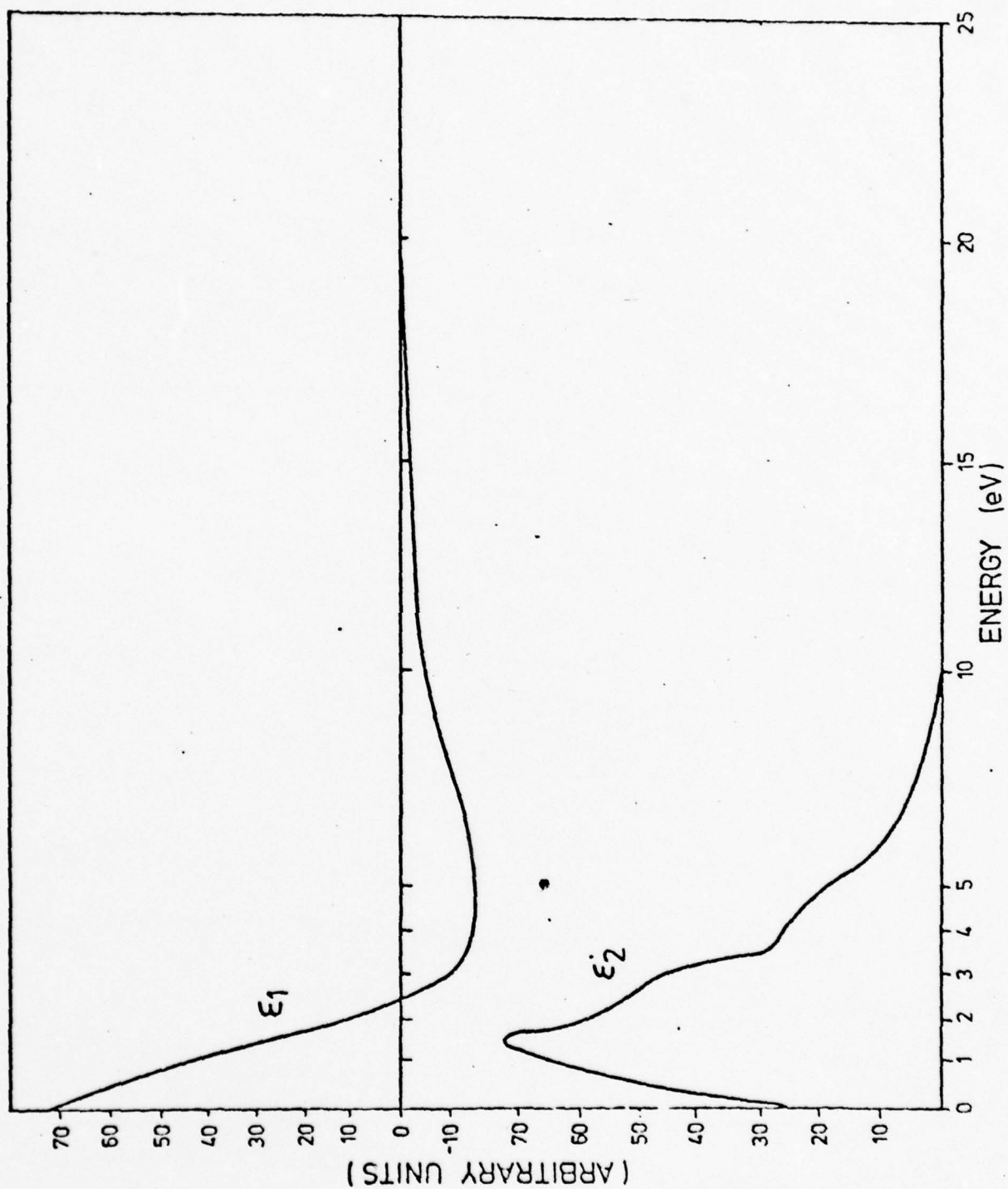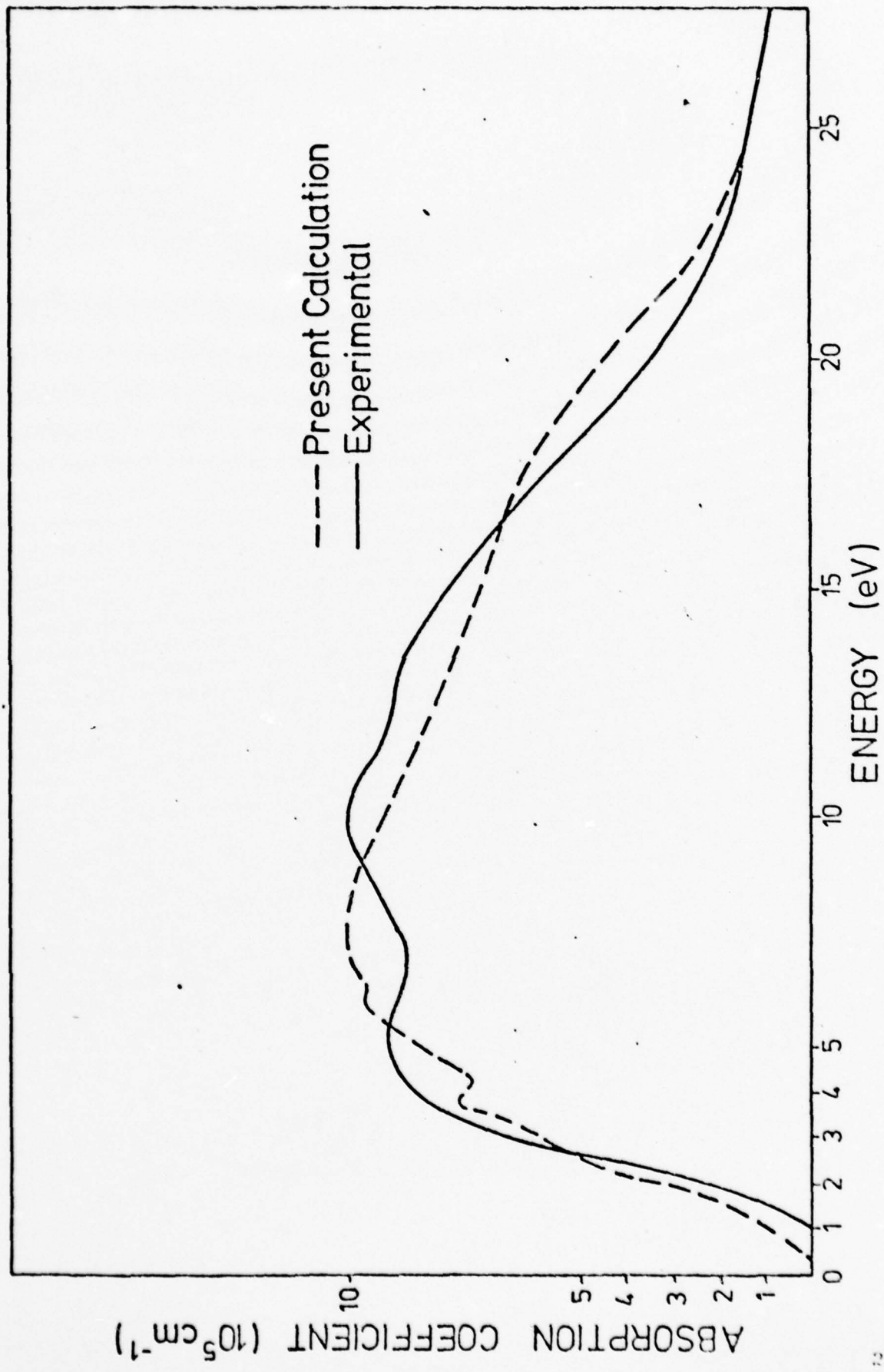
ENERGY (eV)

--- Present Calculation
— Experimental

235
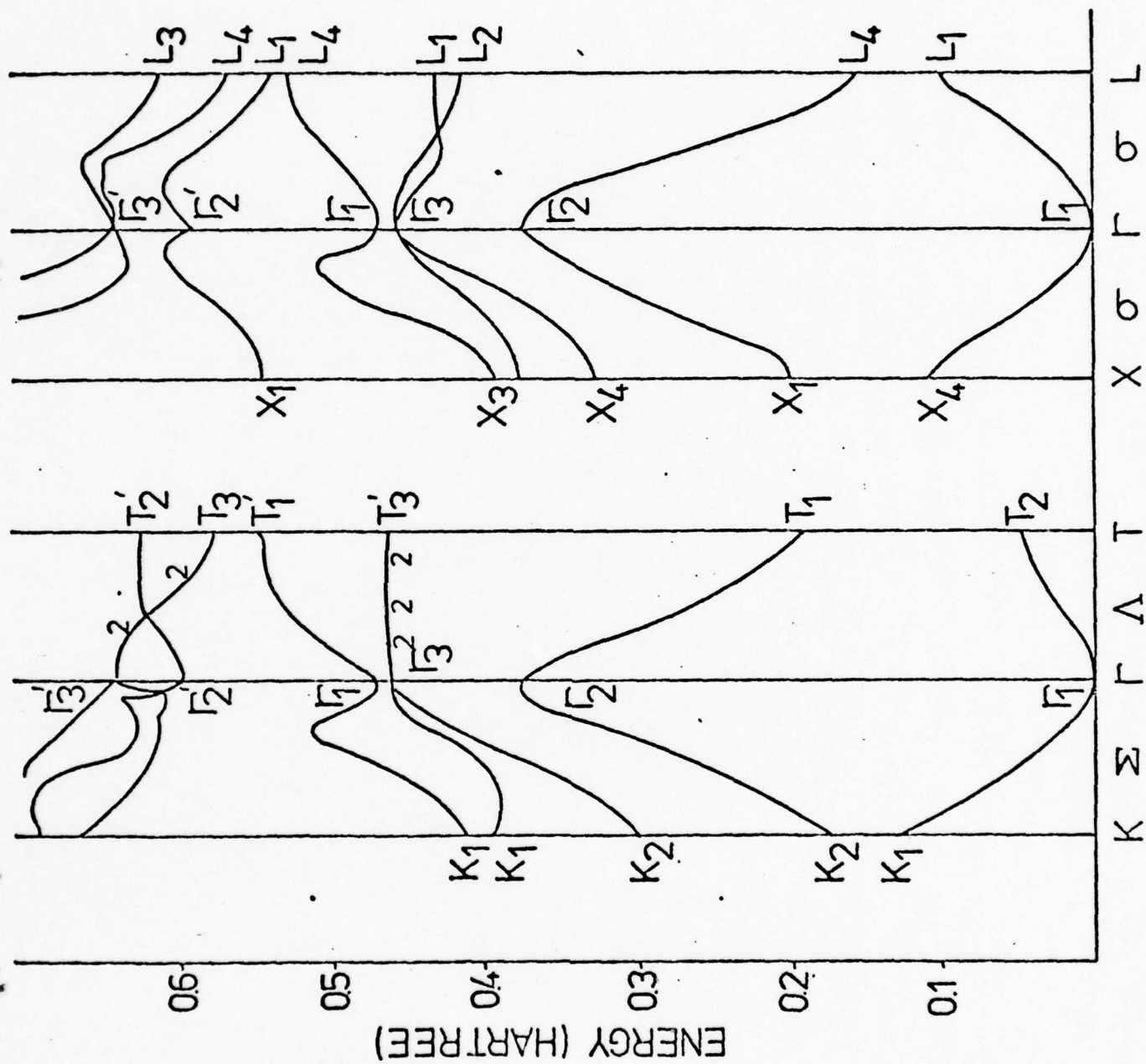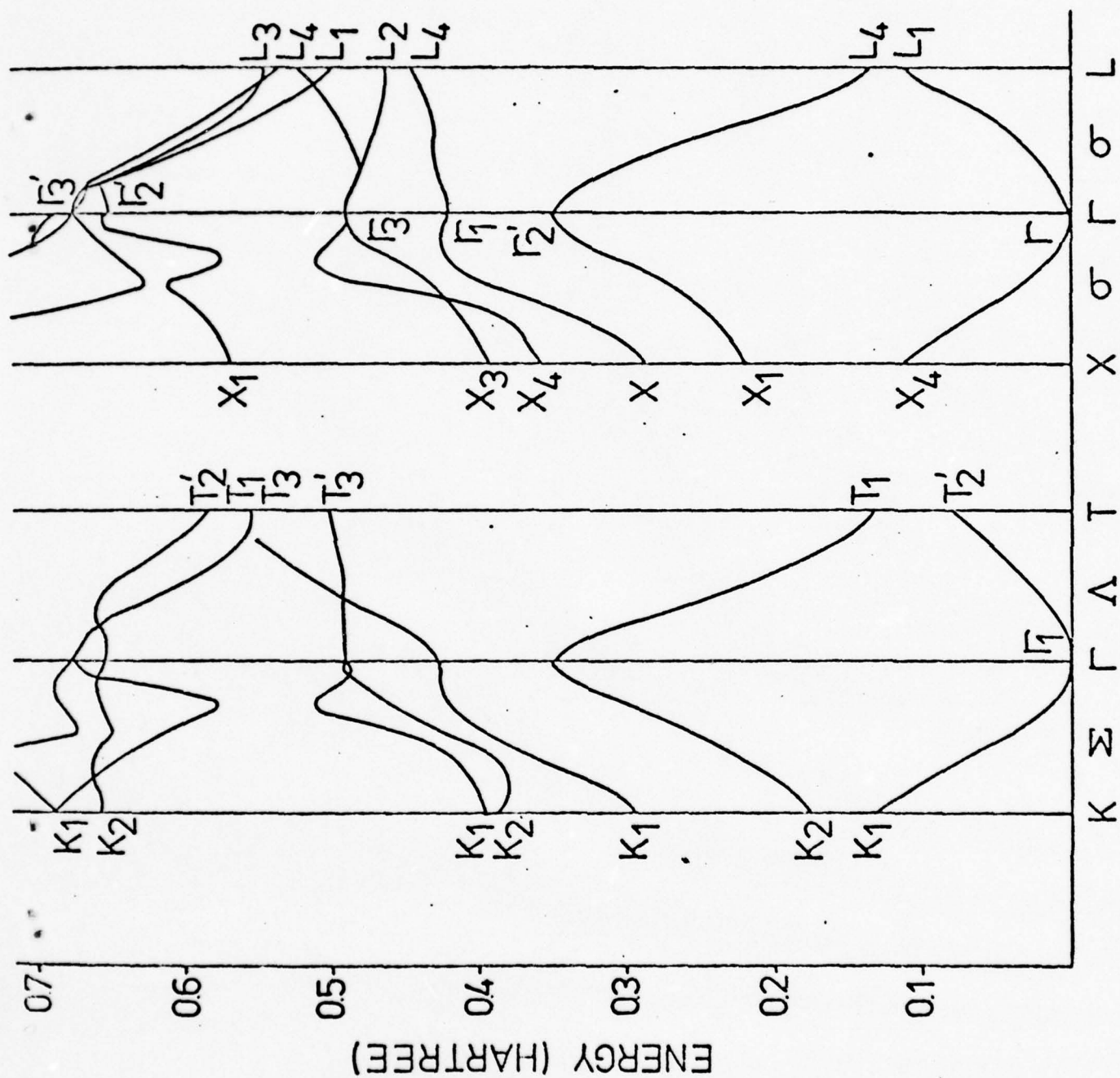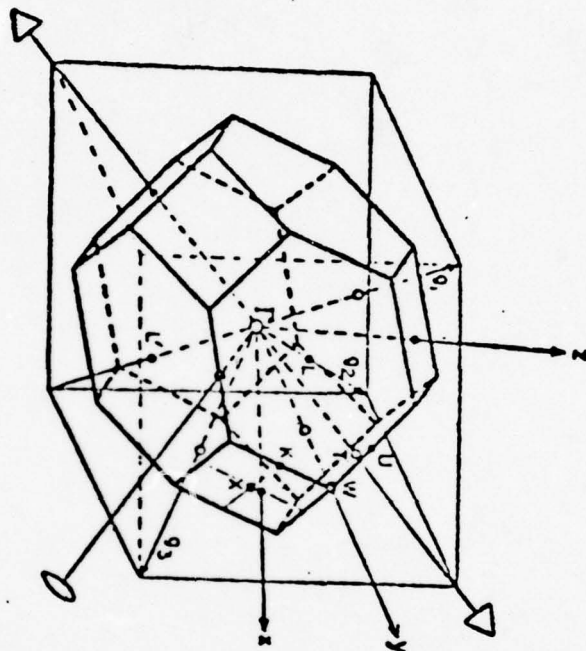
4.5 ELECTRICAL PROPERTIES AND HOPPING TRANSPORT IN AMORPHOUS SILICON CARBIDE FILMS

K. Nair and S. S. Mitra
Department of Electrical Engineering
University of Rhode Island
Kingston, Rhode Island 02881

Abstract

Thin films of amorphous SiC are prepared by rf-sputtering and the conductivity studied in the temperature range $300\ K \geq T \geq 80\ K$ both as a function of temperature and as a function of applied field. Although a few other mechanisms of current transport were observed, much of the dc-conductivity was found to be due to hopping between localized states. Mott's $\exp(T^{-1/4})$ law is obeyed at lower temperatures and the values of the significant Mott's parameters obtained from the results are quite realistic. The dc-conduction at room temperature, at applied fields of the order of 10^5 V/cm, is explained by field-assisted hopping. The ac-conductivity obeys the $\omega^{0.8}$ law at lower frequencies and saturates at frequencies above 100 KHz. It also shows a T^1 dependence. The effect of isothermal annealing is systematically studied.

I. INTRODUCTION

The various current transport mechanisms in dielectric thin films have been extensively studied by many authors[1-4]. In most cases the amorphous films differ from the crystalline ones by the absence of well-defined conduction band and valence band edges and the large density of localized states in the forbidden gap which act as traps. These features of the amorphous dielectrics make it possible to explain their electrical properties by means of models formulated for amorphous semiconductors[5-8]. The transport mechanisms in the case of amorphous semiconductors have been a subject of great interest for the last several years[9]. Although no single model explains all the observed properties, the electrical conduction is usually explained by electronic hopping between localized states below the conduction band. At low temperatures the conductivity, as has been formulated by Mott, is due to hopping between states near the Fermi level and is given by the Mott's law[10],

$$\sigma = \sigma_o \exp\left[-\left(\frac{T_o}{T}\right)^{1/4}\right] \tag{1}$$

At higher temperatures, however, the above law gets modified depending on the applied field, trap distribution, etc.[11-13].

Although crystalline SiC behaves as an insulator, varied values for the resistivity have been reported[14,15]. Thin films of amorphous SiC are generally more conductive than crystalline ones since the transport mechanisms involved are quite different in the two cases. We have studied the de-

conductivity, as a function of applied field,
of thin films of amorphous SiC. Thickness of the samples
used was of the order of 0.5 μm and fields used were around
10^5 V/cm. In this regime the conduction is believed to be
due to field-enhanced hopping[12]. The dc-conductivity as a
function of temperature is studied in detail for temperatures
as low as 80 K where the conductivity obeys the Mott's law.
However, other mechanisms which might contribute to the con-
duction are also considered[16,17]. Most samples showed a
significant amount of conduction by tunneling at very low
temperatures which was temperature-independent similar to
what is found in other dielectric films[16]. For samples of
thickness of the order of 2 μm prepared at low sputtering
power, ionic conduction was found to be dominant.

The frequency dependence of the ac-conductivity of
amorphous SiC is similar to that of other amorphous dielec-
trics in that it obeys $\omega^{0.8}$ law at lower frequencies. As in
other systems with hopping transport, a region in which $\sigma(\omega)$
varies approximately as ω^2 is also observed[7]. At frequencies
above 100 KHz, the conductivity is frequency independent as
found in other amorphous materials[18,19]. As predicted by
Pollak, such a region is also seen at the lower limit of the
frequency[20]. Our results of the frequency dependence and
the temperature dependence at low frequencies of the ac-
conductivity agrees with the model of Pollak which is also
equivalent to the formulation of Mott and Austin[21].

The effect of annealing for long periods at different

temperatures in each of the above measurements is carefully studied. It lowers the dc-conductivity by orders of magnitude which is usually attributed to the decrease in the number of voids or dangling bonds caused by annealing in the as-deposited film[22]. The ac-conductivity also shows similar decrease.

II. EXPERIMENTAL

a. Preparation:

All films were prepared in our laboratory by rf sputtering on glass or quartz substrates with pre-sputtered bottom electrodes. Since most of our samples were of the sandwich configuration, the effect due to the substrate normally observed in the case of high-resistivity materials could be prevented. The bottom electrode was chosen to be of molybdenum in order to prevent contact-induced crystallization[23] and instability while temperature-cycling. The top electrode is either sputtered or evaporated and was chosen from Mo, Ag, Au, Aℓ, In, Au-Sb (99.4 - 0.6), Au-Ge (78-22), Au-Si, etc. The sputtering of SiC was done from a 4" diameter polycrystalline target of intrinsic quality at a typical pressure of 6.0 millitorr of Argon and the sputtering powers were 300 W and 100 W for two sets of samples. The substrate was kept at 9.0 cm away from the target and was water-cooled. The temperature of the substrate was continuously monitored while sputtering and did not run beyond 3 C^{0} above the initial temperature. The samples were tested for amorphicity by X-ray diffraction

at sufficiently long exposure times. All sputtering operations gave amorphous samples. The samples annealed at the highest annealing temperature (400°C) were also found to be amorphous.

The problem of obtaining an ohmic contact to a thin film dielectric is somewhat less severe in the case of amorphous materials because of the large density of localized states in the band gap of the material and the large density of surface states usually present at the interfaces. At low applied fields, the conduction is usually ohmic inside the material and the nature of the contact may play an important role. Previous work on crystalline[24,14,15] and amorphous[25-27] SiC have been either at low fields or with films of very small thickness. Since our measurements were at relatively high fields ($\sim 10^5$ V/cm) the carrier transport may be unlike that at low fields. The effect due to different contact materials was little in the current-voltage characteristic of any of our samples. Further, possibility of the presence of a potential barrier at the interfaces is fairly ruled out as shown in the discussion

The 300 W films studied were of thicknesses 0.5 µm and 0.15 µm and the 100 W films were of thicknesses 0.5 µm and 2.0 µm. The 100 W films showed significantly lower conductivity and thicker films showed bulk effects[28]. The area of a typical sample was 0.25 cm^2.

b. DC Measurements:

The dc-conductivity was estimated by measuring the cur-

rent through the sample for a known applied voltage. The currents were in the range $10^{-5}A$ - $10^{-2}A$ and were measured using a Kiethley 610C Electrometer and the voltage across the sample was measured using a similar instrument. The voltage source was made up of 5.4 V Mercury cells and a potential-divider arrangement. The sample was kept in high vacuum and held at constant temperature while measurements were made. By this arrangement, it was possible to make noise-free measurements even at very small currents. For the σ vs T measurements, a constant voltage (5.4 V) was applied and the corresponding current measured at each temperature. The cooling arrangement was such that the actual temperature of the film could be down to 80 K irrespective of the substrate material. A copper-constantan thermocouple monitored the temperature of the film.

c. Annealing

The annealing of most films was done in an Argon atmosphere at temperatures of $100^{\circ}C$, $200^{\circ}C$, $300^{\circ}C$ and $400^{\circ}C$. The top electrode to the annealed films were deposited usually after annealing. It was found that the films undergo structural change at an annealing temperature of $500^{\circ}C$. This is most likely caused by the Mo bottom electrode while the actual crystallization temperature of amorphous SiC has been found[25] to be around $850-900^{\circ}C$. The annealing times in most cases was 24 hrs., although in some cases it was 12 hrs. Although earlier work[29] shows that annealing times affect the conductivity significantly, annealing times of 12 hrs.

and 24 hrs. respectively, did not show as noticeable a dif-
ference as would those of say 1 hr. and 12 hrs., respectively.

d. AC Measurements

The ac-conductivity was measured using a PAR Model
No. HR-8 Lock-in amplifier and detector system[30] in which
the internally-generated reference signal was used as the
applied voltage to the sample. This voltage could be chosen
from 0 to 0.5 V RMS in which region the current varied line-
arly. A standard resistor of small value (typically 100 Ω
or 10 Ω) compared to the resistance R of the sample is con-
nected in series and the voltage across it is fed into the
input of the lock-in amplifier. By setting the phase control
at zero and at the loss-angle, we obtain two voltages pro-
portional to R and $R/\sqrt{1+R^2\omega^2 C_p^2}$ respectively, where C_p is
the effective parallel capacitance. From these two voltages
R and C_p are calculated which lead to the real parts of $\sigma(\omega)$
and $\varepsilon(\omega)$ respectively. The lock-in amplifier could be used
in the frequency range 1.0 Hz to 150 KHz which is the fre-
quency range of our interest.

III. RESULTS AND DISCUSSION

a. Field-dependence of the dc-Conductivity

A detailed study of the conduction mechanism in the
amorphous SiC thin films should include looking at the vari-
ous conduction processes found in crystalline as well as
amorphous dielectric films. Crystalline SiC being a dielec-
tric, the conduction processes in amorphous SiC apparently
resembles those in crystalline SiC particularly at higher

temperatures and high fields. Previous work on amorphous SiC[25,27] has been at low fields and no field-dependence was investigated extensively. The carrier type was found to be p-type in Mogab and Kingery's[25] work but our studies differ from theirs in that: (i) our samples are prepared by rf-sputtering and at different sputtering conditions; (ii) we consider conduction transverse to the film; and (iii) as mentioned earlier, the applied fields are of the order of 10^5 V/cm.

Figure 1 shows the current-voltage characteristic of a typical 300 W Mo/SiC/Au-Sb structure with the ln I plotted as $\sqrt{F}$, where I is the current for an applied field F, known as the Schottky plot. The fact that the ln I vs $\sqrt{F}$ is fairly linear at high fields may tempt one to assume that the current transport in the material is by either the Schottky process or the Poole-Frenkel process as observed in other dielectric thin films[3,16,31,32]. In the case of Schottky process, the current transport is due to the thermionic emissions across the potential barrier at the metal-insulator interface and the current density is given by[33]

$$J = A^* T^2 \exp\left[-\frac{e(\phi_B - \sqrt{eF/4\pi\varepsilon_i})}{kT}\right] \tag{2}$$

where A^* = effective Richardson constant, ϕ_B = barrier height, ε_i = the insulator dynamic permittivity, k = Boltzman's constant and T = absolute temperature. The Poole-Frenkel process also gives a linear plot of ln I vs $\sqrt{F}$ and the current density has the form[3,32]

$$J \alpha F \exp\left[-\frac{e\left(\phi_B - \sqrt{eF/\pi\varepsilon_i}\right)}{kT}\right] \tag{3}$$

where ϕ_B in this case is the average depths of traps from
the bottom of the conduction band. In the Poole-Frenkel
process, it is assumed that the current transport is car-
ried out by electrons that are thermally excited into the
conduction band from traps that exist in the band gap.
Since this kind of excitation is field-enhanced, it is more
significant at higher temperatures and high fields.

The above two mechanisms are not satisfactory in ex-
plaining our results primarily because they give rise to a
value for the dielectric constant which is too small to be
acceptable for amorphous SiC ($\varepsilon_i/\varepsilon_o \simeq 1.7$ assuming Poole-
Frenkel process and $\varepsilon_i/\varepsilon_o \simeq 0.4$ assuming the Schottky pro-
cess). Further, the linearity of the Schottky plot at high
fields is not to be taken as a conclusive evidence for
either Poole-Frenkel or Schottky mechanism, since tunneling
or Fowler-Nordheim emission would give a similar plot[4]. The
Schottky process assumes the existence of a well-defined
potential barrier at the metal-insulator interface and a
conduction band edge in the material above which the electron
has high mobility, both of which are highly improbable in
our case. We have also found the current density for a
given field to be independent of the contact material and
to be dependent on the thickness of the film, both of which
indicate a bulk-controlled process rather than an electrode-
controlled one. On the other hand, assuming a realistic

magnitude for the density of traps, the contribution to the conduction due to electrons thermally excited from the traps in the band gap into the conduction band as in the Poole-Frenkel process, can be considered to be rather small at the fields and temperatures encountered here ($< 10^6$ V/cm and ~300 K respectively). However, the mechanism we are using in order to explain our results resembles the Poole-Frenkel process in the fact that the conduction is largely bulk-controlled and the existence of large number of localized states in the band gap acting as traps.

We have been able to explain the field-dependence of the conductivity in amorphous SiC satisfactorily by assuming the model formulated by Mott[11] and others[12,13] for hopping conduction in disordered solids. Generally, conduction by hopping dominates only in an amorphous system which is otherwise insulating or semiconducting[12]. In this model, the conduction is interpreted as due to hopping of electrons between localized states with energies near the Fermi level. At low fields, this conduction is ohmic but larger fields give rise to a field-dependent conductivity. Assuming a finite density of localized states at the Fermi level, $N(E_F)$ either due to overlap of conduction and valence band tails as in the CFO model[6] or due to the presence of dangling bonds, Mott[11] obtains the current density for an applied field F to be of the form

$$J \propto \exp(-2\alpha R) \, \sinh(eFR/kT) \exp\left(-\frac{W}{kT}\right) \tag{4}$$

where R = average hopping distance, α = the inverse rate of

fall-off of a typical localized state wavefunction, W = activation energy and T = absolute temperature. This is equivalent to the form obtained by Hill[12] for field-assisted hopping:

$$J \propto \sinh[1.03 \, eF(\alpha \pi N_i)^{1/4} (kT)^{-5/4}] \exp(-CT^{-1/4}) \quad (5)$$

where Hill has considered traps of a uniform density N_i over a band of energies above a depth E_i from the bottom of the pseudo-conduction band (or the mobility edge as in the CFO model).

Shown in Figure 2, is the plot of I vs $\sinh(bV)$ for a typical 300 W sample where the value of b was estimated in each case as follows. For large (bV), $\sinh(bV) \simeq \exp(bV)$. Hence the slope of the tangent of the $\ln I$ vs V plot at large V gives the value of b which has dimensions of $(\text{volt})^{-1}$. It is seen that the I vs $\sinh(bV)$ curve is a straight line at relatively high fields where the $eF < 2\alpha \, kT$ condition holds. At very low fields, the conduction tends to be ohmic as can be seen from the plot. From the value of b, the average density of localized states per unit energy near the Fermi level (or the density of localized traps in the band, as considered by Hill) N_i is calculated assuming a value for α obtained from our other dc measurements (see the following section) $(\alpha \simeq 3 \times 10^7 \text{ cm}^{-1})$. (αN_i) thus obtained has the value 1.33×10^{26} eV^{-1} cm^{-4} which gives $N_i \simeq 4.43 \times 10^{18}$ cm^{-3} eV^{-1} which is quite reasonable.

b. DC Conductivity as a Function of Temperature

Most amorphous semiconductors investigated so far obey

the Mott's law (equ. 1) for conductivity at low temperatures when conduction is by hopping between distant sites[10]. Strictly speaking, this law is expected to hold around liquid helium temperature where the energy transfer between the lattice and the electron during a hop is treated as a one-phonon process. However, similar behavior is observed at higher temperatures as well in many materials[29,34]. In view of this, some modifications to the original formulation due to Miller and Abrahams[35] and Mott[5] have recently been suggested which includes multiphonon effects[36]. There also have been reports of deviation from Mott's law at very low temperatures[37] and unrealistic values for Mott's parameters[22,29,38] which have led some authors to suggest alternative models for hopping transport[39]. In our experiments, we have found that the obtained values for Mott's parameters are quite reasonable unlike most previous workers[22,38].

Figure 3 shows the plot of $\ln(\sigma T^{1/2})$ vs $T^{-1/4}$ for typical 300 W unannealed and annealed films. The different samples subjected to annealing at various temperatures were prepared in the same sputtering operation. Even samples prepared in different operations, but with the same sputtering parameters, varied only within the range of our experimental uncertainty. Figure 4 shows similar plots for 100 W - sputtered samples. From the plots, the following features can be observed:

1. For most part, the $\ln(\sigma T^{1/2})$ vs $T^{-1/4}$ line is a straight line with negative slope.

2. At the lower end, it deviates from the straight line in such a way as to indicate temperature-independent conductivity.

3. At the higher end, in some cases, the conductivity curve indicates a $(\frac{1}{T})$ behavior.

4. For 100 W-sputtered films, the temperature independent part of the conductivity dominates more than that for the 300 W-films. This feature is more noticeable in the case of annealed samples.

Since the measurements are made at a constant applied field, field dependence of conductivity as predicted by Mott[11] or Hill[12] is not relevant in this case. The applied field is such that the conductivity has the temperature dependence as given by the Mott's law, although it is beyond the ohmic region. The $(\frac{1}{T})$ dependence of conductivity at higher temperatures can be attributed to the violation of large-R condition when $(\frac{W}{kT})$ term dominates over the $(2\alpha R)$ term in the expotential[10]. The temperature-independent conductivity at the lower extreme is most likely due to tunneling conduction in which electrons in traps tunnel into the conduction band through the potential barrier which gets appreciably lowered at high applied fields[12]. This is similar to the Fowler-Nordheim process except that it is not a surface phenomenon.

The significant Mott's parameters are calculated from these curves as described elsewhere[29]. The constants σ_o and T_o have the forms

$$\sigma_o = e^2 a^2 \nu_{ph} N(E_F) \tag{6}$$

and

$$T_o = \lambda \alpha^3 / k N(E_F) \tag{7}$$

where e is the electronic charge, a is the hopping distance, ν_{ph} is a phonon frequency obtained from the Debye temperature ($\sim 2.7 \times 10^{13}$ sec^{-1} for SiC), k is the Boltzmann's constant, α is the inverse rate of fall off of the wavefunction of a localized state and $N(E_F)$ is the density of states at the Fermi level. λ is a dimensionless constant and has the value ~ 18.1, according to Ambegaokar, Halperin and Langer[40]. α can be obtained from the values of $\sigma_o\sqrt{T}$ and T_o from the experimental data as

$$\alpha = (21.22 \times 10^{13}/\nu_{ph})[(\sigma_o\sqrt{T})\sqrt{T_o}] \ cm^{-1} \tag{8}$$

and

$$N(E_F) = \lambda \alpha^3/k T_o \ cm^{-3} \ eV^{-1} \tag{9}$$

The average hopping distance R and the average hopping energy W are given as

$$R = [9/8\pi\alpha k T \ N(E_F)]^{1/4} cm \tag{10}$$

and

$$W = [3/4\pi R^3 \ N(E_F)] \ eV \tag{11}$$

Table I shows the values of the above quantities obtained for our samples of different preparation and annealing conditions.

The method of obtaining $\sigma_o\sqrt{T}$ by extrapolating the curve to $T \to \infty$ has been commented upon by many authors[29,39]

and almost always leads to unreasonably high values for $N(E_F)$ and α. In our opinion, these large values are caused by: (i) uncertainties in the method itself and (ii) difficulty in identifying true hopping regions. In many materials[29], usually those of band gap smaller than that of SiC, it is found that intrinsic and extrinsic processes of conduction occurring at higher temperatures increase the slope of the $\ln \sigma\sqrt{T}$ vs $T^{-1/4}$ curve. This makes the identification of true hopping region difficult and often leads to a higher value of the slope. Since T_0 is obtained as $(\text{slope})^4$, the amount of error in T_0 is great. Still greater is the error in the extrapolated value of $\ln \sigma_0\sqrt{T}$, which leads to orders-of-magnitude error in $\sigma_0\sqrt{T}$ and $N(E_F)$. However, as seen from our results, the effect due to intrinsic conduction is rather small in amorphous SiC (most likely because of the large band gap) and the $(\frac{1}{T})$ dependence in some cases is clearly distinguishable from the $T^{-1/4}$ behavior. Because of the above reasons, the values of $\sigma_0\sqrt{T}$ and T_0 are obtained to a good accuracy although some difficulty is encountered with, in the case of samples annealed at high temperatures due to the tunneling component. Hence the procedure adopted in our calculations is as follows:

1. The value of α and $N(E_F)$ are obtained independently for unannealed films and for those annealed at lower temperatures.

2. The above value of α is used to calculate $N(E_F)$ for the other films ($\alpha \sim 3.0 \times 10^7 \text{ cm}^{-1}$). The values of α are

also calculated in each case separately but are not used to estimate $N(E_F)$.

A reasonable value for α is such that α^{-1} is of the order of interatomic distances. Our values for α are very reasonable in contrast to some earlier reports for other materials. The values obtained for $N(E_F)$ also are of the right order and shows good consistency.

c. Annealing Behavior

As can be seen from Figures 3 and 4, annealing generally lowers conductivity by a few orders of magnitude. The value of $N(E_F)$ is seen to be consistently decreasing as a function of annealing temperature. The difference in the value of α for the annealed samples should be considered more to be due to uncertainty in the calculation than as a decrease in the parameter itself. As pointed out in earlier works[22,29,41], the annealing most likely causes a decrease in the number of dangling bonds which contribute largely to the density of localized states at the Fermi level. The decrease of α due to annealing could not, however be confirmed by our results.

The low-power sputtered samples show a significant difference in conductivity like the annealed samples. Annealing still lowers the conductivity by orders of magnitude. It is reasonable to assume that the number of dangling bonds is much less in the low-power sputtered films. It could also be that the number of localized states tailing from the conduction and valence bands are smaller due to reduced disorder. However, the question whether these are caused primarily by

the low sputtering power or the smaller rate of deposition remains unresolved at the present time. Another factor influencing the degree of disorder may be the temperature of deposition[42].

d. AC Conductivity

The behavior of the ac-conductivity and the capacitance of typical 300 W samples are shown in Figures 5 and 6. From the log σ vs log f curves, the following main features can be observed:

1. σ varies approximately as $\omega^{0.8}$ for lower frequencies.

2. At very high frequencies (≥ 100 KHz), $\sigma(\omega)$ tends to be frequency-independent. The same kind of region exists at the lower end of the frequency range also.

3. Between the $\omega^{0.8}$ region and the high-frequency region, there exists a narrow region in which $\sigma(\omega)$ varies as a higher power (~ 1.5) of ω which is more prominant in un-annealed samples.

4. The log C curve has a slope given by $(s-1)$ where s is the slope of the log σ curve at any frequency. Accordingly it varies as $\omega^{-0.2}$ at lower frequencies and as ω^{-1} at high frequencies.

The ac-conductivity at low frequencies (~ 7 Hz, so that it is within the $\omega^{0.8}$ region) as a function of temperature in annealed samples is illustrated by means of Figure 7. It is seen that $\sigma \propto T$ law holds at low temperatures and gradually deviates at higher temperatures. This deviation was found more apparent in unannealed samples.

We have analyzed our results by means of the hopping model and found the results to be in good agreement with the results from the dc measurments. Considering hops between pairs of localized states, Pollak[20] has derived the ac-conductivity in the $\omega^{0.8}$ region to be of the form

$$\sigma_{ac}(\omega) = \frac{\pi^3}{96} N^2(E_F) kT \; e^2 \; a\omega r_\omega^4$$

where r_ω is the mean hopping distance. This is similar to the form obtained by Mott and Austin[21], assuming impurity band conduction and can be written using a $\simeq \alpha^{-1}$

$$\sigma_{ac}(\omega) = \frac{\pi^3}{96} N^2(E_F) \; kT \; \alpha^{-5} \; \omega [\, \ell n(\frac{\nu_{ph}}{\omega})]^4.$$

The factor e^2 is omitted in the above since $N(E_F)$ is often expressed in $eV^{-1} \, cm^{-3}$. It has been found that in most materials[43-45] ω is to be replaced by $\omega^{0.8}$ as pointed out by Pollack[20]. From the results obtained for different samples, the values of $N(E_F)$ obtained assuming $\alpha^{-1} = 3.3 \, Å$ (obtained from the dc measurements) are tabulated in Table I. It is found that they agree well with the values obtained from dc measurements. The $N(E_F)$ obtained from the temperature dependence of σ are also of the right order. The frequency dependent regions at low frequencies and high frequencies are as predicted by Pollak[20]. The saturation frequency has been interpreted as the approximate hopping frequency in the case of GeTe[19] ($\sim 10^5$ Hz) which is of the same order in our case. The effect of multiple hopping can be assumed to be small in our case because the slope of the log σ vs log f

curve does not undergo appreciable change at lower temperatures[19].

IV. CONCLUSION:

All our results are found to be in accordance with the hopping model for conductivity. The density of states as calculated from different experiments is very consistent and of the right order. Much of the uncertainty in obtaining the Mott's parameters from the dc data has been avoided. The effect of annealing has been systematically studied and is in accordance with earlier results. The ac-conductivity displays the $\omega^{0.8}$ behavior as observed in most oxide and chalcogenide glasses and tends to show ω^2 behavior in a narrow frequency range. It was also noted that all sputtered films of different preparation and annealing conditions showed good reproducibility.

REFERENCES

1. R. M. Hill, Thin Solid Films $\underline{1}$ (1967) 39-68.

2. A. K. Jonscher, Thin Solid Films $\underline{1}$ (1967) 213-234.

3. C. A. Mead, Phys. Rev. $\underline{128}$ (1962) 2088.

4. J. J. O'Dwyer, J. Applied Phys. $\underline{37}$ (1966) 599.

5. N. F. Mott, Advan. Phys. $\underline{16}$ (1967) 49.

6. M. H. Cohen, H. Fritzche and S. R. Ovshinsky, Phys. Rev. Lett. $\underline{22}$ (1969) 1065.

7. N. F. Mott, Phil. Mag. $\underline{17}$ (1968) 1259.

8. M. H. Cohen, J. Non-Cryst. Solids $\underline{2}$ (1970) 432-433.

9. A large collection of papers in this area can be found in J. Non-Cryst. Solids $\underline{1}$ through $\underline{4}$.

10. N. F. Mott, Phil. Mag. $\underline{19}$ (1969) 835.

11. N. F. Mott, Phil. Mag. $\underline{24}$ (1971) 911.

12. R. M. Hill, Phil. Mag. $\underline{24}$ (1971) 1307.

13. M. Pollack, J. Non-Cryst. Solids $\underline{8-10}$ (1972) 486.

14. H. Suzuki and T. Iseki, Proc. Third International Conference on SiC, Sept., 1973, R. C. Marshall, J. W. Faust, C. E. Ryan, Eds. (U. of South Carolina Press).

15. G. A. Lomakina, Proc. of Third International Conference on SiC, Sept., 1973, R. C. Marshall, J. W. Faust, C. E. Ryan, Eds. (U. of South Carolina Press).

16. S. M. Sze, J. Applied Phys. $\underline{38}$ (1967) 2951.

17. H. Fritzche in "Amorphous and Liquid Semiconductors" Edited by J. Tauc (Plenum, 1974).

18. W. S. Chan and A. K. Jonscher, Phys.Stat.Solidi. $\underline{32}$ (1969) 749.

19. S. K. Bahl and K. L. Chopra, J. Applied Phys. $\underline{41}$ (1970) 2196.

20. M. Pollack, Phil. Mag. 23 (1971) 519.

21. N. F. Mott and I. G. Austin, Advan. Phys. 18 (1969) 41.

22. M. H. Brodsky, R. S. Title, K. Weiser and G. D. Pettit, Phys. Rev. B1 (1970) 2632; M. H. Brodsky and R. J. Gambino, J. Non-Cryst. Solids 8-10 (1972) 739.

23. M. Toki, Y. Ogawa and Y. Tujiki, Jap. J. Appl. Phys. 8 (1969) 1056.

24. H. Kang and R. B. Hilborn, Proc. Third Intl. Conf. on SiC (1973), R. C. Marshall, J. W. Faust and C. E. Ryan, Eds. (U. of South Carolina Press) p. 493.

25. C. J. Mogab and W. D. Kingery, J. Appl. Phys. 39 (1968) 3640.

26. T. E. Hartman, J. C. Blair and C. A. Mead, Thin Solid Films 2 (1968) 79.

27. E. A. Fagan, Proc. V Intl. Conf. on Amorphous and Liquid Semiconductors, Vol. I, Garmisch-Partenkirchen, Germany Sept., 1973 (Taylor and Frances, London).

28. The measurements on 100W films of thickness ~2 μm are not reported here.

29. D. K. Paul and S. S. Mitra, Phys. Rev. Lett. 31 (1973) 1000.

30. S. Mardix and D. K. Paul, J. Electrochem. Soc. 120 (1973) 275.

31. H. Hirose and Y. Wada, Jap. J. Appl. Phys. 4 (1965) 639.

32. T. E. Hartman, J. C. Blair and R. Bauer, J. Appl. Phys. 37 (1966) 2468.

33. P. R. Emtage and W. Tantraporn, Phys. Rev. Lett. 8 (1962) 267.
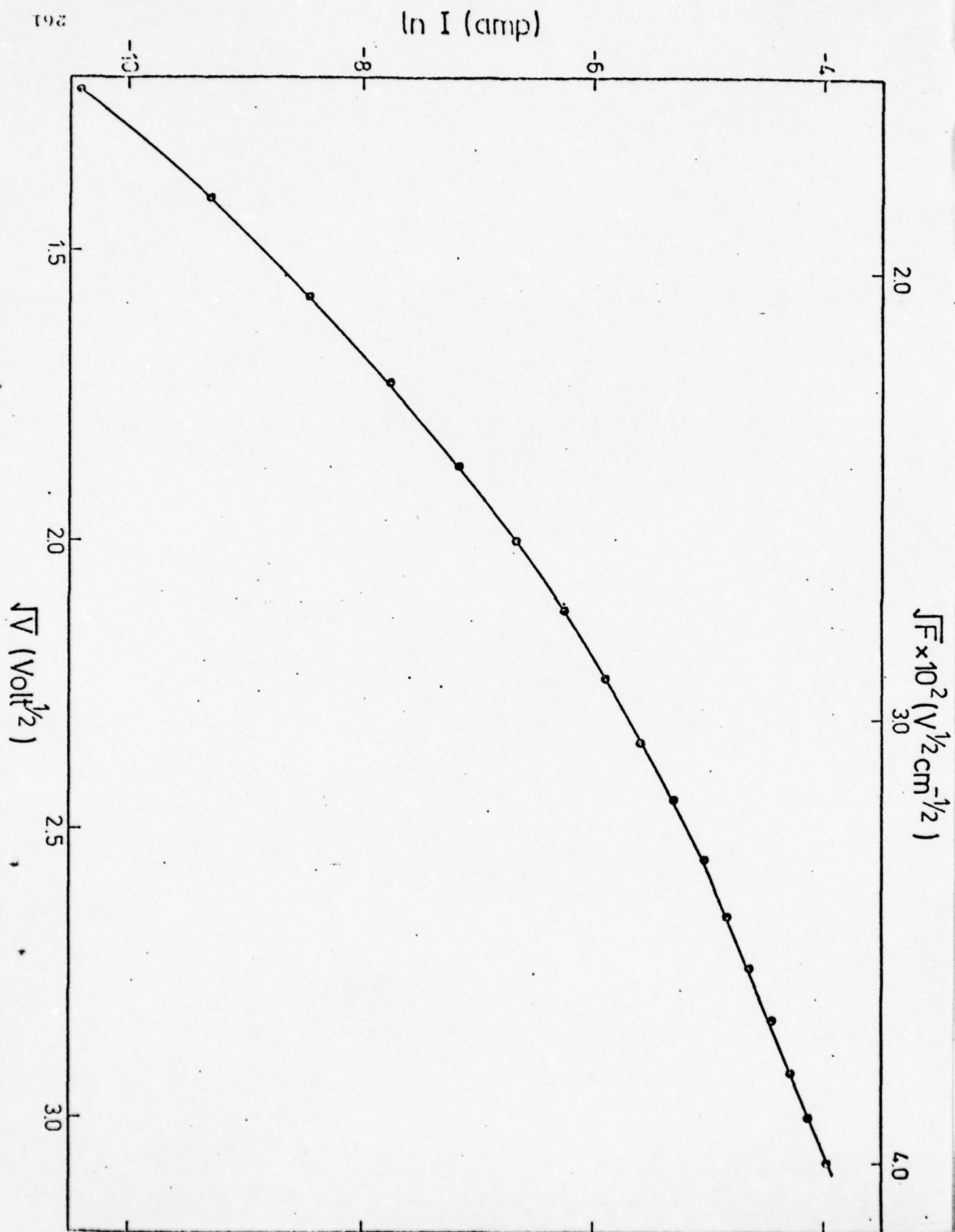
34. G. N. Greaves, J. Non-Cryst. Solids 11 (1973) 427.

35. A. Miller and E. Abrahams, Phys. Rev. 120 (1960) 745.

36. D. Emin, Phys. Rev. Lett. 32 (1974) 303.

37. V. Capek, S. Koc and J. Zemek, J. Non-Cryst. Solids 18 (1975) 95.

38. A. Lewis, Phys. Rev. Lett. 29 (1972) 1555.

39. V. Capek, Czech. J. Phys. B25 (1975) V. Capek (to be published).

40. V. Ambegaokar, B. I. Halperin and J. S. Langer, Phys. Rev. 34 (1971) 2612.

41. W. Beyer and J. Stuke, J. Non-Cryst. Solids 8-10 (1972) 321.

42. J. J. Hauser, Phys. Rev. B8 (1973) 2678.

43. LeCleac'h and J. F. Palmier, J. Non-Crystl. Solids 18 (1975) 265.

44. S. C. Agarwaal, S. Guha and K. L. Narasimhan, J. Non-Cryst. Solids 18 (1975) 429.

45. N. Fuschillo, B. Lalevic and N. K. Annamalai, J. Non-Cryst. Solids 21 (1976) 85.

TABLE I
Mott's parameters for amorphous SiC of various preparation and annealing conditions. The phonon frequency is calculated from the Debye temperature. ($\nu_{ph} = 2.7 \times 10^{13}$ sec^{-1}).

Sputtering power and film thickness	Annealing temp. and duration	T_o (10^8 xK)	α^* (10^7 x cm^{-1})	$N(E_F)$ (cm^{-3}ev^{-1})	$R(150K)$ (10^{-7} x cm)	$W(150K)$ (ev)
300W, .6 μm	Unannealed	1.07	9.35	5.30×10^{19}	3.63	0.094
300W, .6 μm	100°C,24 hrs.	1.27	2.89	4.46×10^{19}	3.79	0.098
300W, .6 μm	200°C,24 hrs.	1.59	5.90	3.58×10^{19}	4.01	0.103
300W, .6 μm	300°C,24 hrs.	1.99	3.31	2.85×10^{19}	4.24	0.110
300W, .6 μm	400°C,24 hrs.	3.05	2.28	1.86×10^{19}	4.72	0.122
100W, .58μm	Unannealed	12.8	----	4.00×10^{18}	6.93	0.179
100W, .58μm	100°C,12 hrs.	13.7	----	3.75×10^{18}	7.04	0.182
100W, .58μm	200°C,12 hrs.	15.5	----	3.31×10^{18}	7.27	0.188

*The value of α is taken as 3.0×10^7 cm^{-1} for all other calculations.

TABLE II
Density of states at the Fermi level $N(E_F)$ evaluated from
the ac conductivity data

(a) from the σ vs ω curve

Film description	Annealing temp. and duration	Extrapolated $\sigma(1\ Hz)$ $(ohm^{-1}cm^{-1})$	$N(E_F)$ $(cm^{-3}eV^{-1})$
300W, .6 μm	Unannealed	7.05×10^{-11}	1.98×10^{21}
300W, .6 μm	100°C, 24 hrs.	2.33×10^{-11}	1.14×10^{21}
100W, 2.0 μm	Unannealed	1.06×10^{-11}	7.69×10^{20}

(b) from σ vs T curve (low temperature)

Film description	Annealing temp. and duration	$N(E_F)$ $(cm^{-3}\ eV^{-1})$
300W, .6 μm	200°C, 24 hrs.	6.45×10^{20}
300W, .6 μm	300°C, 24 hrs.	5.81×10^{20}

FIGURE CAPTIONS

Fig. 1   Schottky plot of a 300W sample of thickness 0.6 μm
and area 0.25 cm^2 at room temperature.

Fig. 2   Plot of I vs sinh (bV) for the same sample as in
Fig. 1, where V is the applied voltage and
b = 0.364 V^{-1}.

Fig. 3   Plot of ln $(\sigma T^{1/2})$ vs $T^{-1/4}$ for 300W samples,
(i) unannealed (line 1); (ii) annealed 24 hrs. at
100°C, (line 2); (iii) annealed 24 hrs. at 200°C
(line 3); (iv) annealed 24 hrs. at 300°C, (line 4)
and (v) annealed 24 hrs. at 400°C, (line 5). The
quantity $(\sigma T^{1/2})$ is in $(\Omega^{-1}$ cm^{-1} K$^{1/2})$.

Fig. 4   Plot of ln $(\sigma T^{1/2})$ vs $T^{-1/4}$ for 100W samples,
(i) unannealed, (line 1); (ii) annealed 12 hrs. at
100°C, (line 2) and (iii) annealed 12 hrs. at
200°C, (line 3).

Fig. 5   Log $\sigma_{a.c.}$ and log C vs log f for unannealed film.
$\sigma_{a.c.}$ is in Ω cm, C is in μF and f is in Hz.

Fig. 6   Log $\sigma_{a.c.}$ and log C vs log f for film annealed
24 hrs. at 100°C.

Fig. 7 $\sigma_{a.c.}$ as a function of T for 300W sample, (i)
annealed 24 hrs. at 200°C (dots) and (ii) annealed
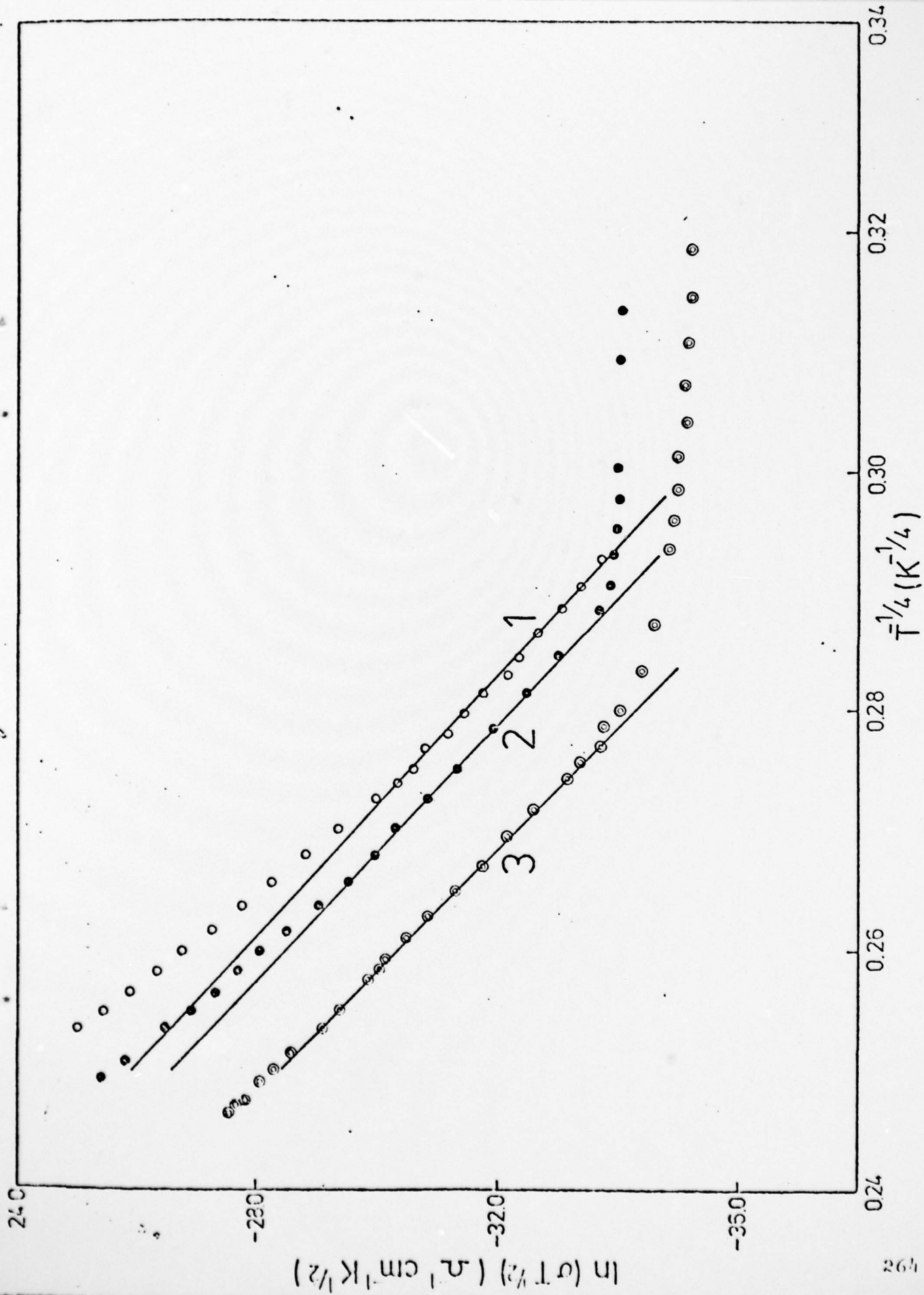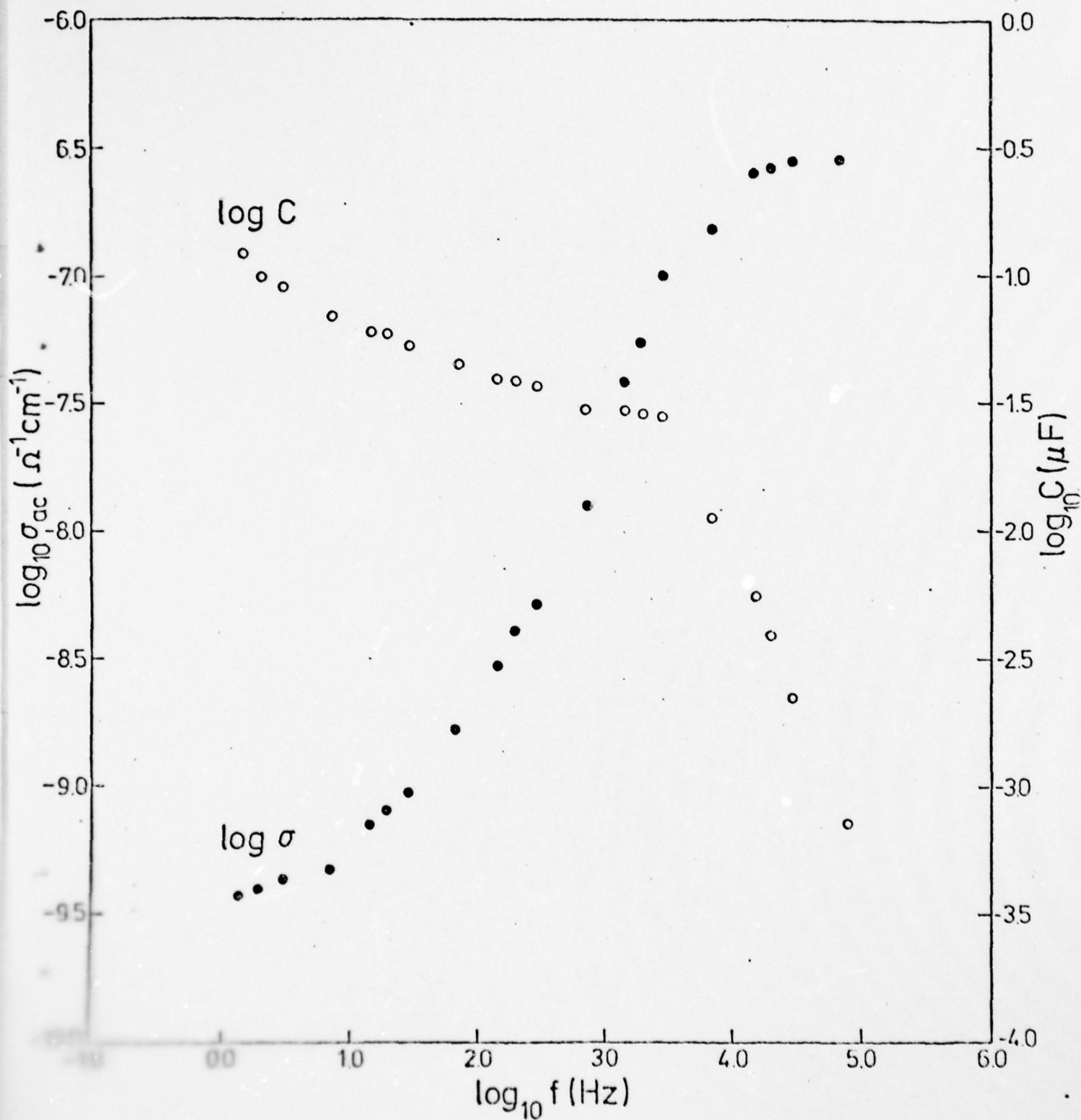24 hrs. at 300°C (circles).
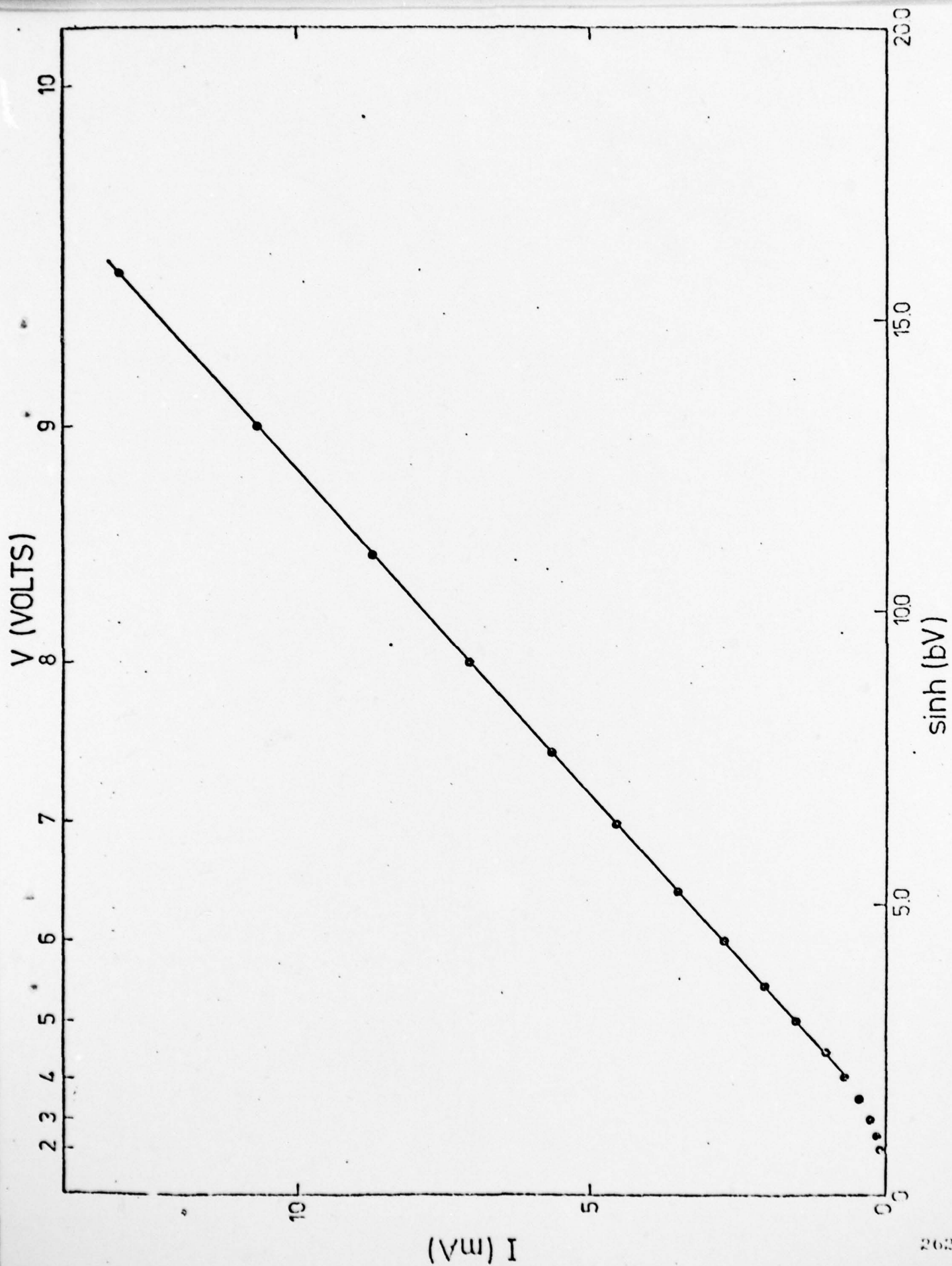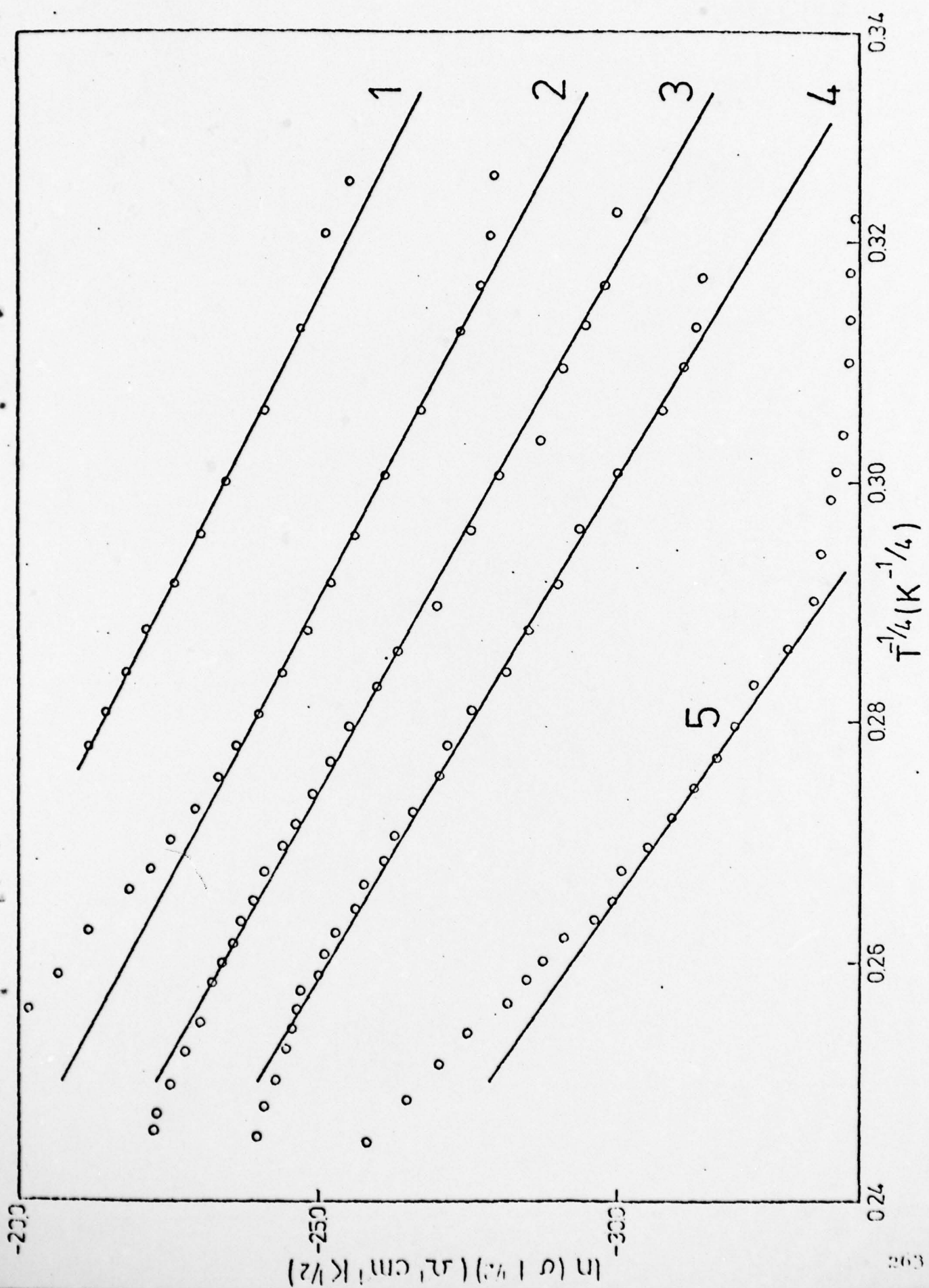
262

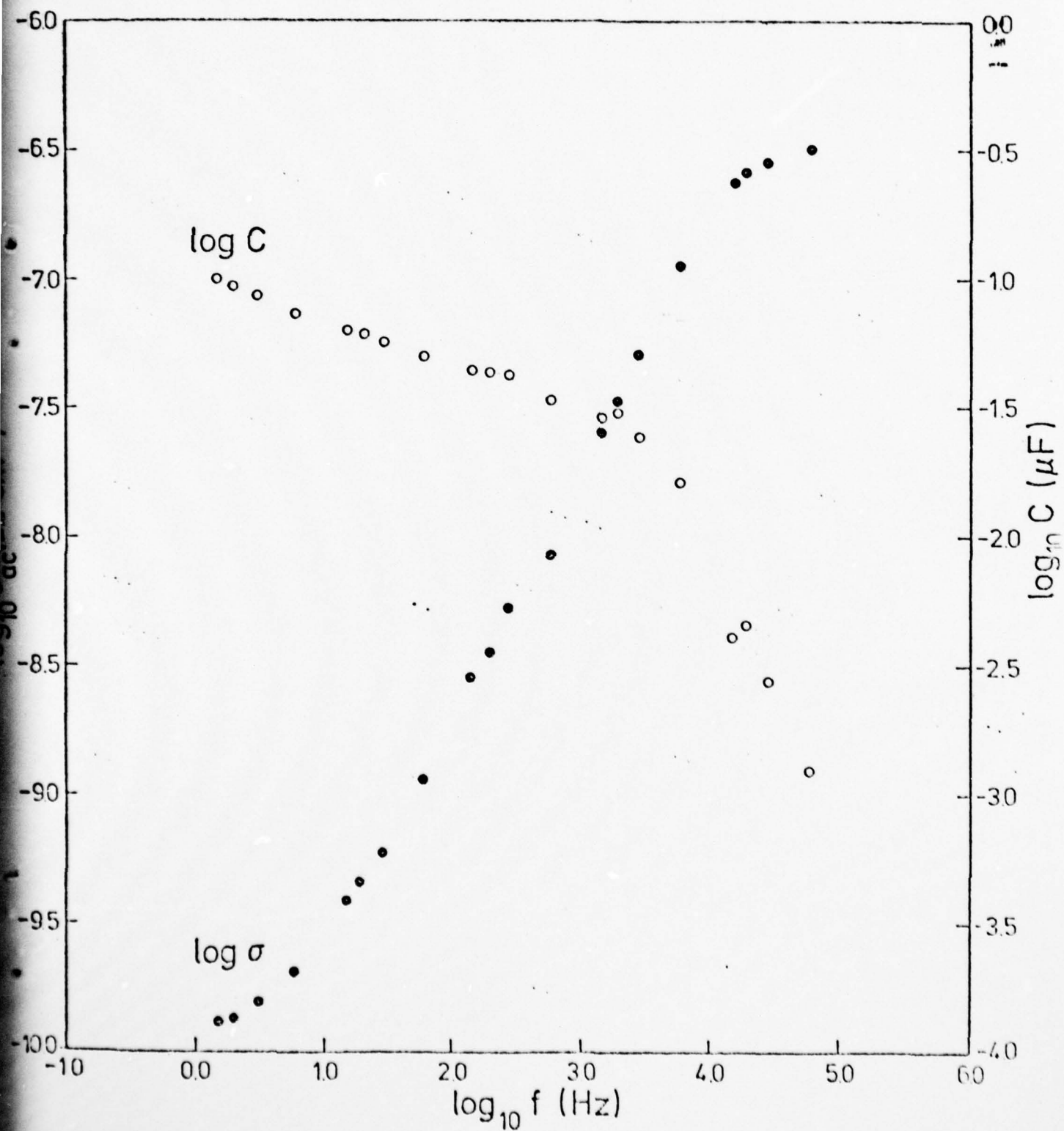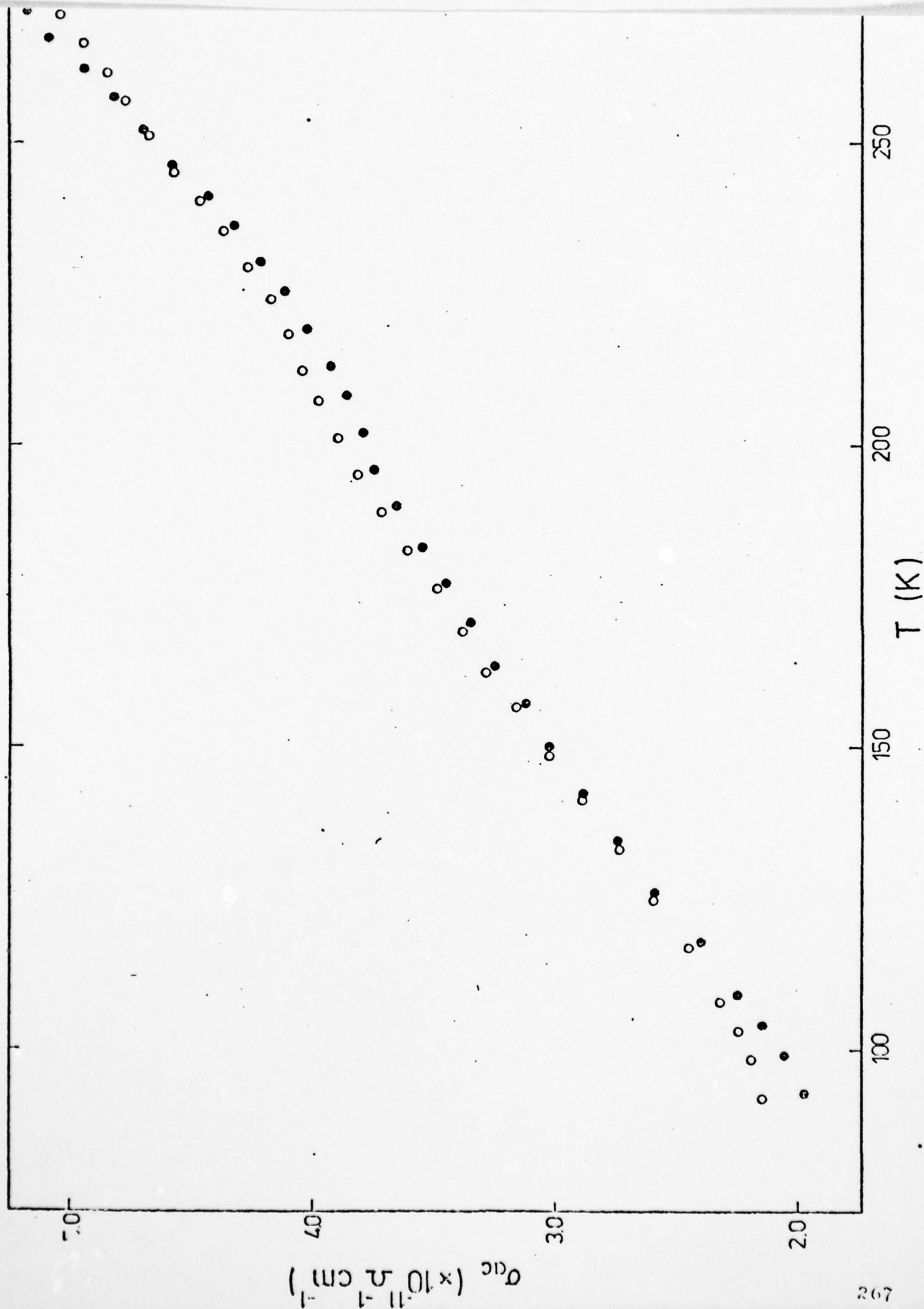Axis labels: $\ln(\sigma\,|\nu^{1/2}|)\,(\pi,\,cm^{-1}\,K^{1/2})$ (vertical), $T^{-1/4}(K^{-1/4})$ (horizontal)

Figs. a Wilson , Fig. 1

V

ELASTO-OPTIC COEFFICIENTS

THEORY OF BRILLOUIN EFFECT: CALCULATION OF
ELASTOOPTIC CONSTANTS OF DIAMOND AND ZINCBLENDE SEMICONDUCTORS

Yet-Ful Tsay[*] and Bernard Bendow
Air Force Cambridge Research Labs (AFSC), Hanscom AFB, Massachusetts, USA

Shashanka S. Mitra[+]
Dept. of Electrical Engineering, Univ. of Rhode Island, Kingston, RI, USA

I. INTRODUCTION

The Brillouin scattering efficiency of solids is determined principally[1] by the elastooptic tensor $\overleftrightarrow{p}$ relating the change in inverse dielectric constant to strain,

$$\Delta(\varepsilon^{-1})_{ij} = p_{ijkl}\tau_{kl} \tag{1}$$

In general $\overleftrightarrow{p}$ is complex, and the scattering is proportional to the absolute square of an appropriate contraction of $\overleftrightarrow{p}$. The scattering efficiency as a function of incident photon frequency must vary slowly on the scale of the Brillouin frequency shift for such a formulation to be valid; these are, in fact, the conditions of interest here. The change in the dielectric properties under strain has been treated previously within a variety of models.[2,3] The purpose of the present work is to calculate these properties within a full band-structure approach. Our calculation accounts in detail for changes in band energies and matrix elements as a function of strain throughout the zone; moreover, we are not limited to small values of the strain in our calculation. In this paper we will restrict attention to various highlights of the method, and present results for the dispersion of $\overleftrightarrow{p}$ in the resonance regime for selected diamond-type crystals. Details of the calculations, and more extensive results including those for zincblende crystals, will be presented elsewhere.[4]

II. METHOD

For diamond and zincblende crystals $\overleftrightarrow{p}$ is characterized by just three independent

---

constants,[5] p_{11}, p_{12} and p_{44}. Defining $\Delta\epsilon_{\perp}$ and $\Delta\epsilon_{||}$ as the changes in dielectric constant for light polarized $\perp$ and $||$ to the direction of applied stress; then p_{11}-p_{12} and p_{44} are both given by

$$\Delta(\epsilon_{\perp} - \epsilon_{||})/3\epsilon^2\tau \qquad (2)$$

where the stress direction is [100] for p_{11}-p_{12} and [111] for p_{44}; τ is an appropriate strain element in each case. Another relation is

$$p_{11} + 2p_{12} = 3K \, d\epsilon/dP/\epsilon^2, \qquad (3)$$

where K is the compressibility and P is hydrostatic pressure. Thus calculation of the optical spectrum under [100], [111] and hydrostatic compressions suffice to determine $\overleftrightarrow{p}$ in the present instance.

We here employ the empirical pseudopotential method, which has been highly successful in accounting for zero-stress optical spectra in semiconductors.[6] Most previous work of this type in the strain problem was limited to high symmetry band gaps, and to small strains which could be regarded as perturbations.[7] We avoid these limitations by calculating the full band structure of the deformed crystal, in which the Bravais lattice is altered; except in the hydrostatic case, the strained crystal has lowered symmetry. In certain strain configurations the relative positions of atoms in a unit cell are not uniquely determined[8] We utilize experimental values for this "internal parameter" when required. In our calculations we assume the transferability of ionic pseudopotentials $v_i(r)$, which amounts to assuming that $v_i(r)$ is independent of the embedding environment. To obtain the Fourier coefficients $V_i(\underline{G})$, where $\underline{G}$ is a reciprocal lattice vector, for the present configurations, we perform a polynominal fit of the unstrained crystal form factors of Ref. (9). One also requires the dielectric function $\epsilon(\underline{q})$ to account for screening of the v_i's, which in the case of hydrostatic pressure may be calculated self-consistently. The analogous procedure for the strain case is more difficult, and since the cell volume is not changed in the configurations we will compute here, we expect the changes in ϵ to be small. We therefore, for simplicity, use the model ϵ of Ref. (10), appropriate for an unstrained crystal, in the latter instance. To calculate the matrix elements, we employ the pseudowavefunction in the standard fashion.[6]

III. RESULTS

We have calculated the band structure and optical constants of Ge and Si under high stress, utilizing the above methods. For [100] and [111] stresses the lattice symmetry becomes tetragonal and trigonal, respectively, and many more points in the zone are required than in the cubic case. We utilize about 400 points, along with a linear interpolation to reduce statistical noise, which may eventually prove insufficient for an accurate account of dispersion in $\Delta\epsilon$. Although the present results must therefore be viewed as preliminary in nature, we believe that the principal trends will remain when the accuracy has been improved.

A principal influence on the optical constants under stress is the shift of the energy bands, which may be characterized in terms of deformation potential (dp) constants. Our results for selected gaps in Si and Ge are displayed in Tb. I, and are seen to compare favorably with experiment overall, although they tend to consistently fall on the high side of the available data. Our investigations have shown most of the dp's to be nearly linear with strain up to $\tau \sim 0.02$.

TABLE I: SELECTED DEFORMATION POTENTIAL CONSTANTS FOR GERMANIUM AND SILICON (in eV).

Gap	Type of Deformation	Germanium			Silicon		
		Theory (this work)	Theory (others)	Experiment	Theory (this work)	Theory (others)	Experiment
$\Gamma_{25',v} \to \Gamma_{2',c}$ (Ge)	Volume	-12.2	-12.8[a], -8.8[b]	-10.3[c] to -8.0[d]	-1.28	0.0[a], -0.6[k], -1.4[l]	-0.98[n]
$\Gamma_{25',v} \to \Gamma_{15,c}$ (Si)	b[100]	-2.5	-2.3[a]	-2.6[e] to -1.8[f]	-2.7	-2.0[a], -2.3[k], -2.4[l]	-1.4[f], -2.4[o]
	d[111]	-6.7	-4.9[a], -5.6[b]	-3.7[f] to -7.0[g]	-7.9	-5.1[a], -4.9[l]	-5.3[f], -3.1[o]
$\Lambda_{3,v} \to \Lambda_{1,c}$	Volume	-6.6	-3.9[a], -4.7[b]	-5.9 ± 0.3[h]	-6.5	-5.8[m], -4.6[l]	-6.1 ± 0.4[n]
	Ξ_u	6.1	4.5[a], 5.2[b]	5.1[e]	5.3	.	-
$X_{1,v}\, X_{4,c}$	Volume	-4.1	-2.3[a]	-4.1[h]	-3.5	-2.8[a], -1.3[k], -2.4[l]	-2.9[h]
$\Gamma_{25',v} \to L_{1,c}$	Volume	-5.0	-3.5[b]	-3.8[i]	-5.4	-3.7[k], -4.2[l], -4.4[m]	.
$X_{1,c}$	Ξ_u	11.6	7.6[b]	11.0[j]	10.8	7.5[a], 6.0[k], 9.6[l]	8.8[f], 8.3[o]

[a]P. Melz, J. Phys. Chem. Sol. 32, 209(1970). [b]L. Saravia & D. Brust, Phys. Rev. 178, 1240(1969). [c]A. Glass, Can. J. Phys. 43, 12(1965).
[d]I. Balsev, Sol. State Comm. 5, 315(1967). [e]F. Pollak & M. Cardona, Phys. Rev. 172, 816(1968). [f]I. Balsev, Phys. Rev. 143, 636(1966).
[g]J. Hill, Phys. Rev. 128, 65(1967). [h]R. Zallen & W. Paul, Phys. Rev. 155, 703(1967). [i]W. Paul, J. Appl. Phys. 37, 2082(1961).
[j]D. Wilson & G. Feher, Phys. Rev. 124, 1068(1961). [k]L. Saravia, J. Phys. Chem. Sol. 15, 1469(1969). [l]I. Goroff & L. Kleinman, Phys.
Rev. 132, 1080(1964). [m]V. Brust and L. Liu, Phys. Rev. 154, 647(1967). [n]F. Schmidt & A. Vetta, Sol. State Comm. 9, 1187(1971).
[o]J. Hensel & G. Feher, Phys. Rev. 129, 1041(1963). [p]J. Aubrey et al, Phys. Rev. 130, 166(1963).
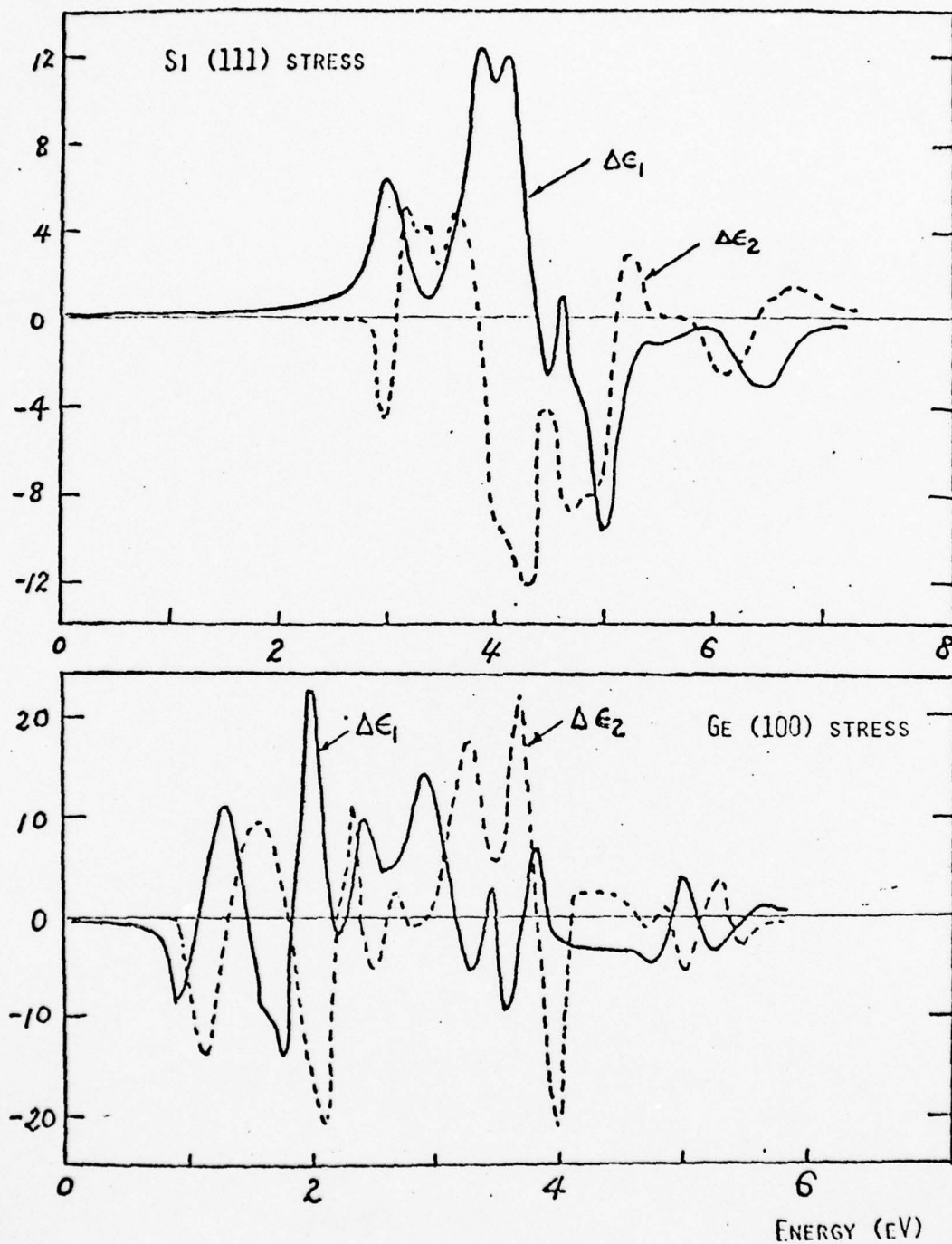
FIGURE 1. Change in complex dielectric constant $\epsilon = \epsilon_1 + i\epsilon_2$ under [100] and [111] stress for Ge, and [111] stress for Si; $\Delta\epsilon \equiv \epsilon_\perp - \epsilon_\parallel$. Strain element $\iota = 0.01$ in both cases.

In Fig. 1 we display results for $\Delta c \equiv c_\perp - c_{||}$ for various stress configurations in Ge and Si. One notes a considerable degree of structure in Δc vs. ω, which would also manifest itself in the Brillouin spectrum, although the details will depend on the scattering geometry. The present predictions display considerably more structure than the measured results of Ref. 11, although certain features are similar. This could well be the result of the larger strain values utilized here, as well as the computational inaccuracies mentioned above. However, our calculations for the hydrostatic case, which allow for a much higher degree of computational accuracy, indicate a substantial degree of structure as well. This suggests that such features are truly characteristic of the stress-induced spectrum, rather than being artifices of the computation.
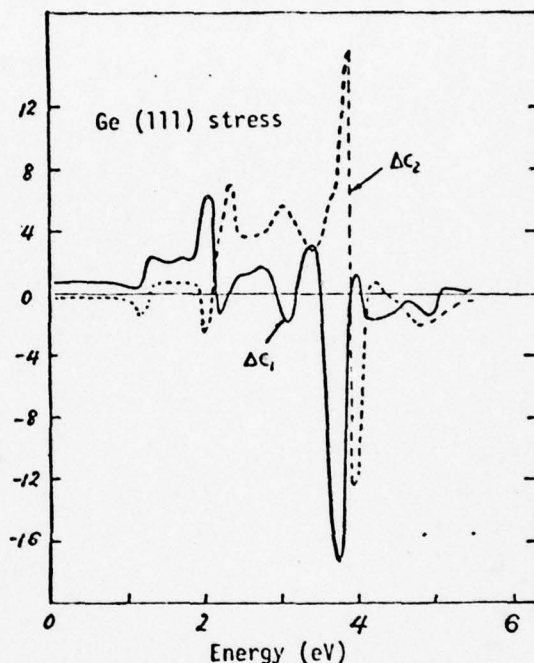

FIGURE 1. (continued)

REFERENCES

1. See, for example, H. Z. Cummins and P. E. Schoen, in "Laser Handbook", edited by F. T. Arecchi and E. O. Schulz-DuBois (North Holland, Amsterdam, 1972).

2. R. M. Martin, Phys. Rev. B1, 4005 (1971).

3. M. Cardona, in "Atomic Structure and Props. of Solids", edited by E. Burstein (Academic, NY, 1972).

4. Y. F. Tsay and B. Bendow, to be published.

5. D. A. Pinnow, op. cit., Ref. 1.

6. See, for example, Vol. 24 of "Solid State Physics", edited by F. Seitz et. al. (Academic, NY, 1973).

7. P. J. Melz, J. Phys. Chem. Solids 32, 209 (1970) and references therein.

8. See, for example, J. C. Phillips, "Bonds and Bands in Semiconductors" (Academic, NY, 1973).

9. M. L. Cohen and T. K. Bergstresser, Phys. Rev. 141, 789 (1966).

10. D. Brust, Sol. State Commun. 9, 481 (1971).

11. G. W. Gobeli and E. O. Kane, Phys. Rev. Lett. 15, 142 (1965).